UQAC

Université du Québec
à Chicoutimi

THÈSE PRÉSENTÉE À

L'UNIVERSITÉ DU QUÉBEC À CHICOUTIMI

COMME EXIGENCE PARTIELLE

DU DOCTORAT EN INGÉNIERIE

PAR

Mohamed Gamal Ramadan Mahmoud

EFFETS DE L'AJOUT DES METAUX TERRES RARES SUR LES PERFORMANCES DES ALLIAGES Al-Cu et Al-Si-Cu

Août 2018

UQAC
Université du Québec
à Chicoutimi

THESIS PRESENTED TO THE

UNIVERSITY OF QUEBEC AT CHICOUTIMI

IN PARTIAL FULFILLMENT OF THE

REQUIREMENT FOR THE DEGREE OF

DOCTOR OF PHILOSOPHY IN ENGINEERING

BY

Mohamed Gamal Ramadan Mahmoud

**EFFECTS OF RARE EARTH METAL ADDITIONS ON THE
PERFORMANCE OF Al-Cu AND Al-Si-Cu BASED ALLOYS**

AUGUST 2018

DEDICATION

My dear son Omar, I know that your brain is different from others however; the thoughts and emotions in it are as real, as valid, as beautiful and as important as anyone's. Omar, it is my pleasure to dedicate this thesis to you.

إهداء لأبني العزيز عمر

RÉSUMÉ

La crise de l'énergie fossile et la direction mondiale pour réduire les émissions de gaz à effet de serre, ont attiré l'attention des chercheurs sur la recherche de matériaux légers pour les applications d'économie d'énergie, en particulier dans les secteurs de l'industrie automobile. Des alliages à base d'aluminium, légers et à haute résistance, avec une résistance comparable à celle des matériaux lourds, tels que les aciers inoxydables et la fonte, pourraient révolutionner l'industrie automobile. Cependant, des facteurs majeurs limitants peuvent entraver leurs applications industrielles. L'un de ces facteurs est que la plupart des alliages d'aluminium ne sont pas capables de maintenir leurs propriétés optimales à des températures supérieures à 150 °C ou 200 °C. En conséquence, d'autres études sont encore nécessaires pour une compréhension globale du comportement des alliages d'aluminium dans le contexte des composants automobiles. La présente étude de recherche à été entreprise pour cette raison. Le projet visait à étudier l'effet de l'ajout des éléments de terres rares (Ce et La) individuellement pour améliorer les performances des alliages étudiés (B0) Al-1.2Si-2.4Cu-0.4Mg-0.4Fe-0.6Mn-0.15Ti (poids %) et (DO) Al-8,0Si-2,4Cu-0,4Mg-0,4Fe-0,6Mn-0,15Ti (% en poids).

La première phase de ce travail consistait à étudier l'effet d'ajouts de 1,0 et 5,0% en poids de RE (Ce/La) sur le comportement de solidification et la caractérisation microstructurale des alliages (AC) étudiés sous faible taux de refroidissement (0,7 °C / s). Les expériences d'analyse thermique (TA) et DSC ont permis d'examiner le comportement de solidification des alliages, tandis que la caractérisation microstructurale a été réalisée à l'aide de SEM / EDS et EPMA / WDS. Les résultats de l'analyse thermique ont révélé que les principales phases observées dans les alliages étudiés sont α-Al, α-Fe, Al-Si, Al2Cu + Q. Les résultats ont également présenté une baisse des paramètres de solidification, y compris les températures de nucléation (α-Al) et la température eutectique (Al-Si) est causée par l'ajout de RE (Ce / La), la baisse est plus nette avec l'ajout de 5,0 wt % de 1,0% en poids de RE (Ce / La). DSC a révélé que l'addition de métaux RE (La ou Ce) conduit à l'apparition de pics exothermiques dans les courbes de solidification et de chauffage entre la précipitation de la phase primaire α-Al et la réaction eutectique (Al-Al$_2$Cu). De plus, les résultats de DSC montrent que dans ce cas, le pic correspondant à la phase Al$_2$Cu est clairement perceptible dans les alliages de base et devient très réduit avec 1,0% en poids de RE (Ce / La), et disparaît avec 5,0% en poids de RE La) ajouts. Les résultats de la microstructure ont révélé que deux types principaux d'intermétalliques contenant des ER ont été documentés: une phase grise sous la forme de boue avec une composition fixe (Al$_{21}$Ti$_2$RE (Ce / La)). En outre, RE (Ce / La) réagirait avec Si, Fe et Cu conduisant à la formation de phase intermétallique contenant du RE blanc avec plusieurs compositions: (i) Alliage B0 (Al$_{11}$RE (Ce / La) $_3$ (Cu, Fe) $_4$Si$_2$,

Al$_4$Ce$_3$Si$_2$, Al$_5$La$_3$Si$_2$ et Al$_6$La$_2$ (Cu, Fe) $_2$Si); (ii) un alliage D0 (Al$_9$RE (Ce / La) $_4$Cu$_2$Si$_4$, Al$_2$RE (Ce / La) Si et Al$_2$CeSi). Lanthane et Ce peuvent se remplacer.

La seconde phase de l'étude a consisté à comprendre l'influence de l'ajout de 0,2 de 0,5 et 1,0% en poids de RE (Ce / La) sur les propriétés de traction des alliages testés à température ambiante, suivant diverses conditions de traitement thermique: AC) et solution traitée thermiquement (SHT). Les traitements de vieillissement (T5, T6 et T7) en référencent aux propriétés mécaniques présentées par les alliages de base et leurs équivalents modifiés par Sr ont également été considérés. Pour soutenir les résultats obtenus, l'analyse quantitative des phases secondaires et la mesure des particules de Si pour les alliages Al-Si-Cu (D0) ont été analysées pour les alliages étudiés. Les résultats ont révélé que lorsque l'addition de RE (Ce / La) augmente de 0,2 à 1,0% en poids, les quantités relatives d'intermétalliques augmentent, ce qui est attribué à la formation de nouveaux composés intermétalliques contenant des RE qui sont observés dans les régions interdendritiques. Les phases RE-intermétalliques sont également observées dans les échantillons traités thermiquement AC et T6 indiquant la nature insoluble de la phase La-intermétallique. Comme attendu, dans l'alliage D0 modifié de Sr moulé a montré la morphologie fibreuse du silicium eutectique. Alors que l'addition de 0,2% en poids de RE (Ce / La) a entraîné une modification partielle de la structure du silicium eutectique. L'efficacité de la modification, cependant, dépend du niveau d'addition de RE (Ce / La). Les résultats des essais de traction ont montré que pour tous les alliages, que ce soit l'alliage de base, le Sr modifié ou ceux contenant des ajouts de RE, les alliages T6 traités thermiquement présentent des valeurs élevées (UTS) par rapport aux SHT, T5 et T7 conditions de traitement. Les alliages traités thermiquement en solution présentent des valeurs de ductilité supérieures à celles obtenues dans les autres conditions. En ce qui concerne l'effet des ajouts de terres rares, les résultats ont indiqué que le niveau utilisé de RE joue un rôle efficace dans la détermination de l'influence de La et Ce sur les propriétés de traction de l'alliage. Les alliages présentant de faibles niveaux d'additions de Ce et de La présentent des valeurs UTS relativement meilleures, qui tendent à diminuer avec une concentration de RE plus élevée. Les résultats ont également conclu que l'influence de 0,2% en poids de RE (Ce / La) sur les propriétés de traction est plus ou moins la même que celle provoquée par l'addition de 150 ppm de Sr.

La dernière phase de ce travail était axée sur l'étude de l'impact de l'ajout de 0,2 de 0,5 et 1,0% en poids de RE (Ce / La) sur les propriétés de traction des alliages traités au T6 à haute température (250 ºC) après 1 et 200 heures de stabilisation à 250 ºC avant les essais. En plus d'étudier les caractéristiques de rupture des échantillons testés en traction dans les directions parallèle et perpendiculaire à l'axe de traction en utilisant la microscopie électronique à balayage (SEM) et la microscopie optique (OM), respectivement. En général, pour les deux alliages B0 et D0, les résultats ont montré que 200 heures de stabilisation à 250 °C entraînent une forte diminution de l'UTS et du YS, couplée à une forte augmentation de la ductilité par rapport aux valeurs obtenues après une heure de stabilisation à même

temperature. En ce qui concerne l'effet des ajouts de terres rares, semblable aux résultats de la température ambiante, 0,2% en poids. % Ce ou l'améliore l'UTS et YS de l'alliage B0 et D0 d'environ 10-15 MPa après une stabilisation d'une heure, avec peu ou pas de changement dans la ductilité. Comparer aux résultats des tests de traction à température ambiante, les alliages à RE plus élevé (Ce / La) conservant de bonnes propriétés de résistance à haute température avec une diminution négligeable comparable à celle des alliages de base, après une stabilisation d'une heure. L'examen au MEB des surfaces fracturées des alliages de base traités à T6 obtenus après 200 h de stabilisation à 250 °C a révélé la présence d'une microvoid, une structure de fossettes fine et uniformément répartie, indiquant une plus grande déformation plastique avant la fracture, en particulier les alliages B0. Dans le cas des alliages renfermant 1,0% en poids de RE (Ce), les fractographes au MEB ont révélé des caractéristiques considérablement différentes avec une grande taille de fossettes, plutôt que des fossettes distribuées uniformes observées dans l'alliage de base. En outre, une fracture de clivage, considérée comme une caractéristique d'une fracture fragile, a été observée. Le résumé des résultats de fractographie au microscope optique a montré que le processus de dommages des alliages étudiés se compose de trois événements mixtes: (i) fissuration des particules (α-Fe, Si), (ii) la formation et la croissance des microfissures, et (iii) microfissures. Cependant, la présence de composés intermétalliques contenant du RE influence le comportement à la rupture des alliages en fonction du pourcentage de RE ajouté. Lors de la déformation plastique, des contraintes sont imposées par la matrice (α-Al) sur les particules dans les microstructures. Des contraintes internes peuvent être induites sur les composés intermétalliques contenant de l'α-Fe, du silicium eutectique et du RE en raison d'une déformation inhomogène dans les alliages étudiés avec addition de RE.

ABSTRACT

The fossil fuel energy crisis and worldwide direction to reduce greenhouse gas emissions have triggered the attention of researchers to look for lightweight materials for energy saving applications especially in the automotive industry. High-strength, lightweight aluminum based alloys with strengths comparable to heavy materials such as stainless steel and cast iron could revolutionize the automobile industry and contribute in solving environmental concerns. However, certain limiting factors may hinder their industrial application. One of these factors is that most aluminum alloys are not able to maintain their optimum properties at temperatures above 150°C or 200 °C. Accordingly, further investigations are still required, to acquire a comprehensive understanding of the behavior of aluminum alloys in the context of elevated temperature applications. The present research study aims at investigating the effect of individual additions of Ce and La rare earth elements on improving the performance of Al-1.2Si-2.4Cu-0.4Mg-0.4Fe-0.6Mn-0.15Ti (wt.%) and Al-8.0Si-2.4Cu-0.4Mg-0.4Fe-0.6Mn-0.15Ti (wt.%) alloys, coded B0 and D0, respectively.

The first phase of this work was to study the effect of 1.0 and 5.0 wt.% additions of RE (Ce/La) on the solidification behavior and microstructural characteristics of the as-cast (AC) alloys under low cooling rate conditions (0.7 °C/s). Thermal analysis (TA) and differential scanning calorimetry (DSC) were used to examine the solidification behavior of the alloys. Microstructural characteristics were examined using scanning electron microscopy/energy dispersive spectrometry (SEM/EDS) and electron probe microanalysis/wavelength dispersive spectroscopy (EPMA/WDS) techniques. The thermal analysis results revealed that the main phases observed in the investigated alloys are α-Al, α-Fe, Al-Si, Al_2Cu and Q-$Al_5Cu_2Mg_8Si_6$ phases. The results also showed a drop in the nucleation temperature of α-Al and eutectic temperature (Al-Si) caused by the addition of RE (Ce/La); the drop was more clearly observed with the 5.0 wt.% RE (Ce/La) addition. DSC analysis revealed that addition of La or Ce leads to the appearance of exothermic peaks between the precipitation of the primary α-Al phase and the (Al–Al_2Cu) eutectic reaction in the solidification and heating curves. Also, the peak corresponding to the formation of the Al_2Cu phase is clearly noticeable in the base alloys (B0 and D0), becomes smaller with 1.0 wt.% RE(Ce/La), and disappears with 5.0 wt.% RE(Ce/La) additions. Microstructures revealed that two main types of RE-containing intermetallic phases were formed: a grey phase in the form of sludge, with a fixed composition $Al_{21}Ti_2RE$ (Ce/La), and white RE-containing intermetallic phases (resulting from reaction of the RE (Ce/La) with Si, Fe, and Cu); The latter exhibited several compositions: ($Al_{11}RE$ (Ce/La)$_3$(Cu,Fe)$_4Si_2$, $Al_4Ce_3Si_2$, $Al_5La_3Si_2$, and Al_6La_2(Cu,Fe)$_2$Si) in the B0 alloys, and (ii) (Al_9RE (Ce/La)$_4Cu_2Si_4$, Al_2RE(Ce/La)Si ,and Al_2CeSi) in the D0 alloys. Lanthanum and Ce can substitute each other.

The second phase of this study focused on understanding the influence of 0.2, 0.5, 1.0 wt.% additions of RE (Ce/La) on the room temperature tensile properties of the alloys, following various heat treatment conditions: as-cast (AC), solution heat-treatment (SHT), and aging (T5, T6 and T7), with reference to the properties exhibited by the base alloys and their Sr-modified counterparts. To support the results obtained, quantitative measurements of the volume faction of intermetallic phases and Si particle characteristics were carried out for the investigated alloys. The results revealed that increasing the RE (Ce/La) addition from 0.2 to 1.0 wt.%, increases the relative amount of intermetallics formed, which are attributed

to the formation of new RE-containing intermetallic compounds observed in the interdendritic regions. The RE-intermetallic phases are also observed in both the AC and T6 heat-treated samples indicating the insoluble nature of the La-intermetallic phase. As expected, the eutectic silicon particles in the as-cast Sr modified D0 alloy had fibrous morphology. While addition of 0.2 wt.% RE (Ce/La) resulted in partial modification of the eutectic silicon structure, the modification efficiency, however, depended on the addition level of RE (Ce/La). The tensile test results showed that the T6-treated alloys, whether the base alloy, the Sr-modified one, or those containing RE additions, exhibited higher (UTS) values compared to the SHT, T5, and T7 heat-treatment conditions. The solution heat-treated alloys displayed ductility values higher than those obtained for the other conditions. With respect to the effect of rare earth additions, the results indicated that the added amount of RE plays an effective role in determining the tensile properties. Alloys with low levels of Ce and La additions exhibited relatively better UTS values than those with higher RE concentrations. The results also revealed that the influence of 0.2 wt.% RE(Ce/La) on the tensile properties is more or less the same as that caused by the addition of 150 ppm Sr.

The last phase of this work investigated the impact of 0.2, 0.5, 1.0 wt.% additions of RE (Ce/La) on the tensile properties of the T6-treated alloys tested at high temperature (250 °C) after 1 and 200 hrs of stabilization at 250 °C prior to testing. The fracture characteristics of the tensile-tested samples in both parallel and perpendicular directions to the tensile axis were examined, using optical microscopy (OM) and scanning electron microscopy (SEM), respectively. In general, for both B0 and D0 alloys, the results showed that 200 hrs of stabilization at 250 °C produces a sharp decrease in the UTS and YS, coupled with a noticeable increase in ductility values, compared to the values obtained following one hour of stabilization at the same temperature. Regarding the effect of rare earth element additions, 0.2 wt.% Ce or La improved the UTS and YS of the B0 and D0 alloys by about 10-15 MPa following one hour of stabilization, with little or no change in the ductility. Compared to the room temperature tensile test results, alloys with higher RE (Ce/La) still maintained good strength values at 250 °C, with negligible decrease compared to those of the base alloys, following one hour of stabilization. SEM examination of the fractured surfaces of the T6-treated base alloys obtained after 200 hrs of stabilization at 250 °C revealed the presence of microvoids, and a fine, and uniformly distributed dimple structure, indicating a larger amount of plastic deformation prior to fracture especially in the B0 alloys. In the case of alloys containing 1.0 wt.% RE(Ce) the SEM fractographs, revealed considerably different characteristics, with large size dimples, rather than the uniformly distributed dimples observed in the base alloy. In addition, cleavage fracture, which considered as a characteristic of a brittle fracture, was observed. Examination of longitudinal sections beneath the fracture surface using an optical microscope showed that the damage process in the investigated alloys consists of three mixed events: (i) particle cracking (α-Fe, Si), (ii) microcrack formation and growth, and (iii) local linkage of microcracks. However, the presence of RE-containing intermetallic compounds influenced the fracture behavior of the alloys as a function of the percentage of the added RE amount. During plastic deformation, stresses are imposed by the matrix (α-Al) on the particles in the microstructures. Internal stresses may be induced on the α-Fe, eutectic silicon, and RE-containing intermetallic compounds due to inhomogeneous deformation in the alloys with RE additions.

ACKNOWLEDGEMENTS

PUBLICATIONS

Publications arising from the present PhD research study

1. A. M. Samuel, E. M. Elgallad, M. G. Mahmoud, H. W. Doty, S. Valtierra, F. H. Samuel, "Rare Earth Metal-Based Intermetallic Formation in Al-Cu-Mg and Al-Si-Cu-Mg Alloys: A Metallographic Study," Advances in Materials Science and Engineering, 2018.

Publications arising from other studies relating to the same PhD research topic

2. M. G. Mahmoud, A. M. Samuel, H. W. Doty, S. Valtierra, F. H. Samuel, "Effect of Rare Earth Metals, Sr, and Ti Addition on the Microstructural Characterization of A413.1 Alloy," Advances in Materials Science and Engineering, 2017.

3. M. G. Mahmoud, A. M. Samuel, H. W. Doty, S. Valtierra, F. H. Samuel, "Effect of Solidification Rate and Rare Earth Metal Addition on the Microstructural Characteristics and Porosity Formation in A356 Alloy," Advances in Materials Science and Engineering, 2017.

4. M. G. Mahmoud, E. M. Elgallad, M. F. Ibrahim, F. H. Samuel, "Effect of Rare Earth Metals on Porosity Formation in A356 Alloy," International Journal of Metalcasting, 2017.

TABLE OF CONTENTS

LIST OF FIGURES

CHAPTER 4 : CHARACTERIZATION OF SOLIDIFICATION BEHAVIOUR

CHAPTER 5: MICROSTRUCTURAL CHARACTERIZATION

CHAPTER 6: ROOM TEMPERATURE TENSILE TESTING RESULTS

CHAPTER 7: HIGH TEMPERARURE TENSILE TEST RESULTS

Appendix A: SEM IMAGES AND EDS SPECTRA OF Al-15% Ce and Al-15% La MASTER ALLOYS

Appendix C: OPTIMIZATION OF THE SHT OF B0 AND D0 ALLOYS

Appendix D: THERMAL ANALYSIS DATA SMOOTHING PROGRAM CODE

Appendix E: METALLOGRAPHIC CHARACTERIZATION IMAGES

LIST OF TABLES

CHAPTER 1

INTRODUCTION AND OBJECTIVES

CHAPTER 1

INTRODUCTION AND OBJECTIVES

1.1   MOTIVATION BEHIND THE THESIS

A growing environmental awareness in both the political and public perspective has led to new guidelines and market demands for limitations of greenhouse gas emissions in many industries, especially for those related to transportation (Figure 1.1(a)). One approach to conserving energy and reducing emissions is by minimizing moving masses (Figure 1.1 (b)). In addition, the rapid escalation of energy prices in the recent years has driven an increase in industrial demand for weight-saving materials in the automotive and aerospace industry as well as throughout the rail and road transport sector [1, 2].
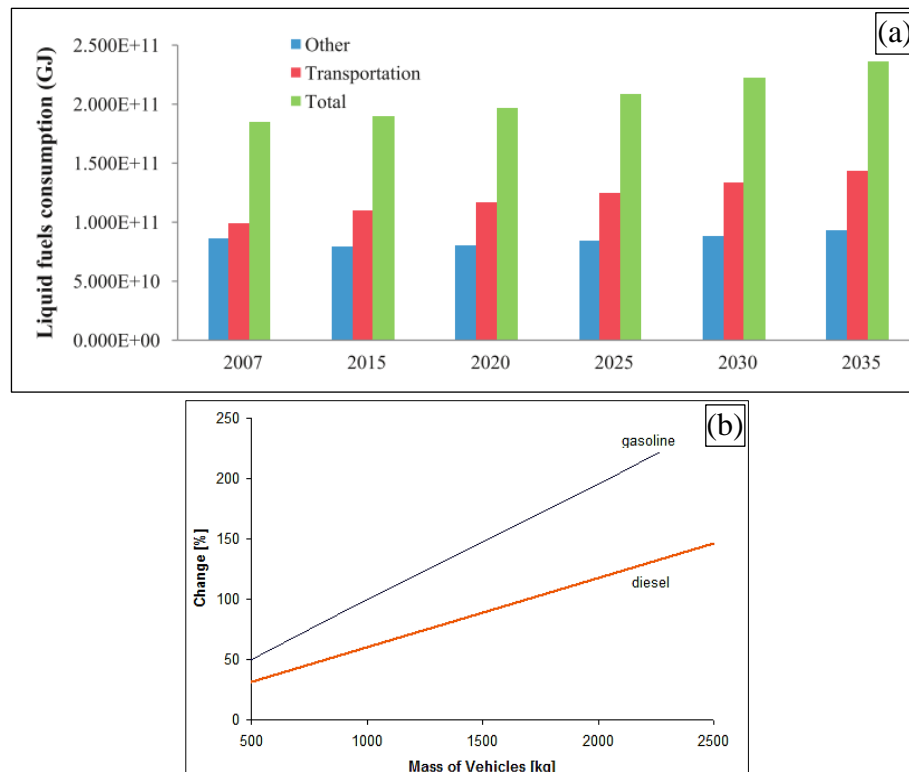
Figure 1.1: (a) Total world liquids consumption , transportation liquids consumption and other sectors liquids consumption between 2007 and 2035 (GJ) [2], (b) Road vehicles fuel consumption vs Mass [3].

Aluminum based alloys are of great interest in this area of application due to their relatively high strength-to-weight ratio, low cost, and provision of affordable improvement in the fuel efficiency(as shown in Figure 1.2). However, still most of aluminum alloys are soft and have inherently low mechanical strength, which hinders more widespread industrial application so further investigation and development of aluminum alloys are still needed. For this reason, the current study was motivated by interesting challenges arising from an interest in the development of aluminum-based alloys for automotive applications.
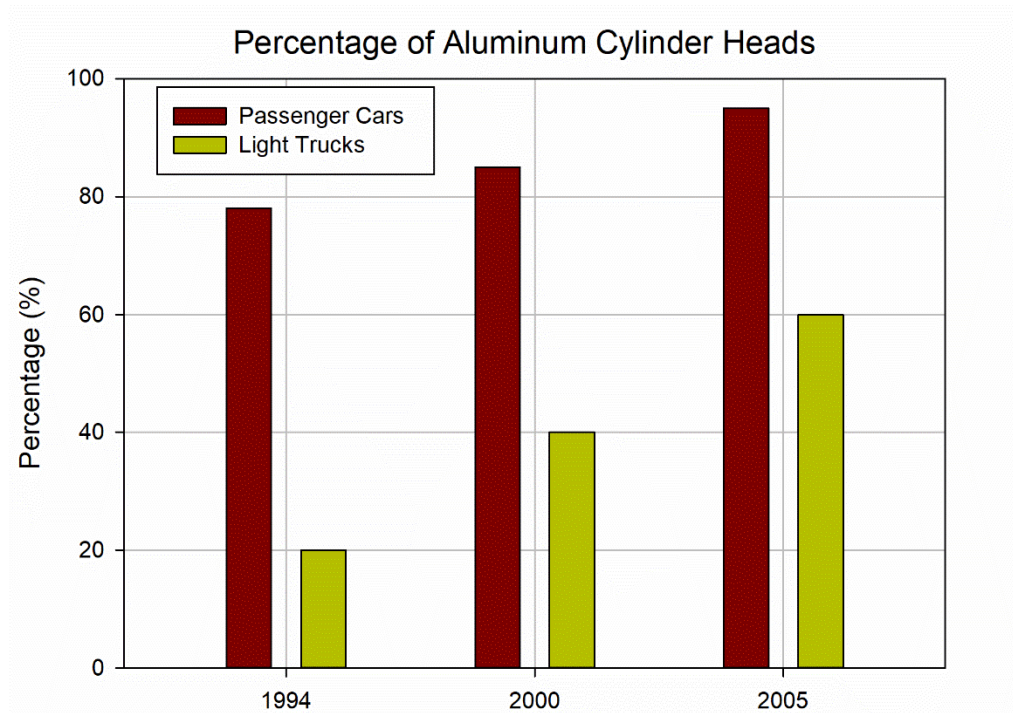
Figure 1.2: Evolution of aluminum as a cylinder head material over approximately the past two decades [4, 5].

1.2 ORIGINALITY OF THE WORK

Aluminum-copper (Al-Cu) based alloys are well known for their excellent properties such as high strength-to-weight ratio, excellent ductility, and good casting performance. In particular, such properties are very attractive to the transport industry, from aerospace to the automotive and naval sectors, where better performance and lower environmental impact can be achieved by decreasing the vehicle weight as maintained in the previous section. Nevertheless, these alloys cannot be produced by recycling aluminum scrap because a high degree of purity is required for casting which, in turn, increases the production cost. In addition, the high copper content in the Al-Cu casting alloys increases the density and cost of this category of alloys since the density of Cu is 9.92 g/cm^3. For example, if the amount of copper is decreased from 3.5 wt.% to 2 wt.%, it decreases the calculated alloy density from approximately 2.93 g/cm^3 to 2.78 g/ cm3, this can be a good achievement, especially when taking into consideration the size of the cast component which will be produced from the new alloy [6]. Another issue to consider is that if the Al-Cu alloy contains a high Si content, this increases the free Si in the aluminum matrix which causes problems from the machinability point of view [7, 8]. To overcome the limitation of Al-Cu alloys, extensive efforts have been made for producing new lightweight Al-Cu casting alloys with acceptable levels of tensile properties, and that are easy to recycle. One of these new alloys is GM220 alloy, being developed by TAMLA (Technologie Avancée des Métaux Légers pour les Applications Automobiles) research group at Université du Québec à Chicoutimi (UQAC) and General Motors, as a promising alloy for use in engine block and cylinder head applications [9].

GM220 alloy contains 2.4 wt.% Cu, 1.2 wt.% Si, 0.4 wt.% Mg, 0.4 wt.% Mn and 0.15 wt.% Ti. Based on this composition, the new alloy has the same phases found in A319 alloy expect for the Al-Si eutectic phase, which ensures a significant response to the precipitation hardening process; in addition to this, its chemical composition makes the new alloy lighter and cheaper to produce than A319 alloys that contains 5.5-6.5 wt.% Si and around 4.0 wt.% Cu. Accordingly, the new alloy can replace 319 alloys in similar applications since it provides higher yield and tensile strengths than does the 319 alloy [7].

Despite the good properties expected of the new alloy, it exhibits a high susceptibility to hot tearing which, in turn, leads to a decrease in the castability and lowers the casting quality, thus leading to deterioration in the tensile properties. The reasons for hot tearing in the new alloy are the low content of Si and Cu which decreases the amount of eutectic silicon formed and results in the long freezing range of the alloy [7].

These drawbacks hindered the use of the Al-Cu alloy GM220 in the industrial sector, so that the alloy required further research and development. In this context, the TAMLA research group conducted various studies to enhance the performance of this alloy to make it suitable for automotive industrial applications. The findings of these studies are discussed briefly and summarized in the following paragraphs.

Nabawy [7] investigated the influence of zirconium (Zr) and scandium (Sc) additions, on the microstructure, tensile properties, and hot tearing susceptibility (HTS) of GM220 alloy. It was found that the hot tearing susceptibility (HTS) decreased proportionally as the mold temperature was increased, decreasing from 21 to 3.0 as the mold temperature was increased from 250 $^{\circ}$ to 450 $^{\circ}$C. Also, it was found that Ti-B or Zr-Ti-B grain refinement additions enhanced the hot tearing resistance of the alloy to a significant level, whereas increasing the Si content reduced the HTS of GM220 alloy [10, 11].

Elgallad [8] investigated the effect of additives of Sr, Ti, Zr, Fe, Mn, and Ag as well as free cutting elements, specifically Sn and Bi, on the mechanical properties and machinability of GM220 alloy in both the as-cast and heat treated conditions. The results showed that:

- The additions of Sr refined the morphology of the α-Fe Chinese script phase and led to a slight improvement in the ductility.

- The additions of Zr improved the tensile properties due to grain refining action.

- Increasing the amount of Fe increased the precipitation of the Chinese script α-Fe phase particles, thus decreasing the tensile properties.

- The addition of Ag has no obvious effect to the strength; this is attributed to the presence of Si, which hinders the vital role of Ag in precipitation hardening.

- The addition of Bi reduces the strength properties in the heat -treated conditions as a result of the Bi-Mg interaction which suppresses the precipitation of the Mg-hardening phases.

- The addition of Sn decreases the strength properties due to the softening effect of Sn and the replacement of Si with Sn in the Mg-hardening phase Mg_2Si, as well as the formation of porosity arising from the melting of Sn during solution heat treatment.

- From the machinability point, the results showed that, with respect to machining performance, GM220 alloys display an acceptable compromise in machining performance between that of A356 and B319 alloys on the one hand, and that of the A319 alloy on the other [12, 13].

In another study, Zaki [14] investigated the effects of different alloying additions of Sr, Ti, Zr, Sc, and Ag, individually or in combination, on the performance of GM220 alloy.

The tensile test bars used in this study were prepared employing the low pressure die casting (LPDC) technique. The results showed that the alloy containing (0.5 % Zr + 0.15% Ti) was the most effective in maximizing the alloy tensile properties over the range of aging temperatures from 155 $^\circ$ to 300 $^\circ$C. Also, adding Ag simultaneously with 0.27 wt.% Zr was beneficial at high aging temperatures, in the range of 240 $^\circ$-300 $^\circ$C; with high addition of Zr (about 0.62 wt%), however, addition of Ag was less effective at the same level of Ti [6].

In spite of these previous studies, further investigations are still needed to fill in missing gaps of information in regard to the effects all metallurgical parameters (alloying additions, heat treatment conditions and testing temperature) on the mechanical properties of this alloy to acquire a comprehensive understanding of its behavior in the context of automotive components, particularly in regard to its performance under high temperature service conditions. The present research study was undertaken for this reason.

1.3   DEFINITION OF THE PROBLEM

Eutectic silicon is a dominant constituent phase in Al-Si alloys, and refining its morphology can further enhance the attractive characteristics of these alloys. The practice of eutectic modification has been developed to produce a refined eutectic structure and can be brought about by using modifier additions, termed chemical modification [15, 16] and/or by applying a high cooling rate, termed quench or chill modification [17, 18].

In chemical modification, commonly used modifier additions such as strontium (Sr), sodium (Na), calcium (Ca), and antimony (Sb) are added to the alloy melt in trace amounts to modify the eutectic silicon morphology from an acicular to a fine fibrous form. However, these traditional modifiers are associated with certain limitations such as fast fading in the case of Na, formation of porosity with the addition of Sr, and toxicity in the case of Sb.

Nevertheless, strontium is most commonly used in industry due to its overall advantages compared to the others. However, the fact that its utilization increases the amount of dross restricts its usage in practice.

Rare earth (RE) metals have also been investigated as modifiers, one of the reasons being their availability in abundance in nature in the form of mischmetal (MM). Cerium (Ce) and Lanthanum (La) elements together comprise approximately 90% of mischmetal (MM) in addition to praseodymium (Pr) and neodymium (Nd). These two elements La and Ce are also the cheapest among the sixteen members of the rare earth metal family [19].

In the case of RE metals, their atomic radii relative to that of silicon (r/r_{si}) lies in the order of ~1.65, a value conducive to modification via the twin plane re-entrant edge (TPRE) mechanism, which promotes the fibrous coral-like growth of the eutectic silicon phase. Generally, from the point of view of modification of the Si phase, all the rare earth metals have an atomic radius ratio that theoretically satisfies the modification efficiency criterion in that the ratio of the modifier element atomic radius relative to that of Si, viz., r/r_{Si}, is close to the optimal value of ~1.65, as shown in Figure 1.3.

Although the previous studies reported in the literature [19] investigated the modification effects of rare earth metals, the mechanism of modification using these elements is still unclear. For example, Nogita et al. [20] investigated the role of Eu and Yb in the modification of Al-10%Si alloys, selecting these two rare earth elements as having the most optimal r/r_{Si} ratios. They found, however, that despite these optimal ratios, only Eu showed a uniform distribution of the modified eutectic Si fibres, similar to the case of Sr modification; whereas Yb precipitated, but not in the eutectic Si or Al, resulting in a refinement of the plate-like eutectic Si rather than a flake-to-fibrous transition. They concluded that the r/r_{Si} ratio used to predict impurity-induced twinning behavior observed in

Si fibres is not sufficient in itself and that all microstructures exhibiting fibrous eutectic silicon must exhibit a uniform distribution of the modifier in the Si phase.
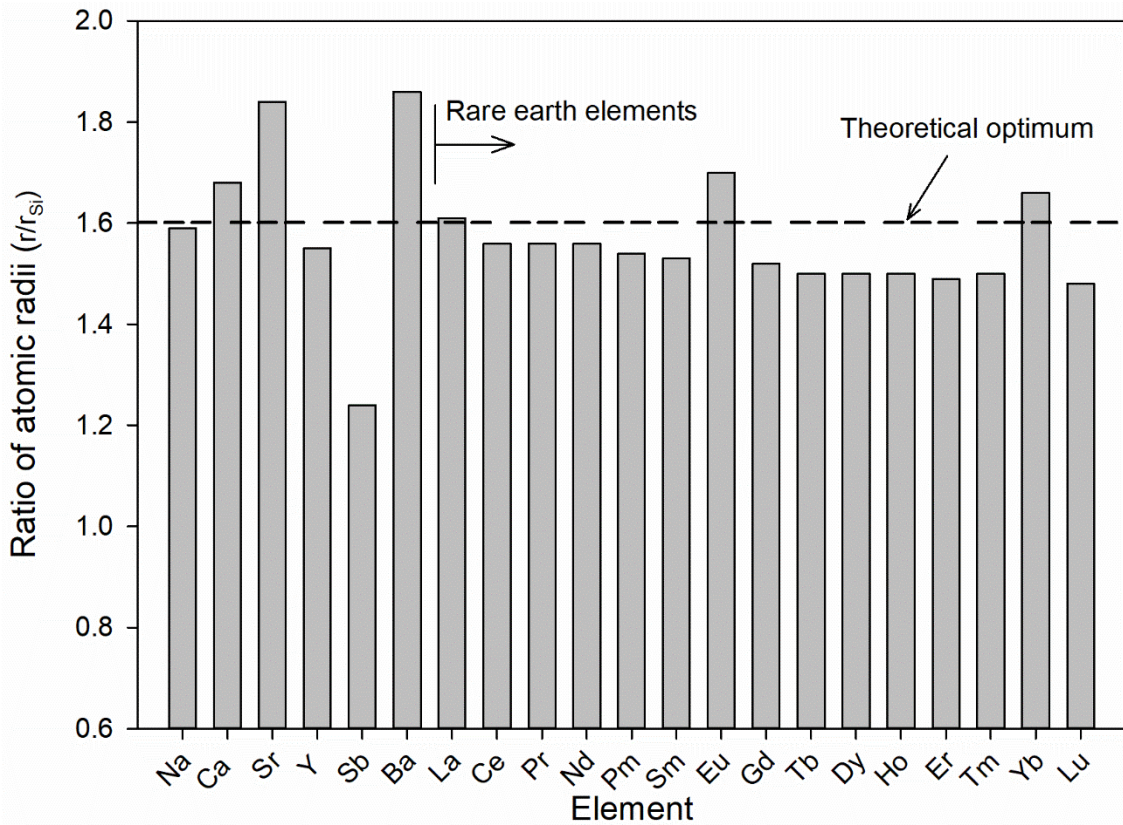
Figure 1.3: Ratio of atomic radii vs. atomic number [21].

In addition to eutectic modification, the ability of RE metals to refine the microstructure of an aluminum alloy, namely the grain size [22], secondary dendrite arm spacing (SDAS) [23, 24] and the β-iron Al_5FeSi intermetallic phase has also been documented in the literature [25]. However, previous literature reveals that there is a lack of investigations on (i) the morphology, size and distribution of the RE-containing intermetallic compounds formed, and (ii) their influence on the tensile properties.

As the use of RE as modifiers has increased in the recent past, this area of research has become increasingly important and needs to be addressed more comprehensively. With this in mind, the main contribution of the current study was to investigate thoroughly the

effects of Cerium (Ce) and Lanthanum (La) on the microstructure and performance of GM220 alloy. A small addition of Strontium (Sr), in the amount of 150 ppm, was also used for purposes of comparison.

1.4 THESIS OBJECTIVES

The main aim of this Ph.D. research project was to investigate the effects of La and Ce additions on the tensile properties of two series of GM220 alloys, subjected to various heat treatment conditions. The two series were prepared using: (i) low Si (1.2 wt.%) B0 alloy, and (ii) high Si (8.0 wt.%) D0 alloy as the base alloys. The influence of individual additions of La and Ce on the microstructure, and the resulting properties and fracture behaviour were also studied. The main objectives of the current study therefore covered:

1. Examining the influence of 1.0 and 5.0 wt.% of Ce and La on the microstructural features and solidification behaviour of the alloys prepared in order to have a better understanding of the phases and intermetallics present in the structure.

2. Studying the effect of the following metallurgical parameters on the tensile properties and the quality index values of B0 and D0 alloys :

    i.   La additions (0.2, 0.5, 1.0 wt.%);

    ii.   Ce additions (0.2, 0.5, 1.0 wt.%);

    iii. Sr addition (150 ppm);

    iv.   Heat treatment conditions.

    - Solution heat treatment (SHT) at 510 $^{\circ}$C for 8 hours ;

    - T5 (aging at 180 $^{\circ}$C for 8 hours) ;

    - T6 (SHT at 510 $^{\circ}$C for 8 hours followed by 8 hours aging at 180 $^{\circ}$C);

    - T7 (SHT at 510 $^{\circ}$C for 8 hours followed by 8 hours aging at 240 $^{\circ}$C);

3. Studying the high temperature tensile properties of T6-heated B0 and D0 alloys subjected to one and 200 hrs of stabilization at the testing temperature of 250 $^{\circ}$C with the different additions of Ce and La (0.2, 0.5, 1.0 wt.%).

4. Correlating the room and high temperature mechanical properties with the microstructural features of the corresponding alloys.

5. Using quality charts based on the tensile properties obtained for various alloy/heat treatment conditions in order to recommend the optimum parameters /conditions for improving the properties of GM220 alloys for use in specific industrial applications.

1.5 THESIS ORGANIZATION

This thesis is scientifically organized into eight chapters as follows:

The opening chapter, CHAPTER 1, defines the motivation and objectives of this research work.

CHAPTER 2 pertains to the literature review covering the general aspects of Al-Cu alloys, followed by an extensive review of the previous studies and investigations on the effect of different types of RE metals on the performance of aluminum alloys.

CHAPTER 3 presents the experimental procedures used and provides details of the alloys and additives used in the current study, the casting and heat treatment procedures used, and the various mechanical testing and microstructural characterization methods employed for determining the alloy properties and examining the microstructures of the alloys obtained in this study.

CHAPTER 4 presents an analysis of the solidification behaviour of the alloys investigated, using differential scanning calorimetry (DSC) and thermal analysis (TA) techniques.

CHAPTER 5 presents the results of the microstructural characterization and phase identification using: (i) Scanning electron microscope (SEM) with Energy dispersive x-ray spectroscopy (EDS) facilities, and (ii) Electron probe micro-analyzer (EPMA) with wavelength dispersive spectroscopy(WDS) facilities.

CHAPTER 6 presents the tensile test results of the investigated alloy obtained at room temperature, while CHAPTER 7 provides the results obtained at elevated temperature, together with a section on the fracture behavior of the tested alloy samples.

CHAPTER 8 presents the conclusions of this study based on the findings presented in CHAPTER 4 through 7, and recommendations for future work. Finally, a list of references and appendices are provided at the end of the thesis.

CHAPTER 2

LITERATURE REVIEW

CHAPTER 2

LITERATURE REVIEW

2.1 FUNDAMENTALS BACKGROUND OF Al-Cu ALLOYS

2.1.1 Microstructure of Al-Cu Alloys

The solidification of Al-Cu alloys starts with the development of a dendritic network followed by a eutectic reaction in the interdendritic regions by means of which the eutectic Al_2Cu is formed in combination with the remaining aluminum [26]. Consequently, the microstracture of Al-Cu alloys consists mainly of primary α-A1 and the Al_2Cu phase. In order to meet the requirements of rapidly developing industrial applications, major alloying elements such as Si and Mg, minor alloying elements such as Ni and Sn, and elements like Ti, Sr, and Mn which modify the microsturcutre are added to Al-Cu alloys to improve their mechanical properties (Figure 2.1) [27]. The addition of these elements is associated with the formation of much more complex intermetallic compounds, part of which are insoluble.

One of the critical issues with respect to the microstructure of Al-Cu alloys is the unwanted presence of impurities in Al-Cu alloys, in particular, iron (Fe) which in turn leads to the formation of insoluble Fe-intermetallic such as $π$-$Al_8Mg_3FeSi_6$, $β$-Al_5Fe_2Si, and α-$Al_{15}(Mn, Fe,Cu)_3Si_2$. These intermetallics are harmful and adversely affect the mechanical properties of the alloy, especially ductility, and lead to formation of excessive shrinkage porosity defects in the casting. A number of investigators have mentioned that the presence of the $β$-Al_5FeSi iron intermetallic phase prevents the liquid metal feeding by blocking the interdendritic liquid-metal channels, thus resulting in the formation of porosity [28-30].
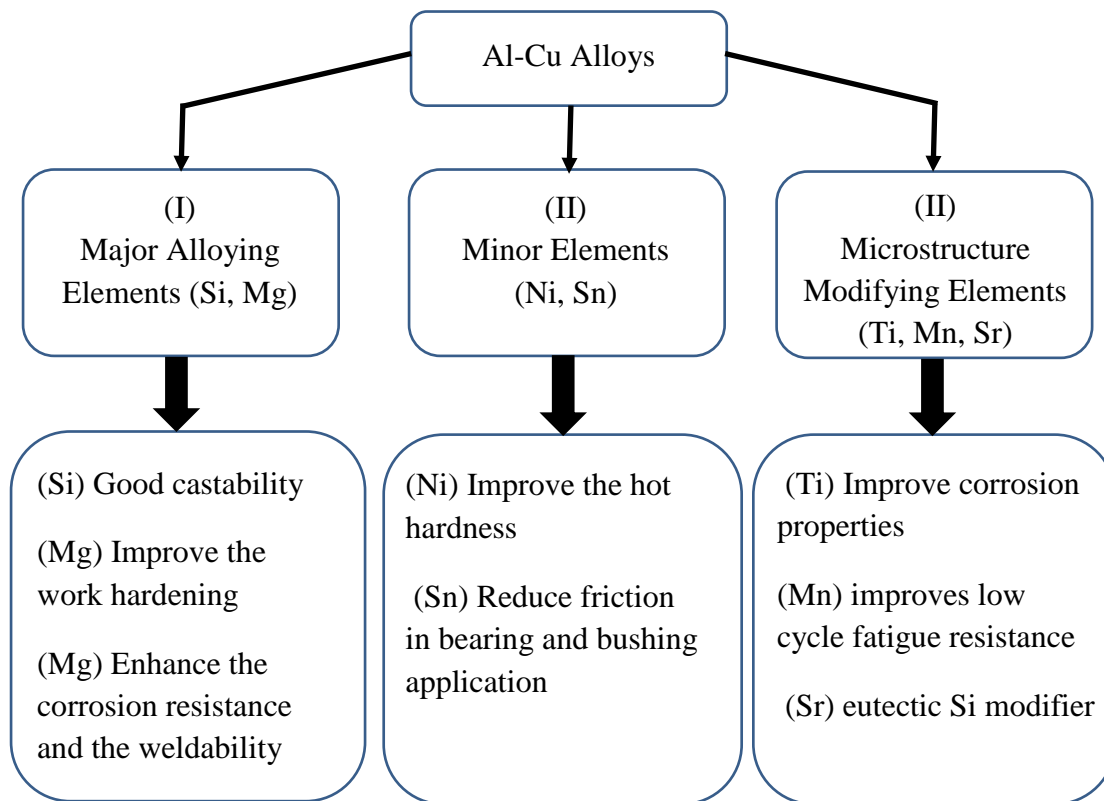
Figure 2.1: Effect of alloying elements on the performance of Al-Cu alloys [27].

2.1.2 Heat Treatment of Al-Cu Alloys

Heat treatment is one of the main techniques applied to enhance the mechanical properties of aluminum casting alloys. Aluminum-copper cast alloys are considered heat-treatable alloys. Figure 2.2 illustrates the temperature ranges of the heat treatments applied to Al-Cu alloys. From Figure 2.2 it may be noted that in order to produce a complete solid solution, the solution heat treatment range of Al-4.5Cu alloy is 515 to 550°C in which the Cu completely dissolves (Figure 2.2). This solid solution will become supersaturated as the temperature decreases to below 515°C. In order to produce the age hardening of an Al-4.5Cu alloy, it should be maintained within a temperature range of 150°C to 220°C for a pre-determined aging period. [31]. In general, in order to age harden Al-Cu alloys, it is important

to conduct the heat treatment process through three steps, as follows: (i) solution heat treatment, (ii) quenching, and (iii) aging, which will be discussed briefly and summarized in subsections 2.1.2.1, 2.1.2.2, and 2.1.2.3, respectively.
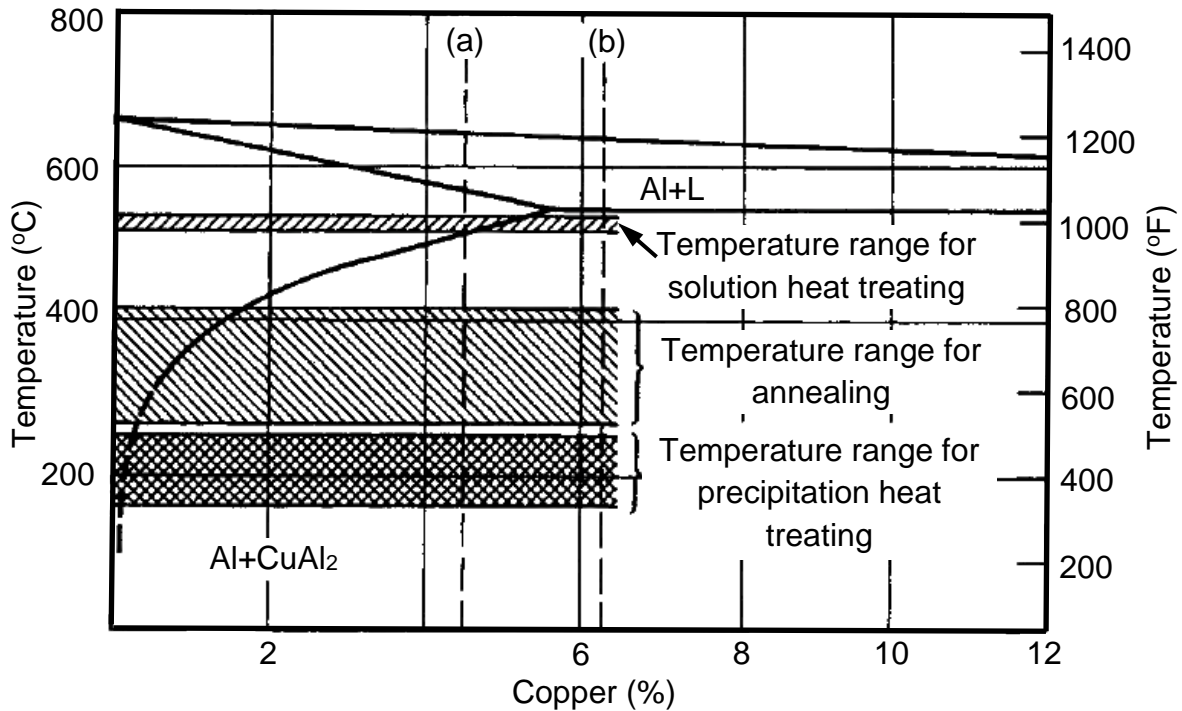
Figure 2.2: Heat treatment temperature range for heat treating of Al-Cu alloys [31].

2.1.2.1   Solution Heat Treatment

The solution heat treatment process is carried out to maximize the solubility of elements in the matrix such as Cu and Mg, to help in dissolving the intermetallic phases which are formed during solidification, and to increase the homogeneity of the microstructure. Temperature and time are the main parameters which control the solution heat treatment process. The temperature of solution treatment, in particular, is considered a critical parameter in Cu-containing alloys due to the occurrence of incipient melting of the Cu phases.

Samuel [32] summarized the topic of incipient melting of $Al_5Mg_8Si_6Cu_2$ and Al_2Cu intermetallics in 319-type alloys and concluded that, although a high solution temperature enriches the Cu concentration in the supersaturated solid solution structure, there is a critical temperature for Cu-containing aluminum alloys such as 319 alloy which cannot be exceeded due to the occurrence of incipient melting. This critical temperature is determined based on the lowest eutectic-melting point of the intermetallic constitution or, in other words, of the melting point of the phases last to solidify. Copper-rich intermetallics, such as Al_2Cu (θ) and $Al_5Mg_8Cu_2Si_6$ (Q), are the main intermetallics facing the possibility of melting during solution heat treatment because of their low melting points of 507°C and 525°C, respectively [26] . The incipient melting takes place at and above the corresponding eutectic temperature as a result of the reduction in the Gibbs free energies as postulated by Reiso et al. [33].

In alloys containing silicon as an alloying element, the Si particle morphology has a vital role in characterizing the mechanical properties. Under normal cooling rates, the silicon particles appear as coarse acicular needles, which act as crack initiators and reduce the mechanical properties to an observable degree. This type of deleterious silicon morphology is responsive to treatment by means of chemical or thermal modification. When applying thermal modification, the casting is subjected to a high temperature solution heat treatment for the required length of time. A number of studies by Apelian et al. [34], Tillova and Panuskova [35], and Li et al. [36] investigated the effects of thermal modification on silicon particles. In these studies, it was found that the silicon particles became modified through a special sequence triggered by the breaking down of silicon particles into small fragments followed by the gradual spheroidization of these fragments. Prolonged solution heat treatment causes the undesired coarsening of silicon particles. The high solution temperature

leads to high rates of spheroidization and coarsening. The main driving force for the spheroidization and coarsening of silicon particles is the reduction of surface energy.

2.1.2.2   Quenching

The purpose of this stage is to maintain a high degree of supersaturated solid solution as well as to provide excess vacancies, all of which may be obtained by applying a high cooling rate. Quenching is a critical heat treatment stage in which the subsequent precipitation behaviour is determined. Heterogeneous precipitation occurs intensively at intermediate temperatures under low cooling rates because of relatively high supersaturation and high diffusion rates. Accordingly, the resulting heterogeneous precipitation at low quenching rates will consume the solutes from the matrix and, consequently, will reduce the subsequent age-hardening response. This outcome leads to lower ultimate tensile and yield strength, as well as lower ductility values and fracture toughness [37-39]. The high quenching rate in Al-Cu alloys or Cu-containing alloys tends to enhance strength values.

It should be noted that the quenching medium is the factor, which determines the quenching rate and heat extraction rate. The quenching medium for wrought alloys is usually cold water, whereas the castings and complex shape parts are immersed or quenched in warm water between 65°C and 80°C or in solutions such as polyalkylene glycol. Molten salt and low-melting eutectic baths have also been used as quenching media [40, 41].

2.1.2.3   Aging

The age hardening of aluminum-copper alloys has been the subject of intensive scientific investigation for a number of decades now by numerous researchers [42-44]. Throughout the aging process, the supersaturated solid solution is decomposed by heating it to a point below the equilibrium solvus line as well as to below the GP solvus line to produce

artificial aging, or otherwise by keeping it at room temperature for an extended length of time in order to produce natural aging. Figure 2.3 illustrates the solvus lines of the different metastable and stable phases of the Al-Cu binary system. At the beginning of the precipitation process, the solute atoms segregate in special crystallographic planes of the matrix forming zones (GPZI and GPZII). These zones are fully coherent with the matrix and measure 1-5 nm. Depending on the aging temperature and aging time, these zones can be developed to subsequent semi-coherent metastable and equilibrium phases.

The fully coherent precipitates usually form and remain more stable at higher aging temperatures than the semi-coherent and non-coherent precipitates because of their lower solvus lines, as may be seen in Figure 2.3. The presence of fully coherent zones and the semi-coherent metastable phase strengthens the matrix by inhibiting and/or hindering the dislocation movement [45].
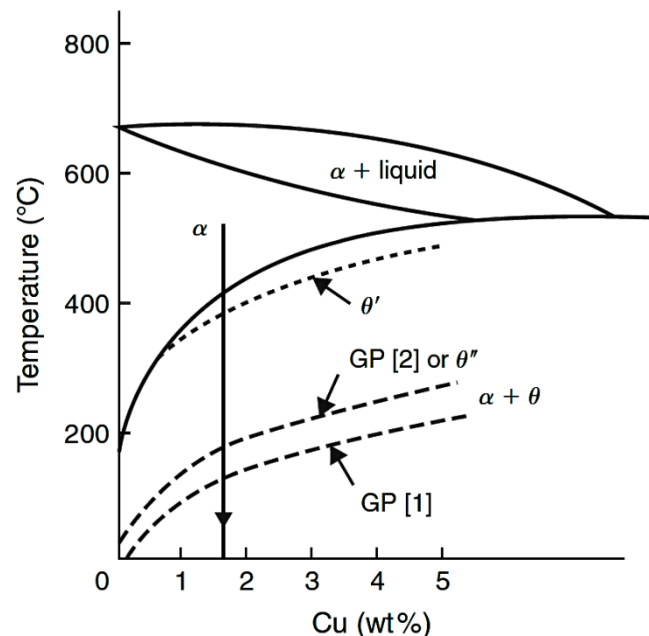
Figure 2.3: Partial equilibrium diagram of Al-Cu alloys representing the solvus lines of the metastable and equilibrium phases [45]

2.2 QUALITY INDICES OF ALUMINUM-SILICON ALLOYS

2.2.1 Concept of the Quality Index

The mechanical properties of Al-Si casting alloys are related directly to various metallurgical parameters involved in the production process. The quality of Al-Si castings can be expressed in terms of their mechanical properties through a concept knows as quality index. The quality of Al-Si casting alloys is considered a key factor in selecting an alloy casting for a particular engineering application. Deciding upon the right alloy quality thus involves reaching a suitable compromise between numerous factors to present the least possible risk with maximum performance in combination with adequate cost effectiveness. Alloy composition, solidification rate, heat treatment procedures, casting defects, and such microstructural features as grain size and intermetallic phases, are all parameters, which closely affect alloy quality since they also influence the mechanical properties of the casting. The concept of quality indices and quality charts has been proposed by several researchers as listed below in chronological order. In what follows, only the models proposed by Drouzy et al. and Câceres, being the ones most commonly used, will be presented in subsections 2.2.2 and 2.2.3, respectively.

a) Quality Index (Q) proposed by Drouzy et al. [46].

b) Quality Index (Q_N) proposed by Din et al. [47].

c) Quality Index (Q_c) proposed by Câceres [48, 49].

d) Quality Index (Q_D) proposed by Alexopowlos and Panteiakis [50-53].

e) Quality Index (Q_E) proposed by Tiryakioglu et al. [54].

2.2.2 Quality Index (Q) Proposed by Drouzy et al.

Based on their investigations of the tensile properties of Al-7%Si-Mg alloys, Drouzy et al. [46] were the first to propose the concept of quality index in 1980 to define the quality of aluminum alloy castings, where the quality index Q provided a correlation to the tensile properties of the alloy, through the use of an equation relating the quality index to the ultimate tensile strength and elongation to fracture as presented by Equation 2.1:

$$Q = \sigma_{UTS} + d\log{(E_f)} \qquad \qquad \text{Equation 2.1}$$

where Q is the quality index in MPa, σ_{UTS} refers to the ultimate tensile strength in MPa; E_f refers to the percentage elongation to fracture; and the parameter d is material constant and was empirically found to equal to 150 MPa for Al-7%Si-Mg alloys.

On the other hand, the study of correlations between tensile strength, 0.2% yield strength, and percentage elongation-to-fracture in cast aluminum alloys showed that the probable yield strength, YS (MPa), may be estimated using Equation 2.2 .

$$\sigma_{P(YS)} = a\,\sigma_{UTS} + b\log{(E_f)} + c \qquad \qquad \text{Equation 2.2}$$

where the coefficients a, b, and c for Al-7Si-Mg were determined as 1, 60, and -13, respectively, while the constants b and c are expressed in units of MPa [55].

From the above equations, quality charts can be generated, where the two equations represent sets of parallel iso-Q and iso-YS lines. Equation 2.1 is used to generate the iso-Q lines in the quality charts proposed by Drouzy et al. [46], whereas Equation 2.2 is used to generate the iso-probable yield strength lines. The quality chart generated using Equation 2.1 and Equation 2.2 is shown in Figure 2.4. These quality charts are generated for use as a simple method of evaluating, selecting, and also predicting the most appropriate

metallurgical conditions which may be applied to the castings to obtain the best possible compromise between tensile properties and casting quality.
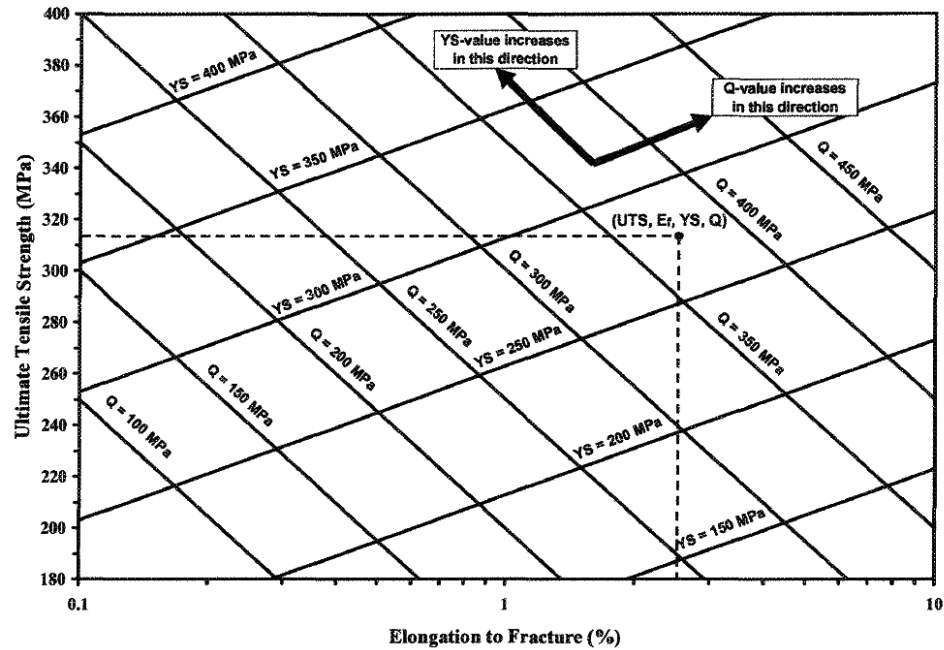
Figure 2.4: Example of quality chart proposed by Drouzy et al. [46]

2.2.3 Quality Index (Qc) proposed by Câceres

The drawback of the quality index concept proposed by Drouzy et al [46] is that it was given no proper theoretical grounding or explicit physical meaning. This gap in its physical basis has been bridged by the analytical model created by Caceres [48, 49] which allows calculation of the quality index from knowledge of the parameters of the deformation curve, namely, the strength coefficient of the material and the strain-hardening exponent. The analytical model by Câceres is based on the assumption that the deformation curves of the material can be described with Holloman equation given in Equation 2.3 and represented by log-log plot of true stress versus true strain, as shown in Figure 2.5 [56, 57]

22

$$\sigma = k\varepsilon^n \qquad \text{Equation 2.3}$$

were σ is the true stress, ε is the true plastic strain, n is the strain-hardening exponent, and K is the strength coefficient. The values of n and K may be calculated from a log-log plot of true stress versus true strain, as shown in Figure 2.5.
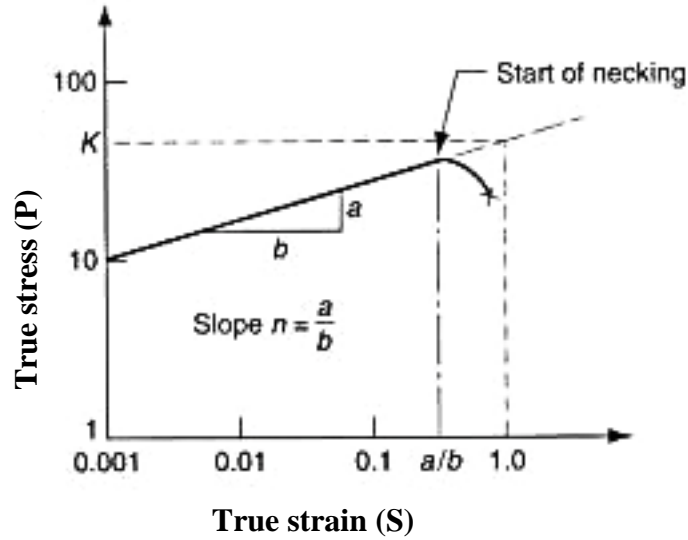
Figure 2.5: True stress strain -curve plotted in log scale

The strain hardening exponent n calculated from Equation 2.4

$$n = \left(\frac{\varepsilon}{\sigma}\right)\left(\frac{d\sigma}{d\varepsilon}\right) \qquad \text{Equation 2.4}$$

The true stress σ and the engineering stress P are related by Equation 2.5

$$\sigma \, A_f = P \, A_0 \qquad \text{Equation 2.5}$$

where A_0 and A_f are the initial and final cross sectional areas, respectively. According to the assumption that the volume is constant during deformation, Equation 2.6 can be obtained as follows:

$$\frac{A_0}{A_f} = e^{\varepsilon_t} \qquad\qquad \text{Equation 2.6}$$

where ε_t is the total true strain which has elastic and plastic components. From Equation 2.3, Equation 2.5, and Equation 2.6, Equation 2.7 can be determined.

$$P = K\,\varepsilon^n\,e^{-\varepsilon_t} \cong K\,S^n\,e^{-S} \qquad\qquad \text{Equation 2.7}$$

where S is the engineering plastic strain. In Equation 2.7 , the sign $\cong$ indicates that the elastic strain component as well as the difference between the engineering and true strain have been disregarded. The latter is a reasonable assumption for casting alloys due to their limited ductility.

Equation 2.7 has been used to draw the family of solid flow curves for the A356 alloy (Al-7%Si-0.4%Mg) with K = 430 MPa, as shown in Figure 2.6. The curves are identified by values which vary between 0.2 for as-quenched samples and 0.08 for samples at 170°C for 6 hours. The values of the strength coefficient, K, and the strain hardening exponent, n, were obtained from the true stress-true strain curves of Al-7%Si-Mg alloys [49]. The YS-values on the right hand side axis indicate the flow stress (MPa) at an offset strain of 0.2%. As reported by Câceres [48], for a given aging condition the flow curve of the most ductile samples represents the locus of the UTS/elongation-to-fracture points of the samples with the same yield stress but lower ductility. Thus, the solid flow curves in Figure 2.10 may be interpreted in terms of the concept of Drouzy et al. [46] as corresponding to "iso-YS" lines, relating UTS and elongation-to-fracture, each for a particular aging condition.
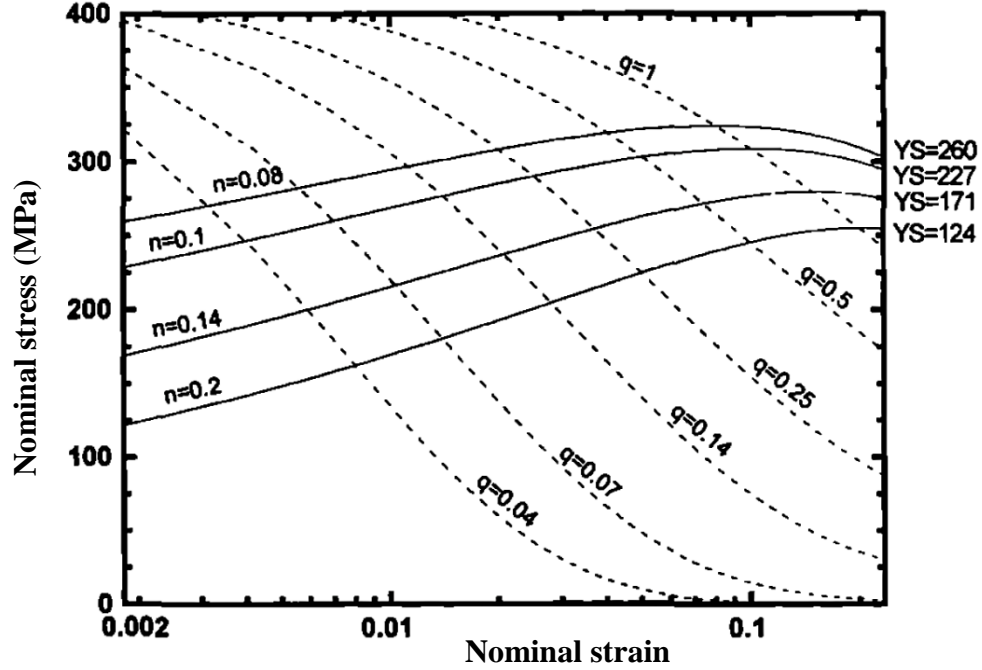
Figure 2.6: The quality index chart proposed by Câceres for A356 alloy [48].

In the case of high ductility castings, tensile failure involves some amount of necking. Necking begins when the Considère criterionis met [58, 59], that is $y=1$, where y is the strain-hardening parameter defined as

$$\gamma = \left(\frac{1}{\sigma}\right)\left(\frac{d\sigma}{d\varepsilon}\right)$$

Equation 2.8

On comparison between Equation 2.4 and Equation 2.8, it can be found that $\gamma = n/\varepsilon$. Thus, when $\gamma = 1$, this implies that $\varepsilon^* = n$, where ε^* is the true plastic strain at the onset necking. Assuming the $S^* = \varepsilon^* = n$, the relative ductility parameter q, defined as the ration between the engineering plastic strain at failure q, defined as the ration between the engineering plastic strain at failure, S_f, and the engineering plastic strain at the onset of necking S^*, is given by

$$q = \left(\frac{S_f}{S^*}\right) = \left(\frac{S_f}{n}\right)$$

Equation 2.9

25

From Equation 2.7 and Equation 2.9, Equation 2.10 can be defined as

$$P = K \, S^{s/q} \, e^{-S}$$

Equation 2.10

Figure 2.6 illustrates that, Equation 2.10 can be used to generate the lines representing contours of constant relative ductility called "*iso-q*" lines, each line identified by a *q*-value. The usefulness of q resides in the fact that it expresses how far a particular sample is from its maximum possible ductility. The sample, which deform up to or beyond necking (i.e. $q \geq 1$) have the highest combination of elongation and UTS or be of the best quality possible, while the samples which fail before the onset of necking (i.e. $q \geq 1$) will be of lesser quality . This concept provides a straight forward physical meaning for the quality index, Q, in terms of the relative ductility parameter, it implies that "*iso-q*" lines are roughly equivalent to the "*iso-Q*" generated by Drouzy et al. [46].

2.3 REVIEW ON THE EFFECTS OF RARE EARTH METALS

In this section, the microstructures and mechanical properties of aluminum alloys containing different rare earth elements additions are discussed. A number of scientific investigations are reported in the literature on the effects of rare earth elements and mischmetal (MM), which is a mixture of RE elements found in abundance in nature with Cerium (Ce) and Lanthanum (La) together comprising approximately 90% of mischmetal. The RE metals investigated include Cerium (Ce), Lanthanum (La), Yttrium (Y) [60-70], Erbium (Er) [21, 71-83], Neodymium (Nd) [84-88], Ytterbium (Yb) [21, 60, 61, 89-95], Samarium (Sm) [19, 96-101], Scandium (Sc) [102-111], Europium (Eu) [21, 112-114], and Gadolinium (Gd) [115]. Among these, as the effects of MM, Ce, La and mixture additions of Ce and La were investigated in the present study, only these will be discussed the subsections 2.3.1, 2.3.2, 2.3.3, and 2.3.4 that follow.

26

2.3.1 Effects of Mischmetal (MM) Additions

Yuyong et al. [116] investigated the effects of small amounts of mischmetal (MM) on the dendrite arm spacing, and the Brinell hardness of Al-1.0% Mg-0.5% Si alloy. Their results showed that in the range of 0.5 - 4.0 wt.% MM the hardness increased by more than 30% and dendrite arm spacing decreases from 50 µm to 18 µm. Ravi et al. [117] investigated the mechanical properties, and microstructure of cast Al-7Si-0.3Mg(LM25/356) and reported that the addition of above 1.0 wt.% of MM lowered the YS, UTS and percent elongation with increase in the Brinell hardness. The mechanical properties decreased due to the formation of Ce and La hard intermetallic compounds in the matrix and consumption of a certain amount of Mg toward formation of these compounds, which led to reduction in the strengthening constituent Mg_2Si formed, contributing to the observed decrease.

Chang et al. [118, 119] reported on the microstructure and thermal analysis of Al-21wt.% Si alloys with MM addition. Their results showed that 2.0 wt.% MM additions lead to a morphological change in the primary Si crystals from star-like to polyhedral shape [118]. The thermal analysis results revealed that addition of 3.0 wt.% of MM leads to depression of 12-17 ^{o}C in the primary Si reaction temperature and 2-7 ^{o}C in eutectic Si temperature. Zhang et al. [120] reported that increasing the level of MM additions to in situ Al-15Mg_2Si composite alloy leads to: (i) a reduction in the size of Mg_2Si particles, (ii) a change in the morphology of eutectic Mg_2Si from a fibrous to a flake like, and (iii) formation of RE-containing compounds in the form of $Al_{11}RE_3$.

Ravi et al. [121] studied the effect of 1.0 wt.% MM additions on the microstructural characteristics and the room and elevated temperature tensile properties of Al-7Si-0.3Mg

(LM 25/356) alloy containing excess iron up to 0.6 wt.%. With addition of 1.0 wt.% to the LM25 alloys, the results showed that:

(i)   Alloys with Fe contents ranging from 0.2 to 0.6 wt.%, exhibit grain refinement and partial modification of the eutectic silicon and the finer intermetallic compounds formed with Ce, La, and other elements, thereby improving the strength as well as the ductility of the alloy relative to the same alloys without an MM addition.

(ii)   Alloys containing 0.6 wt.% Fe , led to the formation of fine and fibrous shaped intermetallic compounds containing Fe and Si with fine and fibrous shape, which reduced the effective amount of Fe available for formation of β and π phases, thereby reducing the size and volume of Fe-containing intermetallic, which, in turn, reduced the deleterious effect of Fe and improved the strength and ductility of the alloy.

Weiwei et al. [122] investigated the influence of different levels of MM up to1.0 wt.% additions to microstructures and properties of a high strength aluminum cast alloy. They found that MM addition refined the grain size of the alloy studied and changed the eutectic Si morphology from needle-like and laminar to a granular type. Also, with the increase of the MM level, the tensile strength and elongation of the alloy first increase and then begin to decrease. Alloy with 0.7 wt.% MM exhibited the highest mechanical properties. In another study, Chong et al. [123] studied the combined effects of P and MM on the microstructure and mechanical properties of hypereutectic Al-20%Si alloy. It was observed that, in general, alloys with the addition of 0.08% P and 0.60% MM exhibited highest mechanical properties and had the optimal microstructure compared with the alloy with no addition; refinement of the primary Si particles from 66.4 µm to 23.3 µm, and the eutectic silicon from 8.3 µm to 5.2

µm, was also noted. With respect to the mechanical properties, the ultimate tensile strength improved from 256 MPa to 306 MPa, and the ductility increased from 0.35% to 0.48%.

El Sabaie et al. [124-127] investigated the influence of MM, cooling rate and heat treatment on the hardness and microstructural observation of unmodified and Sr-modified A319.1, A356.2 and A413.1 Al-Si casting alloys. From these studies, the authors noted the following:

(i)   In general, the hardness measurements revealed that the hardness values of the as-cast alloys were higher at high cooling rates than at low cooling rates. With addition of MM, the hardness decreased at both cooling rates [125].

(ii)   The addition of MM to the non-modified as-cast alloys partially modified the eutectic silicon particles. This effect was more pronounced in the A413.1 and A319.1 alloys, compared to A356.2 alloy [126].

(iii)   The effect of MM as a modifier is more effective at high cooling rate (corresponding to DAS~40 µm) than at the low cooling rate (DAS~120 µm) for all the as-cast non-modified alloys [126].

(iv)   MM-containing intermetallic phases were observed at high and low cooling rates, each exhibiting a specific Ce/La ratio and morphology. Many of these MM-containing intermetallic phases were found to contain Sr, which confirmed the interaction of MM with Sr [127].

Li et al.[128] studied the effect of combined additions of MM, Fe and Mn on the microstructure and performance of A390 alloy. They showed that the combined addition is an effective way to improve the strength of A390 at elevated temperature, which increased by 25%. Other studies by Zhu et al. [129, 130] reported the effects of 0.1-1.0 wt.% Ce-based MM additions on the microstructure, tensile properties and fracture behavior of as-cast and

T6-treated A356 alloys. The main findings from their work are listed below for the conditions.

MM-modified as-cast A356 alloys [129]

(i) MM-containing intermetallic compounds cannot act as potential nucleate sites for primary α-Al phases.

(ii) The modification effect of MM depends on the addition level. Minor additions of MM (less than 0.2 wt.%) result in partial modification, while more than 0.3 wt.% MM leads to full modification.

(iii) The fracture path goes through the interdendritic region composed of eutectic silicon and MM-containing intermetallic compounds.

MM-modified T6 A356 alloys[130]

(i) T6 heat treatment has great influence on the spheroidization of eutectic silicon particles in MM-modified A356 alloys than that in the unmodified alloys.

(ii) The UTS, YS, and %EL of the T6-treated A356 alloys with and without modification are improved due to the spheroidization of eutectic silicon particles and Mg_2Si precipitation hardening.

(iii) SEM images show that the MM-modified T6 A356 alloy undergoes ductile fracture. It is worth noting that the eutectic silicon and MM-containing intermetallic particles provide the weak locations for initiation the fracture.

Mousavi et al. [131] investigated the effects of different level of additions (0.0-1.0 wt.%) of La-based MM and heat treatment on the microstructure and tensile properties of two different sections of Al-Si casting alloy A357. The results showed that optimum levels of MM additions are 0.1 wt.% and 0.3 wt.% for thin and thick sections of the casting,

respectively. Examination of the microstructure characterization showed that at high level of addition, a new AlSiLa intermetallic phase was detected. In addition, the results demonstrated that T6 heat treatment improved the tensile properties of the modified alloys.

Jiang et al. [23] reported the effects of MM addition on the microstructure, tensile properties and fracture behavior of as-cast and T6 A357 alloy. The results obtained showed that addition of MM reduced the size of the primary α-Al dendrites i.e., the SDAS value and also improved the eutectic Si particle morphology. Accordingly, the MM-modified A357 alloy exhibited improvement in the tensile properties, particularly the elongation, in the T6-treated condition. The fracture surface of the tensile-tested sample of the unmodified alloy showed a clear brittle fracture, whereas that of the MM-modified A357 alloy exhibited dimple rupture and cracked eutectic Si particles, resulting in superior ductility.

Zhang et al. [22] studied the cooling rate sensitivity of AlTiB grain refiner, MM and ALTiB-MM additions and the resultant effects on the microstructure and mechanical properties of A356 alloy in laboratory scale experiments and in actual industrial application (production of alloy wheels). The results demonstrated that the AlTiB-MM addition provided the most effective and synergetic refinement compared to the individual AlTiB or MM additions. In addition, the properties of A356 alloy wheel refined by the AlTiB-MM addition were improved significantly. The tensile strength, yield strength, and elongation of the wheel spokes improved by approximately 11.3%, 10.8% and 44.1%, respectively.

Dang et al. [132] investigated the effects of rare earth (RE) additions in the form of Al-10%RE master alloy and pouring temperature (1124 K through 1524 K in increments of 100 K) on the microstructure and mechanical properties of T6-treated Al-25%Si alloy. The authors observed that for the unmodified alloy, the primary Si morphology was transformed form platelets to fine polyhedral form, and the average size decreased with increasing pouring

31

temperature (from 125 µm at 1124 K to ~ 62 µm at 1524 K). With a 1.2 wt.% RE addition, the primary Si exhibited a small blocky morphology, with an average particle size of 47 µm. In addition, the study showed that T6 MM-Al-25%Si alloy exhibited an improvement in the mechanical properties compared to the unmodified alloy, where the maximum tensile strength and elongation (208.3 MPa and 1.01%) where obtained for the sample modified with 1.2 wt.% RE followed by the T6 heat treatment. The RE contained a mixture of Ce and La derived from mischmetal.

   In another study, Zhang et al. [133] reported the effect of MM additions on the microstructure and performance of Al-3.0 wt.% Mg alloy used for producing electromagnetic shielding wire. The strength reached the highest value with 0.3 wt.% MM addition; the elongation varied little when the MM addition was no more than 0.2 wt.% MM. However, the excessive addition of MM would be harmful to the microstructure and properties of Al-3.0 wt.% Mg alloys.

2.3.2 Effects of Cerium Additions

Xiao et al. [134] investigated the precipitation hardening response, microstructure and mechanical properties of three Al-Cu-Mg-Ag based alloys containing 0.0, 0.20 and 0.45 wt.%Ce, using transmission electron microscopy (TEM) and differential scanning calorimetry (DSC). It was found that increasing the Ce content from 0.0 to 0.45 wt.% increased the tensile strength at all test temperatures up to 350 ^{o}C. The high strength of the alloys with Ce is attributed to the high density and high thermal stability of fine Ω precipitates. In another study, Xiao et al. [135] reported that the minor addition of 0.2 wt.% Ce to the alloy together with 0.25 wt.% Ti induced a harmful effect on the mechanical properties. This was attributed to the formation of the intermetallic $Al_xTi_6Ce_3Cu$

intermetallic compound that decreased the tensile strength of the as-cast alloy and reduced the age hardening response.

Zhang et al. [136] studied the effect of Ce additions on the modification mechanism of the hypereutectic Al-18Si alloy under different casting condition. They reported that with Ce addition, the morphology of the primary Si changed from a branched shape to a fine shape. Also, the modification of the eutectic Si improved with increasing the Ce addition to the melt, where the modification of the eutectic Si in areas away from the primary Si was more obvious than in regions close to the primary silicon particles.

Song et al. [137] reported on the effect of combined and individual additions of 0.3 wt.% Ce and 0.2 wt.% Ti on the microstructure and mechanical properties of Al-Cu-Mg-Ag alloy. The results arising from this investigation showed that individual addition of Ce or Ti can decrease the grain size of the as-cast alloy, increase the nucleation rate of the Ω (metastable Al_2Cu) phase, inhibit the growth of the Ω phase during aging, and thereby increase the volume fraction and decrease the spacing of Ω phase. Based on these microstructural effects, the yield strength and tensile strength of the alloy are increased. However, combined addition of Ce and Ti leads to the formation of (Ce, Ti)-containing intermetallic compounds and increases the grain size during casting, but have no influence on the nucleation and the growth of the Ω phase during aging. The alloy containing both Ce and Ti has a relatively lower Vickers hardness and strength compared to the alloy containing individual additions of Ce or Ti. In another research, Song et al. [138] reported that Ce improves the thermal stability of the Ω phase by decreasing the diffusion velocity of the Cu atoms, and hence decreasing the coarsening speed of the phase, as well as through the aggregation of Ce atoms at the Ω phase/Al matrix interface, increasing the energy barrier for

the thickening of the Ω phase plates which coarsen through a ledge nucleation mechanism. The strength of the Al-Cu-Mg-Ag alloy is improved, as a result.

Kores et al. [139] investigated the effects of different levels of Ce additions on the microstructure, thermal behaviour and mechanical properties of hypereutectic AlSi17CuMg alloy. The results showed that additions of Ce (up to 1.0 wt.% Ce) can achieve refinement of the primary and eutectic Silicon morphology .In general, the alloy with 1.0 wt.% Ce addition exhibited the best results with respect to the microstructural and strength properties. It was also observed that the addition of 1.0 wt.% Ce produced the greatest reduction in the liquidus temperature from 686.6 ºC to 591.9 ºC.

Tsai et al. [140] investigated the modification effect of different levels of Ce on the microstructure, thermal analysis and mechanical properties of cast A356 aluminum alloys. They reported that A356 alloy modified with 1.0 wt.% Ce greatly improved eutectic silicon modification; however, the thermal analysis revealed that there is no direct relation between the eutectic growth temperature and silicon modification. The microstructural characterization showed that two kinds of Ce-containing intermetallic phases were found, including Ce-23Al-22Si and Al-17Ce-12Ti-2Si-2Mg (in wt.%). While the ductility of the Ce modified alloys was enhanced for Ce addition of 0.6 wt.% and above, there was no positive effect on the ultimate tensile strength, which was attributed to the formation of the Al-17Ce-12Ti-2Si-2Mg phase which reduced the amount of free Mg available for precipitation of the Mg_2Si strengthening phase.

Voncina et al. [141, 142] reported the effects of various concentrations of Ce (0.0, 0.01, 0.02, 0.05 and 0.1 wt.%) on the solidification and mechanical properties of AA A360 (Al-10%Si-0.5%Mg) alloy .The results showed that the solidus temperature decreased with increasing Ce addition. The eutectic ($\alpha_{Al}+Mg_2Si$) temperature also decreased with Ce

addition. It was found that the precipitation enthalpy decreased with the Ce addition, while precipitation occurred more rapidly and intensively, indicating increased reaction kinetics. Mechanical properties like tensile strength and hardness also increased with the Ce addition, where the hardness of the investigated alloy may be attributed to the phase composed of Al, Ce, Mg and Si. It is worth noting that in another study Voncina et al. [142] reported that addition of Ce to A380 alloy led to a change in the morphology of eutectic Al_2Cu phase from ″crumbled″ to fully formed (finer eutectic-like to blocky form) and caused the formation of small primary crystals of α_{Al} which resulted in grain refining of the alloy. A needle-shaped AlCeCuSi phase ($Al_9Ce_2Cu_5Si_3$) was also detected.

Chen et al.[143] studied the effects of Ce and Sr addition on the nucleation of primary α-Al phase dendrites in hypoeutectic Al-7%Si-Mg cast alloy. They found that with addition of Ce and Sr, the grain size of the dendritic α-Al phase becomes well refined, decreasing from 150 µm to 90 µm, and is attributed to the exponential increase in nucleation frequency (10^{24}), compared to the unmodified alloy, and restricted growth.

The effect of Ce addition (0.0, 0.3, 0.5, 0.8 and 1.0 wt.%) on the microstructure and mechanical properties of hypereutectic Al-20%Si alloy were investigated by Li et al. [144], where they found that with increasing the Ce addition level, the primary Si crystals were significantly refined and the morphology of the eutectic Si phase was modified from coarse platelet like to a fine fibrous structure. Accordingly, the ultimate tensile strength (UTS) and elongation (%El) increased by 68.2% and 53.1%, respectively, as a result of these effects.

Ye et al. [145] investigated the influence of Ce content (0.2% and 0.4 wt.%) on the impact properties and microstructures of 2519A aluminum alloy, a new version of 2519 alloy (with a higher Cu/Mg ratio) used for armor material. Based on the results of their research, it

was found that 0.2 wt.% Ce addition leads to an increase in the volume fraction of the precipitation phase, in addition to more dispersive and homogeneous distribution of finer θ' (Al_2Cu) precipitates, which result in improving the ability of the alloy for absorbing impact energy. Formation of Al_8Cu_4Ce phase which is thermally stable at high temperature is also expected to enhance the high temperature mechanical properties of the alloy. Yii et al. [146] reported that the addition of Ce in the Al-20%Si alloys refined the Si primary phase as the Ce additions were increased. The results also showed that addition of Ce in the range of 0.46 to 2.24 wt.% led to the formation of fine cells dispersed in the Al-matrix. These cells consisted of a mixture of eutectic Si particles and Ce-containing intermetallic phases (Al_3Ce and $CeAl_{1.2} Si_{10.8}$). The amount of the intermetallic phases increased with increasing Ce addition.

Promising scientific investigations were made by Ahmad and coworkers [24, 147, 148] on the influence of Ce on the microstructure of a commercial Al-11%Si-Cu-Mg eutectic cast alloy (ADC12). The main finding from their studies are summarized below.

(i)   The addition of Ce to ADC12 alloy leads to improvement in the Si particles modification and reduces the Si particle size by 62% [147].

(ii)   Cooling rate has no significant effect in the 1.5 wt.% Ce-modified ADC12 alloy, compared to the base alloy and this may be attributed to formation of intermetallic phases [147].

(iii)   Investigation of the Al-Si eutectic phase using the thermal analysis technique showed that addition of Ce had a significant effect on the nucleation, growth, and minimum temperatures of Al-Si, and decreased as the Ce concentration increased, and refinement of the Si structure was observed up to 1.0 wt.% Ce.

In addition, the growth and nucleation temperatures of the Al–Cu phase, which is the last phase to solidify, also increased with the increased with increasing level of Ce. The formation of Ce-containing intermetallic compounds such as Al-Si-Ce and Al-Si-Cu-Ce affected the degree of Si modification [148].

(iv)   Ce addition refined the secondary dendrite arm spacing (SDAS) by approximately 36%. In addition, the tensile strength and quality index of Al-11%Si-Cu-Mg increased to 237.6 MPa and 265 MPa, respectively, after the addition of 0.1 wt.% Ce [24].

2.3.3   Effects of Lanthanum Additions

Yi and Zhang [149, 150] investigated the influence of La added in pure rare earth element form on the modification of hypereutectic Al-17%Si and Al-22%Si alloys. Different morphologies of the primary Si phase were observed, namely, feathery, polygonal, star-shaped and platelet forms. They reported that the eutectic Si in unmodified Al–Si alloys appears, in the form of long needle-like crystals, while discrete and interconnected coral and rod-like eutectic Si particles are observed in alloys with the addition of La. They also observed that with La addition, the La rich containing intermetallic phase formed grows into a variety of morphologies, such as needle-like, broken rod-like (in pores), spherical and flat platelet. With the addition of La to hypereutectic Al-17%Si alloy, La begins to form intermetallic compound, especially when La addition exceeds approximately 1.0 wt.%. These compounds could be represented as $Al_1Si_2La_2$ containing $LaSi_2$ and an unknown ternary Al_xSi_yLa phase [144]. In another research Yi et al. [151] reported that the addition of 3.0

wt.% La to A390 alloy leads to only a slight modification of the silicon particles as a result of the formation of the compounds $Al_7Si_7Cu_2La_{3.5}$ and $Al_5Mg_8Cu_6Si_6$.

Ouyang et al. [152] stated that addition of La to hypereutectic Al-Si alloys can enhance the effect of phosphorus on the modification of the primary Si phase, and the higher the La content at the Al-Si interface, the smaller the primary Si particle size obtained. In another research, the influence of different amounts of La on the microstructure and mechanical properties of A356 alloys was investigated by Tsai et al. [153]. Their findings indicated that the modification efficiency with respect to the microstructures, and mechanical properties obtained with 1.0 wt.% La are similar to those observed with the use of 0.01 wt.% Sr. Furthermore, the results of thermal analysis revealed that there is no direct relationship between eutectic growth temperature and silicon morphology/modification rating.

A mechanism by which La modifies the Fe-bearing intermetallics in a 6xxx series Al alloy was proposed by Mosseinifar et al. [154]. They reported that during solidification, the addition of lanthanum results in the formation of the $La(Al,Si)_2$ phase, depleting the remaining melt of Si. In addition, they hypothesized that the decreased Si/Fe ratio in the melt caused by the presence of La favors the formation of the α-AlFeSi phase, which is less detrimental to the formability of the alloy than the β-AlFeSi phase. Yuan et al. [155] reported that La addition decreased the peak-aged hardness during the aging process of Al-Mg-Si-Zr alloys based on AA 6201. However, increasing the La content to 0.3% led to a poor elongation at fracture.

Huang and Yan [156] investigated the effects of various La additions on the microstructure of as-cast ADC12 (Al-11%Si-Cu-Mg) alloy. The results indicated that the α-Al and eutectic Si crystals were modified with the addition of 0.3 wt.% La. The eutectic Si crystals showed a granular distribution. At the same time, the alloy possessed the best

mechanical properties. However, as the La addition was increased beyond 0.3 wt.%, the microstructure coarsened gradually and the mechanical properties decreased as a result.

In another study, Song et al. [157] analyzed the impact of different additive amounts of La (0.0, 0.3, 0.6, and 0.9 wt.%) on the microstructure and hot crack resistance of ADC12 alloy. The results showed that, as the La added increased from 0.0% to 0.6 wt%, the structure of the α-Al phase gradually varied from a well-developed dendritic crystal into fine dendritic crystal, equiaxed crystal and spheroidal crystal; the eutectic silicon varied from needle-like or tabular shape into fine rod-like shape; the hot cracking force of the alloy also gradually decreased. Optimum alloy modification, alloy refinement and hot cracking resistance were achieved at 0.6 wt.% La addition. However, when the additive amount of La reached 0.9 wt.%, the excessive amount of La segregated at the grain boundaries, forming intermetallic phases.

A scientific study made by Chen et al. [158] to investigate the effects of combined addition of La and B (boron) on the grain refinement of Al-Si casting alloys, revealed that such additions can effectively refine the grains of Al-Si alloys compared to the individual addition of boron. This work also reported that with addition of La, the tensile properties of the alloy, in particular, the elongation are enhanced.

The effects of trace addition of La (0.05%- 0.1 wt.%) on the microstructures and tensile properties of B-refined and Sr-modified Al-11%Si-1.5%Cu-0.3%Mg casting alloys were investigated by Lu et al. [159]. It was found that introducing La/B in the weight ratio of 2:1 produced well refined of α-Al grains and modified eutectic Si particles in the alloy studied, as well as strengthening intermetallic precipitates which improved the ultimate tensile strength and elongation from 234 to 270 MPa and from 4.0 to 5.8%, respectively.

Ahmad et al. [160] carried out a systematic study of the effects of various La concentrations on the solidification parameters of eutectic Al-Si-Cu-Mg alloy. They reported that the nucleation and growth temperatures of eutectic Si decreased when 0.3 wt.% La was added, whereas with 1.0 wt.% La, a large depression in temperature was obtained. The thermal analysis results recorded a faster freezing time with La addition.

Qiu et al. [161] investigated the synergistic effect of Sr and La on the microstructure and mechanical properties of A356.2 alloy. It was found that, with the addition of 0.5 wt.% Al-6Sr-7La master alloy, the alloy exhibited optimal microstructure and mechanical properties, with the secondary dendrite arm spacing (SDAS) decreasing to 17.9 μm and the acicular eutectic silicon transforming to a fibrous form. With the improved microstructure, the ultimate tensile strength, yield strength and elongation of the alloy (with 0.5 wt. % Al-6Sr-7La) increased to 228.15 MPa, 108.13 MPa and 11.92%, respectively, which were much better than that of the "traditionally treated" A356.2 alloy (using 0.2 wt.% Al-5Ti-1B for grain refining and 0.2 wt.% Al-10Sr for Si modification). Similarly, Tang et al. [156] studied the effect of Sr and La addition on the microstructure and mechanical properties of a secondary Al-Si-Cu-Fe alloy. The metallographic quantification results indicated that addition of different levels of Sr and La modification agents, added in the form of Al-10%Sr and Al-10%La, produced varied refinement effects on the mean length of needle-like phases and SDAS value. The total dosage of Sr and La varied from 0.04 to 0.2 wt.% (Sr/La=1:1). The minimum mean length of needle-like phases (Sr/La=1:1) and the SDAS value (Sr/La=1:5) were obtained by setting the addition amount of the modification agent at 0.12 wt.%. The mean length of the needle-like phase dropped from 364 to 55.3 μm, while the SDAS decreased from ~ 22 to 9.7 μm, i.e., by 84.5% and 55.8%, respectively.

Further to the above studies [161, 162], Ding et al. [163] investigated the effect of solution treatment on the microstructure and mechanical properties of A356.2 alloy modified with Al-Sr-La master alloy. The optimal solution treatment parameters for A356.2 aluminum alloy treated with Al–6Sr–7La comprised solution treated at 540 $^{\circ}$C for 3 h, followed by quenching in warm water at 60 $^{\circ}$C. In addition, it was reported that under these conditions, the alloy exhibited the optimal microstructure, eutectic silicon morphology, UTS, YS, and %EL values, which proved beneficial to the subsequent aging process.

In a recent article, Li et al. [164] have investigated the effects of Ti and La additions on the microstructure and mechanical properties of B-refined and Sr-modified Al-11%Si alloys. Their findings show that the addition of 0.05 wt.% B induces a transformation of the eutectic Si from finely fibrous to coarse plate-like morphology in the Al-11%Si alloy modified with 0.02 wt% Sr, owing to the poisoning of impurity induced twinning (IIT) mechanism, so that the eutectic Si growth occurs only by the twin plane re-entrant (TPRE) mechanism. Both Ti and La can neutralize the poisoning effect of the interaction between Sr and B in the Al–11%Si alloy; however, the neutralizing effect of La is dependent on the addition sequence. The combined addition of La and B elements promotes the effective refinement of α-Al grains, but an inhomogeneous modification of eutectic Si phases is also observed, leading to a slight decrease in the elongation.

2.3.4   Effects of Mixed Cerium and Lanthanum Additions

Aguirre-De la Torre et al. [165] investigated The effect on microstructure and mechanical properties of the automotive A356 aluminum alloy reinforced with 0.2 wt.% Al-6Ce-3La (ACL). In this study, the ACL was added to the molten A356 alloy in the as-received condition and also processed by another route, employing mechanical milling and powder metallurgy techniques. Scanning electron microscopic observations indicated a homogeneous dispersion of La/Ce phases using both routes. In regard to the mechanical properties, however, the modified A356 alloy with the ACL added in the as-received condition, showed an improvement in the mechanical performance of the A356 alloy over that reinforced with the mechanically milled ACL. Also, Wang et al. [165, 166] studied the effects of mixed La and Ce rare earth additions on the microstructure and properties of Al-0.75%Mg-0.6%Si alloy. The results showed that the mixed addition of La and Ce had a positive effect on the grain refinement of the investigated alloy. Accordingly, the tensile strength and elongation of Al-0.75%Mg-0.6%Si gradually increased with the increase in the amount of La and Ce added.

Another study carried out by Du et al. [167] investigated the effect of 0.25 wt.% and 0.50 wt.% mixed additions of Ce and La on the microstructure and mechanical properties of an Al-Cu-Mn-Mg-Fe alloy. With mixed addition, two intermetallic phases, Al_8Cu_4Ce and Al_6Cu_6La, were formed. The results also showed that the 0.25 wt.% addition could promote the formation of a denser precipitation of $Al_{20}Cu_2Mn_3$ and $Al_6(Mn,Fe)$ phases, which improved the mechanical properties of the alloy at room temperature. However, up to 0.50 wt.% Ce-La addition promoted the formation of coarse Al_8Cu_4Ce phase, in addition to the Al_6Cu_6La and $Al_6(Mn, Fe)$ phases, which resulted in weakened mechanical properties.

2.4 SUMMARY

The review of the literature presented in this chapter has highlighted the numerous studies that have been carried out on the effects of rare earth elements, in particular, Ce and La, on the microstructure and mechanical properties of aluminum alloys. While a number of these investigations have been undertaken by Chinese researchers, due likely to the easily available natural source of rare earth in the form of mischmetal, studies by other researchers are also reported.

Previous studies carried out by TAMLA research group have investigated the influence of rare earth elements and mischmetal on the performance of A356, A413.1 and other Al-Si alloys [168-174]. With the more recent focus on the development of new Al-Cu based alloys for high temperature performance of automotive components, it was considered worthwhile to also investigate the effects of Ce and La rare earth metal additions to these alloys, taking into consideration low and relatively high Si levels.

Putting the importance of rare earth elements (REEs) into proper perspective, very recently, University of Kentucky researchers have reported producing nearly pure rare earth concentrates from Kentucky coal sources [175]. The patent pending process developed by Honaker and Zhang is a low cost and environmentally friendly recovery process. Interest in rare earth elements is currently at its peak in the U.S.A., with the Department of Energy investing millions in research, as REEs constitute essential components of diverse technologies in the high-tech and renewable energy industries.

CHAPTER 3

EXPERIMENTAL PROCEDURES

CHAPTER 3

EXPERIMENTAL PROCEDURES

3.1 INTRODUCTION

Figure 3.1 shows a detailed summary of the experimental procedures that were used in the current study to carry out Phases I, II and III of the work. Microstructural observations, phase identification and the solidification behaviour of the alloys investigated were carried out in Phase I, while the tensile properties of these alloys at ambient and elevated temperatures were studied in Phase II and Phase II, respectively.

As will be described in the next section, ingots of the base alloy GM220 used in this study were supplied in two lots, the first being the original alloy containing 1.1 wt.% Si (low Si level alloy), and the second, containing a higher amount of Si, namely 8 wt.% (high Si level). These two alloys represent the base alloys B0 and D0 to which the rare earth additions of Ce and La were made to produce the B and D series of alloys studied.

The casting procedures used to prepare test bars for tensile testing, the thermal analysis and DSC experiments used to examine the solidification behavior of the alloys, the heat treatments and tensile testing procedures, and the techniques employed for microstructural characterization are presented in subsequent sections of this Chapter.

Experimental Phases	Material Selection	Material Processing	Material Characterization
Phase-I	• Base Alloys B0& D0 alloys • Additions 1.0 &5.0 wt.% La & Ce	• Casting using graphite mold (Cooling rate: 0.7 ^{0}C/s)	• Microstructure observation using (EPMA/WDS) &(SEM/EDS) • Solidification behaviour analysis using (DSC/TA)
Phase-II	• Base Alloys B0 & D0 alloys • Additions (0.2, 0.5 &1.0 wt.% La & Ce) and 150 ppm Sr	• Casting using Metallic Mold (Cooling rate 10.0 ^{0}C/s) • Heat Treatment (SHT, T5, T6 &T7)	• Eutectic Si particle measurements OM and image analysis software • Intermetalic volume fraction SEM and image analysis software • Mechanical tensile test at RT
Phase-III	• Base Alloys B0 & D0 alloys • Additions (0.2, 0.5 &1.0 wt.% La & Ce)	• Casting using Metallic Mold (Cooling rate :10.0 ^{0}C/s) • Heat Treatment (T6 with one hr /200 hrs stabilization @250°C prior to testing)	• Mechanical tensile test at HT • Fractography Fracture behaviour (SEM) Section beneath the fracture (OM)

Figure 3.1: Synopsis of experimental procedure

3.2 MATERIALS SELECTION

The main raw materials used in the present study were GM220B and GM220D alloys (supplied by General Motors, USA), as shown in Figure 3.2, with chemical compositions of Al-1.1% Si-2.1% Cu-0.35% Mg-0.4% Fe-0.05% Mn-0.05% Ti (wt.%)and Al-8% Si-2.1% Cu-0.35% Mg-0.4% Fe-0.05% Mn-0.05% Ti (wt.%), respectively. Rare earth elements Ce and La of high purity (99.9%) were supplied by Stanford Advanced Materials, USA [176] and were used for making the various Ce and La additions to the base B0 and D0 alloys. Alloys so prepared were classified based on the Si content, and the Ce and La addition levels made as listed in Table 3.1.

Figure 3.2:GM220B and GM220D as received ingots

Table 3.1: Classification of alloys tested in the current study

Alloy	Composition (wt.%)								
	Cu	Si	Mg	Fe	Mn	Ti	La	Ce	Sr
Low Si									
B0	2.4	1.2	0.4	0.4	0.6	0.15	0	0	0
B0+0.2 wt.% La	2.4	1.2	0.4	0.4	0.6	0.15	0.2	0	0
B0+0.5 wt.% La	2.4	1.2	0.4	0.4	0.6	0.15	0.5	0	0
B0+1.0 wt.% La	2.4	1.2	0.4	0.4	0.6	0.15	1	0	0
B0+5.0 wt.% La	2.4	1.2	0.4	0.4	0.6	0.15	5	0	0
B0+0.2 wt.% Ce	2.4	1.2	0.4	0.4	0.6	0.15	0	0.2	0
B0+0.5 wt.% Ce	2.4	1.2	0.4	0.4	0.6	0.15	0	0.5	0
B0+1.0 wt.% Ce	2.4	1.2	0.4	0.4	0.6	0.15	0	1	0
B0+5.0 wt.% Ce	2.4	1.2	0.4	0.4	0.6	0.15	0	5	0
B0+150 ppm Sr	2.4	1.2	0.4	0.4	0.6	0.15	0	0	0.015
High Si									
D0	2.4	8	0.4	0.4	0.6	0.15	0	0	0
D0+0.2 wt.% La	2.4	8	0.4	0.4	0.6	0.15	0.2	0	0
D0+0.5 wt.% La	2.4	8	0.4	0.4	0.6	0.15	0.5	0	0
D0+1.0 wt.% La	2.4	8	0.4	0.4	0.6	0.15	1	0	0
D0+5.0 wt.% La	2.4	8	0.4	0.4	0.6	0.15	5	0	0
D0+0.2 wt.% Ce	2.4	8	0.4	0.4	0.6	0.15	0	0.2	0
D0+0.5 wt.% Ce	2.4	8	0.4	0.4	0.6	0.15	0	0.5	0
D0+1.0 wt.% Ce	2.4	8	0.4	0.4	0.6	0.15	0	1	0
D0+5.0 wt.% Ce	2.4	8	0.4	0.4	0.6	0.15	0	5	0
D0+150 ppm Sr	2.4	8	0.4	0.4	0.6	0.15	0	0	0.015

3.3   MATERIAL PROCESSING

Casting of the alloys used in the current study were prepared using the gravity die (permanent mold) casting process, followed by heat treatment. Details of the casting and heat treatment procedures employed are described below.

3.3.1   Casting Procedures

The raw material ingots were cut into smaller pieces and melted in a 40-Kg capacity SiC crucible, using an electrical resistance furnace as shown in Figure 3.3(a). The melting temperature was maintained at $750 \pm 5°C$. All alloys prepared were grain refined using Al-5% Ti-1% B to obtain levels of 0.15 wt.% Ti. Additions of La and Ce rare earth metals were made in amounts of 0.2 , 0.5, and 1.0 wt.% using Al-15% La and Al-15%Ce master alloys (see Appendix A for details of these master alloys). For purposes of comparison, individual additions of 150 ppm Sr were also made to the two base alloys. In each case, the melts were degassed for 15-20 min employing a graphite impeller rotating at 130 rpm, using pure dry argon, and then the melt was carefully skimmed to remove oxide layers from the surface before casting.

The melt was poured into an ASTM B-108 permanent mold (preheated at 450°C to drive out moisture), for preparing the tensile test bar castings, as shown in Figure 3.3(b). Each casting provides two test bars, with a gauge length of 70 mm and a cross-sectional diameter of 12.7 mm, as shown in Figure 3.3(c) and (d). Three samplings for chemical analysis were also taken simultaneously at the time of the casting; this was done at the beginning, in the middle, and at the end of the casting process to ascertain the exact chemical composition of each alloy. The chemical analysis was carried out using a Spectrolab-JrCCD Spark Analyzer. The Average values of the actual chemical compositions of the alloys

prepared are listed in Appendix B. Master alloys were added just before degassing to ensure homogeneous mixing of the additives together with the degassing.
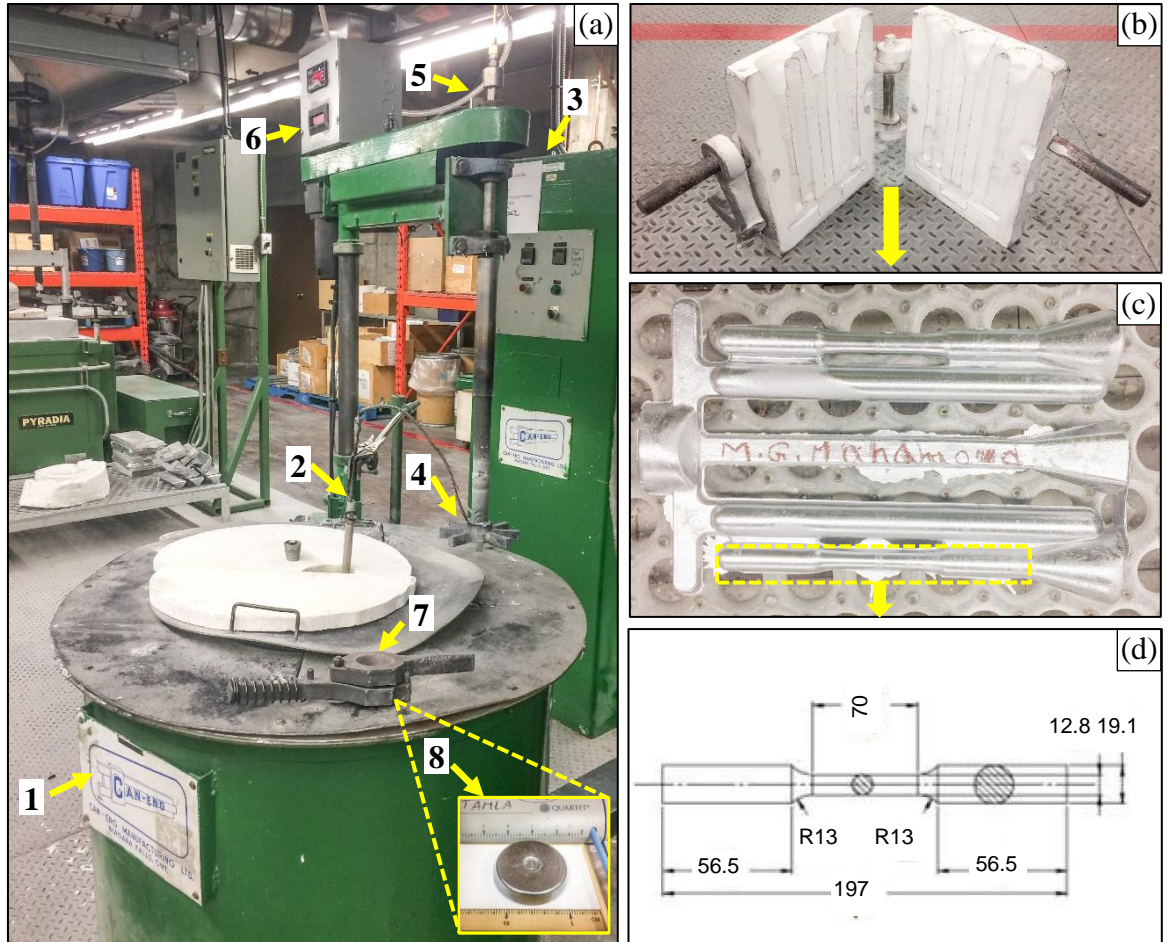
Figure 3.3: (a) Melting setup, (b) ASTMB-108 permanent mold, (c) actual tensile test casting, and (d) Geometry of the tensile test bar (Dimension in mm). The labeled arrows in (a) indicate (1) electrical resistance furnace, (2) K-type thermocouple, (3) temperature control units, (4) graphite degassing impeller, (5) argons supply hoses, (6) step motor, (7) chemical analysis sampling mold, and (8) Chemical analysis sample.

3.3.2 Heat Treatment Procedures

The heat treatments for this study was carried out using the Lindberg Blue M electric furnace shown in Figure 3.4. The tensile test bars prepared for Phase II of the study were subjected to solution heat treatment (SHT), as well as T5, T6, and T7 heat treatment regimes. Details of the heat treatment parameters used for the alloys are summarized in Table 3.2. In

Phase III, while all the tensile test bars underwent T6 heat treatment, however, half of the test bars were stabilized in the testing furnace at 250 °C for 200 hrs prior to the testing.Appendix C presented attached information relating to optimization of the solution heat treatment regime of B0 and D0 alloys.
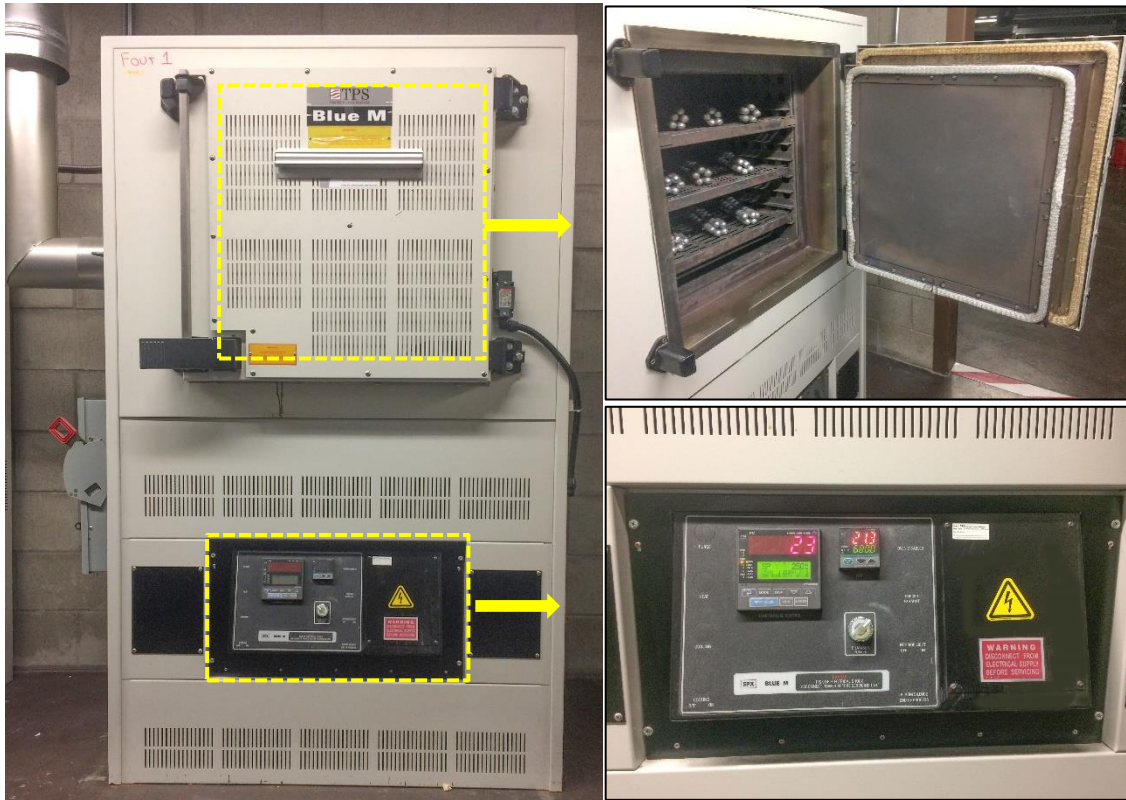
Figure 3.4: Lindberg Blue M Electric Furnace.

Table 3.2: Heat treatments for the cast alloys tested.

Heat Treatment Condition	Solution Temperature, [°C]	ST Holding Time, [hr]	Quenching Temperature [°C]	Aging Temperature, [°C]	Aging Time, [hr]
SHT	510	8	70	None	None
T5	None	None	None	180	8
T6	510	8	70	180	8
T7	510	8	70	240	4

3.4   MATERIAL CHARACTERIZATION TESTS

3.4.1   Characterization of Solidification Behavior

In order to determine the solidification behaviour of B0 and D0 alloys and identify the main reactions occurring during the solidification and their corresponding temperatures, the commonly used techniques of thermal analysis and differential scanning calorimetry (DSC) were employed. Details of each technique are presented in subsections 3.4.1.1 and 3.4.1.2.

To prepare the required alloy compositions, ingots of the as-received GM220B and GM220D alloys were cut into smaller pieces, cleaned, and then dried. The melting process was carried out in a cylindrical graphite crucible of 2-kg capacity, using a smaller electrical resistance furnace; the melting temperature was maintained at 780°C; the alloys were grain-refined by adding 0.15%Ti as Al-5%Ti-1%B master alloy in rod form. Additions of Ce and La were made to the two base alloy melts using Al-15%La and Al-15%Ce master alloys, in order to study the effect on the microstructure and the phases formed in the corresponding alloys. The melts thus prepared were used for carrying out thermal analysis experiments, as described in the next subsection. In this context, the Ce and La additions of 1.0 and 5.0 wt.% were made to facilitate the formation and identification of the RE phases formed.

3.4.1.1   Thermal Analysis

To determine the reactions taking place during the solidification process, the molten metal was poured into a 600 °C preheated cylindrical graphite mold (dimensions: 100 mm height, 60 mm top diameter) so as to obtain near-equilibrium solidification conditions at a slow cooling rate of 0.7 °C/s, and facilitate identifying the phase obtained. For the analysis, a high sensitivity Type-K (chromel-alumel) thermocouple, insulated using a double-holed

ceramic tube, was inserted through a hole at the bottom of the graphite mold and reaching up to one third the mold height along the centerline. The thermocouple was connected to an NI SCXI-1000 high-speed data acquisition system linked to a computer to record the temperature-time data using DASYLAB software, as shown in Figure 3.5.
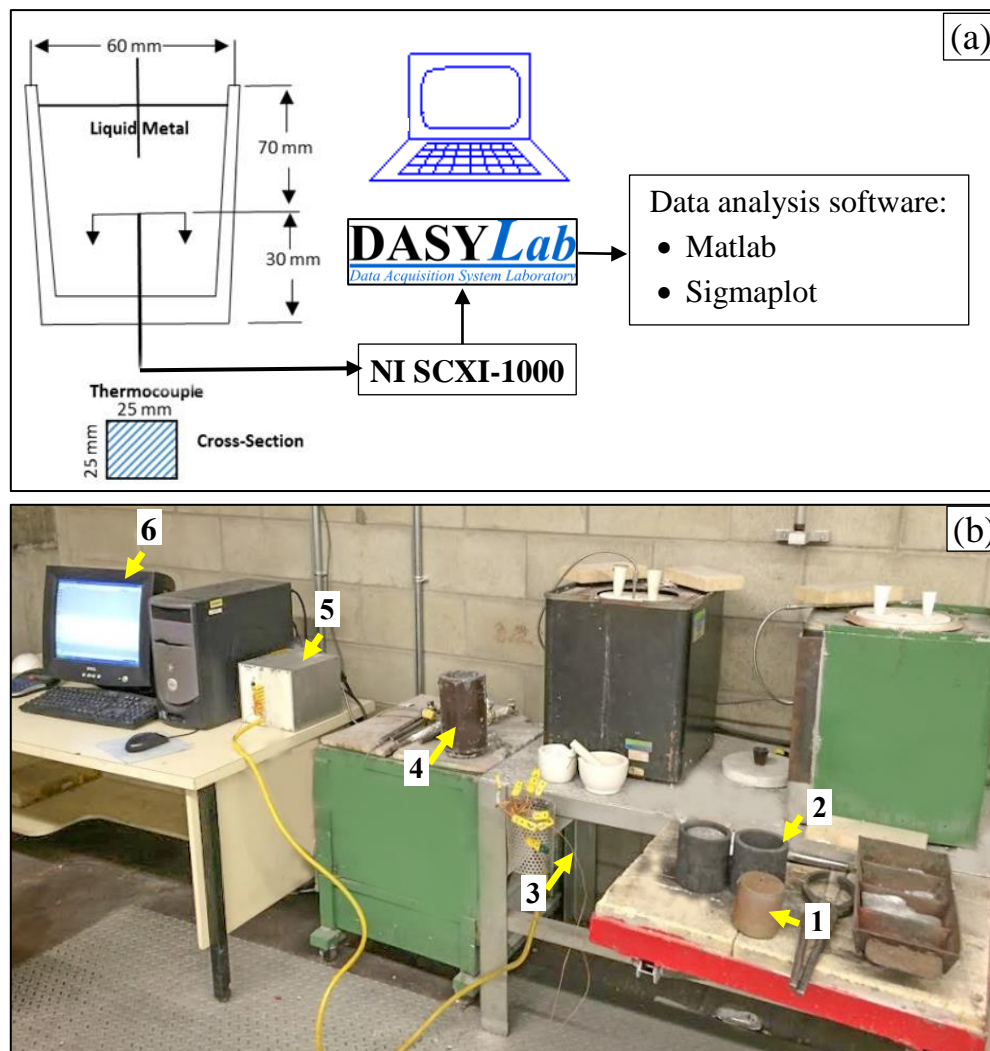
Figure 3.5:(a) Schematic diagram, and (b) actual set-up used for thermal analysis. The arrows in (b) indicate (1) final casting, (2) graphite mold, (3) K-type thermocouple, (4) 2-kg capcity crucible, (5) NI SCXI-1000 data acquisition system, and (6) DASYLAB software.

The data was collected continuously every 0.1 second, and plotted in the form of cooling curves. The curves were smoothed using MATLAB software, the program for which is provided in Appendix C. Finally, the first derivative cooling curves were produced using SIGMAPLOT data analysis software to analyze the data.

3.4.1.2 Differential Scanning Calorimetry (DSC) Test

Differential scanning calorimetry, or DSC, is a thermoanalytical technique in which the difference in the amount of heat required to increase the temperature of a sample and a reference is measured as a function of temperature. The reference and sample are both maintained at nearly the same temperature throughout the experiment. Generally, the temperature program for a DSC analysis is designed such that the sample holder temperature increases linearly as a function of time. The reference sample should have a well-defined heat capacity over the range of temperatures to be scanned [177]. Figure 3.6(a) is a schematic diagram of the set-up used for conducting the DSC analysis.

A Perkin-Elmer DSC8000 differential scanning calorimeter operating under a protective atmosphere of pure argon was used to study the solidification behaviour of the alloys used in the current study, as shown in Figure 3.6(b). The mass of the DSC sample was approximately 20 mg. The scans were performed in three stages as follows: (i) heating from 400° to 700 °C at a heating rate of 10 °C/min, (ii) holding at 700 °C for 1 min, and (iii) cooling from 700° to 400 °C at a cooling rate of 10 °C/min. Three samples were tested for each alloy condition and the results were found to be almost identical. The corrected DSC curve of each sample was determined by subtracting the two DSC scans. The first scan was conducted with the sample, while the second one was conducted without the sample under the same testing conditions of the sample scan. The purpose of this procedure was to obtain

baseline-corrected thermogram data. The DSC curve of each alloy condition was subsequently obtained by averaging the three corrected curves of the three respective samples where the uncertainty in determining the peak temperatures did not exceed ±2 °C.

Figure 3.6:(a) Schematic of DSC analysis, (b) Perkin-Elmer DSC 8000 used for conducting the DSC analysis.

3.4.2 Microstructural Characterization

In the current study, microstructural examination of the alloy samples and characterization of the phases obtained were carried out employing both optical and electron microscopy techniques, in conjunction with image analysis, and EDS/WDS analysis facilities, respectively available with these techniques, for quantification and phase identification purposes. Table 3.3 summarizes the tasks for which these various techniques were used and in which phases of the study they were employed.

Table 3.3: Microscopic techniques used for microstructural characterization.

Microscope Type	Characterization Description	Experimental Phases		
		I	II	III
Optical Microscope (OM)	Eutectic Si particle measurement using image analysis software		✓	
	Microstructures of tensile-tested samples beneath the fracture surface (parallel to tensile direction)			✓
Scanning Electron Microscope (SEM)	Microstructural characterization and phase identification using EDS	✓		
	Intermetallic volume fraction using image analysis software		✓	
	Microstructures of fracture surface of tensile-tested samples (perpendicular to tensile direction)			✓
Electron Probe Microanalyzer (EPMA)	Microstructural characterization and phase identification using WDS	✓		

The microscopes used in each case are shown in Figure 3.7 through Figure 3.8. The optical microscope shown in Figure 3.7 was used in conjunction with a Clemex Vision PE image analysis system for quantification purposes, namely, measurements of secondary dendrite arm spacing (SDAS) and eutectic Si particle characteristics.

A JEOL JSM-6480LV scanning electron microscope coupled with an energy dispersive X-ray spectrometer (EDS) was used for examining the microstructures and semi-quantitative analysis of the phases observed using EDS, measuring the volume fraction of intermetallic phases formed, as well as examining the fracture surfaces of tensile-tested alloy samples (Figure 3.8).

A JEOL JXA-8900 electron probe microanalyzer (EPMA), equipped with a wavelength dispersive spectrometer (WDS) was also employed for examining the microstructures and identification of the new intermetallic phases formed (Figure 3.9).
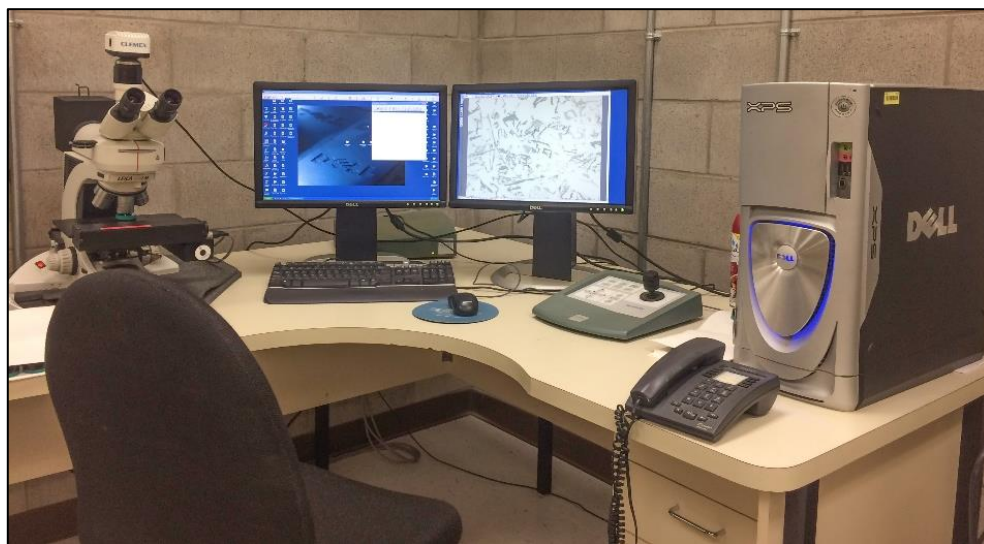
Figure 3.7: Optical microscope-Clemex Vision PE image analysis system.
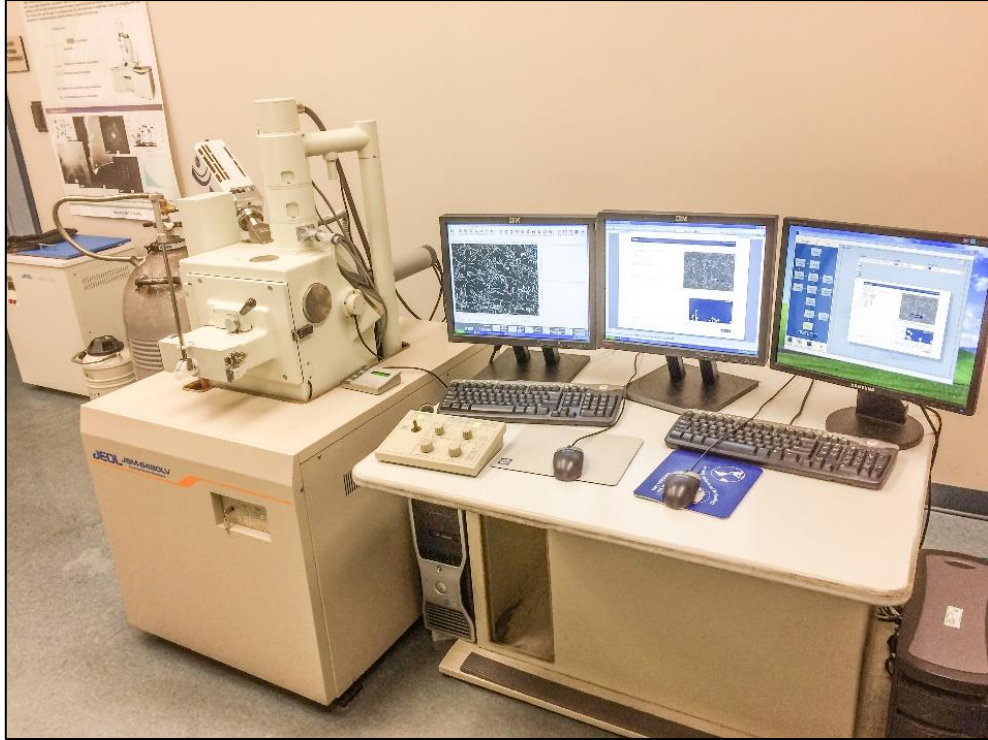
Figure 3.8: JEOL JSM-6480LV scanning electron microscope equipped with an energy dispersive X-ray spectrometer (EDS).

Figure 3.9 : JEOL JXA 8900L WD/ED electron probe microanalyzer coupled with a wavelength dispersive spectrometer (WDS).

For examining the microstructures of the alloys/casting prepared, polished metallographic samples were prepared using standard polishing procedures. Samples were sectioned from the graphite mold casting as well as from the tensile test bars in the as-cast, heat-treated and tested condition, and mounted in bakelite using a Struers Labopress-3 Mounting Press. The samples were then ground and polished to the desired fine finish by means of a Struers Tegrapol-35 Grinder-Polisher (see Figure 3.10). The grinding was carried out using SiC abrasive papers of 120, 240, 320, 400, 600, 800 grit sizes in order of sequence. The polishing was carried out using polycrystalline diamond powder suspension, with particle size 3.0 µm and 1.0 µm for rough and fine polishing, respectively. Struers DP-lubricant was used in both stages as a cooling and lubricating medium. Finally, to produce a mirror-like surface, the ultimate polishing stage was completed using 1.0 µm colloidal silica suspension with water as a coolant and lubricant. After polishing, the mounted samples were washed with a mix of soap and alcohol, and then dried using compressed air.

Figure 3.10: (L) Struers LaboPresss-3 and (R) TegraForce-5 machines, for mounting and polishing samples for metallography.

3.4.3 Mechanical Tensile Testing

The tensile test for the purposes of the current study were carried out at ambient and at elevated temperature. A detailed description of the testing procedures used in the two cases is provided in subsections 3.4.3.1 and 3.4.3.2.

3.4.3.1 Tensile Testing at Ambient Temperature

All test bar samples used in Phase II of the study were tested at ambient temperature in the as-cast, solution heat-treated (SHT), and T5, T6 and T7 heat treated conditions using an MTS Servohydraulic mechanical testing machine as shown in Figure 3.11, at a strain rate of 4×10^{-4} s^{-1}. An extensometer (with a 50.8 mm range) was used to measure the extent of deformation in the samples. The tensile properties, yield strength (YS) at 0.2% offset strain, ultimate tensile strength (UTS), and percent elongation (%El), were obtained from the data acquisition system of the machine, and analyzed using the Testworks 4 software designed for tensile testing. Five samples were tested for each alloy/condition examined in Phase II, giving a total of 200 bars per alloy type (8 alloying additions x 5 heat treatment conditions x 5 bars) and a total of 400 bars for the B0 and D0 alloys investigated.
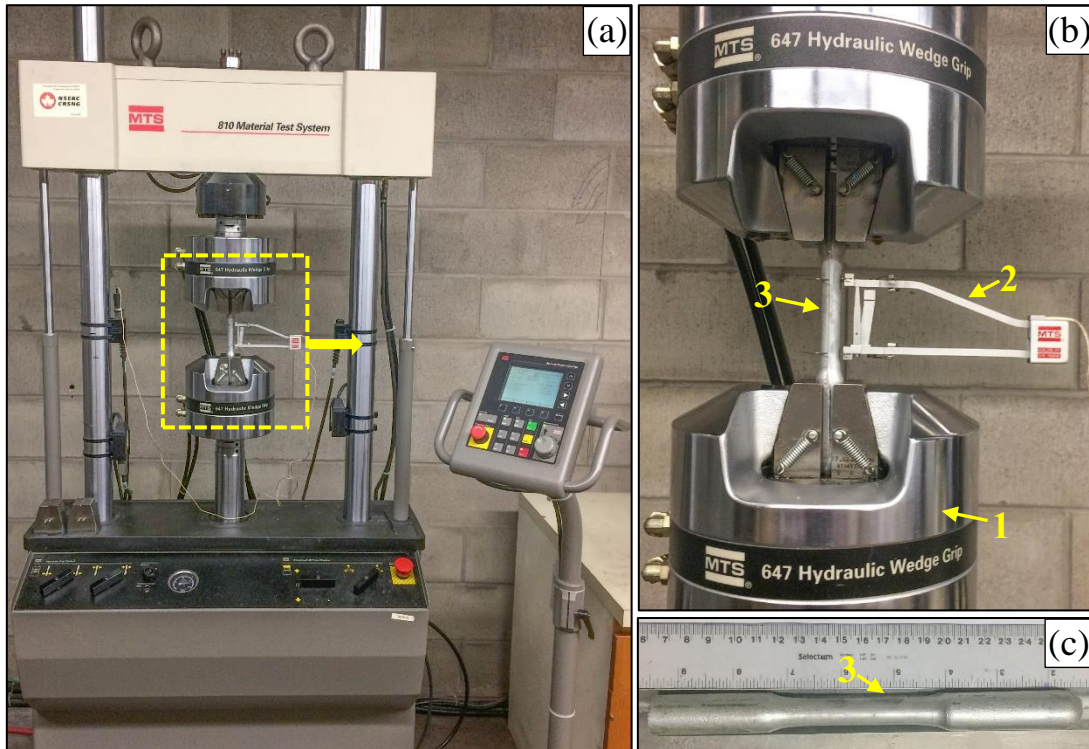
Figure 3.11: (a) MTS tensile testing machine (b) Strain gauge extensometer attached to tensile bar being tested, and (c) tested sample. The arrows indicate (1) hydraulic grips, (2) extensometer, and (3) tested sample.

3.4.3.2 Tensile Testing at Elevated Temperature

Tensile tests at elevated temperature were carried out using an Instron Universal Mechanical Testing machine as shown in Figure 3.12. For Phase III of the work, the tensile test bars were used in the T6 heat-treated condition. The test bar was mounted in the testing chamber, pre-set to a temperature of 250 °C. The sample was maintained for 1.0 hr at 250 °C before starting the test, using the same strain rate of 4×10^{-4} s^{-1}. Five test bars were used for each alloy composition/condition studied in this part of the study. The average UTS, YS, and %El values obtained from five tests were considered as representing the tensile properties of that alloy/condition. Thus, the tests carried out in Phase III covered 70 bars per alloy type (7 addition levels x 2 heat treatment conditions x 5 test bars), and a total of 140 bars for the B and D alloys overall.
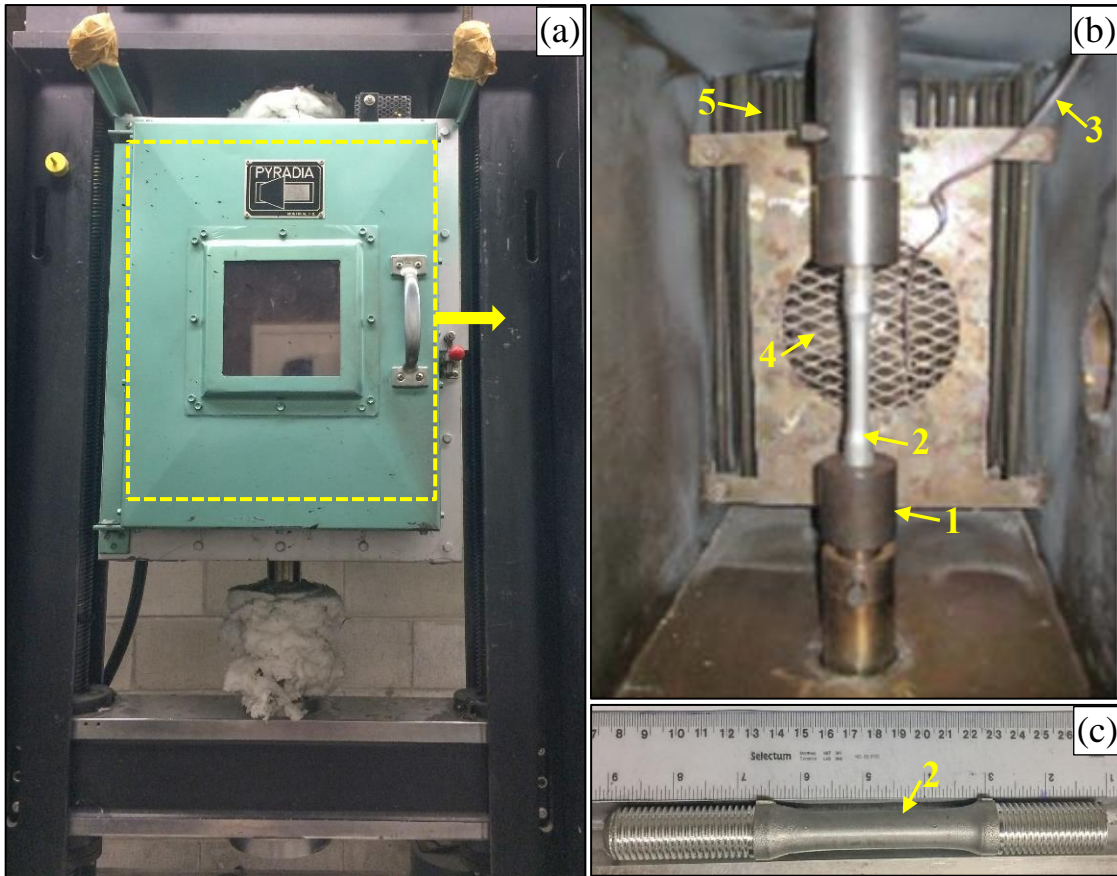
Figure 3.12: (a) Instron Universal mechanical testing machine (b) chamber for elevated temperature testing, and (c) tested samples. The arrows indicate (1) thread grips, (2) tested samples, (3) thermocouple, (4) air circulation fan, and (5) induction heating coil.

CHAPTER 4

CHARACTERIZATION OF SOLIDIFICATION BEHAVIOUR

CHAPTER 4

CHARACTERIZATION OF SOLIDIFICATION BEHAVIOUR

4.1 THERMAL ANALYSIS

The thermal analysis technique can be successfully used as a convenient method for studying the solidification behaviour of an alloy, and for verifying the effectiveness of quality determining metallurgical measures such as the modification and grain refining of cast aluminum alloys. In regard to the modification effects of rare earth metals, previous investigations have indicated that the thermal analysis results showed that there is no direct relationship between the modification rating and eutectic growth temperature [140, 151]. Thus far, the modification and refining effects remain controversial [160]. Accordingly, the thermal analysis technique was utilized to evaluate and characterize the solidification behaviour of the investigated Al-Cu (B0) and Al-Si-Cu (D0) alloys containing 0.0, 1.0, 5.0 wt.% of RE (Ce/La). It is worth nothing that in order to evaluate the solidification parameters easily, the solidification for the current work was obtained at a slow cooling rate (0.7 $^{\circ}$C/s). This is because when the molten metal or alloy is solidified at a high cooling rate, the latent heat of any reaction during the solidification process is released quickly, and the reaction peaks in the cooling curve and first derivative curve are too difficult to detect [178].

4.1.1 Al-Cu (B0) Alloy

Figure 4.1 illustrates the cooling curve and its first derivative obtained from the thermal analysis of B0 alloy. Several reactions take place during the course of solidification, as marked by different numbers on the first derivative curve. These numbers correspond to the reactions listed in Table 4.1. As may be seen from Figure 4.1, alloy B0 starts to solidify

at 648.8 °C (Reaction 1) with the development of the α-Al dendritic network, followed by formation of the α- $Al_{15}(FeMn)_3Si_2$ iron intermetallic phase (Reaction 2) at 647.5 °C and the Π-$Al_8Mg_3FeSi_6$ phase (Reaction 3) at 606.8 °C; following which the eutectic Al_2Cu and Q-$Al_5Mg_8Si_6Cu_2$ phases precipitate as the last reactions (Reaction 5) at 499 °C toward the end of solidification.
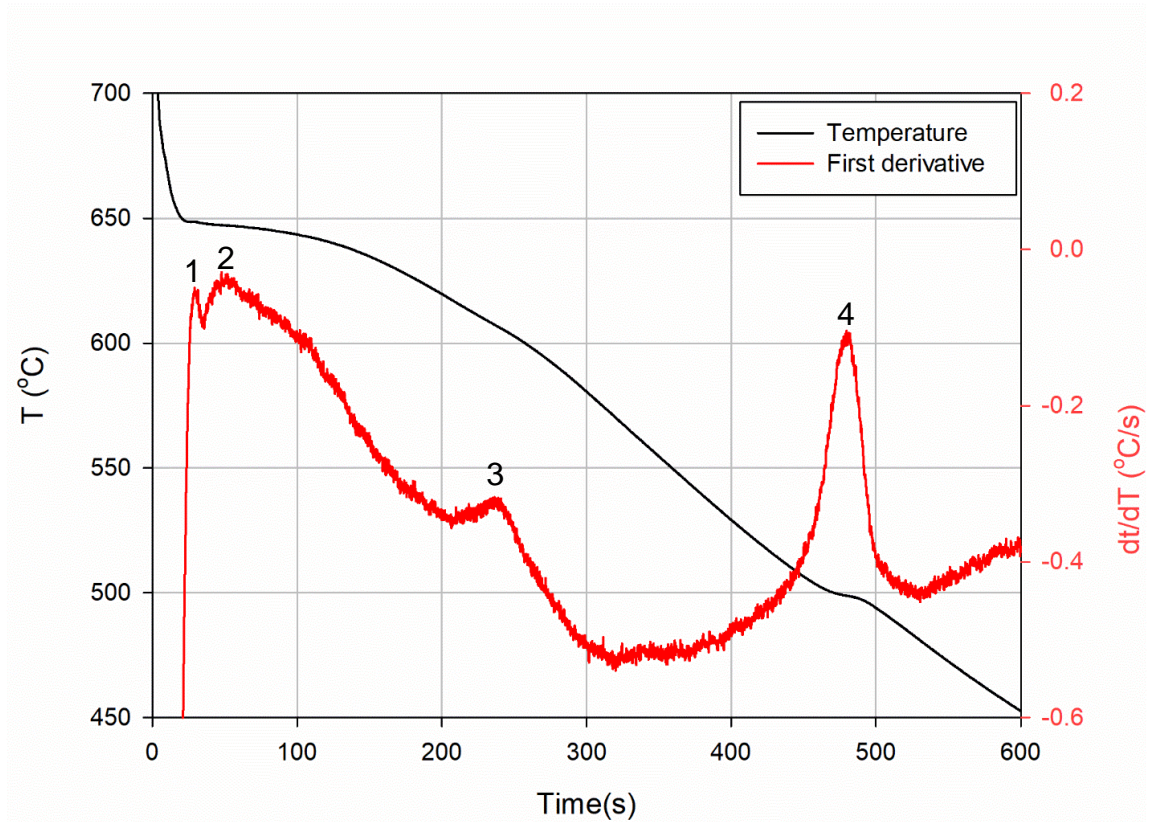
Figure 4.1: The typical cooling curve and first derivative obtained from the thermal analysis of B0 alloys.

Table 4.1: Solidification reactions observed in the B0 alloy.

Reaction No.	Approximated temperature (^{o}C)	Suggested precipitated phase
1	648.8	α-Al
2	647.5	α-Fe ($Al_{15}(FeMn)_3Si_2$)
3	606.8	Π-$Al_8Mg_3FeSi_6$
4	499	Al_2Cu + Q-$Al_5Mg_8Si_6Cu_2$

Figure 4.2 illustrates that there are two characteristic temperatures which can be measured from the cooling curves. These temperatures are (i) the minimum temperature, T_M, defined as the first noticeable change on the derivative of the cooling curve, and (ii) the growth temperature, T_G, defined as the maximum reaction temperature reached after recalescence, where the recalescence (ΔT_R) the difference in temperatures between T_M and T_G [160, 179]. In the current study, all the alloys investigated were refined with 0.15 wt.% Ti, so that the difference between T_M and T_G is not noticeable.
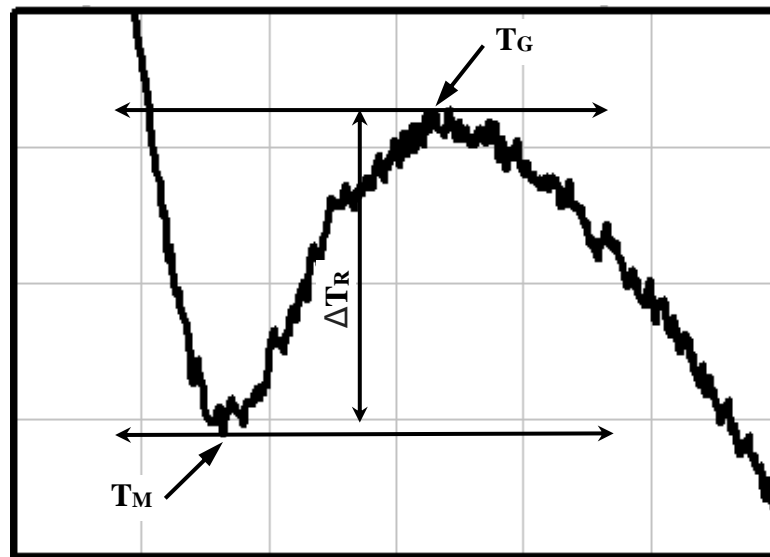
Figure 4.2: Solidification parameters: minimum temperature (T_M), growth temperature (T_G) and recalescence (ΔT_R).

Figure 4.3 and Figure 4.4 show the solidification cooling curves of B0 alloy with different RE Ce and La concentrations in α-Al, respectively. With regard to the effect of the Ce and La additions on the maximum growth temperature of α-Al ($T_G^{\alpha-Al}$), Figure 4.3 shows that upon adding 1.0 wt.% Ce to B0 alloy, the $T_G^{\alpha-Al}$ decrease from 648.6 °C to 643 °C. When the amount of Ce added is increased to 5.0 wt.%, the $T_G^{\alpha-Al}$ is lowered to 628 °C.
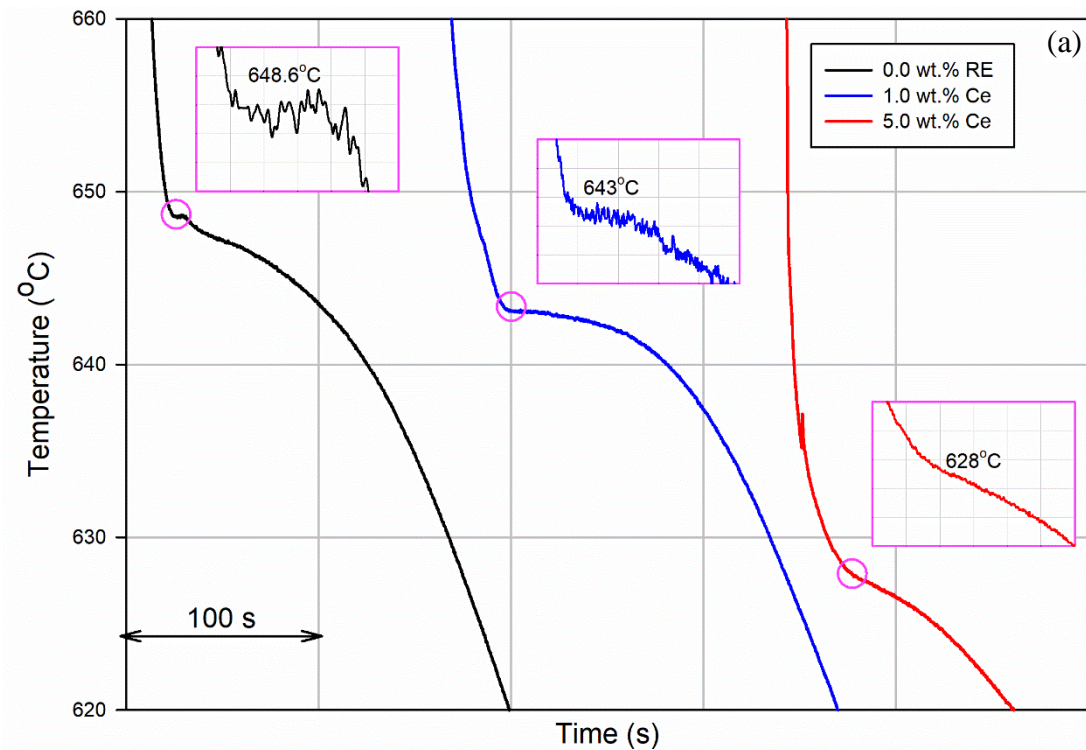
Figure 4.3: Assembly of cooling curves depicting the solidification of primary α-Al in B0 alloys with Ce additions.

Similar to the case of Ce, Figure 4.4 shows that as the amount of La added to B0 alloy is increased, the reduction in the magnitude of $T_G^{\alpha-Al}$ is increased, going from 648.6 °C for the base B0 alloy to 644 °C and 631.5 °C at 1.0 and 5.0 wt.% additions of La, respectively. It can be observed that the Ce and La elements have similar effects because of their similar physical properties.
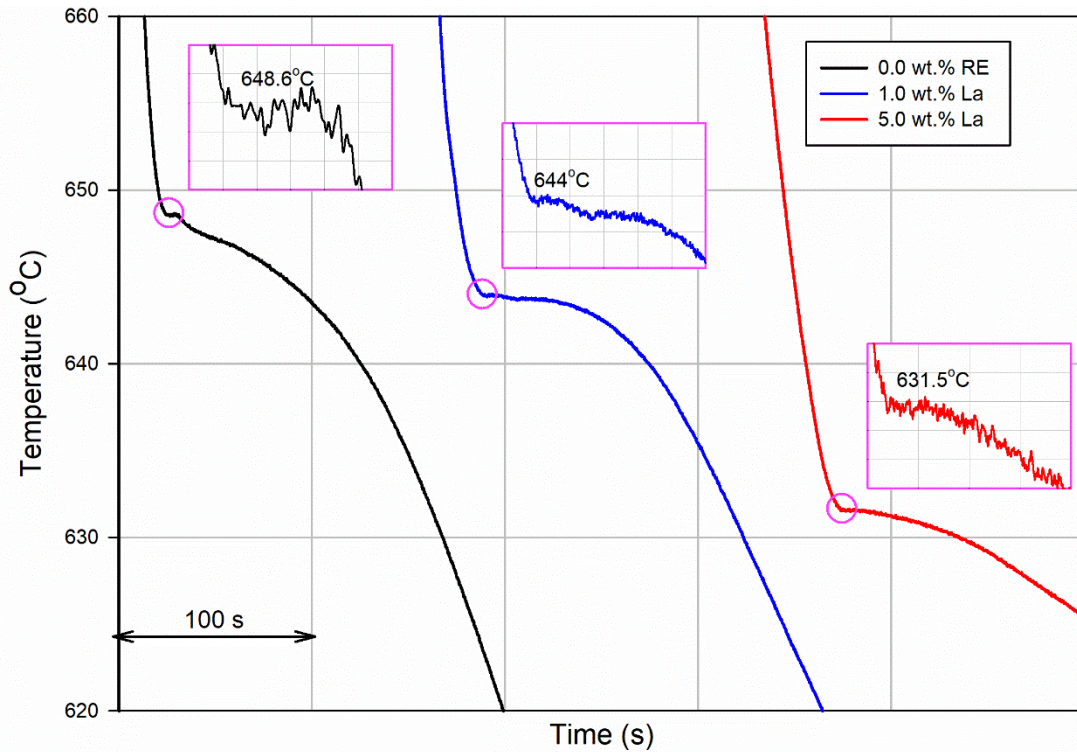
Figure 4.4: Assembly of cooling curves depicting the solidification of a primary α-Al in B0 alloys with La additions.

4.1.2 Al-Si-Cu (D0) Alloy

The solidification curve of D0 alloy-which has a composition similar to B0 alloy expect for its high Si content of 8.0 wt.%, obtained from its temperature-time data is shown in Figure 4.5, with its first derivate plot. The reactions which occur during solidification are marked by the numbers 1, 2, 3 and 4 as may be seen from Table 4.2. In Figure 4.5, peak 1 to 4 correspond to precipitation of the α-Al dendritic network at 603.8 $^{\circ}$C; precipitation of α-Fe (Al$_{15}$(FeMn)$_3$Si$_2$) at 602.8 $^{\circ}$C; precipitation of eutectic Al-Si phase at 568.8 $^{\circ}$C; and finally, precipitation of eutectic Al$_2$Cu + Q-Al$_5$Mg$_8$Si$_6$Cu$_2$ phases at 502 $^{\circ}$C. As expected, the D0 alloy shows a strong peak for the eutectic Al-Si reaction compared to B0 alloy (which contains 1.2 wt.% Si).
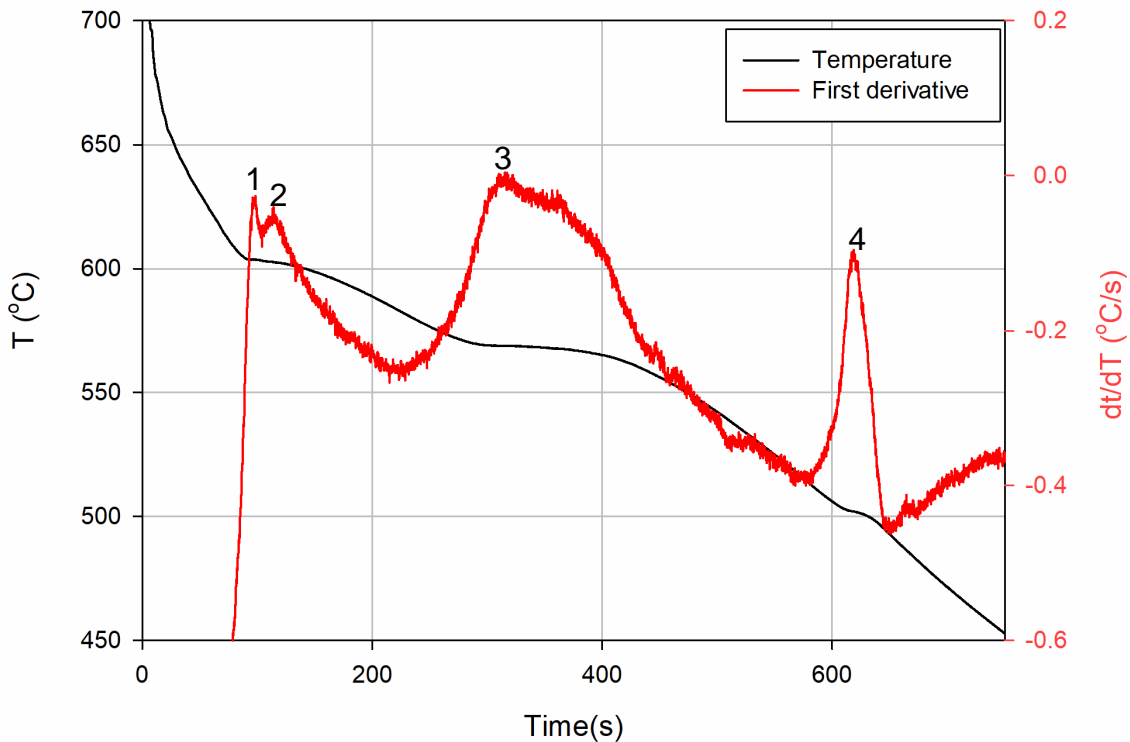
Figure 4.5: The Typical cooling curve and first derivative obtained from the thermal analysis of D0 alloy.

Table 4.2: Solidification reactions observed in the D0 alloy.

Reaction No.	Approximate temperature (°C)	Suggested precipitated phase
1	603.7	α-Al
2	602.8	α-Fe ($Al_{15}(FeMn)_3Si_2$)
3	568	Al+Si eutectic
4	502	Al_2Cu + Q-$Al_5Mg_8Si_6Cu_2$

Solidification curves of α-Al and Al-Si phases were plotted for the D0 base alloy (0.0 wt.% RE) and those with La and Ce (1.0 and 5.0 wt.%), as shown in Figure 4.7. Compared to the results presented in section 4.1.1 for B0 alloy, interestingly, Figure 4.7 shows that the difference between T_M and T_G (the definition has been given previously in section 4.1.1) are

clearly noted in the cooling curves for α-Al and Al-Si phases for D0 alloy treated with Ce and La additions, especially at the 5.0 wt.% addition level. However, the difference between the two temperatures is not noticeable in the base D0 alloy, which may be attributed with the formation of RE intermetallic phases that may consume the amount of Ti available where the latter plays an important role in reducing the amount of recalescence (the difference between T_M and T_G).

The effects of the Ce addition on the minimum $T_M^{\alpha-Al}$, T_M^{Al-Si}, and growth $T_G^{\alpha-Al}$, T_G^{Al-Si} temperatures are shown in Figure 4.6. The $T_M^{\alpha-Al}$ decreased by 4.2 and 6 °C, upon the addition of 1.0 and 5.0wt.% Ce, so that addition of Ce resulted in lowering the $T_M^{\alpha-Al}$ temperature of the D0 base alloy. In other words, the nucleation in the base alloy starts earlier than in the alloys with RE addition. With respect to the growth temperature, the 1.0 and 5.0 wt.% Ce additions decreased the $T_G^{\alpha-Al}$ value by 3.2 and 4.7 °C, respectively. Thus the Ce addition affects the cooling curves of D0 alloy in the α-Al region. With regard to eutectic Al-Si reaction region, Figure 4.6 shows that the minimum eutectic temperature T_M^{Al-Si} decreased slightly upon increasing the Ce addition to 1.0 wt.% but dropped sharply, by 11.3 °C, with 5.0 wt.% Ce. The T_G^{Al-Si} temperature decreased to 568.6 °C upon 1.0 wt.% Ce and further decreased to 558.7 °C with 5.0 wt.% Ce .
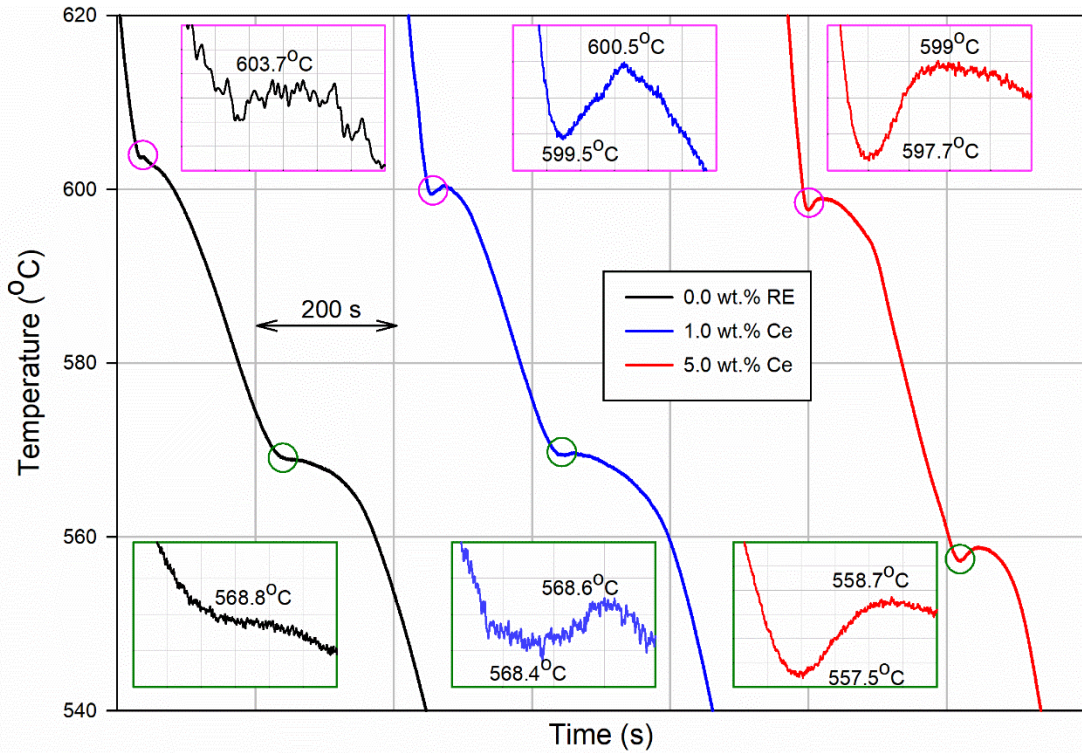
Figure 4.6: Assembly of cooling curves depicting on the solidification of a primary α-Al and Al-Si eutectic phases in D0 alloy with Ce additions.

Figure 4.7 illustrates the solidification curves of α-Al and Al-Si phases in D0 base alloy and D0 alloy containing La additions. Generally, the $T_M^{\alpha-Al}$ for D0 alloy was measured at 603.7 ℃, and dropped to 599.5 ℃ and 593.2 ℃ with 1.0 and 5.0 wt.% La addition, respectively. Furthermore, Figure 4.7 shows that the growth temperature $T_G^{\alpha-Al}$ decreased by 3.2 and 7.9 ℃ for the two additions. The minimum eutectic temperature T_M^{Al-Si} dropped slightly, from 568.8 to 568.1 ℃ with 1.0 wt.% La, whereas upon increasing the La addition to 5.0 wt.%, the T_M^{Al-Si} dropped sharply to 551.2 ℃. The T_G^{Al-Si} temperature decreased to 568.3 ℃, and further to 552.5 ℃, for the two La additions.
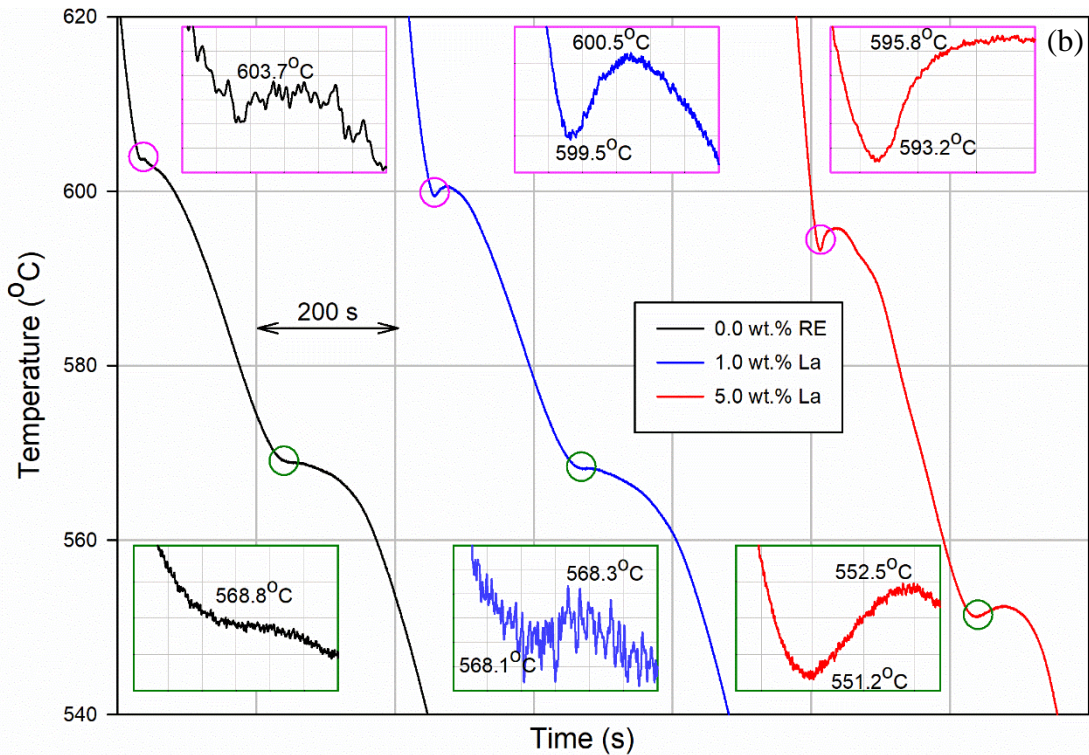
Figure 4.7: Assembly of cooling curves depicting the solidification of a primary α-Al and Al-Si eutectic phases in D0 alloy with La additions.

The T_G^{Al-Si} temperature is often used as a reference for describing the modification level, and it has been suggested that a modification rating can be automatically obtained from this temperature without the need for microstructural analysis [179]. Reference [17] reported that the modification of Al-11%Si-Cu alloys was influenced by the amount of decrease in T_G^{Al-Si}, with additions of modification elements such as Bi, Sb, and Sr. In regard to the effect of RE used as modifying agents, Tsai et al. [140] reported that the results of thermal analysis indicated that the addition of Ce decreases the eutectic growth temperature, however there is no direct relationship between the modification rating and T_G^{Al-Si}. The findings reported in the previous section for the present study are in accordance with the results presented in references [140, 148], and [24, 93, 119, 160, 180].

4.2   DIFFERENTIAL SCANNING CALORIMETRY (DSC) RESULTS

Although thermal analysis is the most common technique used in research investigations to study the solidification behavior of aluminum alloys, due to its advantages as noted in the previous section 4.1, nevertheless, the technique has restricted capability. Thus, a more advanced technique is recommended to overcome these limitations. Accordingly, in this section DSC runs were performed in the temperature range 400-700 $^{\circ}$C at the rate of 10 $^{\circ}$C/min in order to identify the solidification reactions that formed the La or Ce intermetallic phases in the B0 and D0 alloys and to support the data obtained from thermal analysis.

4.2.1   Al-Cu (B0) Alloy

Figure 4.8 illustrates the DSC heating curves of the B0 base alloy, and B0 alloy with 1.0 and 5.0 wt.% Ce additions . Generally, all alloys exhibited two common major exothermic peaks (A and B) at temperatures ranging from 637 to 653 $^{\circ}$C, and 511 to 518 $^{\circ}$C, respectively. The two peaks can be attributed to the following reactions: peak A corresponds to the formation of the primary α-Al and α-(Al$_{15}$(FeMn)$_3$Si$_2$) iron intermetallic phases, while peak B is attributed to Al$_2$Cu and Q-Al$_5$Mg$_8$Si$_6$Cu$_2$ phases. These results are in keeping with the thermal analysis results presented in section 4.1.1. It is worth noting that peak B is clearly noticeable in the base alloy, becomes much reduced with 1.0 wt.% Ce, and then disappears with 5.0 wt.% Ce addition, as displayed in a in Figure 4.8. The disappearance of this peak from DSC curve in the last results from the fact that Ce reacts with the Cu existing in the B0 alloy to form the white Ce containing intermetallic phase. Also, the DSC curves of B0 alloy with 1.0 and 5.0 wt.% Ce displayed a small endothermic peak D at a temperature 623 $^{\circ}$C. This peak may be attributed to the melting of the white Ce-containing intermetallic phase.

The 5.0 wt.% containing B0 alloy exhibited an additional endothermic peak (C) at 630 °C. This peak corresponds to the melting of the grey Ce-containing intermetallic phase. The nature of the white and grey RE(Ce/La) containing intermetallic will be discussed in the next chapter.
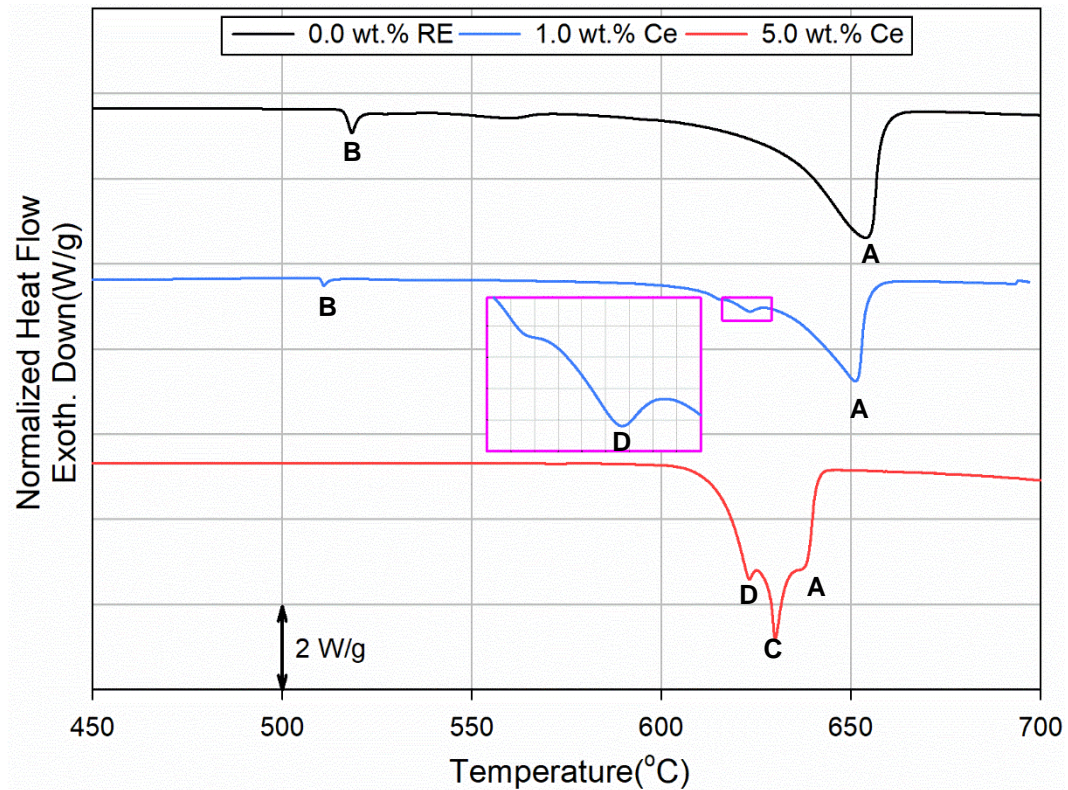
Figure 4.8: DSC melting curves of B0 alloy with 1.0 and 5.0 wt.% of Ce additions.

Figure 4.9 shows the DSC solidification curves of the B0 alloys containing the same concentrations of Ce addition. One common exothermic peaks (marked A) appears on these curves, at temperatures ranging from 630 to 645 °C. This peak corresponds to the solidification of the α-Al phase. Only the solidification curve of B0 alloy displays the peak marked B, at 502 °C, attributed to the formation of Al_2Cu and Q phases. The endothermic peak D appearing in the DSC curves of B0 alloy containing 1.0 and 5.0 wt.% Ce at 612 °C,

would correspond to the precipitation of the white Ce-intermetallic phase. Only the DSC curve of B0 alloy with 5.0 wt.% Ce exhibited an endothermic peak C appearing at 615 °C, which may be attributed to the solidification reaction of the grey Ce-containing intermetallic phase. The absence of this peak from the DSC curve of the 1.0 wt.% Ce-containing alloy may suggest that a small amount of the grey phase solidified along with the white phase in the same solidification reaction.
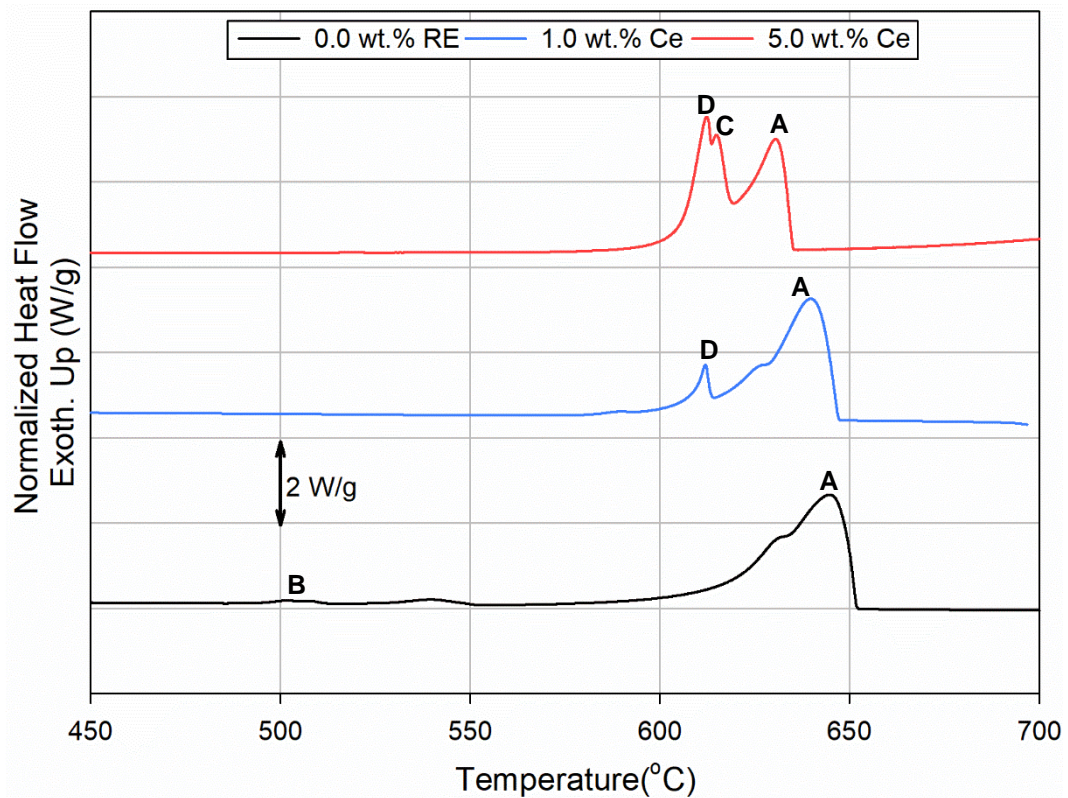
Figure 4.9: DSC solidification curves of B0 alloy with 1.0 and 5.0 wt.% of Ce additions.

Figure 4.10 shows the heating curves of B0 alloys containing 1.0 and 5.0 wt.% La additions. Similar to the case Ce addition, all alloys exhibited in common two major exothermic peaks (A and B) at temperatures ranging from 635 to 653 °C and 510 to 518 °C, respectively. Likewise, Peak B disappeared from the heating curves of the B0 alloy containing 5.0 wt.% La. Exothermic peaks marked D appear in the DSC curves of B0 alloy

with 1.0 and 5.0 wt.% La at 625 ºC. These peaks may be attributed to the solidification reaction of the La-containing intermetallic grey and white phase.
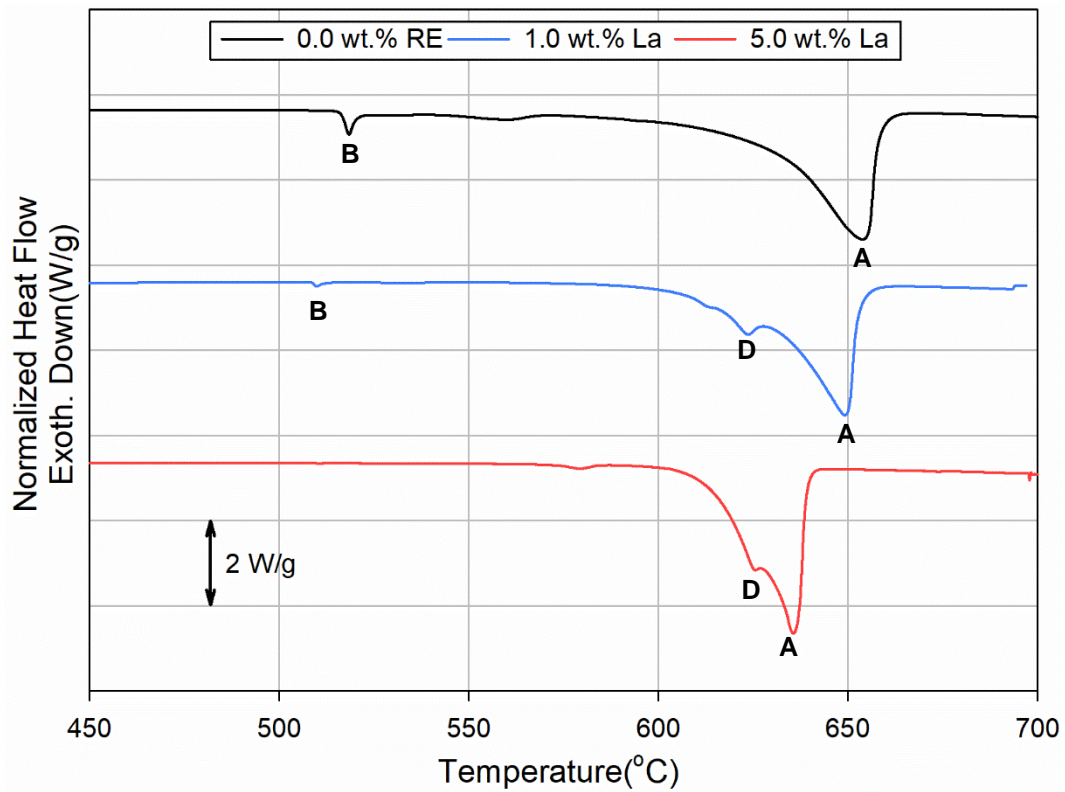
Figure 4.10: DSC melting curves of B0 alloy with 1.0 and 5.0 wt.% of La additions.

The DSC solidification curves of the B0 alloy containing the same concentrations of La addition are shown in Figure 4.11. In general, one common exothermic peaks (marked A) appeared on theses curves, at temperatures ranging from 623 to 645 ºC, whereas only the solidification curve of the B0 base alloy displayed the peak marked B at 502 ºC. The DSC curves of B0 alloy with 1.0 and 5.0 wt.% La additions displayed the endothermic peak D which appeared at 611 ºC. This peak would correspond to the solidification of the white La-containing intermetallic phase. Only the solidification curve of B0 alloy with 5.0 wt.% La displayed the endothermic peak C at 615 ºC, attributed to the solidification of the grey La-containing intermetallic phase.
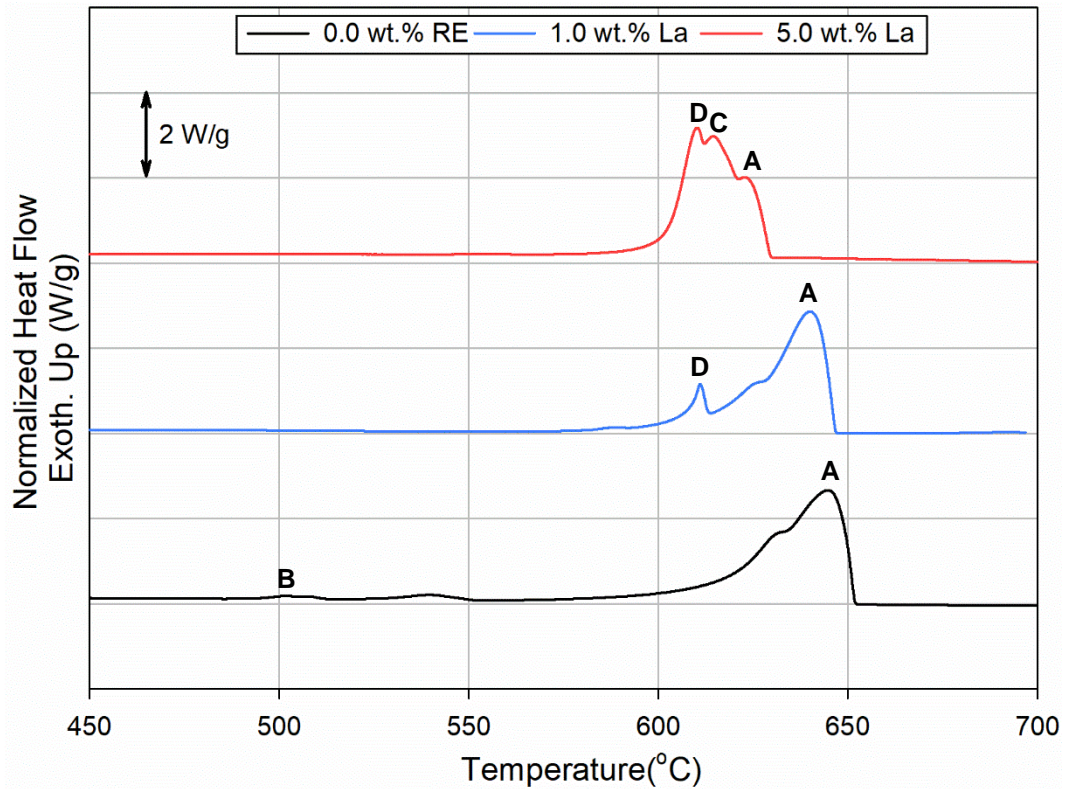
Figure 4.11: DSC solidification curves of B0 alloy with 1.0 and 5.0 wt.% of La additions.

4.2.2 Al-Si-Cu (D0) Alloy

The DSC heating curves of the D0 alloys containing different levels of Ce addition (0.0, 1.0, and 5.0 wt.%) are shown in Figure 4.8. In general, it was found that the investigated alloys exhibited mainly three exothermic peaks (A, B, and C) in common, within the temperature range of 608 to 600 °C, 587 to 570 °C, and 510 to 521 °C, respectively, depending on the Ce level. The three peaks corresponded to the melting of the primary α-Al and α-iron intermetallic phases (peak A), the eutectic Al-Si phase (peak B), and the Al_2Cu and Q- phases (peak C). These finding support the thermal analysis results presented in section 4.1.2. Also, it may be seen from Figure 4.8 that the magnitude of peak C corresponding to the Al_2Cu and Q- phases is noticeably larger in the D0 base alloy compared to the alloy with 1.0 wt.% Ce addition, and is totally absent in the D0 alloy containing 5.0 wt.% Ce. As discussed earlier in

section 4.2.1, the disappearance of this peak is attributed to the reaction of Ce with the Cu present in the alloy to form Ce-containing intermetallics, thus depleting the formation of the copper phases.

Also, the DSC curves of D0 alloy with 5.0 wt.% Ce addition displayed small endothermic peaks (D, E, and F) at temperatures of 586 °C , 553 °C and 550 °C , respectively. Peak D can be attributed to the melting of the grey Ce-containing intermetallic phases, while peaks E and F correspond the white Ce-containing intermetallic phase.
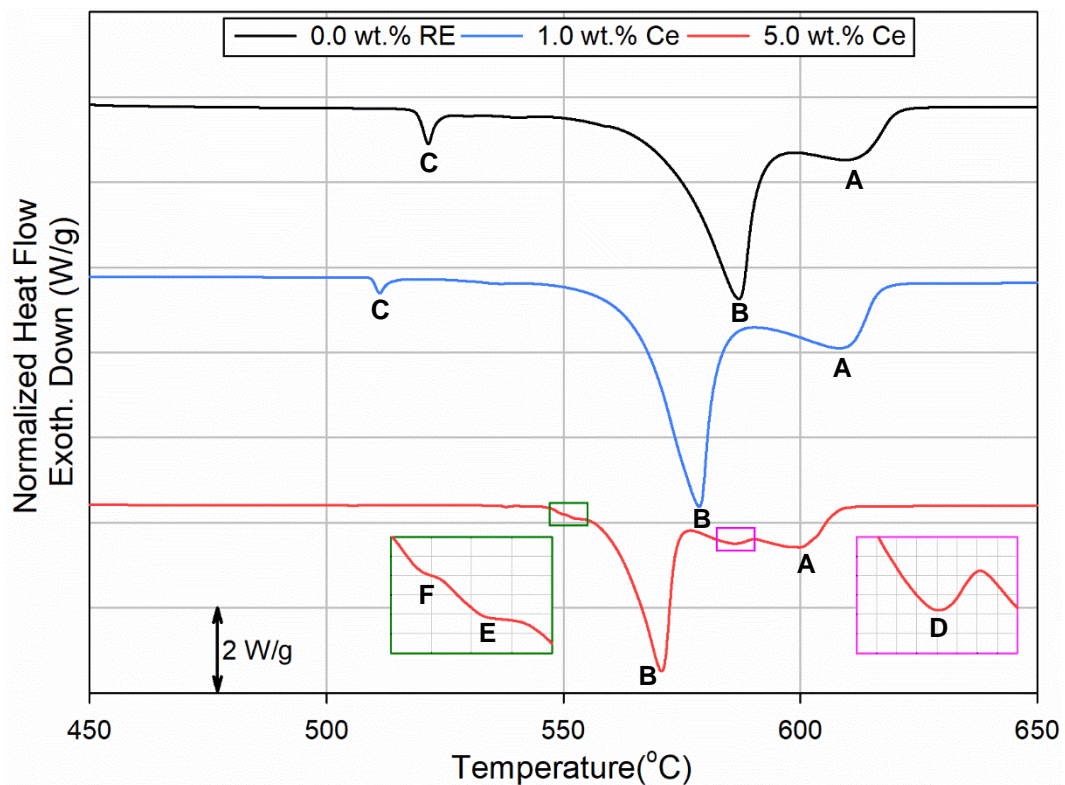
Figure 4.12: DSC melting curves of D0 alloy with 1.0 and 5.0 wt.% of Ce additions.

Figure 4.13 shows the DSC solidification curves of the D0 alloy without and with Ce additions. In keeping with the DSC heating curves, Figure 4.13 indicated that the DSC solidification curves of D0 alloys displayed two exothermic peaks (A and B) in common, at temperatures ranging from 594.5 to 607ºC and 555 to 570 ºC, respectively. A third

exothermic peak C was observed in the DSC solidification curves of the base alloy and D0 alloy with 1.0 wt.% Ce, in the temperature range of 499.7 to 508 ^oC. As before, these three peaks can be attributed to the solidification reactions corresponding to the primary α-Al and α-Fe phases (peak A), eutectic Al-Si phase (peak B), and Al_2Cu and Q- phases (peak C). It also may be seen from Figure 4.13 that a small exothermic peak marked E was found on the solidification curve of D0 alloy containing 1.0 wt.% Ce at 554^oC, corresponding to the white Ce-intermetallic phase. The disappearance of this peak from DSC curve of the 5.0 wt.% Ce-containing alloy may suggest that the white phase solidified in the same solidification reaction of Al-Si phase(peak B). Also, it is interesting to note that Figure 4.13 has no specific peak representing the solidification reaction for the formation the grey Ce-intermetallic phase. It is suggested that the grey phase solidified after the α-Fe phase (Peak-A).
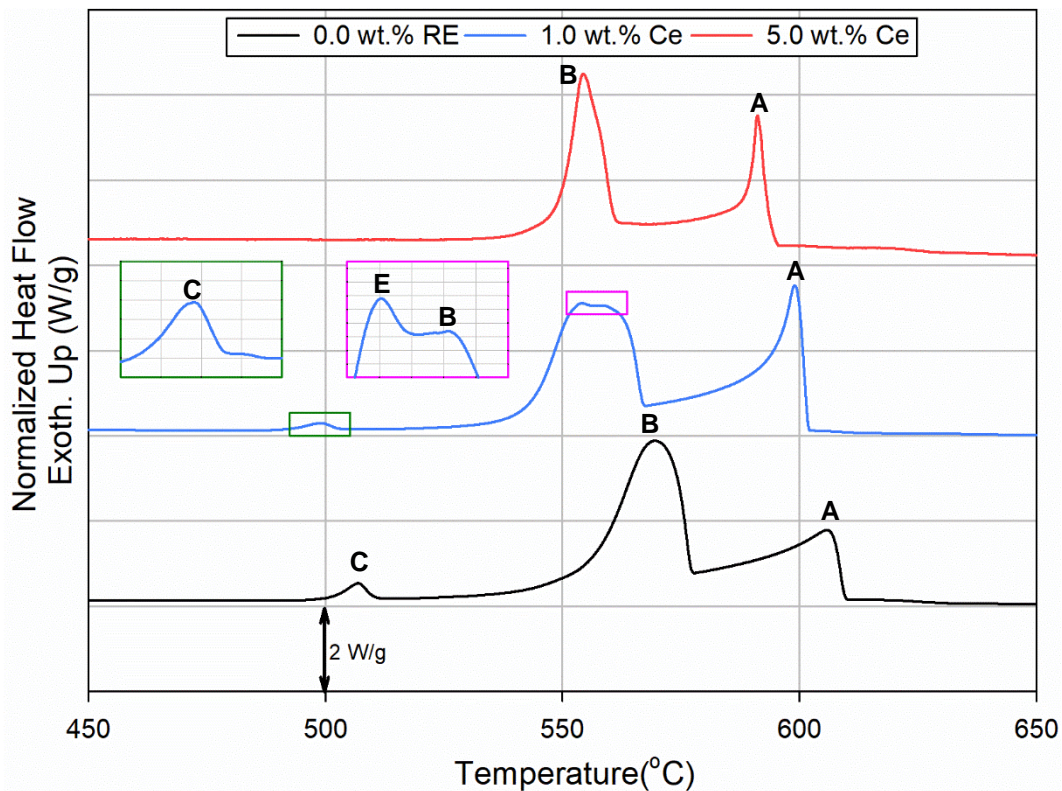
Figure 4.13: DSC solidification curves of D0 alloy with 1.0 and 5.0 wt.% of Ce additions.

The heating curves of D0 alloy containing various concentrations of La (0.0, 1.0, and 5.0 wt.%) are shown in Figure 4.14. Similar to the case of the Ce additions, the DSC curves for all alloys displayed three common exothermic peaks (A, B, and C) at temperatures ranging from 608 to 604 ℃ , 587 to 569.5 ℃, and 521 to 506.3 ℃, respectively. The DSC melting curves of D0 alloy with 5.0 wt.% La displayed a small exothermic peak marked D at temperature 599.6 ℃. This peak may be attributed to the melting reaction of the grey La intermetallic phase. Exothermic peaks E and F also appear in the melting curves of D0 alloy with 5.0 wt.% La, at 539.5 and 525 ℃, respectively. These peaks may correspond to the white La intermetallic phase.
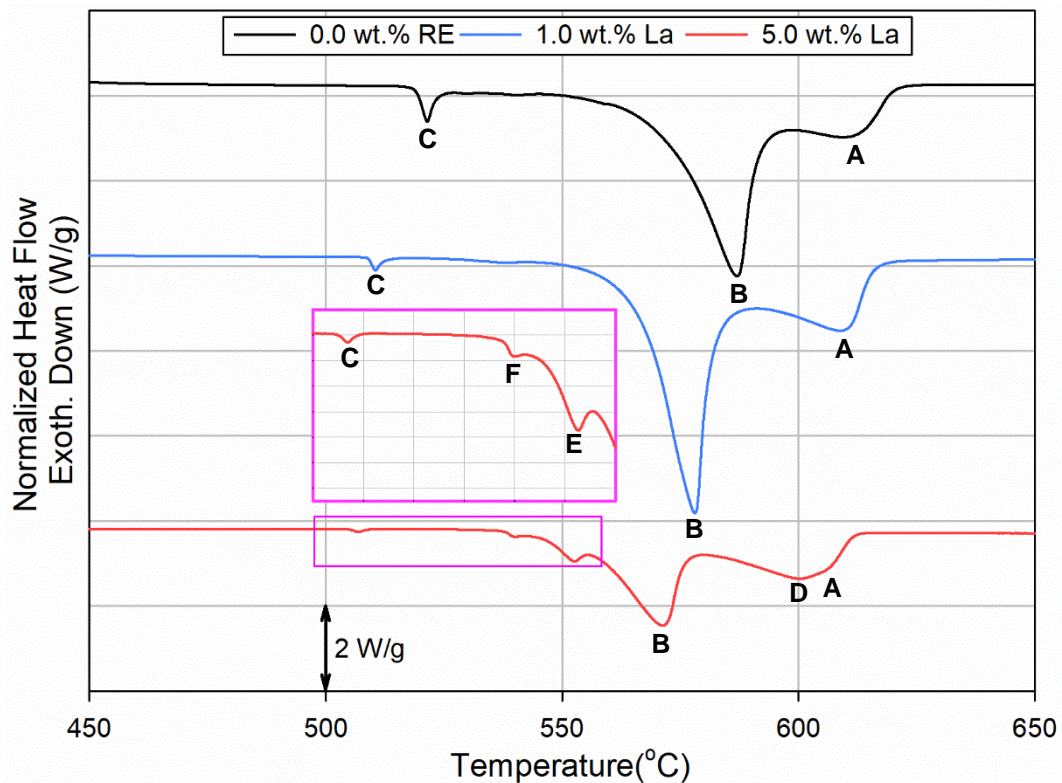
Figure 4.14: DSC melting curves of D0 alloy with 1.0 and 5.0 wt.% of La additions.

Samilar to the DSC heating curves, Figure 4.15 shows that the DSC solidification curves of the D0 base alloy and D0 alloy with 1.0 and 5.0 wt.% La additions displays two common exothermic peaks (A, and B) at temperatures of ranging from 593 to 607 ºC, and 546.3 to 570 ºC, respectively. The DSC solidification curves of the base alloy and D0 alloy with 1.0 wt.% La displayed a common exothermic peak marked C in the temperature range of 498 to 508 ºC. A small exothermic peak D at 556 ºC was found in the DSC solidification curve for D0 alloy with 1.0 wt.% La; this peak may be corresponding to the melting of the La white phase. In addition, two exothermic peaks (E and D) were observed in the DSC solidification curve for D0 alloy with 5.0 wt.% La at 580 ºC and 526 ºC, respectively, attributed to the solidification of the grey La intermetallic phase (peak E) and white La intermetallic phase (peak D).
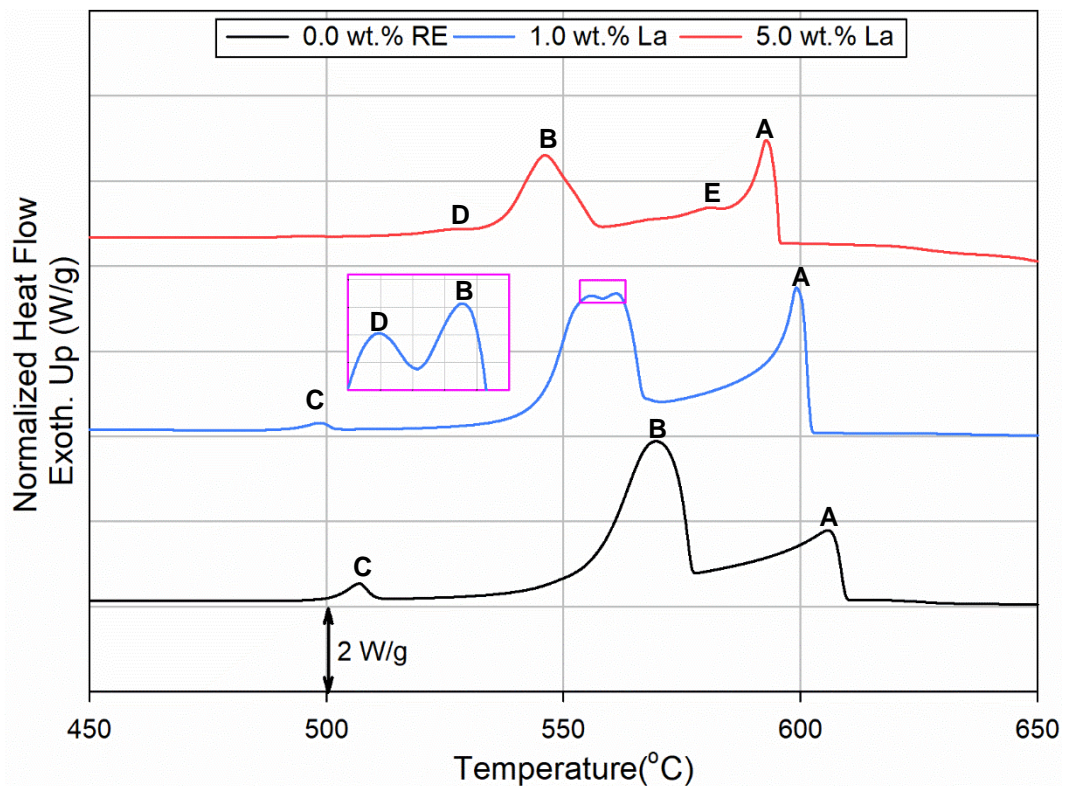
Figure 4.15: DSC solidification curves of D0 alloy with 1.0 and 5.0 wt.% of La additions.

Finally, a series of optical micrographs of the B0 and D0 alloys containing 1.0 and 5.0 wt.% RE(Ce/La) taken at x50 magnification are presented in Figure 4.16, Figure 4.17, Figure 4.18, and Figure 4.19. These micrographs reveal the importance of adding Ti in refining the grain size. However, due to the high affinity of Ti to react with the RE metals, this lead to precipitation of a large amount of RE-containing intermetallics, as discussed previously. The observed increase in the freezing zone in the RE-treated alloys may lead to formation of shrinkage porosity. Since the molten metal was not degassed prior to casting, the volume fraction of porosity may not be reliable.

As mentioned previously, the observed depression in the eutectic temperature due to addition of RE metals is not necessarily related to modification of the eutectic Si particles, as shown in Figure 4.18, and Figure 4.19. It should be mentioned that only La revealed partial modification but was not as effective a modifier, as seen in Figure 4.19(c). For example, the Si particle average area is initially 17.85 µm2 compared to 15.64 μm^2 and 10.67 μm^2 with the addition of 5.0% of Ce and 5.0% La, respectively.
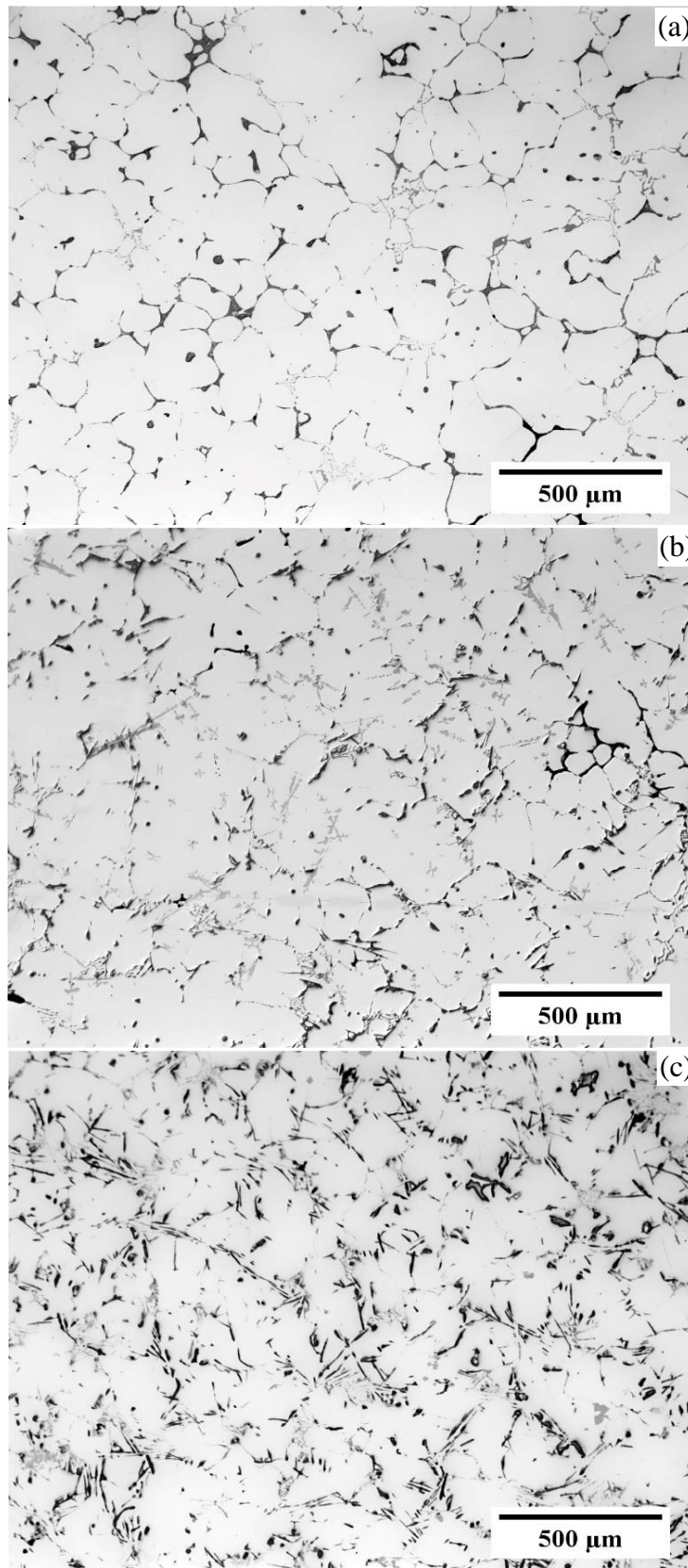
Figure 4.16: Optical micrographs of as-cast B0 alloys containing (a) 0.0 wt.%RE, (b) 1.0 wt.% Ce, and (c) 5.0 wt.% Ce.
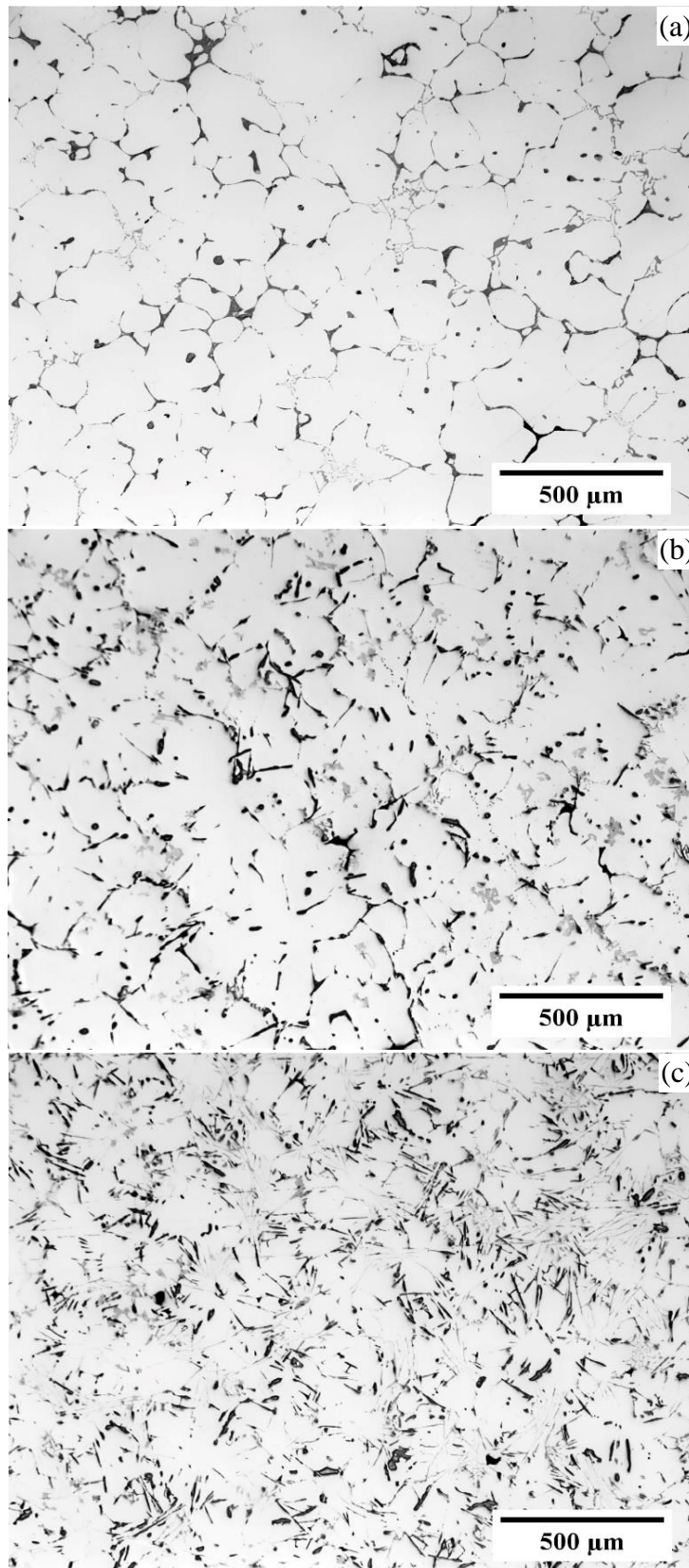
Figure 4.17: Optical micrographs of as-cast B0 alloys containing (a) 0.0 wt.%RE, (b) 1.0 wt.% La, and (c) 5.0 wt.% La.
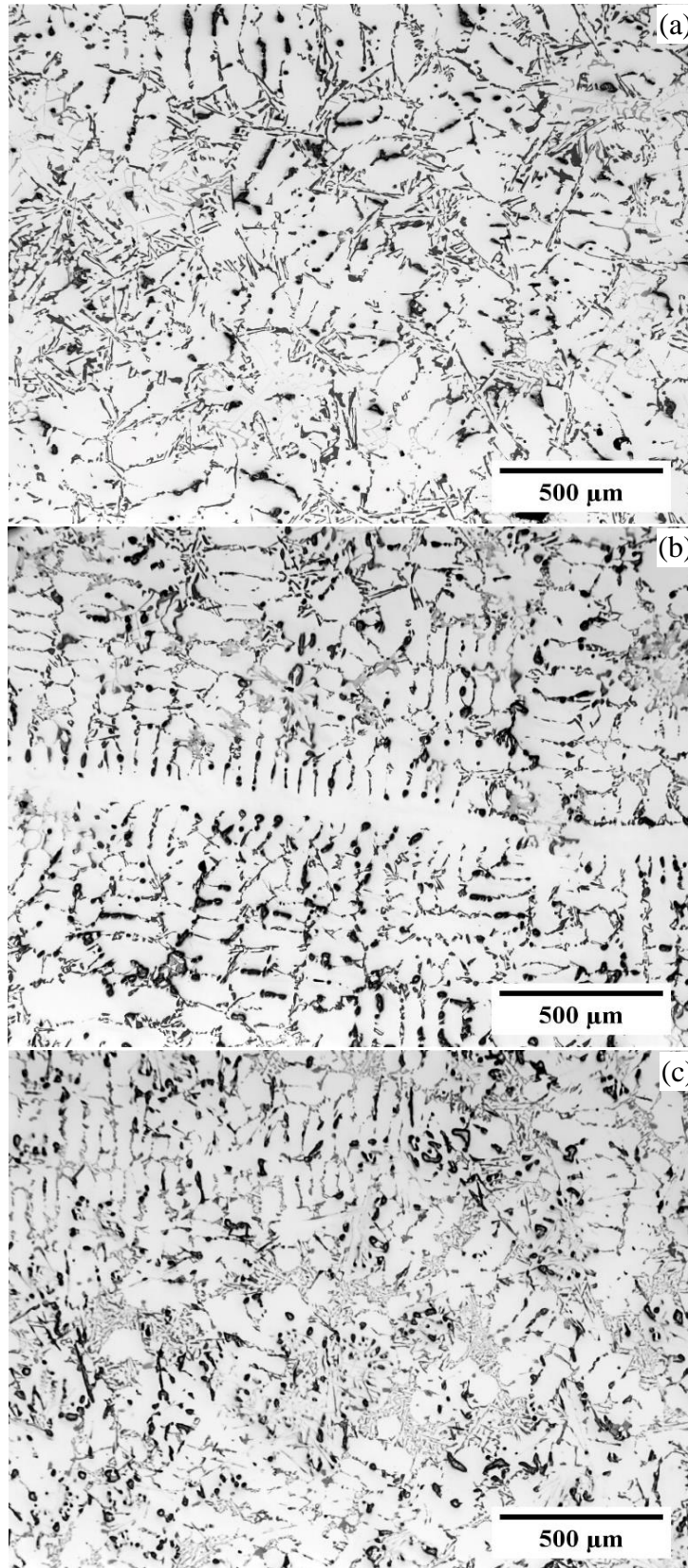
Figure 4.18: Optical micrographs of as-cast D0 alloys containing (a) 0.0 wt.%RE, (b) 1.0 wt.% Ce, and (c) 5.0 wt.% Ce.
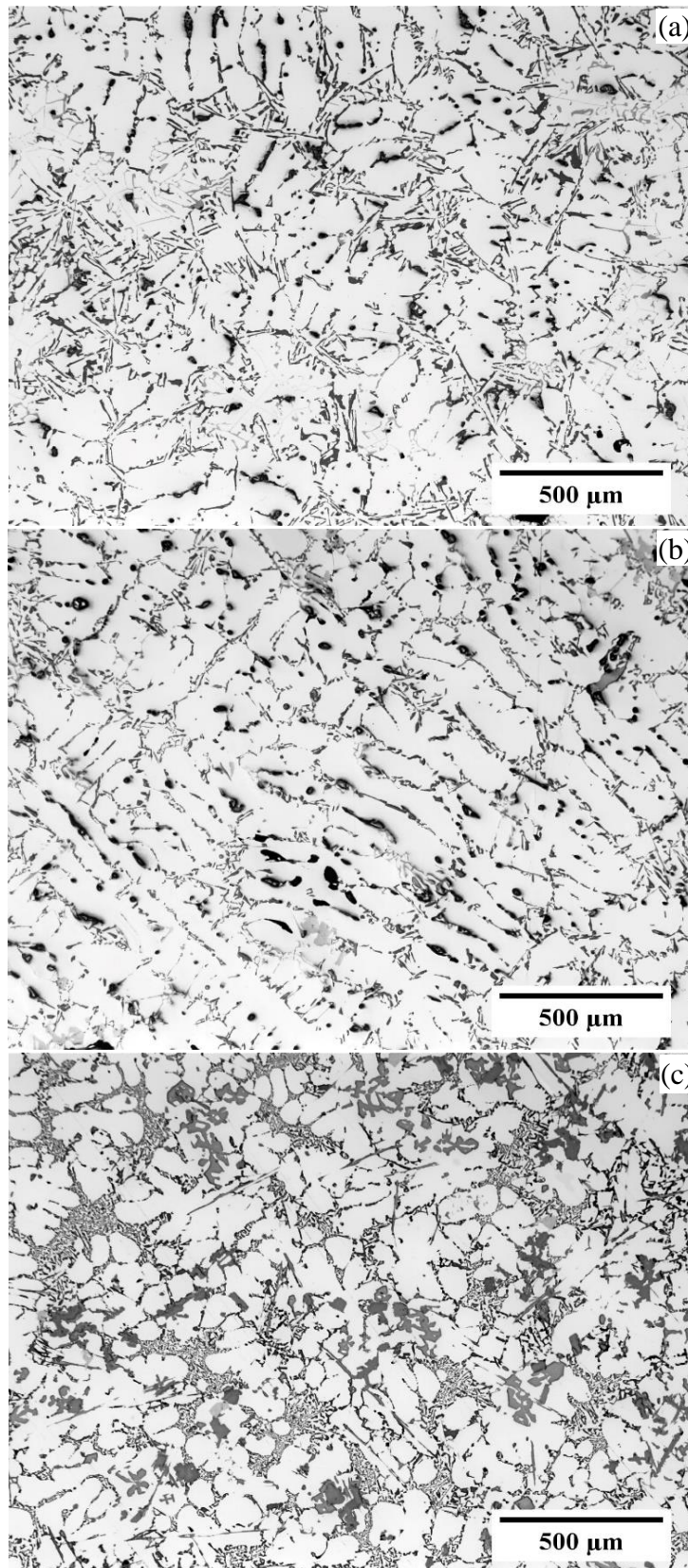
Figure 4.19: Optical micrographs of as-cast B0 alloys containing (a) 0.0 wt.%RE, (b) 1.0 wt.% La, and (c) 5.0 wt.% La.

CHAPTER 5

MICROSTRUCTURAL CHARACTERIZATION

CHAPTER 5

MICROSTRUCTURAL CHARACTERIZATION

5.1 INTRODUCTION

In general, it could be expected that the addition of RE (Ce/La) to B0 and D0 alloys investigated would result in the formation of RE-Containing intermetallics, in addition to those already expected to occur on account on the alloying elements contained in these alloys. In addition to, the solidification characteristics results presented previously in CHAPTER 4 must be correlated with metallographic examinations. Accordingly, the microstructures of polished samples of the alloys were examined using a scanning electron microscope (SEM) equipped with an energy dispersive X-ray spectrometer (EDS), and an electron probe micro-analyzer (EPMA) coupled with a wavelength dispersive spectrometer (WDS).

After the thermal analysis of the investigated Al-Cu (B0) and Al-Si-Cu (D0) alloys containing 0.0, 1.0, 5.0 wt.% of RE (Ce/La) was carried out, samples were sectioned from the corresponding casting, close to the thermocouple tip, as shown previously in Figure 3.5. The samples from these casting were obtained at low cooling rate (0.7 ^{o}C/s), providing enough time for the intermetallics and other phases formed to grow large enough in size to facilitate phase identification using energy dispersive X-ray spectrometric (EDS), and wavelength dispersive spectrometric (WDS) facilities associated with SEM and EPMA equipment used in this study. The results are presented in section 5.2 and 5.3, respectively.

5.2 SEM OBSERVATIONS

In this section, using a scanning electron microscope (SEM) equipped with an energy dispersive X-ray spectrometer (EDS), a series of backscattered electron (BSE) micrographs combined with chemical analysis will be presented to illustrate the effect of 0.0, 1.0, and 5.0 wt.% of RE metals (Ce/La) on the morphology and density of the precipitated intermetallic of as-cast B0 and D0 alloys.

5.2.1 Al-Cu (B0) Alloy

The B0 base alloy contains 2.4 wt.% Cu, 1.2 wt.% Si, 0.4 wt.% Mg, 0.6 wt.% Mn, and 0.15 wt.% Ti; it can hence be classified as an Al-Cu alloy. Based on its composition, the B0 alloy displays the three main phases: θ-Al_2Cu, Q-$Al_5Mg_8Si_6Cu_2$, and the Chinese script-like α-$Al_{15}(Fe,Mn)_3Si_2$ phases, as shown in Figure 5.1(a, b). It can be seen from the backscattered image in Figure 5.1(a) that the Al_2Cu phase precipitates in both block-like and eutectic-like forms whereas the $Al_5Mg_8Si_6Cu_2$ phase appears as small particles growing out of the Al_2Cu phase. The absence of free Si in the microstructure implies that the Si content of the alloy was consumed in the formation of the Q-$Al_5Mg_8Si_6Cu_2$ and α-$Al_{15}(Fe,Mn)_3Si_2$ phases.

At the same time, it was observed that the platelet-like β-Al_5FeSi phase was not in evidence because of the high Mn/Fe ratio (~1) of the alloy, which promotes the formation of the α-Fe phase at the expense of the β-Fe phase. The elements in the phases observed in the as-cast base B0 base alloy were identified using energy dispersive X-ray spectrometry (EDS), as shown in Figure 5.1(c). The results are found to be in agreement with results presented in CHAPTER 4.
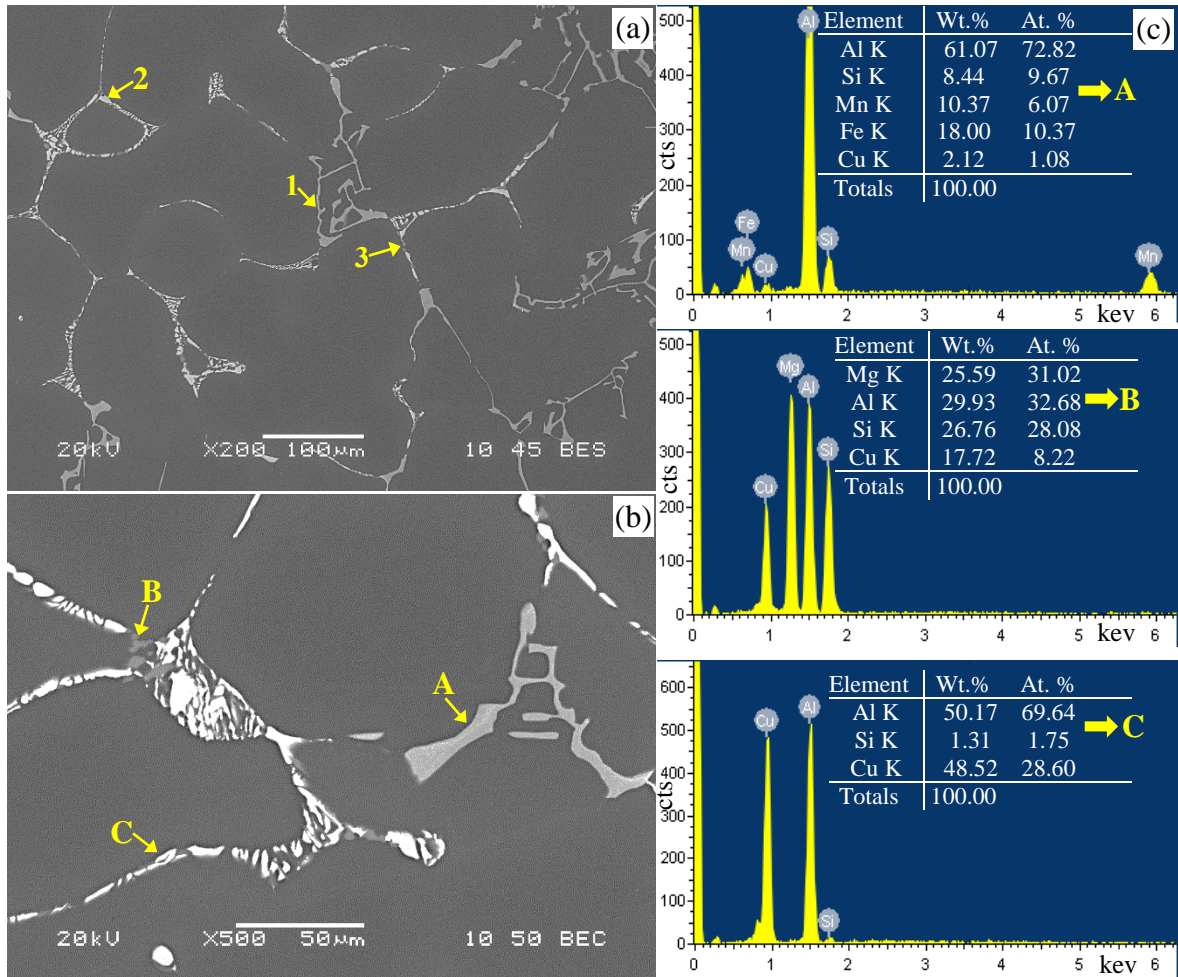
Figure 5.1: Backscattered electron (BSE) images showing the microstructure of as-cast B0 base alloy at (a) low magnification, (b) high magnification, and (c) EDS analysis of locations marked A, B and C in (b). The arrows indicate (1) α-$Al_{15}(Fe,Mn)_3Si_2$, (2) Q-$Al_5Mg_8Si_6Cu_2$, and (3) θ-Al_2Cu.

Figure 5.2 and Figure 5.3 show the BSE images of B0 alloys with 1.0 and 5.0 wt.% Ce contents in the as-cast condition. Compared to the B0 base alloy, the microstructures are changed upon adding different levels of Ce. In general, Ce reacts with other pre-existing elements to form intermetallic particles. Addition of Ce results in the precipitation of an extensive amount of thin, long particles of a white phase. Addition of Ti + RE causes the precipitation of a grey phase in the form of "sludge" as shown in Figure 5.2(b) and Figure 5.3(b); this phase has been reported by Tsai et al. [140]. These intermetallic particles

act as the nuclei for the α-Al phase during the primary stage of solidification, as the Ce-containing intermediate phase has the same crystal structure (fcc) and a closely similar lattice as the α-Al grains. These observations agree well with those reported by Zhang et al [181]. Based on the compositions listed in Figure 5.2 (c) and Figure 5.3(c), the Fe-based sludge should precipitate at about 650°C, which exceeds the melting temperatures of the two alloys. Similarly, the grey-phase particles (judging by their morphology) could as well have precipitated in the liquid state prior to solidification and acted as nucleation sites for the white phase.
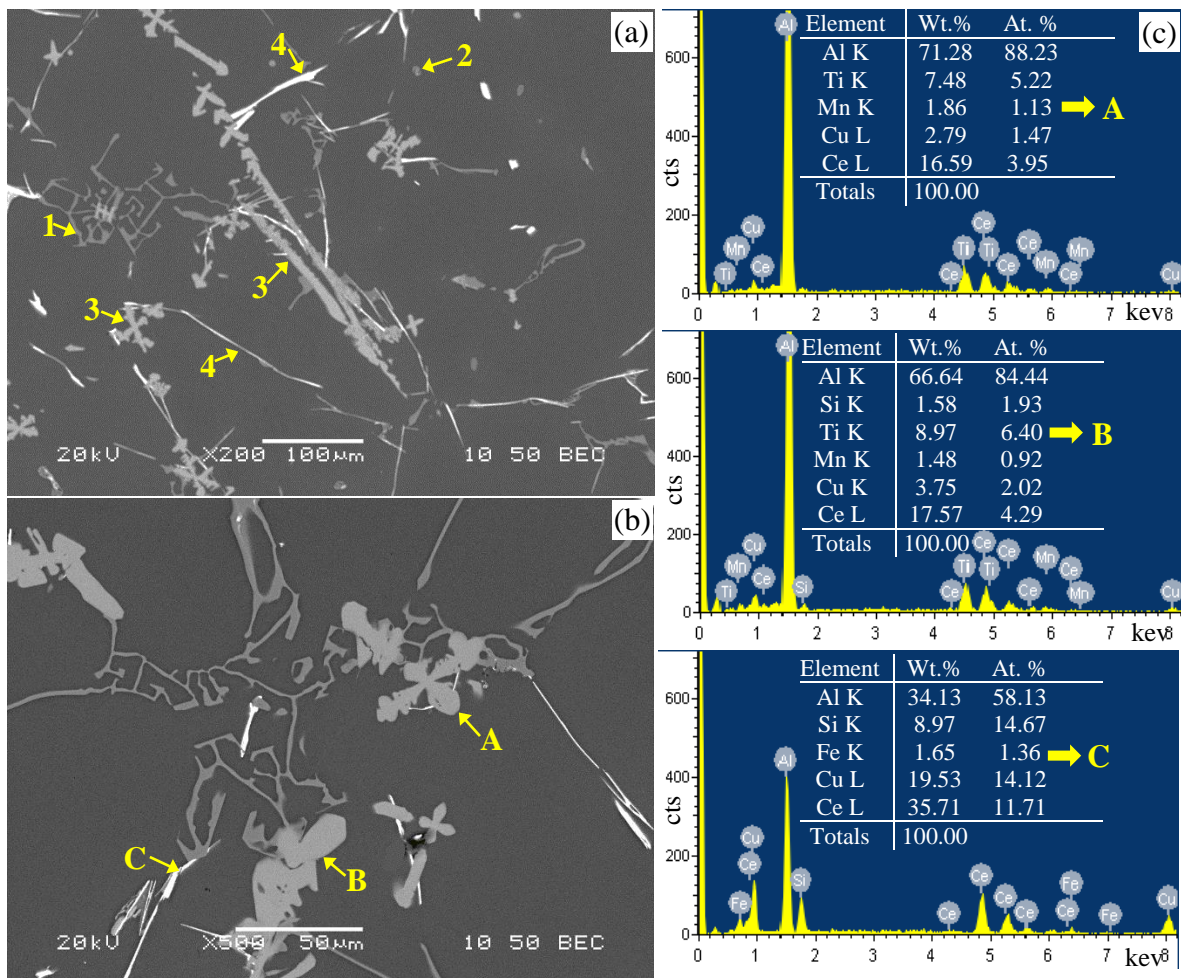
Figure 5.2: Backscattered electron (BSE) images showing the microstructure of as-cast B0 alloy with 1.0 wt.% Ce addition at (a) low magnification, (b) high magnification, and (c) EDS analysis of locations marked A, B and C in (b). The arrows indicate (1) α-Fe, (2) Al₂Cu, (3) grey phase AlTiCeCu, and (4) white phase AlSiCuCe.
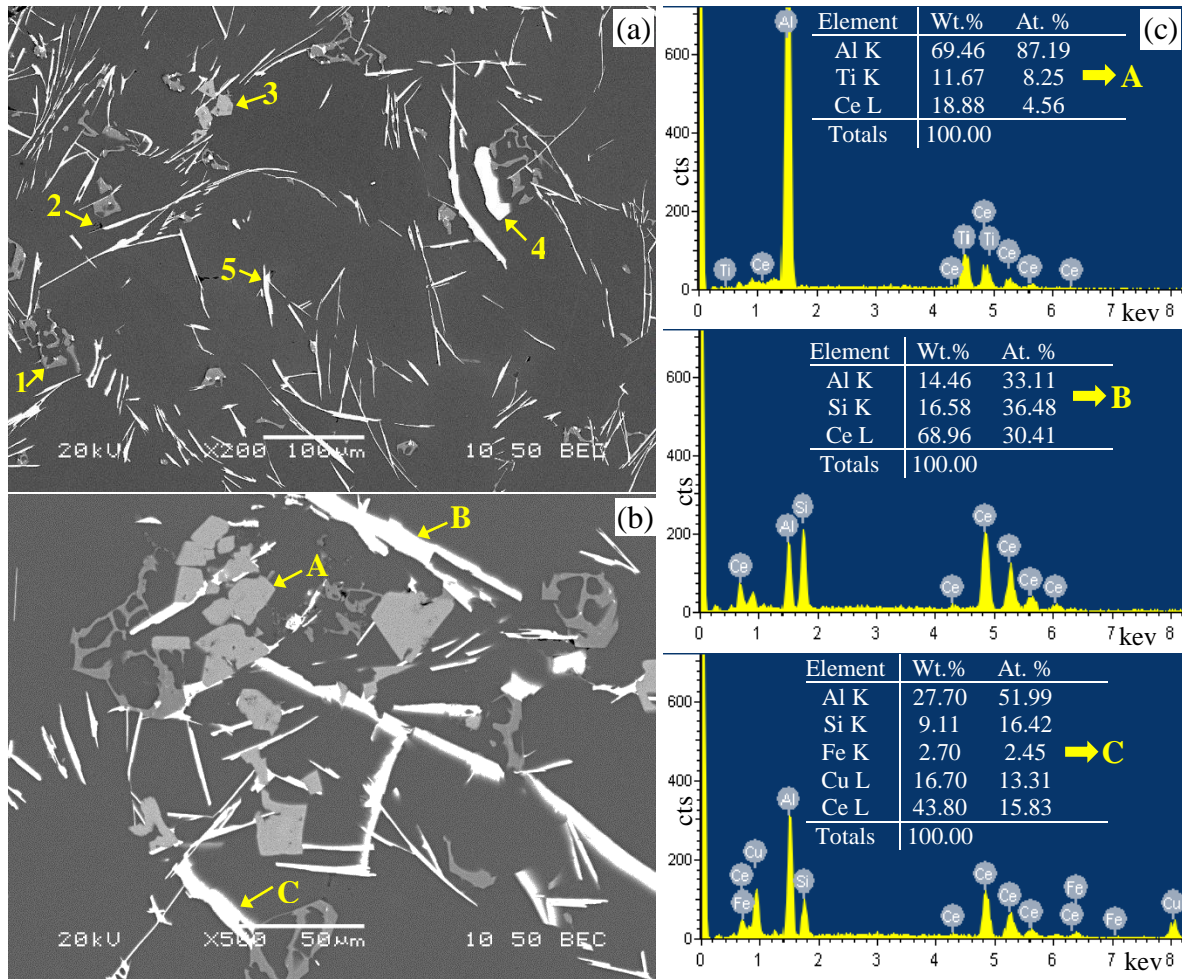
Figure 5.3: Backscattered electron (BSE) images showing the microstructure of as-cast B0 alloy with 5.0 wt.% Ce addition at (a) Low magnification, (b) high magnification, and (c) EDS analysis of locations marked A, B, and C in (b). The arrows indicate (1) α-Fe, (2) Mg_2Si, (3) grey phase AlTiCe, (4) white phase AlSiCe, and (5) white phase AlSiCuCe.

An important point that should be taken in consideration is that, when compared to 1.0 wt.% Ce addition, it can be seen from Figure 5.3 that Increasing the Ce level addition to 5.0 wt.% resulted in totally consuming the amount of Cu present in the base alloy, so that no θ-Al_2Cu phases is formed, as was confirmed by the DSC analysis results described in CHAPTER 4. Accordingly, Ce reacts with Cu to form two white phases (AlSiCuCe) and AlSiCe; the first phase already observed with 1.0 wt.% Ce addition, and the second one formed when the Ce addition is increased to 5.0 wt.% . As this increased level of Ce addition,

the $Q-Al_5Mg_8Si_6Cu_2$ also disappears. Consequently, the existing amount of Mg in the alloy reacts with Si to form Mg_2Si phase, as shown Figure 5.3(a). This was not observed in case of 1.0 wt.% Ce addition.

The BSE images obtained from as-cast alloy samples of B0 alloys containing 1.0 and 5.0 wt.% La additions are shown in Figure 5.4 and Figure 5.5, respectively. Compared to the results mentioned above, both La and Ce found to have more or less the same effect on the microstructures, with the La- and Ce-containing intermetallics also displaying similar morphologies.

Backscattered electron (BSE) images depicting the morphology, size and distribution of intermetallic compounds observed in the B0 alloy samples containing Ce and La additions, and obtained in the as-cast condition, are presented in Figure 5.6 and Figure 5.7. A comparison between the B0 base alloy and B0 containing RE(Ce/La) addition, Figure 5.6(b, c) and Figure 5.7(b, c) reveals that as the RE(Ce/La) addition increases from 1.0 to 5.0 wt.%, the relative amount of intermetallic particles formed increases, attributed to the formation of new RE-containing intermetallic compounds. In addition, Figure 5.6 and Figure 5.7 also show that these RE intermetallic compounds were observed to precipitate along the interdendritic regions

The aspect ratio, roundness, and volume fraction, describing the intermetallic compounds in the B0 alloy with Ce and La additions are presented in Figure 5.8 and Figure 5.9, respectively. From Figure 5.8, as the addition level of Ce increases, the volume fraction increases from 3.3% to 8.7%, while Figure 5.9 shows that the volume fraction increases from 3.3% to 11.1% with increase in the La addition. The average values of roundness and aspect ratio lie in the ranges of 0.39-0.31 and 3.0-5.37, respectively, for the Ce additions, and 0.39-0.27 and 3.0-6.32, respectively, for the La additions.
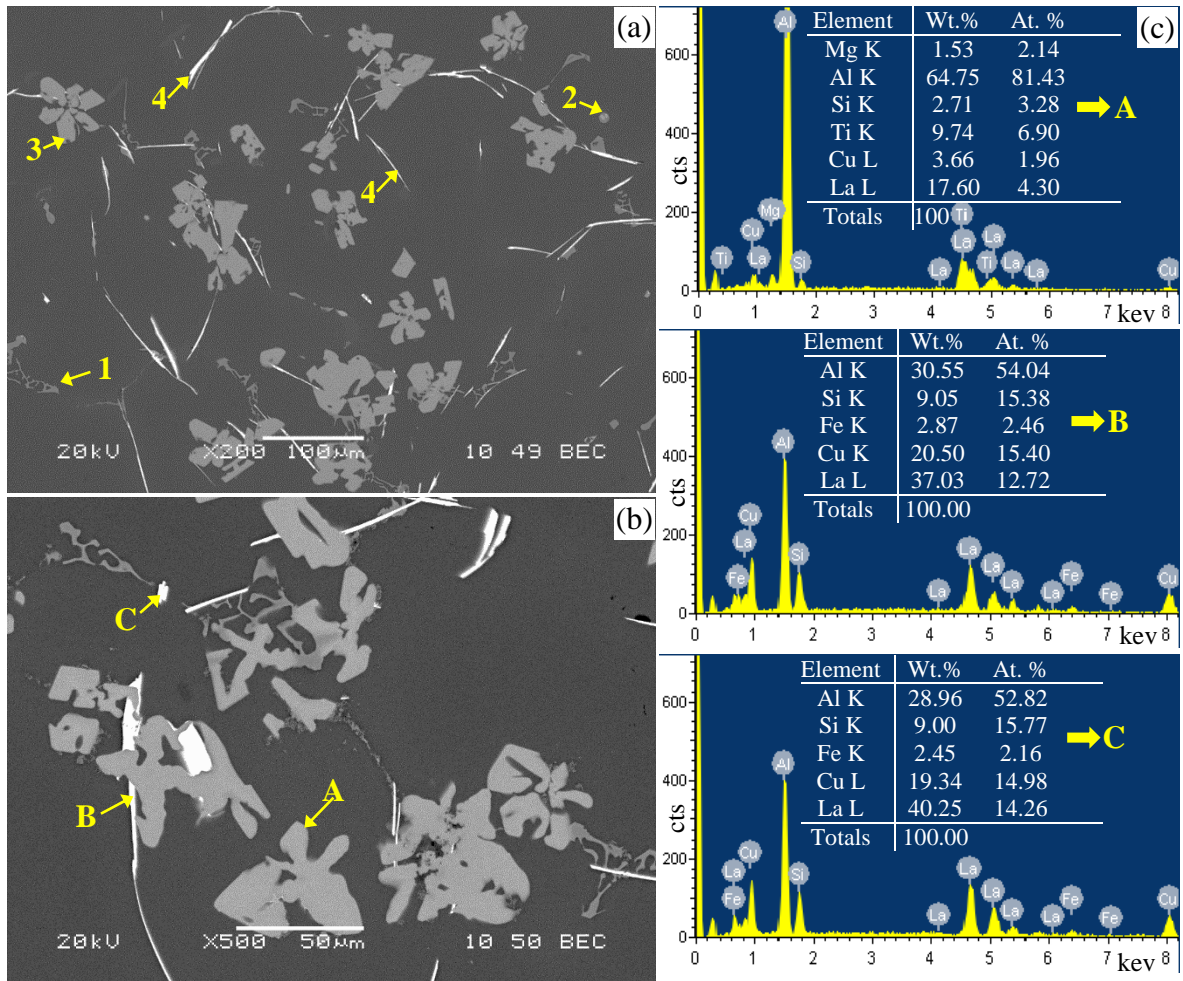
Figure 5.4: Backscattered electron (BSE) images showing the microstructure of as-cast B0 alloy with 1.0 wt.% La addition at (a) low magnification, (b) high magnification, and (c) EDS analysis of locations marked A, B, and C in (b). The arrows indicate (1) α-Fe, (2) Al$_2$Cu, (3) grey phase AlTiLa, and (4) white phase AlSiCuLa.
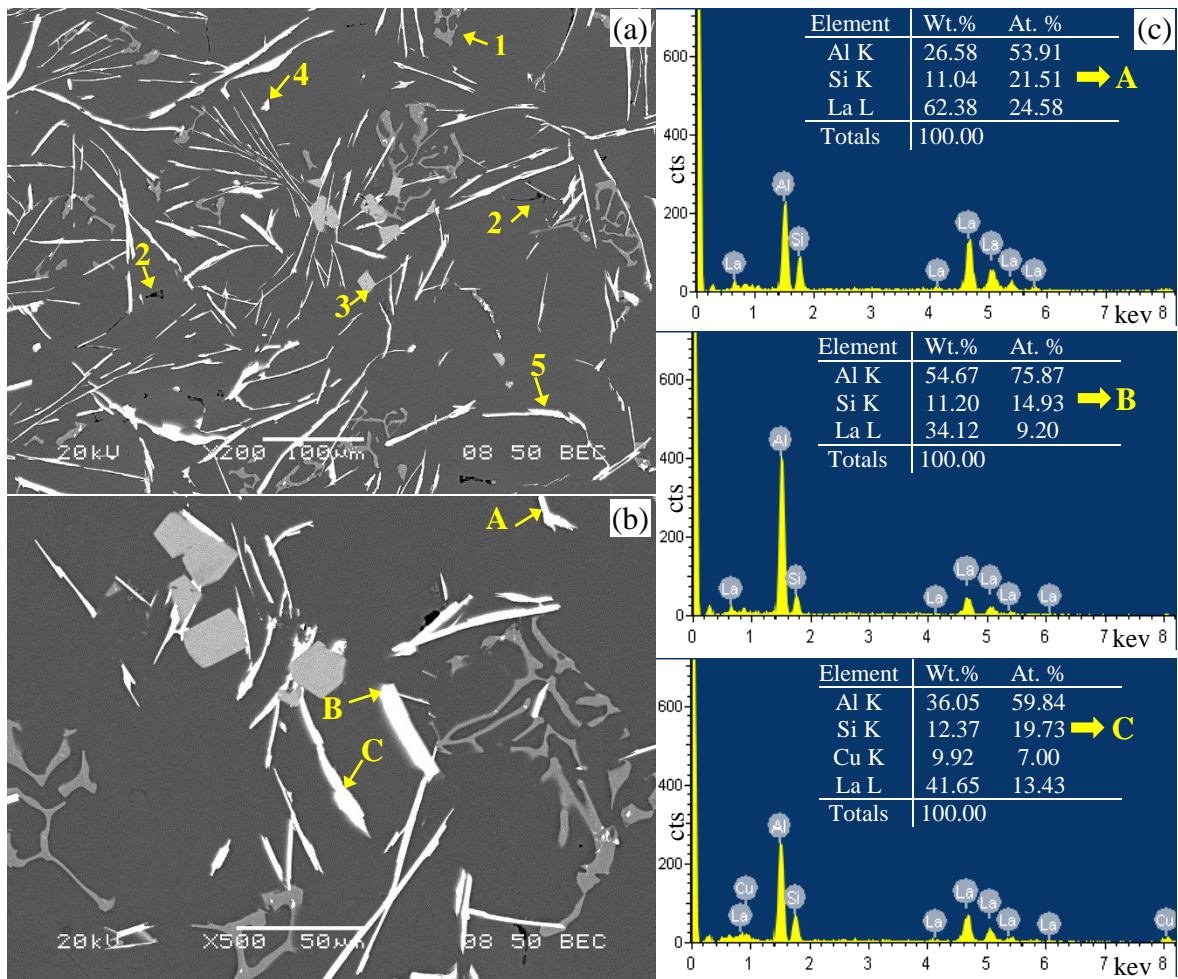
Figure 5.5: Backscattered electron (BSE) images showing the microstructure of as-cast B0 alloy with 5.0 wt.% La addition at (a) low magnification, (b) high magnification, and (c) EDS analysis of locations marked A, B, and C in (b). The arrows indicate (1) α-Fe, (2) Mg$_2$Si, (3) grey phase AlTiLa, (4) white phase AlSiLa, and (5) white phase AlSiCuLa.
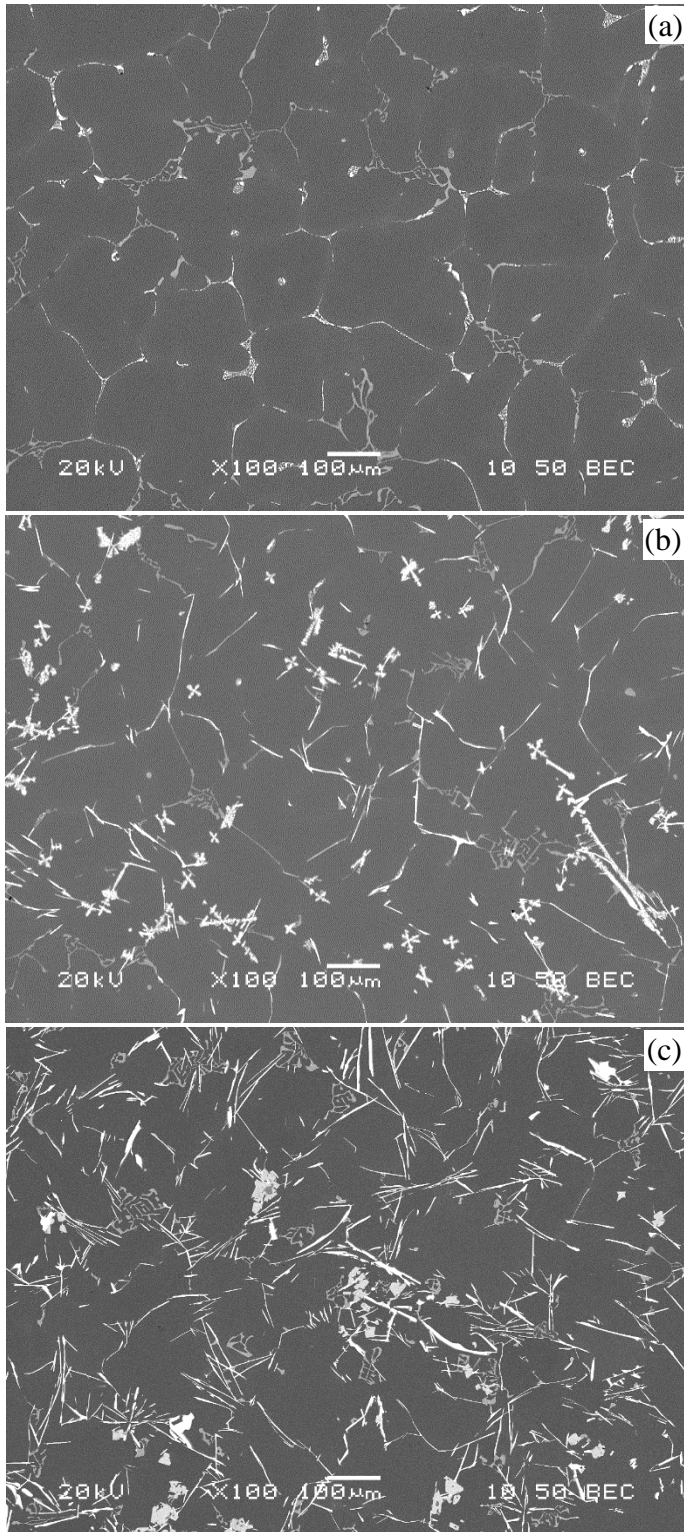
Figure 5.6: Backscattered electron (BSE) images showing the microstructures of as-cast B0 alloy containing (a) 0.0 wt.%RE, (b) 1.0 wt.% Ce, and (c) 5.0 wt.% Ce.
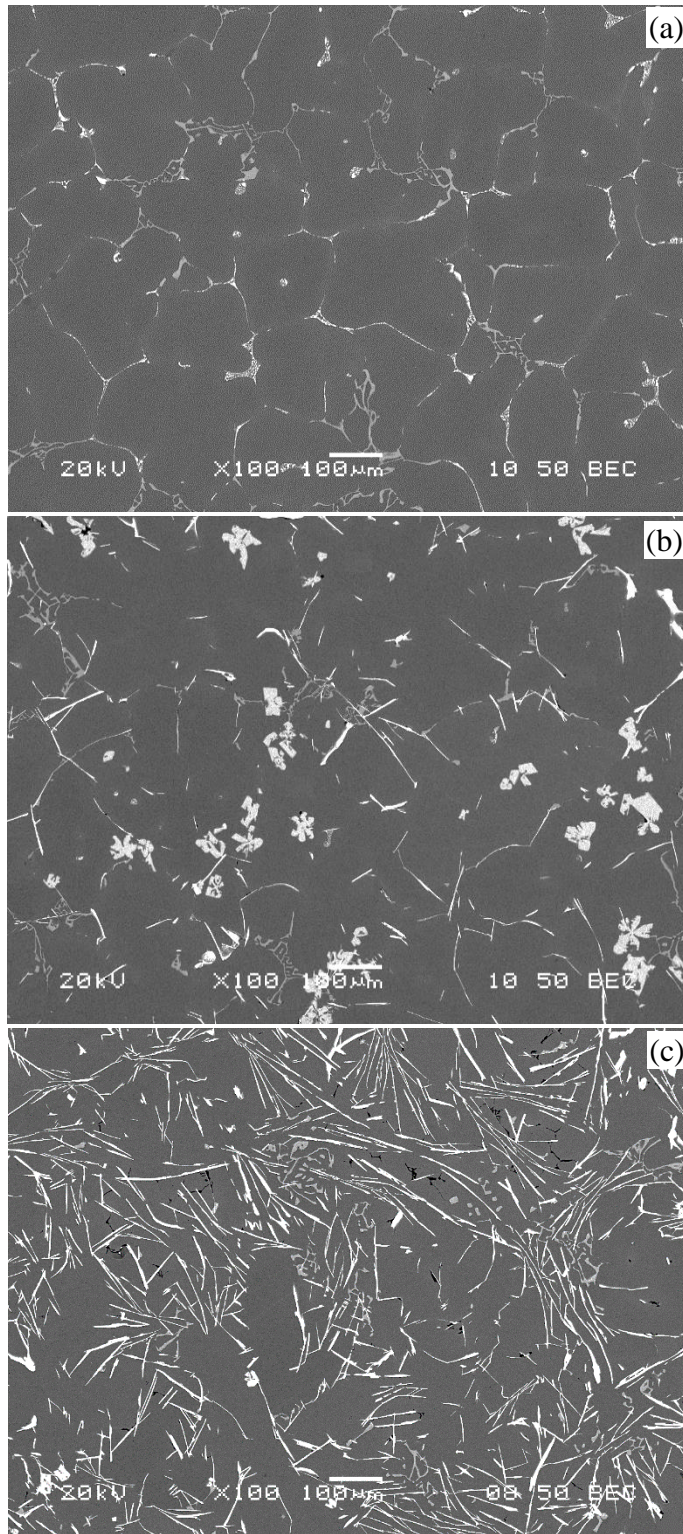
Figure 5.7: Backscattered electron (BSE) images showing the microstructures of as-cast B0 alloy containing (a) 0.0 wt.%RE, (b) 1.0 wt.% La, and (c) 5.0 wt.% La.
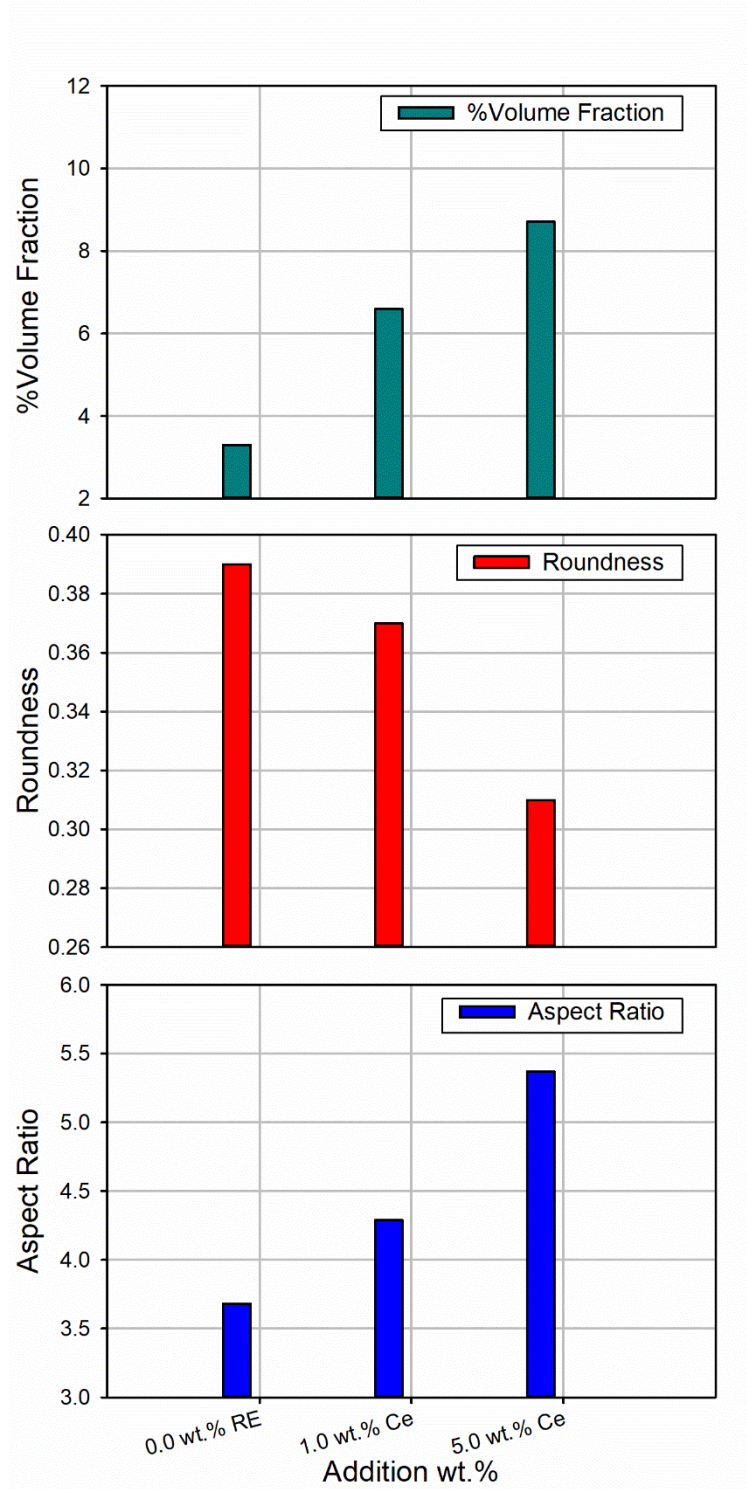
Figure 5.8: Key parameters of %volume fraction, roundness and aspect ratio describing the characteristics of intermetallic compounds in as-cast B0 alloy with various additions of Ce (0.0, 1.0, and 5.0 wt.%).
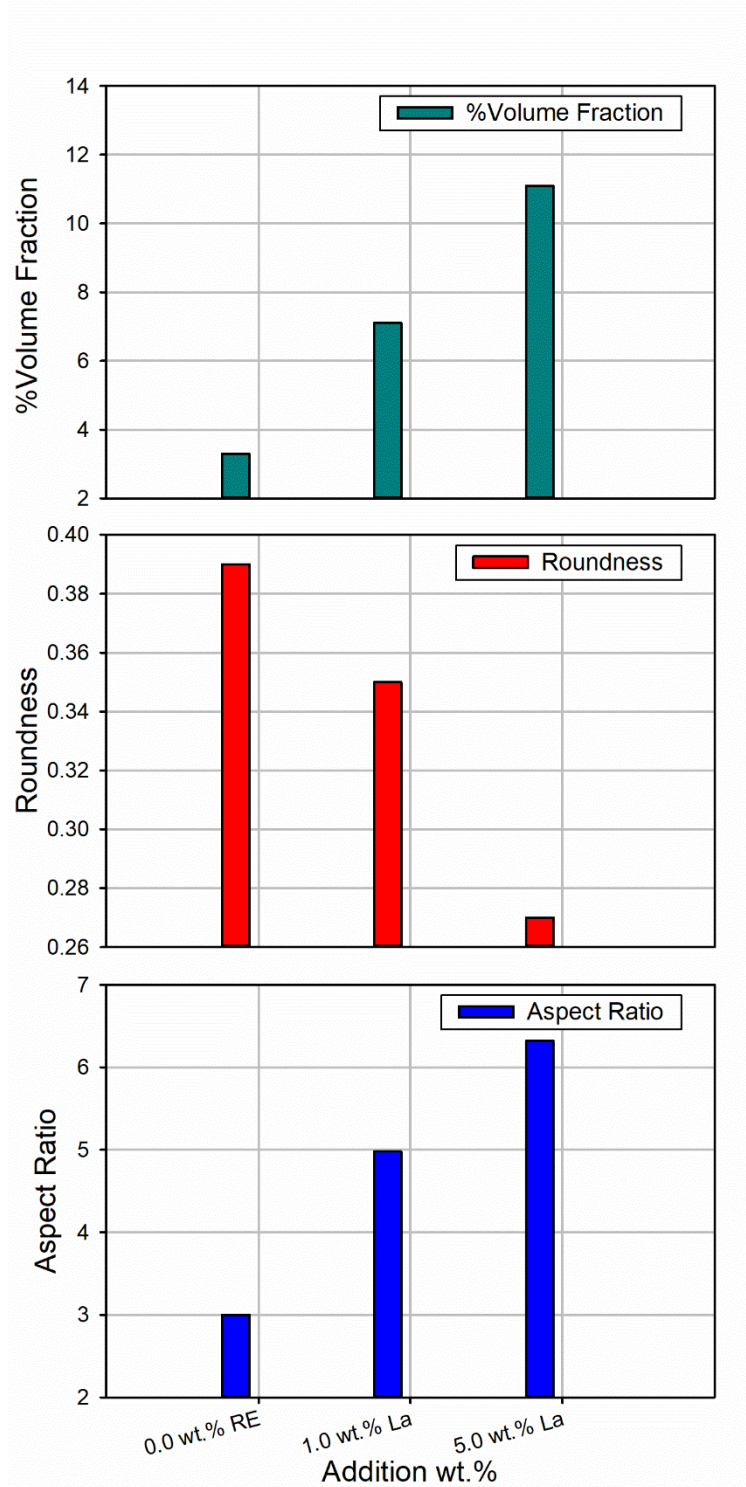
Figure 5.9: Key parameters of %volume fraction, roundness and aspect ratio describing the characteristics of intermetallic compounds in as-cast B0 alloy with various additions of La (0.0, 1.0, and 5.0 wt.%).

5.2.2 Al-Si-Cu (D0) Alloy

Figure 5.10(a) and (b) show the BSE images of as-cast D0 alloy at low and high magnifications, respectively. Based on the nominal composition of the alloy, four main types of secondary phases were observed in the microstructure: dark grey phases embedded in the matrix corresponding to the Si phase (blocky and long platelet eutectic Si_e); bright phase particles corresponding to the copper aluminide (θ-Al_2Cu) and the Q-$Al_5Mg_8Si_6Cu_2$ phases, and the Chinese script α-$Al_{15}(Fe,Mn)_3Si_2$ phases particles,

Element	Wt.%	At. %
Al K	59.20	70.01
Si K	11.75	13.35
Mn K	14.33	8.32
Fe K	13.48	7.70
Cu K	1.23	0.62
Totals	100.00	

→ A

Element	Wt.%	At. %
Mg K	12.57	14.70
Al K	57.35	13.35
Si K	20.18	20.43
Cu K	9.90	4.43
Totals	100.00	

→ B

Element	Wt.%	At. %
Al K	41.50	62.10
Si K	0.91	1.30
Cu K	57.6	36.60
Totals	100.00	

→ C
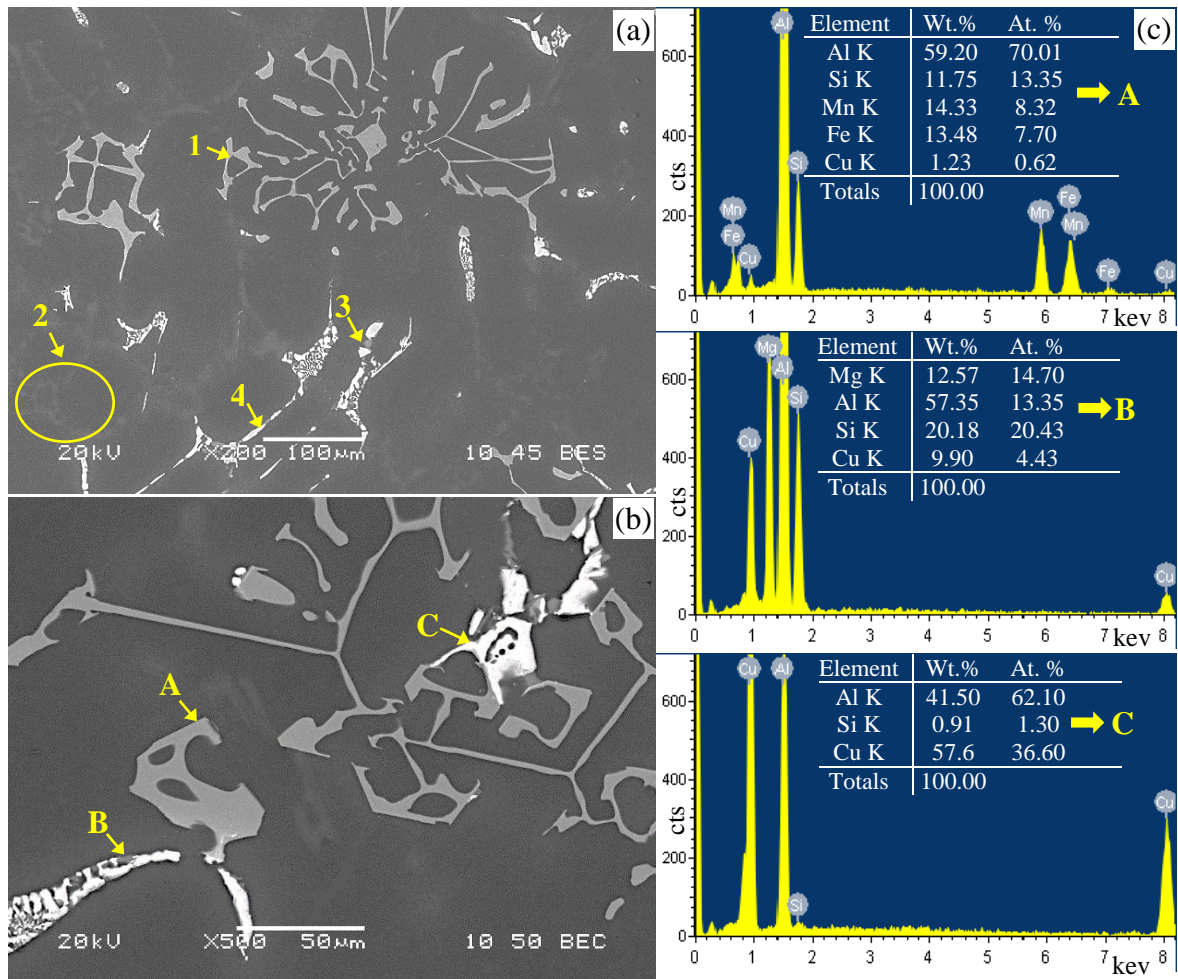
Figure 5.10: Backscattered electron (BSE) images showing the microstructures of as-cast D0 base alloy at (a) low magnification, (b) high magnification and (c) EDS analysis of locations marked A, B and C in (b). The arrows indicate (1) α-$Al_{15}(Fe,Mn)_3Si_2$, (2) eutectic Si, (3) Q-$Al_5Mg_8Si_6Cu_2$, and (4) θ-Al_2Cu.

distinguished by the their script morphology. The chemical compositions of these phases were confirmed by the corresponding energy dispersive X-ray spectra (EDS) show in Figure 5.10(c).

The microstructure of D0 alloy containing various RE contents were examined using backscattered electron imaging. The corresponding BSE images are displayed in Figure 5.11(a, b), Figure 5.12(a, b), Figure 5.13(a, b), and Figure 5.14 (a, b). The RE-containing intermetallic phases observed in these images were identified from their EDS spectra shown in Figure 5.11(c), Figure 5.12(c), Figure 5.13(c), and Figure 5.14 (c), respectively, showing the analyses of spots A, B, and C corresponding to the intermetallic phases observed in (b) in each case.
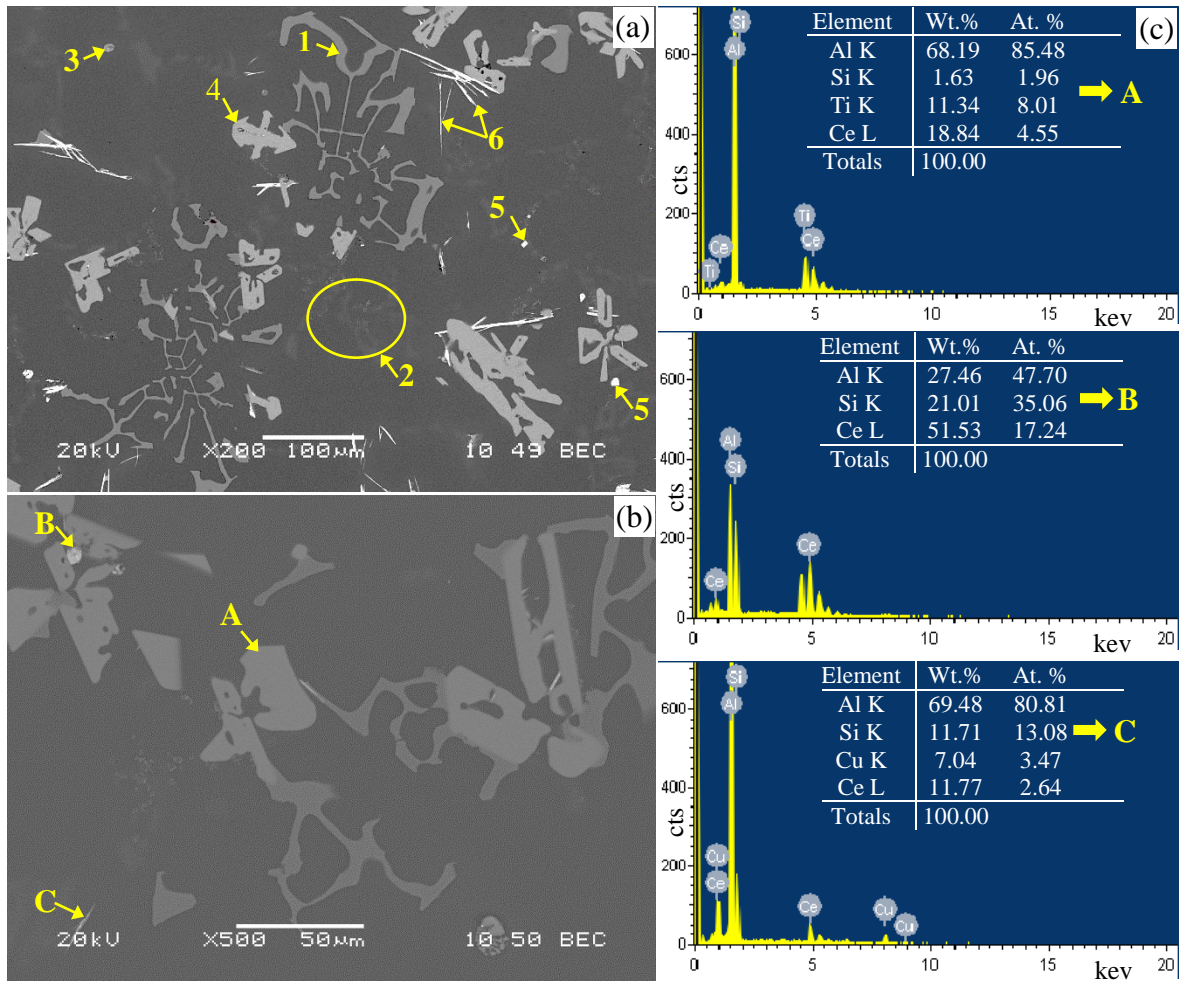
Figure 5.11: Backscattered electron (BSE) images showing the microstructures of as-cast D0 alloy with 1.0 wt.% Ce addition at (a) low magnification, (b) high magnification and (c) EDS analysis of locations marked A, B and C in (b). The arrows indicate (1) α-$Al_{15}(Fe,Mn)_3Si_2$, (2) eutectic Si, (3) θ-Al_2Cu, (4) grey phase AlTiCe, (5) white phase AlSiCe, and (6) white phase AlSiCuCe.
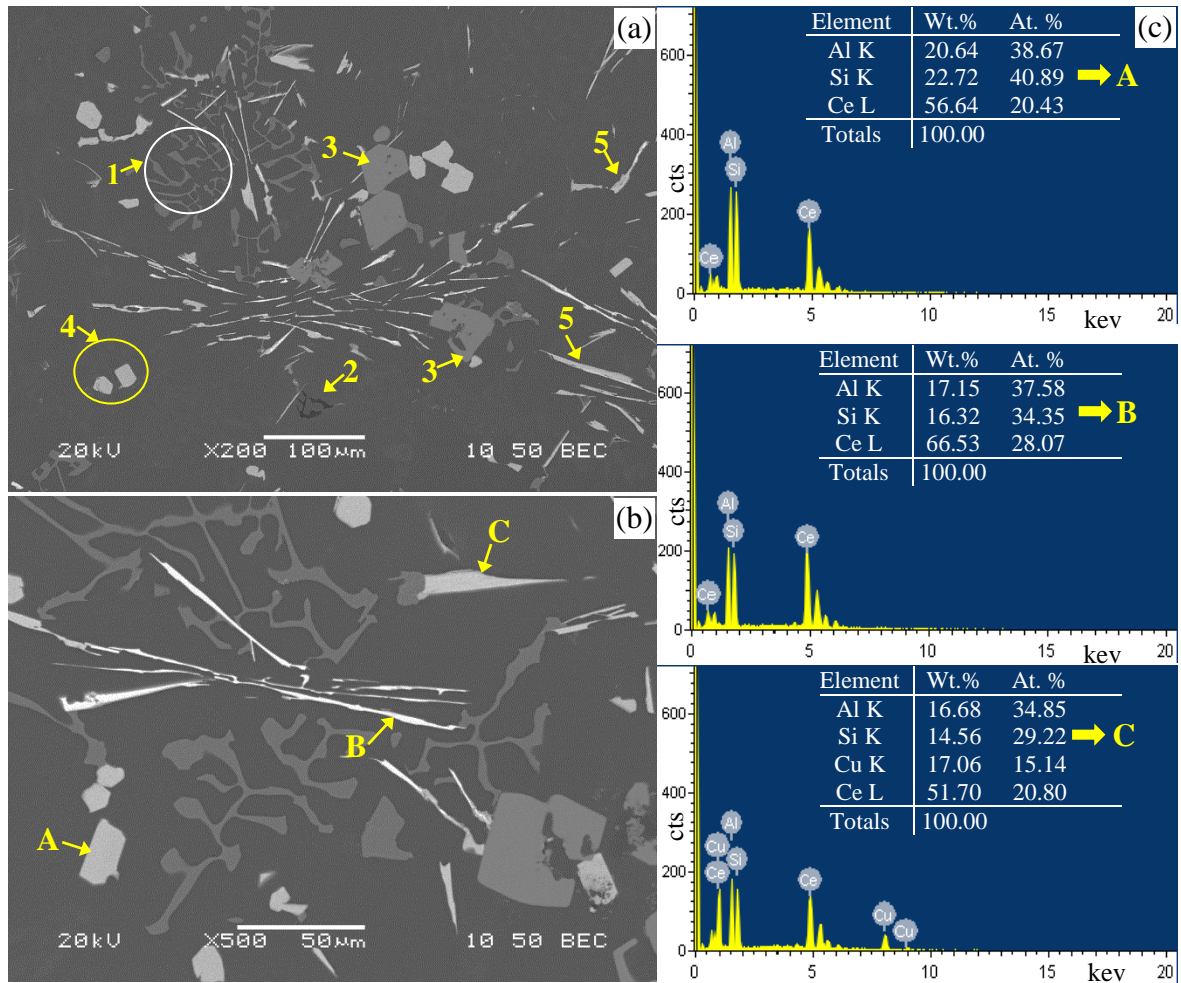
Figure 5.12: Backscattered electron (BSE) images showing the microstructures of as-cast D0 alloy with 5.0 wt.% Ce addition at (a) low magnification, (b) high magnification and (c) EDS analysis of locations marked A, B and C in (b). The arrows indicate (1) α-$Al_{15}(Fe,Mn)_3Si_2$, (2) Mg_2Si (3) grey phase AlTiCe, (4) white phase AlSiCe, and (5) white phase AlSiCuCe.

It should be mentioned here that, when D0 alloy was used, observations of the intermetallics formed were similar to those noted for the B0 alloys; that is, the amount of Si seems to have no bearing on the precipitation of the RE-containing intermetallic phases. However, two important points must be highlighted: the first one being that, with 1.0 wt.% RE(Ce/La) addition, and as seen in Figure 5.11(b), Figure 5.13(b), the white phase AlSiRE appears in the form of spots, and contains no Cu. This type of phase was not observed in the case of the B0 alloy when the same level of RE addition was used. This could be ascribed to

the increased Si level (8.0 wt.%) of the D0 alloy compared to the B0 alloy (containing 1.2 wt.% Si), leading to the formation this phase, as confirmed by EDS analysis - see Figure 5.11(c) and Figure 5.13(c). The second point to note is that the addition of an appropriate amount of RE (Ce/La) markedly increased the volume fraction of the Chinese character-like α-$Al_{15}(Fe,Mn)_3Si_2$ phase. This result agrees well with the observations of Ao et al. [182].
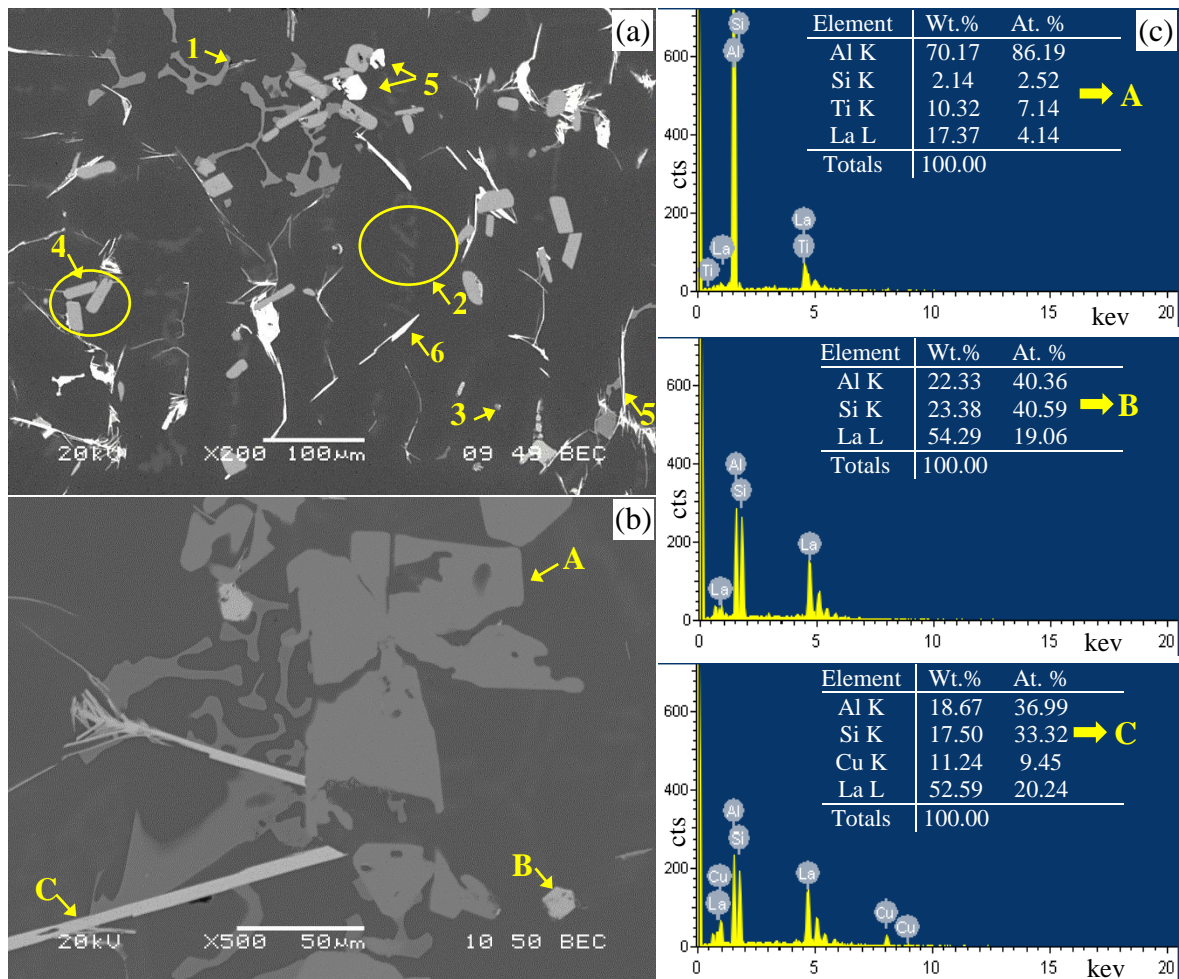
Figure 5.13: Backscattered electron (BSE) images showing the microstructures of as-cast D0 alloy with 1.0 wt.% La addition at (a) low magnification, (b) high magnification and (c) EDS analysis of locations marked (A), (B) and (C) in (b). The arrows indicate (1) α-$Al_{15}(Fe,Mn)_3Si_2$, (2) eutectic Si, (3)θ-Al_2Cu, (4)grey phase AlTiLa, (5) white phase AlSiLa, and (6) white phase AlSiCuLa.
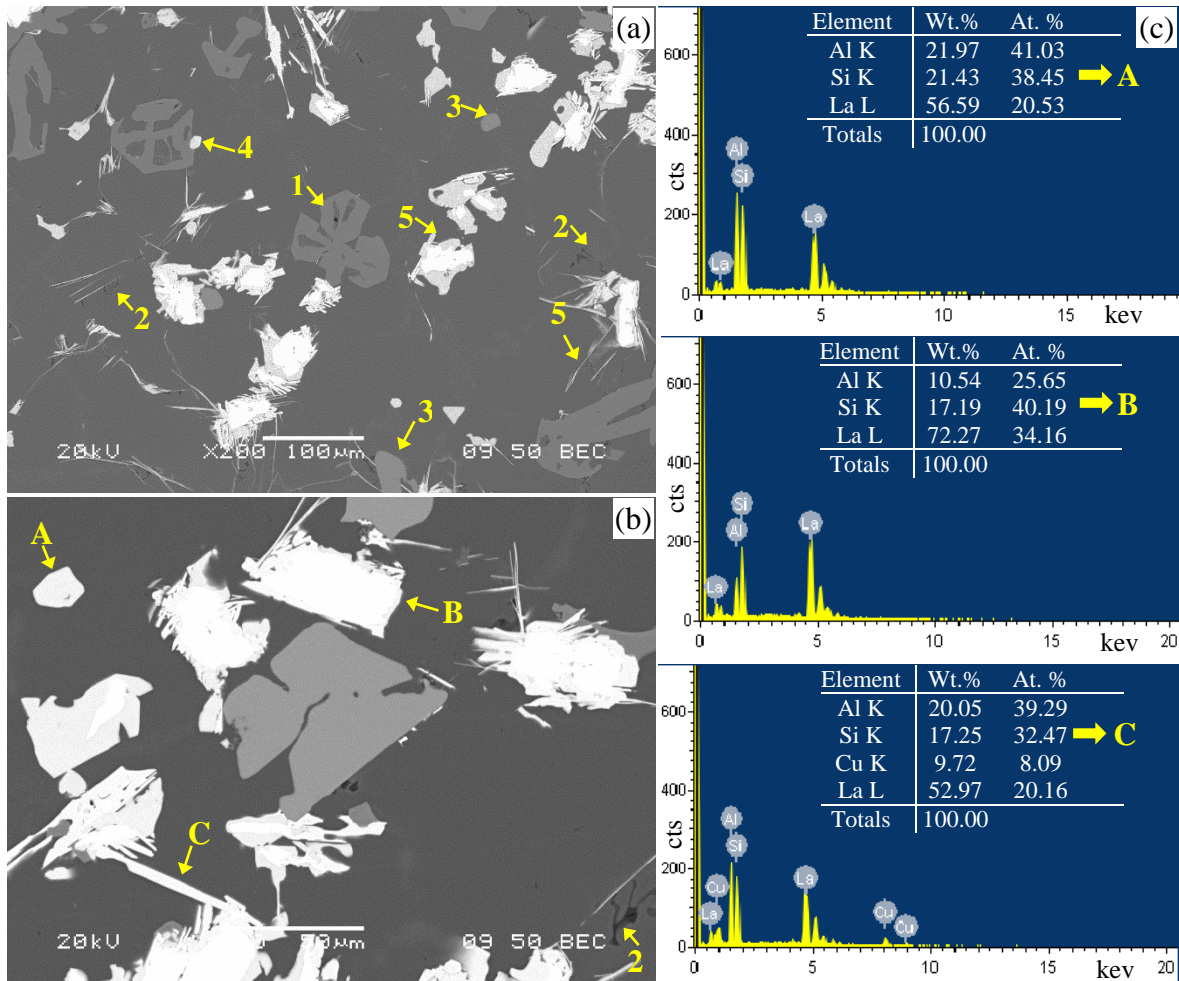
Figure 5.14: Backscattered electron (BSE) images showing the microstructures of as-cast D0 alloy with 5.0 wt.% La addition at (a) low magnification, (b) high magnification, and (c) EDS analysis of locations marked A, B, and C in (b). The arrows indicate (1) α-$Al_{15}(Fe,Mn)_3Si_2$, (2) Mg_2Si (3) grey phase AlTiLa, (4)white phase AlSiLa, and (5) white phase AlSiCuLa.

Figure 5.15 and Figure 5.16 compare the backscattered electron (BSE) images showing the morphology, size and distribution of intermetallic compounds observed in the as-cast D0 alloys with those obtained with additions of Ce and La, respectively. In each of these figure, the images shown in (b) and (c) reveal that as the RE (Ce/La) addition increases from 1.0 to 5.0 wt.%, the amount of intermetallic phase present increases compared to the D0 base alloy shown in Figure 5.15(a) and Figure 5.16(a), due to the formation of RE-containing intermetallic compounds, which precipitate in the interdendritic regions.

The morphology of the RE-intermetallic phases depends on the RE level of addition: with 1.0 wt.% RE addition, they appear in the form of spot type particles, as seen in in Figure 5.15(b) and Figure 5.16(b); whereas when the RE level is increased to 5.0 wt.% the RE-containing intermetallic compounds exhibit coarse block-like coarse lath-like morphologies, as demonstrated by Figure 5.15 (c) and Figure 5.16 (c).

Figure 5.17 and Figure 5.18 display the volume fraction, roundness, and aspect ratio parameters of the intermetallic compounds formed in the D0 alloys with Ce and La additions, respectively. As Figure 5.17 illustrates, the volume fraction increases from 4.81% to 8.6%, with the increase in Ce additions. On the other hand, in the case of the La additions, the volume fraction increases from 4.81% to 18.7%, as shown in Figure 5.18. The change in the size and morphology of the RE-intermetallic compounds with the increase in the RE additions is reflected by the increase in the aspect ratio values, and to a certain extent by the decrease in the roundness values at 5.0 wt.% additions.
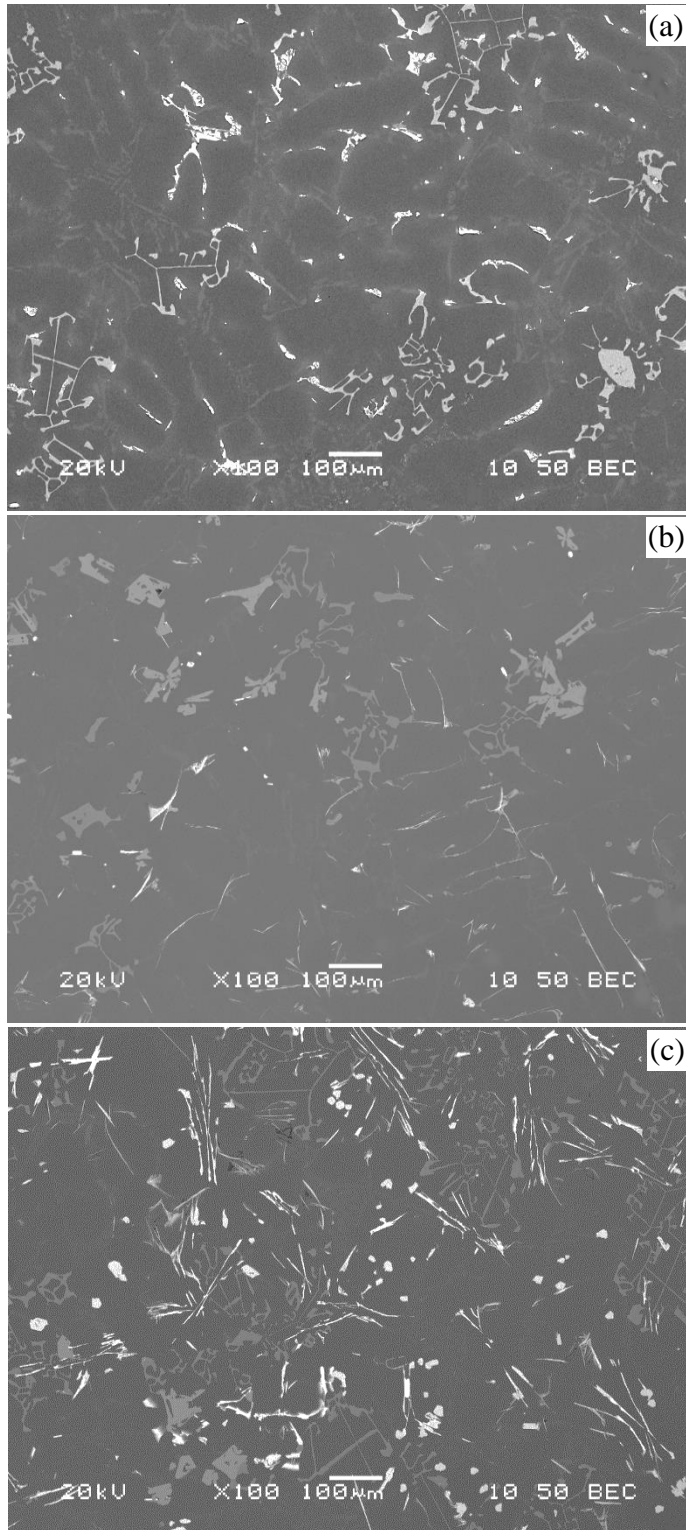
Figure 5.15: Backscattered electron (BSE) images showing the microstructures of as-cast D0 alloys containing (a) 0.0 wt.%RE, (b) 1.0 wt.% Ce, and (c) 5.0 wt.% Ce.
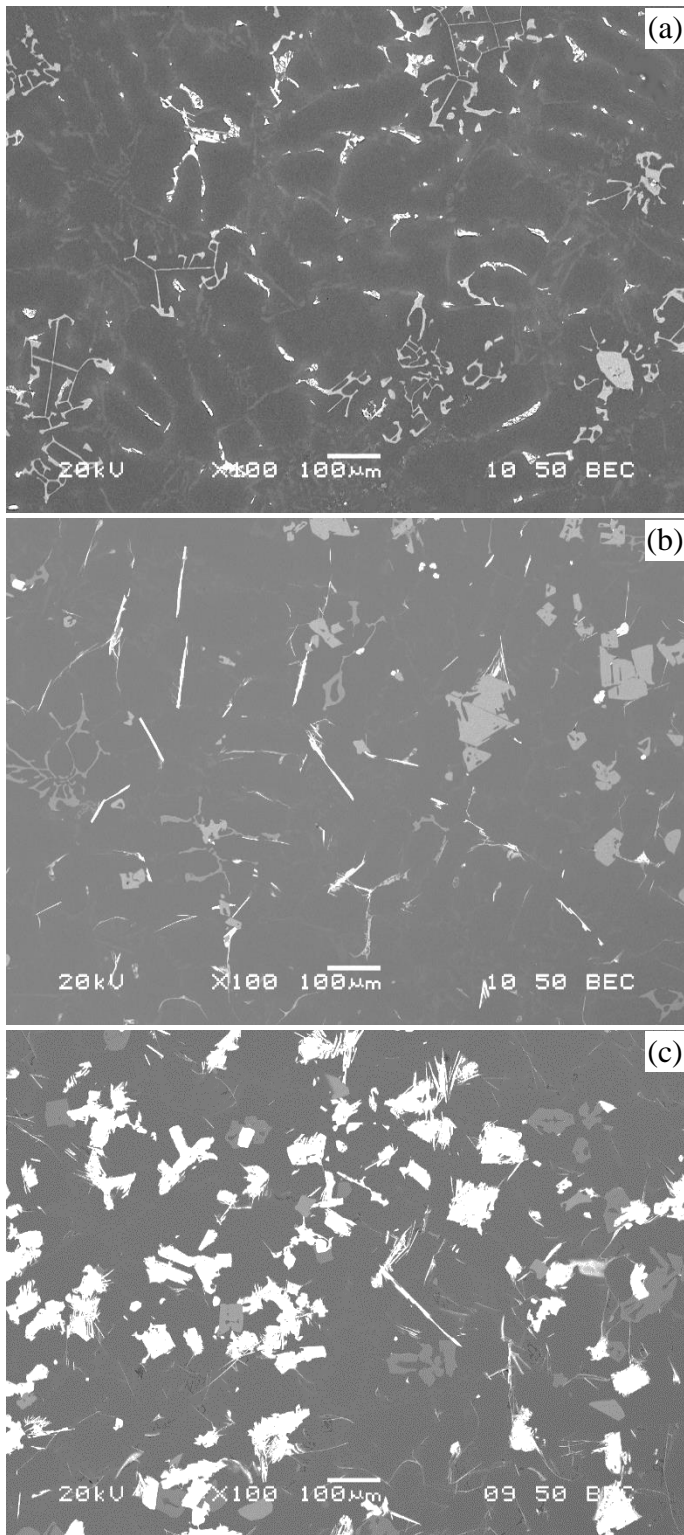
Figure 5.16: Backscattered electron (BSE) images showing the microstructures of D0 as-cast alloys contaning (a) 0.0 wt.%RE, (b) 1.0 wt.% La, and (c) 5.0 wt.% La.
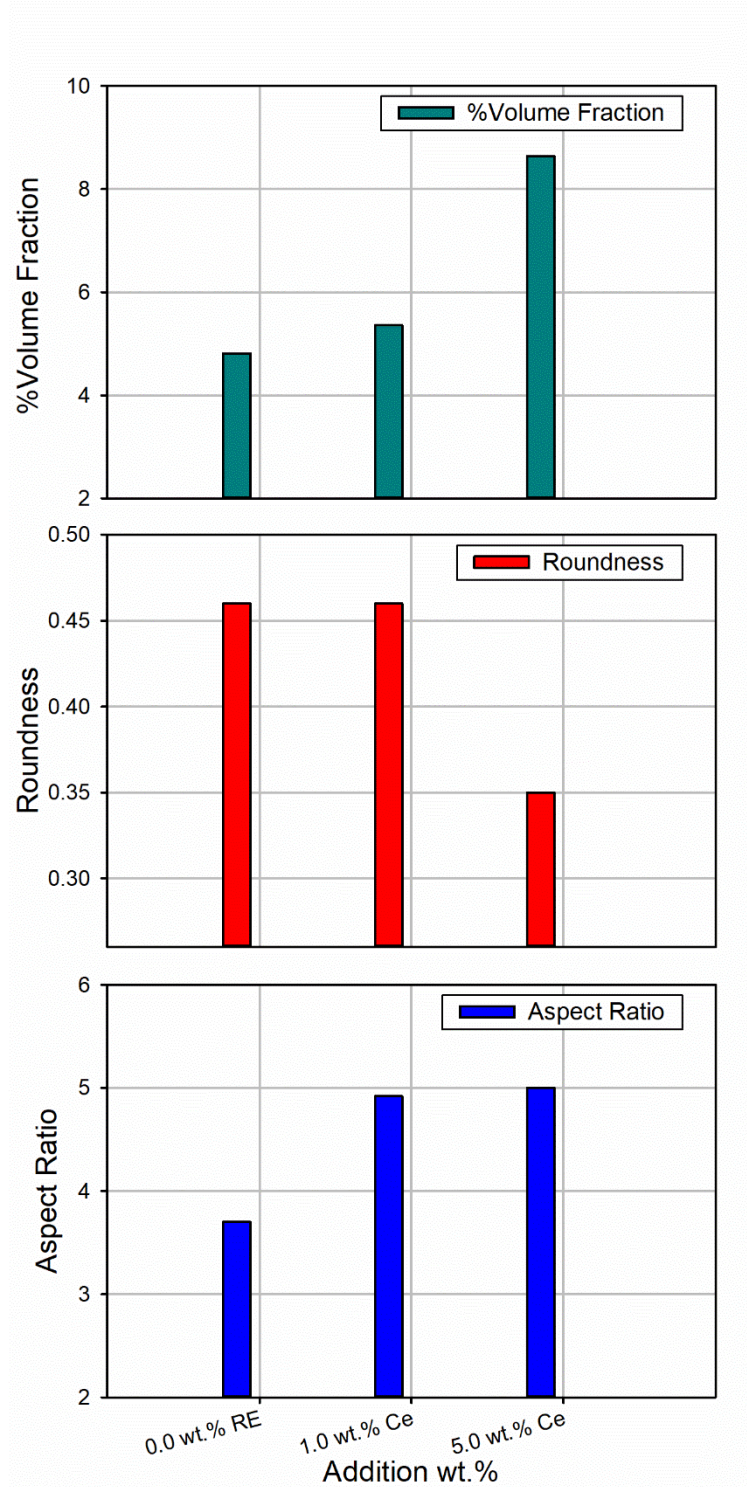
Figure 5.17: Key parameters of %volume fraction, roundness and aspect ratio describing the characteristics of intermetallic compounds in as-cast D0 alloy with various additions of Ce (0.0, 1.0, and 5.0 wt.%).
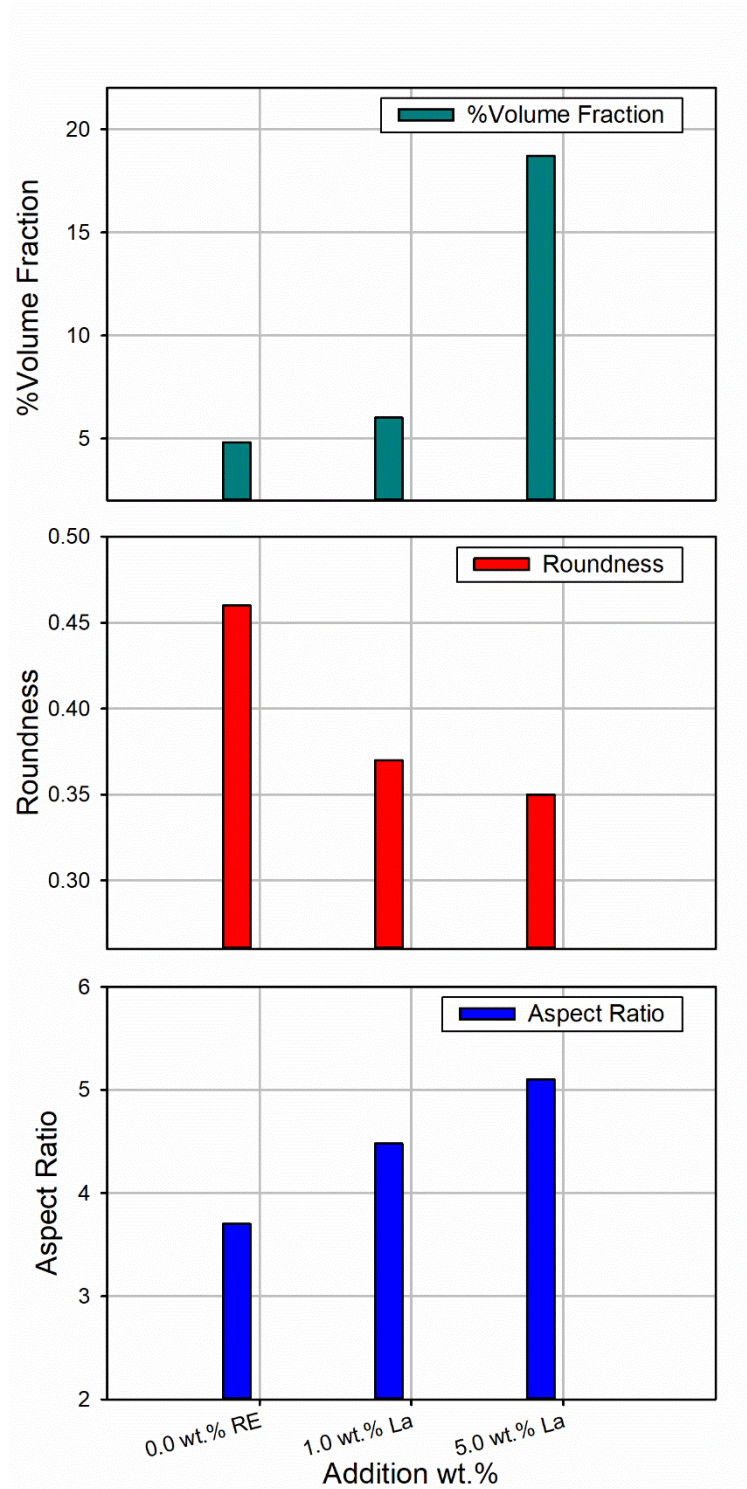
Figure 5.18: Key parameters of %volume fraction, roundness and aspect ratio describing the characteristics of intermetallic compounds in as-cast D0 alloy with various additions of La (0.0, 1.0, and 5.0 wt.%).

5.3 ELECTRON PROBE MICROANALYSIS (EPMA)

Identification of intermetallic phases in the as-cast samples of B0 and D0 alloys containing 1.0, and 5.0 wt.% RE (Ce/La) were carried out using electron probe microanalysis (EPMA) coupled with energy dispersive X-ray spectroscopic (EDS) and wavelength dispersive spectroscopic (WDS) analyses. The results are presented in this section.

5.3.1 AL-Cu (B0) Alloy

Figure 5.19, Figure 5.21, Figure 5.22, and Figure 5.24 show the BSE Image and corresponding X-ray images of various elements observed in samples of as-cast B0 alloys with 1.0, and 5.0 wt.% RE (Ce/La) additions. In order to identify the different phases observed in the microstructures, and to determine their compositions, WDS (Figure 5.20, and Figure 5.23) and EDS (Table 5.1, Table 5.2, Table 5.3, and Table 5.4) analyses were carried out simultaneously, using the electron probe microanalyzer. Backscattered images taken from areas of interest in the as-cast B0 alloy samples with 5.0 wt.% RE (Ce/La) is provided in Appendix E in Figure E-1 and Figure E-2, for the Ce and La additions, respectively.

Figure 5.19, and Figure 5.22 shows the distribution of Al, RE (Ce/La), Cu, Fe, Si, and Ti in such particles observed in the B0 alloy sample with 1.0 wt.% RE (Ce/La), while Figure 5.21 and Figure 5.24 depicts the distribution of Al, Cu, RE (Ce/La), and Ti in the B0 alloy sample with 5.0 wt.% RE (Ce/La).

The above-mentioned figures show the distribution of Ce and La in the grey-phase particles compared to Ti and Si. From these figures, it is evident that Ti is the main element in the grey phase, with traces of RE and Si. Moreover, Figure 5.21 reveals the possibility of the precipitation of grey phase on the existing Ti-rich particles (possibly Al3Ti particles).

111

Considering the white phase, observed in Figure 5.22, and Figure 5.24, Cu has a relatively higher affinity to react with La compared to Fe as inferred from their relative intensities and the size of their corresponding peaks in Figure 5.23(b). It should be borne in mind that the white platelets are very thin (less than 1.5 µm thick) which would explain the variation in their composition (the diameter of the area examined by the electron beam is ~3 µm). Based on these observations, it would be reasonable to say that the grey phase (due to its larger size) would exhibit a definite composition overall, whereas the composition of the white phase would vary from one particle to another.

The WDS analysis carried out on the phases observed in the B0 alloys are presented in Table 5.1, Table 5.2, Table 5.3, and Table 5.4 . Based on the obtained analysis, the grey phase has a fixed composition so, that suggested chemical formula for this phase could be written as $Al_{21}Ti_2RE$ (RE = La or Ce). On the other hand, the white phase has several compositions caused by its reactivity with the other elements in the matrix, particularly Si, Cu, and Fe. The suggested chemical formulas for the white phases particles formed in the B0 alloys are listed below:

(i)   1.0 wt.% La-containing alloy : $Al_{11}Ce_3(Cu,Fe)_4Si_2$

(ii) 5.0 wt.% La-containing alloy : $Al_{11}La_3(Cu,Fe)_4Si_2$, $Al_5La_3Si_2$, and
      $Al_6La_2(Cu,Fe)_2Si$

(iii) 5.0 wt.% Ce-containing alloy : $Al_{11}La_3(Cu,Fe)_4Si_2$

(iv) 5.0 wt.% Ce-containing alloy : $Al_4Ce_3Si_2$ and $Al_{11}Ce_3(Cu,Fe)_4Si_2$
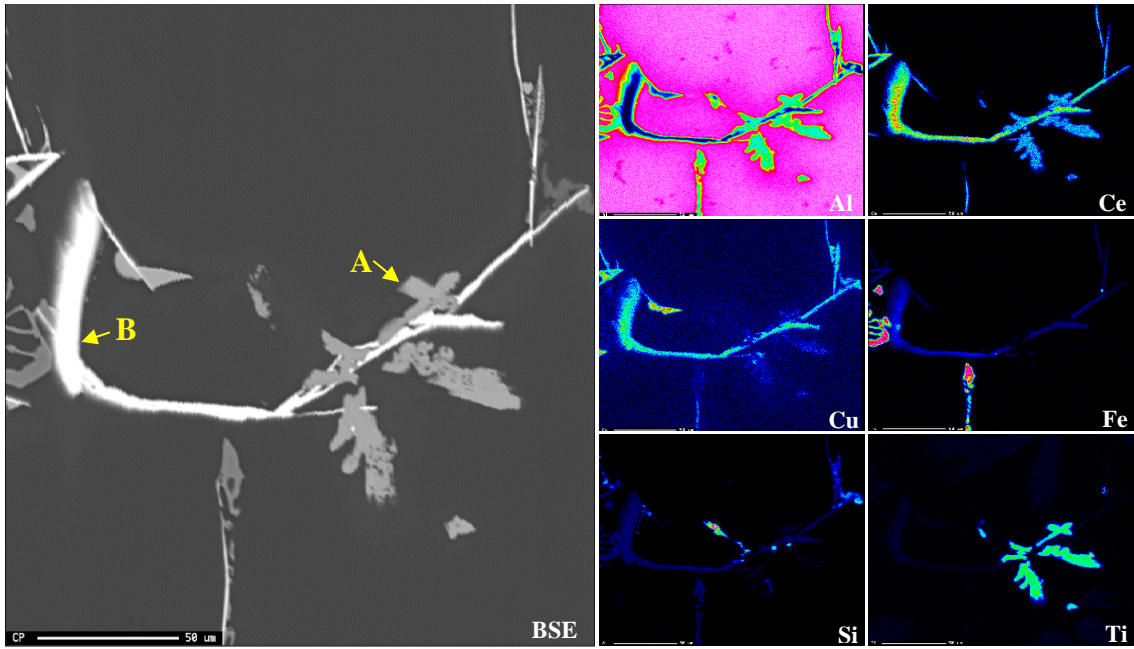
Figure 5.19: Backscattered electron image of as-cast B0 alloy with 1.0 wt.% Ce addition and corresponding X-ray images of Al, Ce, Cu, Fe, Si and Ti.
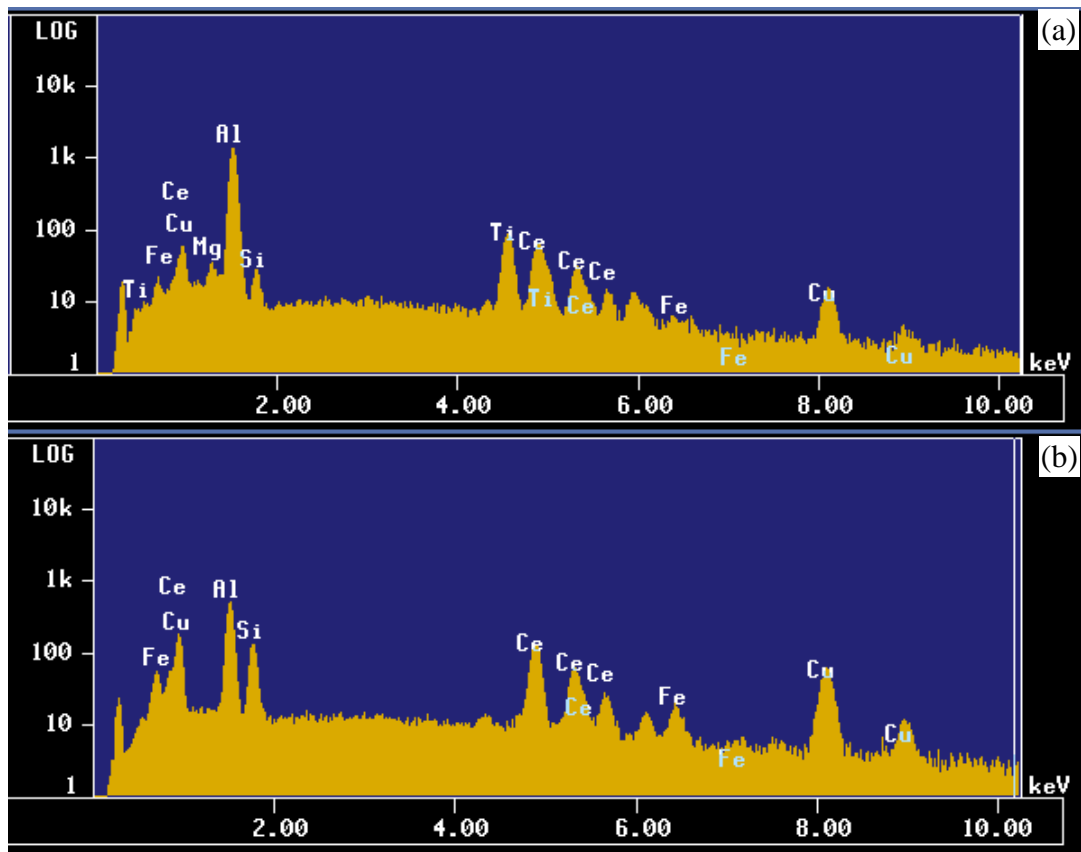
Figure 5.20: EDS spectra of locations marked A and B in Figure 5.19, corresponding to (a) grey phase, and (b) white phase.
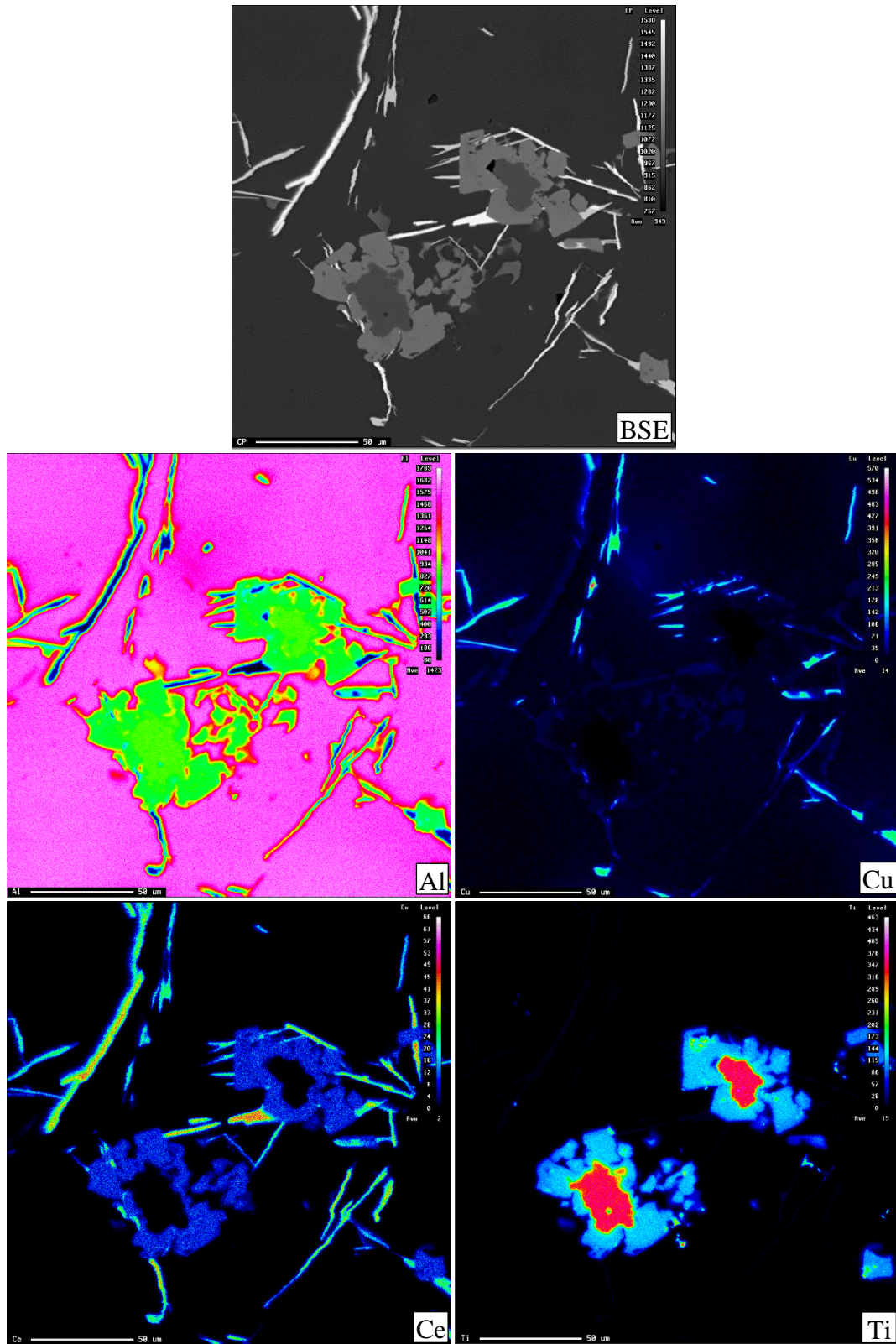
Figure 5.21: Backscattered electron image of as-cast B0 alloy with 5.0 wt.% Ce addition and corresponding X-ray images of Al, Cu, Ce and Ti.

Table 5.1: WDS analysis of the RE intermetallic phases observed in B0 alloy with 1.0 wt.% Ce.

Phase Color	Elements (At.%)						Suggested phase
	Al	Ti	Fe	Cu	Si	Ce	
Grey-1	82.80	6.208	0.030	2.721	1.893	3.959	$Al_{21}Ti_2Ce$(with trace of Cu and Si)
Grey-2	81.74	5.566	0.034	3.518	2.148	3.897	$Al_{21}Ti_2Ce$(with trace of Cu and Si)
Grey-3	84.26	5.610	0.047	2.065	1.396	3.929	$Al_{21}Ti_2Ce$(with trace of Cu and Si)
Grey-4	83.97	6.048	0.079	1.914	1.591	3.924	$Al_{21}Ti_2Ce$(with trace of Cu and Si)
Grey-5	81.38	5.891	0.043	3.191	2.760	3.948	$Al_{21}Ti_2Ce$(with trace of Cu and Si)
White-1	55.06	0.000	1.891	16.93	13.29	12.27	$Al_{11}Ce_3(Cu,Fe)_4Si_2$
White-2	52.25	0.000	2.485	16.58	14.26	13.67	$Al_{11}Ce_3(Cu,Fe)_4Si_2$
White-3	53.37	0.000	2.143	19.08	13.26	11.53	$Al_{11}Ce_3(Cu,Fe)_4Si_2$
White-4	54.22	0.000	2.156	16.59	13.45	13.19	$Al_{11}Ce_3(Cu,Fe)_4Si_2$

Table 5.2: WDS analysis of the RE intermetallic phases observed in B0 alloy with 5.0 wt.% Ce.

Phase Color	Elements (At.%)						Suggested phase
	Al	Ti	Fe	Cu	Si	Ce	
Grey-1	85.92	8.113	0.000	0.261	0.871	4.205	$Al_{21}Ti_2Ce$
Grey-2	86.83	7.153	0.010	0.327	0.515	4.247	$Al_{21}Ti_2Ce$
Grey-3	87.19	7.178	0.002	0.348	0.619	4.219	$Al_{21}Ti_2Ce$
Grey-4	87.00	7.292	0.007	0.336	0.609	4.193	$Al_{21}Ti_2Ce$
Grey-5	86.75	7.256	0.019	0.427	0.810	4.241	$Al_{21}Ti_2Ce$
White-1	42.15	0.000	0.121	1.428	22.34	33.90	$Al_4Ce_3Si_2$
White-2	55.71	0.000	2.833	15.79	10.00	15.64	$Al_{11}Ce_3(Cu, Fe)_4Si_2$
White-3	41.46	0.522	0.105	1.367	23.12	33.33	$Al_4Ce_3Si_2$
White-4	55.04	0.000	2.782	16.32	10.82	14.98	$Al_{11}Ce_3(Cu, Fe)_4Si_2$
White-5	44.12	0.000	0.053	0.913	22.49	32.38	$Al_4Ce_3Si_2$
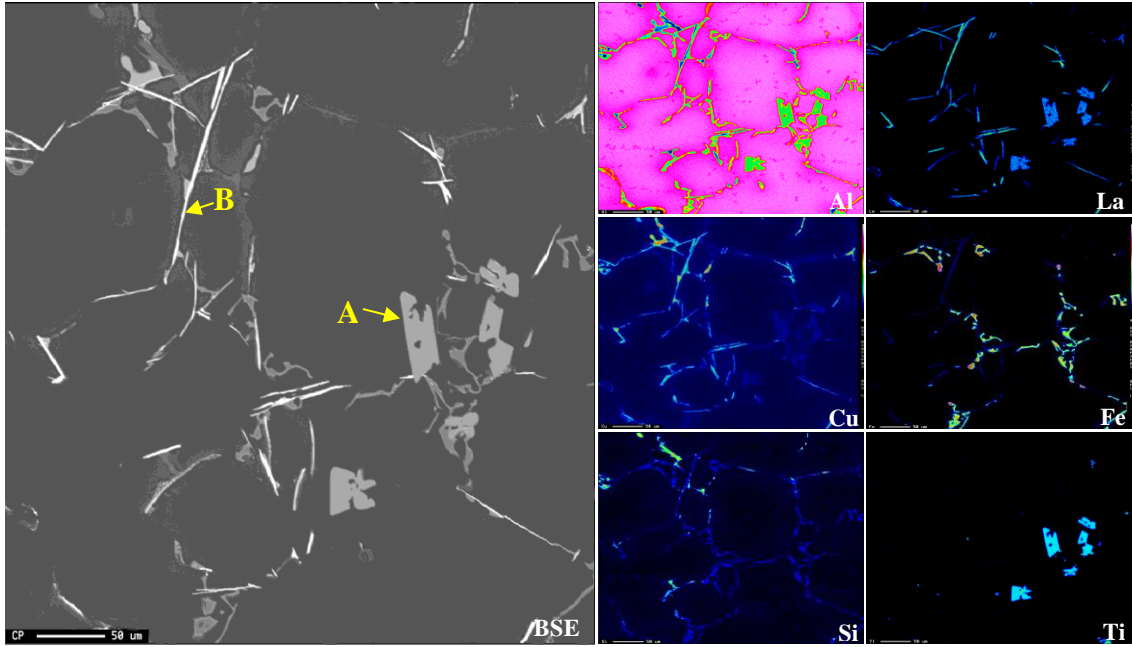
Figure 5.22: Backscattered electron image of as-cast B0 alloy with 1.0 wt.% La addition and corresponding X-ray images of Al, La, Cu, Fe, Si and Ti.
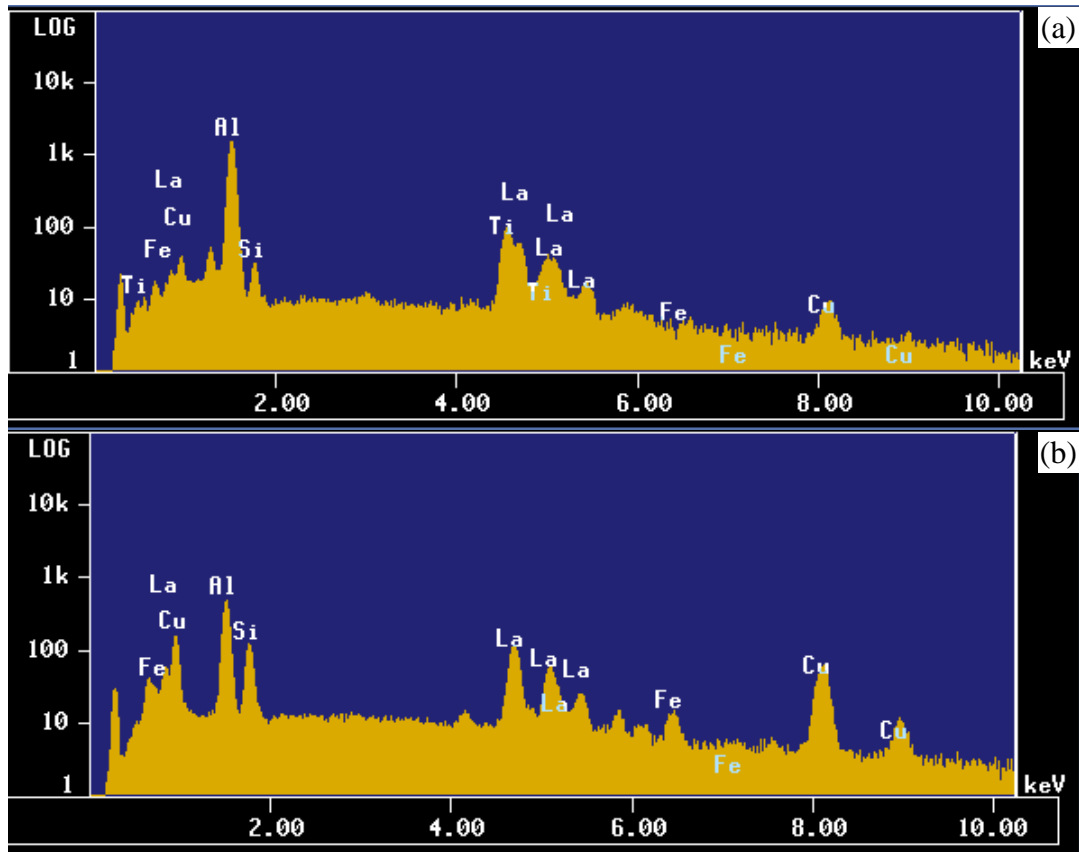
Figure 5.23: EDS spectra of locations marked A and B in Figure 5.22, corresponding to (a) grey phase, and (b) white phase.
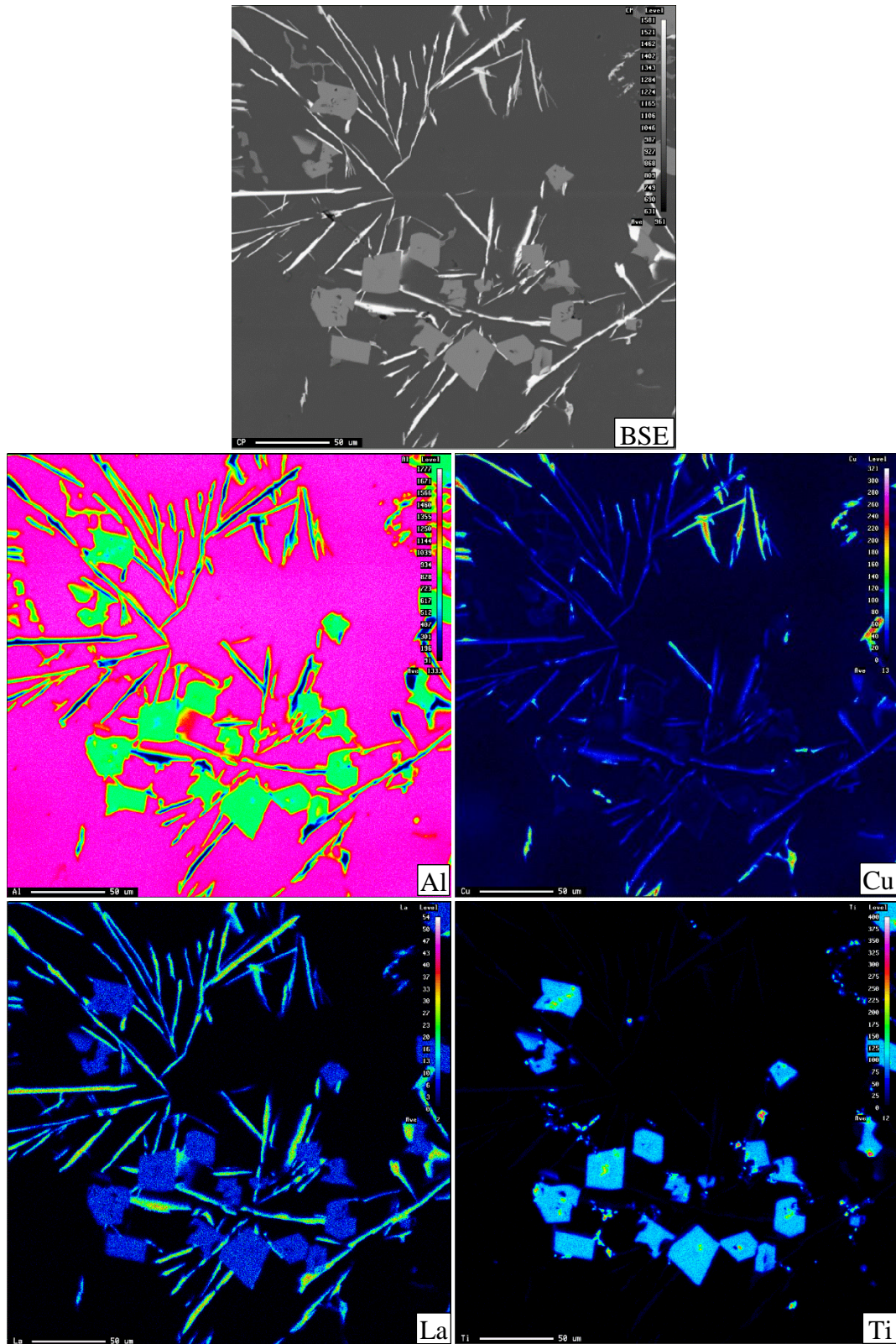
Figure 5.24: Backscattered electron image of as-cast B0 alloy with 5.0 wt.% La addition and corresponding X-ray images of Al, Cu, La and Ti.

Table 5.3: WDS analysis of the RE intermetallic phases observed in B0 alloy with 1.0 wt.% La.

Phase Color	Elements (At.%)						Suggested phase
	Al	Ti	Fe	Cu	Si	La	
Grey-1	82.59	6.511	0.017	1.765	2.322	3.698	$Al_{21}Ti_2La$ (with trace of Cu and Si)
Grey-2	83.28	6.469	0.015	1.748	2.040	3.684	$Al_{21}Ti_2La$ (with trace of Cu and Si)
Grey-3	84.91	6.568	0.003	1.167	1.515	3.724	$Al_{21}Ti_2La$ (with trace of Cu and Si)
Grey-4	82.66	6.612	0.008	1.653	2.277	3.609	$Al_{21}Ti_2La$ (with trace of Cu and Si)
Grey-5	85.32	6.378	0.033	1.122	0.961	3.628	$Al_{21}Ti_2La$ (with trace of Cu and Si)
White-1	54.57	0.000	1.904	17.45	12.25	12.82	$Al_{11}La_3(Cu,Fe)_4Si_2$
White-2	53.30	0.000	2.227	16.45	12.82	14.18	$Al_{11}La_3(Cu,Fe)_4Si_2$
White-3	53.97	0.000	2.295	15.70	12.91	14.12	$Al_{11}La_3(Cu,Fe)_4Si_2$
White-4	56.14	0.000	1.541	17.57	12.02	11.91	$Al_{11}La_3(Cu,Fe)_4Si_2$

Table 5.4: WDS analysis of the RE intermetallic phases observed in B0 alloy with 5.0 wt.% La.

Phase Color	Elements (At.%)						Suggested phase
	Al	Ti	Fe	Cu	Si	La	
Grey-1	84.75	7.215	0.014	0.374	0.358	4.343	$Al_{21}Ti_2La$
Grey-2	82.26	6.420	0.053	1.293	0.579	4.351	$Al_{21}Ti_2La$
Grey-3	84.27	7.317	0.013	0.344	0.496	4.330	$Al_{21}Ti_2La$
Grey-4	85.22	7.428	0.009	0.258	0.333	4.320	$Al_{21}Ti_2La$
Grey-5	84.32	7.730	0.012	0.451	0.408	4.384	$Al_{21}Ti_2La$
White-1	56.46	0.000	2.598	14.97	9.812	15.83	$Al_{11}La_3(Cu,Fe)_4Si_2$
White-2	59.69	0.000	2.384	14.42	9.076	13.97	$Al_{11}La_3(Cu,Fe)_4Si_2$
White-3	56.64	0.000	2.942	14.43	10.12	15.61	$Al_{11}La_3(Cu,Fe)_4Si_2$
White-4	46.52	0.000	0.000	3.426	18.30	31.44	$Al_5La_3Si_2$
White-5	56.33	0.000	2.686	15.70	9.508	15.45	$Al_{11}La_3(Cu,Fe)_4Si_2$
White-6	50.39	0.000	0.000	2.654	18.09	28.52	$Al_5La_3Si_2$

5.3.2 Al-Si-Cu (D0) Alloy

The backscattered electron images and corresponding X-ray images of as-cast D0 alloys with 1.0, and 5.0 wt.% RE (Ce/La) additions are presented in Figure 5.25, Figure 5.27, Figure 5.29, and Figure 5.31. As mentioned previously, WDS and EDS analyses were carried out to identify and distinguish between the different types of particles, as shown in Figure 5.26, Figure 5.28, Figure 5.30, and Figure 5.32 and Table 5.5, Table 5.6, Table 5.7, and Table 5.8, respectively.

The distribution of Al, RE (Ce/La), Cu, Fe, Si, and Ti elements in the phases particles observed in the D0 alloys with 1.0 wt.% RE (Ce/La) additions are presented in Figure 5.25, and Figure 5.27. For the D0 alloys with 5.0 wt.% RE additions, Figure 5.27 shows only the distribution of Ce, and Ti while Figure 5.31 depicts the distribution of Al, Cu, RE (Ce/La), and Ti.

In comparison to B0 alloy, also the addition of RE (Ce/La) to the D0 alloy also resulted in the formation of two different intermetallic phases, coloured white and grey in the BSE images shown in Figure 5.25, Figure 5.27, Figure 5.29, and Figure 5.31. Based on the EDS analysis, these phases are Al-Si-Cu-RE (Ce/La) and Al-Ti- RE (Ce/La), respectively, with stoichiometric compositions that were calculated based on WDS analysis as listed in Table 5.5, Table 5.6, Table 5.7, and Table 5.8.

The grey phase observed in the case of the D0 alloy had a chemical compositions close to that found in the case of the B0 alloy when adding La and Ce. On the other hand, the white phase exhibited different compositions compared to that noted in the B0 alloy. This ascribed to the high Si level (8.0 wt.%) in D0 alloy in addition to the high RE additions (5.0 wt.%), where the Si, Al, and Cu interact with the RE (Ce/La) to form the white phase with

119

different chemical compositions.

An interesting observation may be made in regard to the interaction between the RE and transition metals, in particular Cu and Fe. Figure 5.31 shows the interaction between La and Cu in the D0 alloy containing 5.0 wt.% La. Lanthanum platelets seem to attract Cu at their edges as shown in Figure 5.31(b) which is an enlarged portion of the BSE image in Figure 5.31(a).

Table 5.5, Table 5.6, Table 5.7, and Table 5.8 summarizes the WDS analysis carried out on the phases observed the D0 alloys. The composition of the grey phase may be written as $Al_{21}Ti_2RE$ (RE = La or Ce). In contrast, the white phase has been observed with a several compositions caused by its reactivity with the other elements in the matrix, particularly Si, Cu, and Fe. The phases formed are as follows:

  (i)   1.0 wt.% Ce-containing alloy : $Al_9Ce_4Cu_2Si_4$

  (ii) 5.0 wt.% Ce-containing alloy: Al_2CeSi

  (iii) 1.0 wt.% La-containing alloy : $Al_9La_4Cu_2Si_4$

  (iv) 5.0 wt.% La-containing alloy: $AlLaSi$, Al_2LaSi, and $Al_9La_4Cu_2Si$
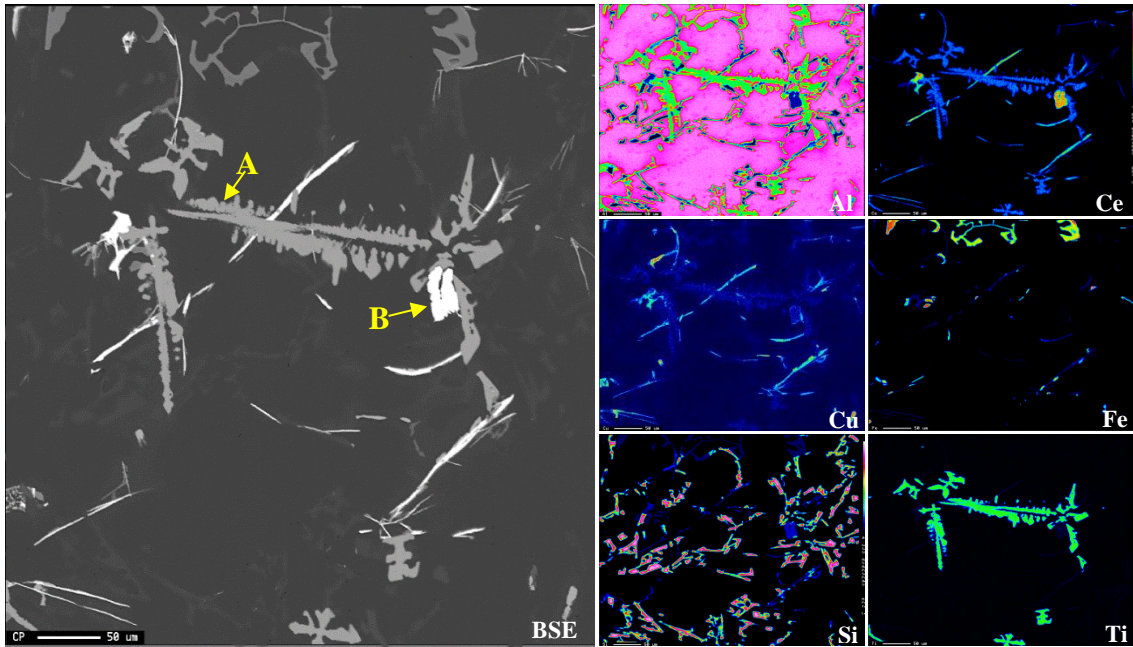
Figure 5.25: Backscattered electron image of as-cast D0 alloy with 1.0 wt.% Ce addition and corresponding X-ray images of Al, La, Cu, Fe, Si and Ti.
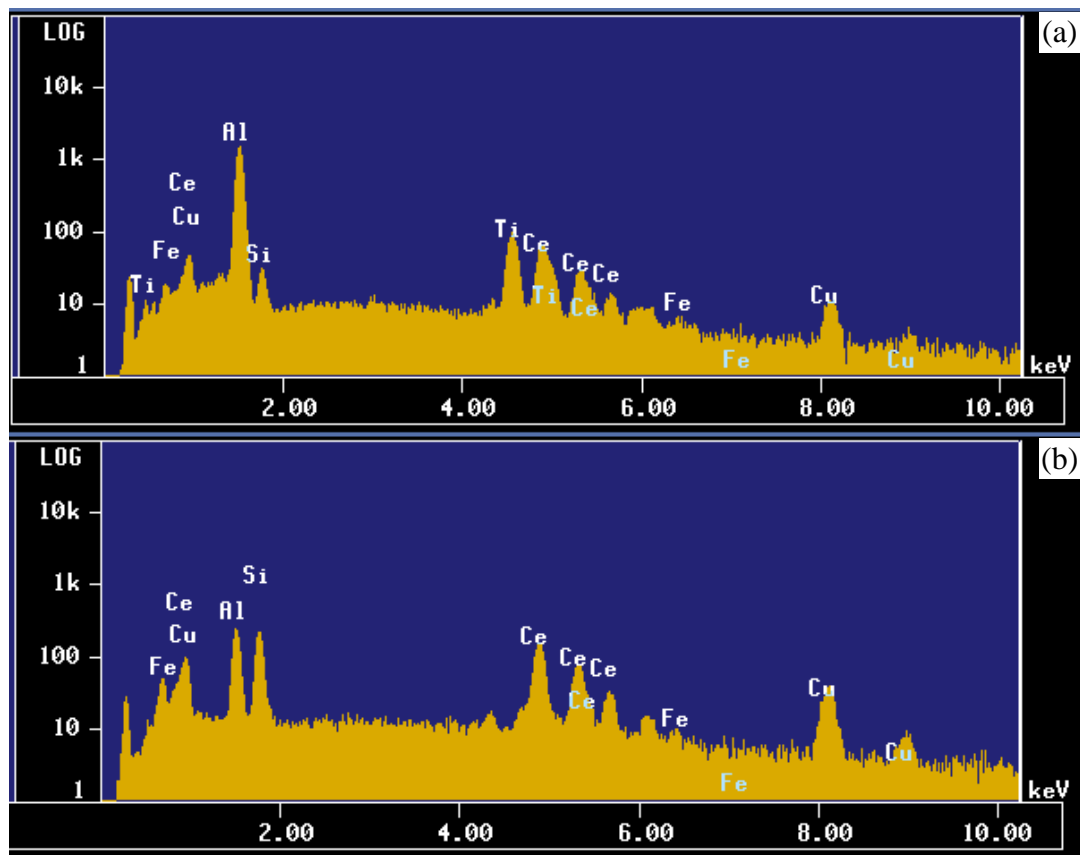
Figure 5.26: EDS spectra of locations marked A and B in Figure 5.25, corresponding to (a) grey phase, and (b) white phase.
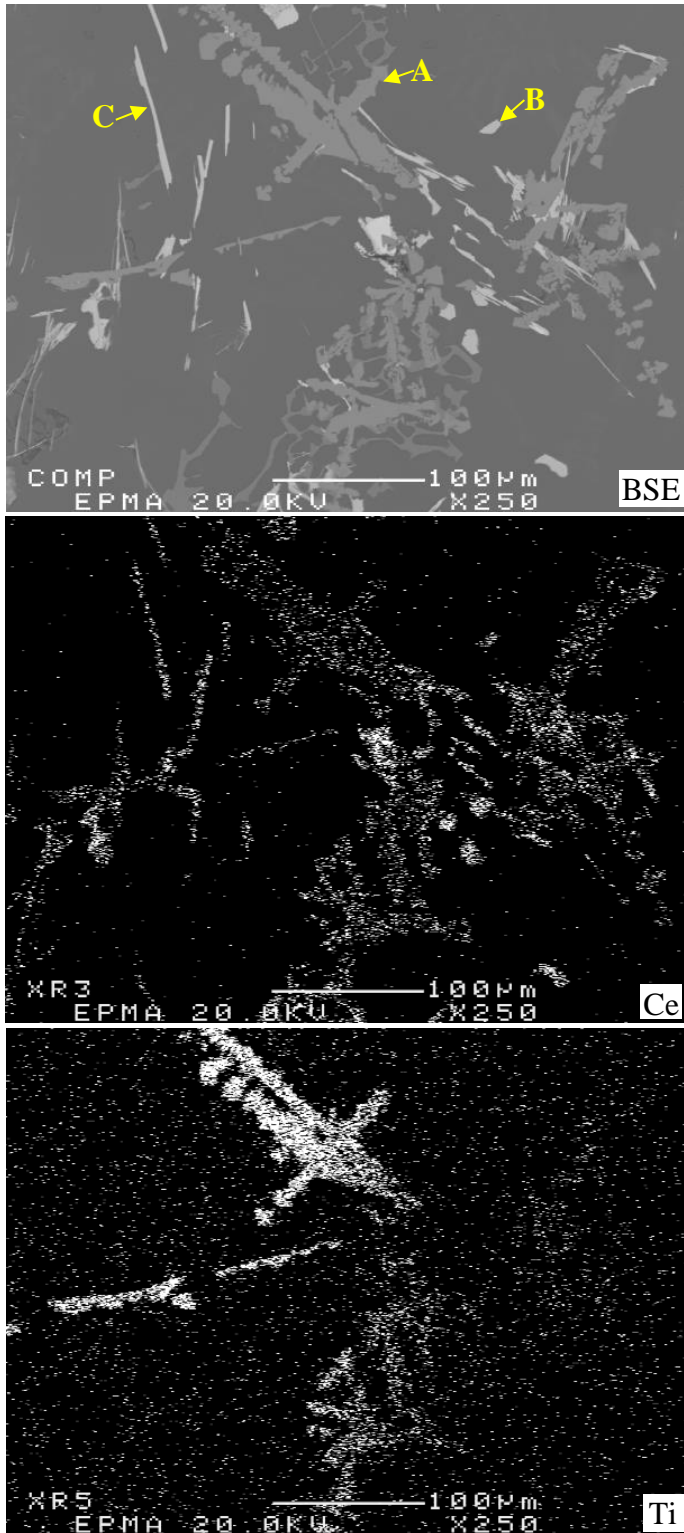
Figure 5.27: Backscattered electron image of as-cast D0 alloy with 5.0 wt.% Ce addition and corresponding X-ray images of Ce and Ti.
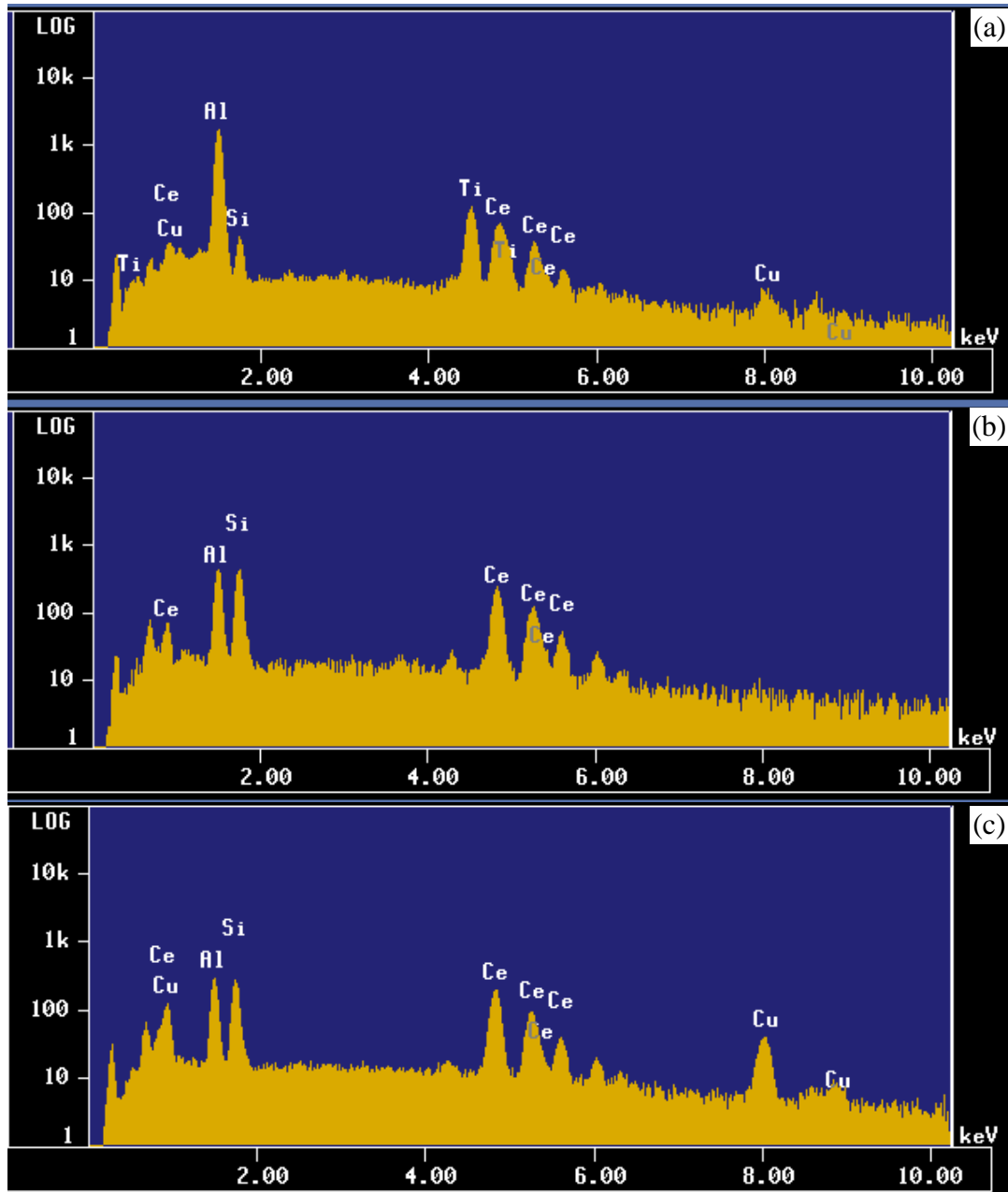
Figure 5.28: EDS spectra of locations marked A, B, and C in Figure 5.27
corresponding to (a) grey phase, (b) white phase AlSiCe, and (b) white phase
AlSiCuCe.

Table 5.5: WDS analysis of the RE intermetallic phases observed in D0 alloy with 1.0 wt.% Ce

Phase Color	Elements (At.%)						Suggested phase
	Al	Ti	Fe	Cu	Si	Ce	
Grey-1	84.41	6.426	0.025	2.050	1.526	4.009	$Al_{21}Ti_2Ce$ (with trace of Cu and Si)
Grey-2	83.08	6.516	0.052	2.308	2.726	4.053	$Al_{21}Ti_2Ce$ (with trace of Cu and Si)
Grey-3	83.88	6.696	0.015	1.963	2.278	4.019	$Al_{21}Ti_2Ce$ (with trace of Cu and Si)
Grey-4	83.66	6.423	0.013	2.278	2.331	3.972	$Al_{21}Ti_2Ce$ (with trace of Cu and Si)
Grey-5	84.60	6.630	0.025	1.734	1.872	4.003	$Al_{21}Ti_2Ce$ (with trace of Cu and Si)
White-1	40.54	0.000	0.069	12.38	26.96	18.58	$Al_9Ce_4Cu_2Si_4$
White-2	40.44	0.000	0.069	11.80	27.73	18.56	$Al_9Ce_4Cu_2Si_4$
White-3	46.08	0.000	0.112	12.04	24.28	16.52	$Al_9Ce_4Cu_2Si_4$
White-4	40.21	0.000	0.122	12.97	27.04	18.45	$Al_9Ce_4Cu_2Si_4$
White-5	40.57	0.000	0.096	12.24	26.96	18.78	$Al_9Ce_4Cu_2Si_4$

Table 5.6: WDS analysis of the RE intermetallic phases observed in D0 alloy with 5.0 wt.% Ce

Phase Color	Elements (At.%)						Suggested phase
	Al	Ti	Fe	Cu	Si	Ce	
grey-1	85.78	6.314	0.014	1.080	1.388	4.156	$Al_{21}Ti_2La$(with trace of Cu and Si)
grey-2	85.40	6.228	0.015	1.410	1.431	4.134	$Al_{21}Ti_2La$ (with trace of Cu and Si)
grey-3	84.52	6.255	0.019	1.777	1.869	4.265	$Al_{21}Ti_2La$ (with trace of Cu and Si)
grey-4	83.99	6.394	0.008	2.558	1.601	4.187	$Al_{21}Ti_2La$ (with trace of Cu and Si)
grey-5	85.53	6.377	0.015	0.946	1.659	4.272	$Al_{21}Ti_2La$(with trace of Cu and Si)
white-1	51.26	0.000	0.000	0.073	25.64	21.82	Al_2CeSi
white-2	45.37	0.000	0.000	0.276	28.55	24.59	Al_2CeSi
white-3	45.49	0.000	0.017	0.292	28.42	24.56	Al_2CeSi
white-4	45.15	0.000	0.014	0.259	29.20	24.20	Al_2CeSi
white-5	51.86	0.000	0.009	0.077	25.33	21.46	Al_2CeSi
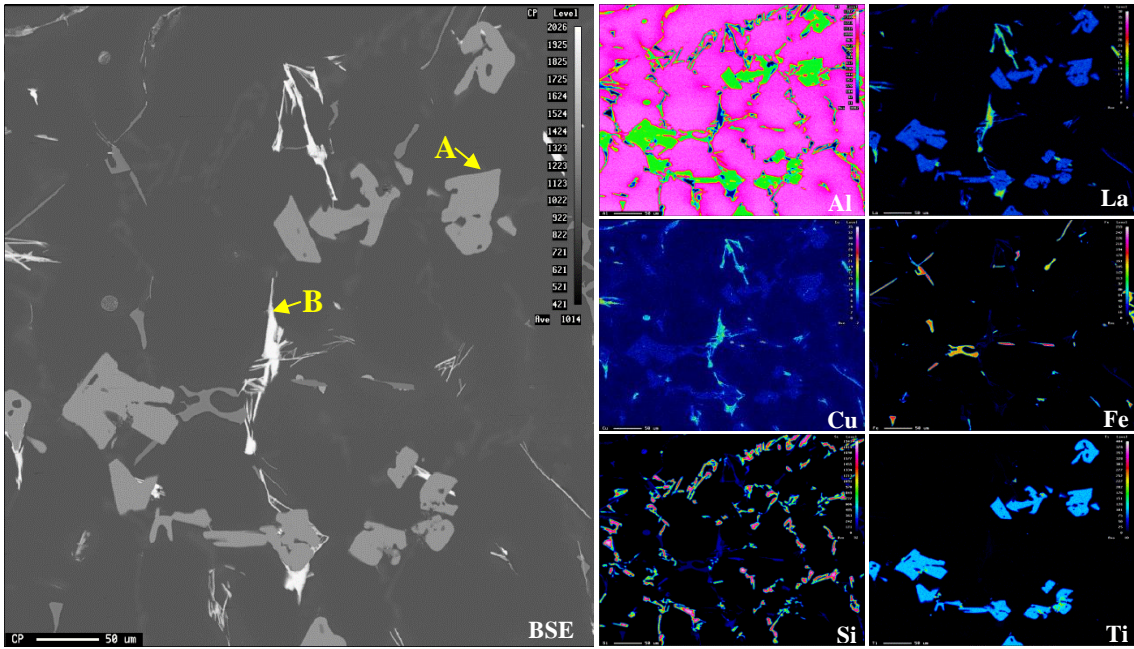
Figure 5.29: Backscattered electron image of as-cast D0 alloy with 1.0 wt.% La addition and corresponding X-ray images of Al, La, Cu, Fe, Si and Ti.
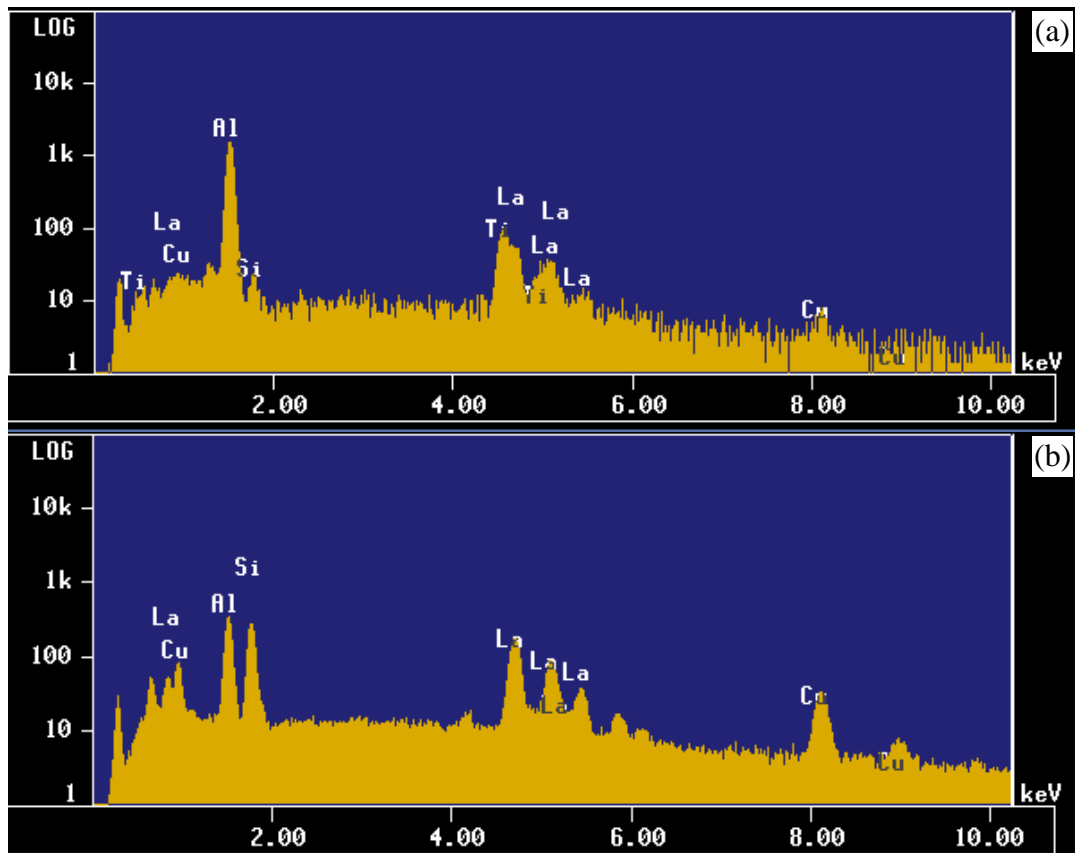
Figure 5.30: EDS spectra of locations marked A and B in Figure 5.29, corresponding to (a) grey phase, and (b) white phase.

(a)

(b)
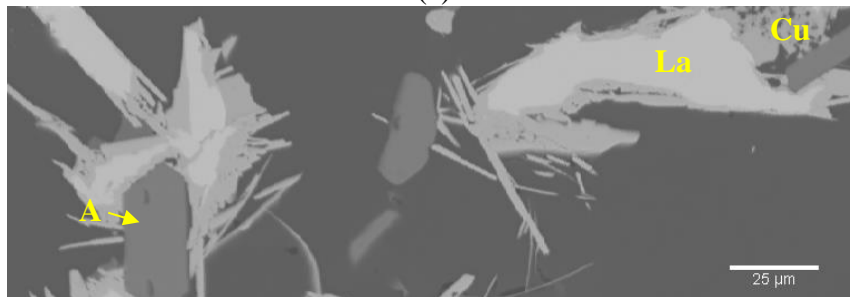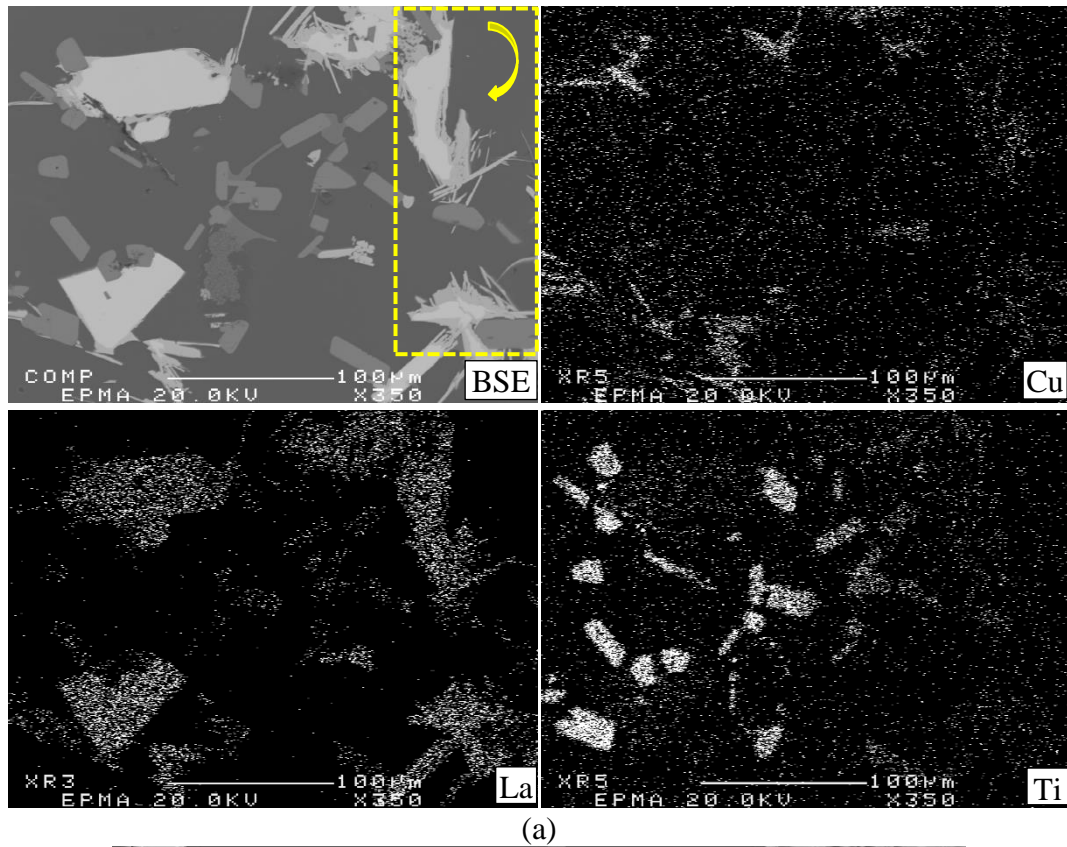
Figure 5.31: (a) Backscattered electron image of as-cast D0 alloy with 5.0 wt.% La addition and corresponding X-ray images of Cu, La, and Ti, (b) enlarged image of selected area in (a).
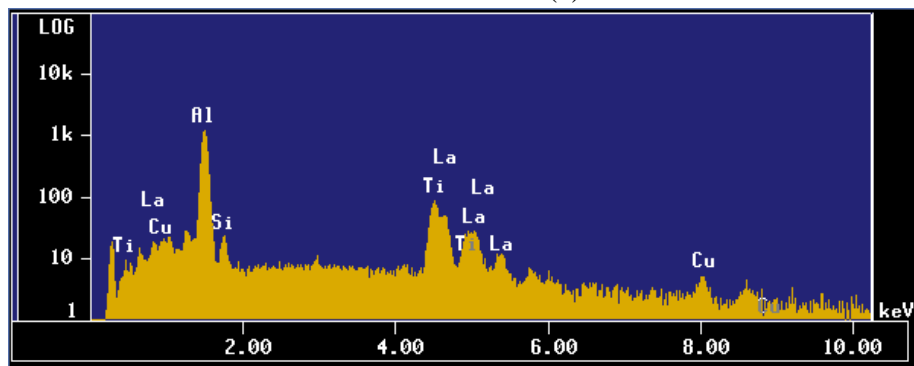
Figure 5.32: EDS spectra of locations marked A in Figure 5.31(b) corresponding to grey phase.

Table 5.7: WDS analysis of the RE intermetallic phases observed in D0 alloy with 1.0 wt.% La

Phase Color	Elements (At.%)						Suggested phase
	Al	Ti	Fe	Cu	Si	La	
Grey-1	85.49	7.652	0.049	0.647	1.401	3.441	$Al_{21}Ti_2La$ (with trace of Cu and Si)
Grey-2	85.81	7.768	0.000	0.539	1.008	3.593	$Al_{21}Ti_2La$ (with trace of Cu and Si)
Grey-3	85.34	7.760	0.005	0.579	1.161	3.571	$Al_{21}Ti_2La$ (with trace of Cu and Si)
Grey-4	85.57	7.839	0.006	0.584	1.158	3.677	$Al_{21}Ti_2La$ (with trace of Cu and Si)
Grey-5	84.48	7.771	0.005	0.738	1.399	3.682	$Al_{21}Ti_2La$ (with trace of Cu and Si)
White-1	45.98	0.000	0.012	9.483	24.28	18.70	$Al_9La_4Cu_2Si_4$
White-2	44.90	0.000	0.170	9.545	24.06	19.56	$Al_9La_4Cu_2Si_4$
White-3	44.77	0.000	0.052	10.58	23.47	19.24	$Al_9La_4Cu_2Si_4$
White-4	45.20	0.000	0.004	9.710	23.55	19.86	$Al_9La_4Cu_2Si_4$
White-5	46.27	0.000	0.078	9.778	22.07	20.00	$Al_9La_4Cu_2Si_4$

Table 5.8: WDS analysis of the RE intermetallic phases observed in D0 alloy with 5.0 wt.% La

Phase Color	Elements (At.%)						Suggested phase
	Al	Ti	Fe	Cu	Si	La	
Grey-1	85.74	6.676	0.013	0.469	0.801	3.815	$Al_{21}Ti_2La$ (with trace of Cu and Si)
grey-2	85.39	6.543	0.035	0.606	0.919	3.767	$Al_{21}Ti_2La$ (with trace of Cu and Si)
Grey-3	85.48	6.343	0.046	0.707	0.888	3.764	$Al_{21}Ti_2La$(with trace of Cu and Si)
grey-4	85.20	6.439	0.013	0.588	1.033	3.832	$Al_{21}Ti_2La$(with trace of Cu and Si)
Grey-5	85.33	6.588	0.008	0.691	1.262	3.846	$Al_{21}Ti_2La$ (with trace of Cu and Si)
White-1	33.13	0.000	0.021	0.269	30.26	34.31	AlLaSi
White-2	34.56	0.000	0.000	0.426	27.51	35.37	AlLaSi
White-3	35.03	0.000	0.000	0.343	27.63	35.01	AlLaSi
White-4	36.57	0.000	0.000	0.290	25.93	35.23	AlLaSi
White-5	34.72	0.000	0.006	0.344	27.82	35.20	AlLaSi
White-6	50.11	0.000	0.000	0.083	26.49	20.95	Al_2LaSi
White-7	45.61	0.000	0.017	8.933	22.79	20.53	$Al_9La_4Cu_2Si_4$

CHAPTER 6

ROOM TEMPERATURE TENSILE TESTING RESULTS

CHAPTER 6

ROOM TEMPERATURE TENSILE TESTING RESULTS

6.1 QUANTITATIVE METALLOGRAPHIC ANALYSIS

As mentioned in the Introduction section1.3, RE metals act as modifiers of the eutectic silicon phase, Thus, the modification effect of the as-cast and T6 heat-treated D0 alloys containing 8.0% Si was examined for the additions of Ce and La, using an optical microscope, accompanied by quantitative measurements of the Si particle characteristics using a Clemex image analysis system in conjunction with the optical microscope. In addition, the shape (roundness and aspect ratio) and volume fraction of the intermetallic compounds formed with the additions of Ce and La were characterized for the as-cast B0 and D0 alloys samples using scanning electron microscopy. It is worth noting that the samples characterized and presented in this section were obtained at high cooling rate (10.0 ºC/s), as mentioned previously in CHAPTER 3 on Experimental Procedures (Figure 3.1).

6.1.1 Quantitative Analysis of Secondary Phases

An image analyzer (ImageJ) [183] was used to quantitatively measure the volume fraction (%VF), roundness and aspect ratio of the secondary phases from ten SEM images taken at 200x magnification. The characteristics of the secondary phases observed in the as-cast B0 and D0 alloys samples are presented in subsections 6.1.1.1 and 6.1.1.2, respectively.

6.1.1.1 Al-Cu (B0) Alloy

Figure 6.1 and Figure 6.2 illustrate the backscattered electron (BSE) images showing the morphology, size and distribution of intermetallic compounds observed in the as-cast the alloys with additions of Ce and La, respectively. Figure 6.1(b-d) and Figure 6.2 (b-d) reveal that as the RE (Ce/La) addition increases from 0.2 to 1.0 wt.%, the relative amount of

intermetallic phase observed increases compared to the B0 base alloy shown in Figure 6.1(a) and Figure 6.2(a), due to formation of RE-containing intermetallic compounds. These RE intermetallic compounds were observed in the interdendritic regions. In addition, the morphology of the RE intermetallic is based on the RE level of addition since, a small amount of RE (0.2 wt.%), as shown in Figure 6.1 (b) and Figure 6.2 (b) they are formed in the microstructures with spot-like in shape. In another side, Figure 6.1 (d) and Figure 6.2 (d) illustrates that when RE addition increases to 1.0 wt.%, amount of RE-containing intermetallic compounds with coarse block-like and coarse lath-like morphologies can be observed in the microstructures.
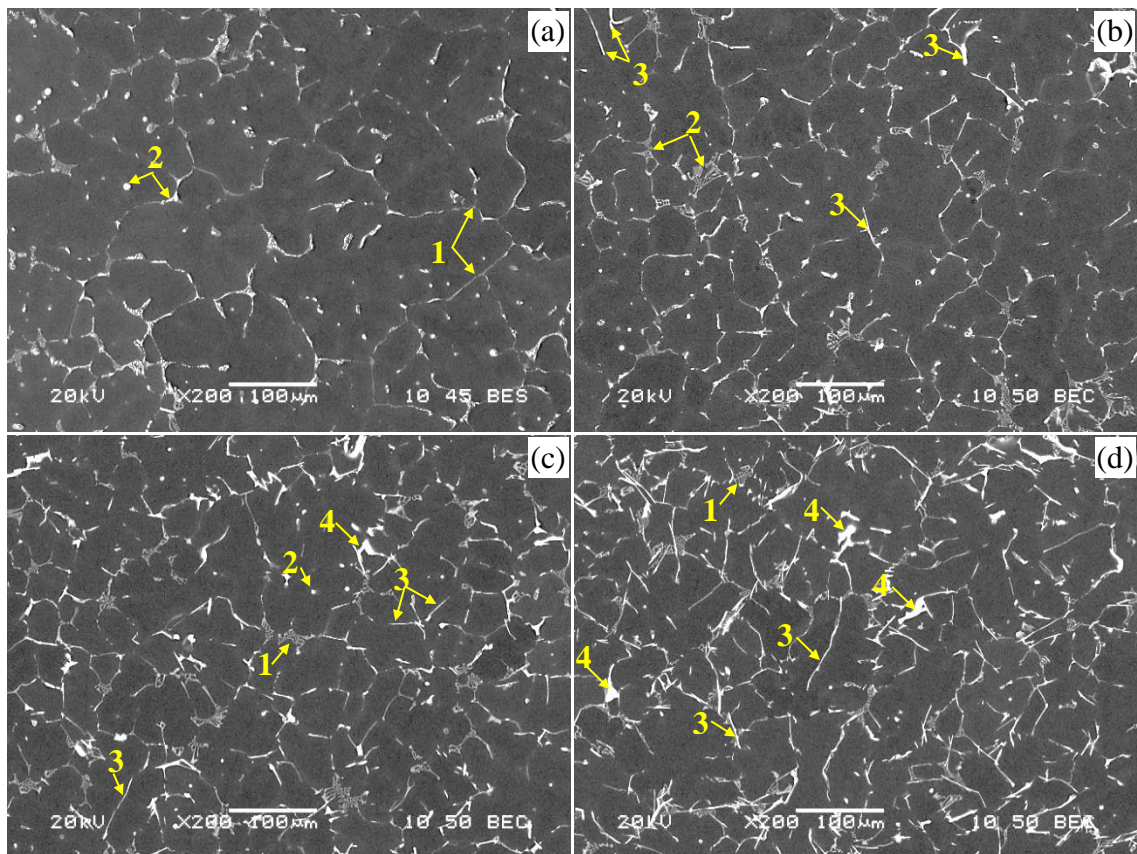
Figure 6.1: Backscattered electron (BSE) images showing the microstructures of the B0 alloys: (a) 0.0 wt.% RE, (b) 0.2 wt.% Ce, (c) 0.5 wt.% Ce, (d) 1.0 wt.% Ce. The arrows indicate (1) α-Fe, (2) Al_2Cu, (3) Ce containing intermetallic phase, and (4) Ce rich containing intermetallic phase.
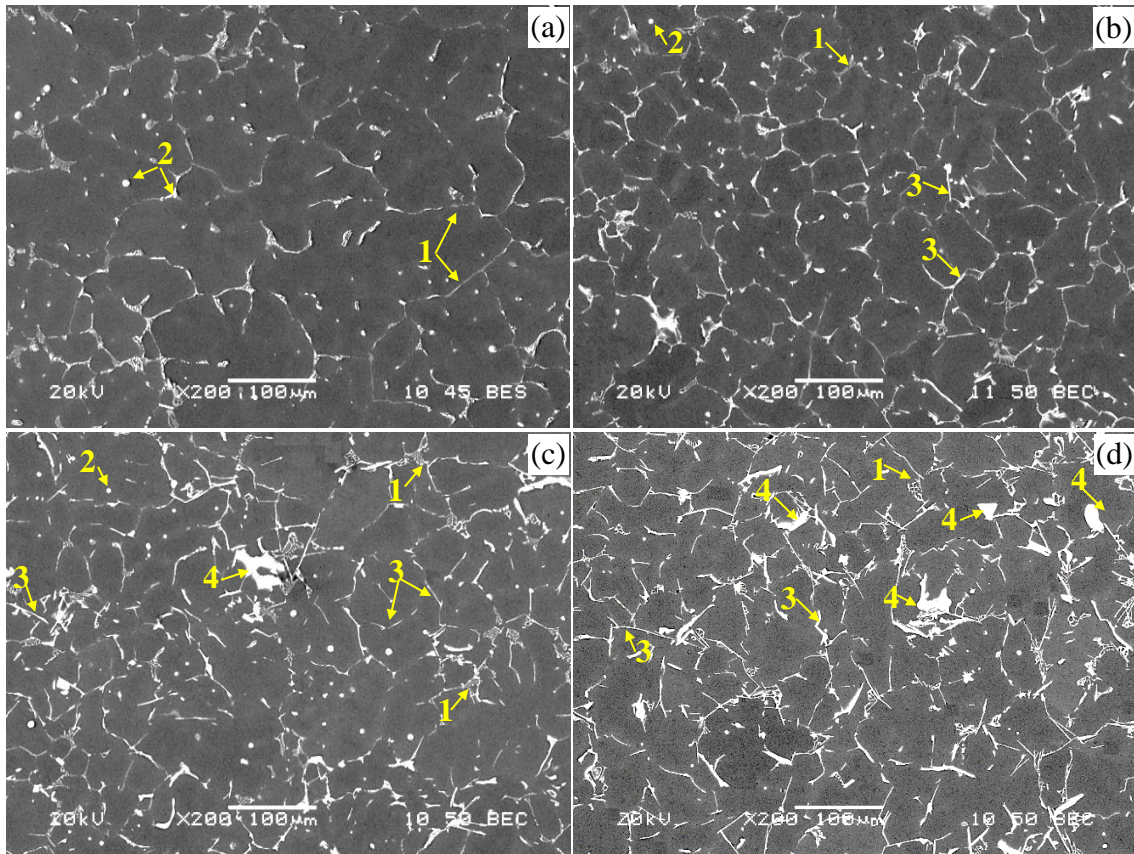
Figure 6.2: Backscattered electron (BSE) images showing the microstructures of the B0 alloys: (a) 0.0 wt.% RE, (b) 0.2 wt.% La, (c) 0.5 wt.% La, (d) 1.0 wt.% La. The arrows indicate (1)α -Fe, (2) Al_2Cu, (3) La containing intermetallic phase, and (4) La rich containing intermetallic phase.

The key parameters, i.e., mean diameter, aspect ratio, roundness, and volume fraction, describing the intermetallic compounds in the B0 alloy with Ce and La additions are presented in Figure 6.3 and Figure 6.4, respectively. From Figure 6.3, as the addition level of Ce increases, the volume fraction increases from 3.8% to 6.63%. Likewise, Figure 6.4 shows that the volume fraction increases from 3.8% to 7.19% as the addition of La is increased. From Figure 6.3, it may be seen that as the level of Ce increases to 1.0 wt.%, the average values of roundness decreases from 0.47 to 0.34, while the aspect ratio increases from 2.94 to 4.67, indicating the coarse an irregular morphologies in which these inermetallics appear. Similar observation are noted for La additions, where Figure 6.4

131

displays a similar increase in the average aspect ratio from 2.94 to 4.61, and a decrease in the

average value of roundness from 0.47 to 0.35 as the La addition reaches 1.0 wt.%.
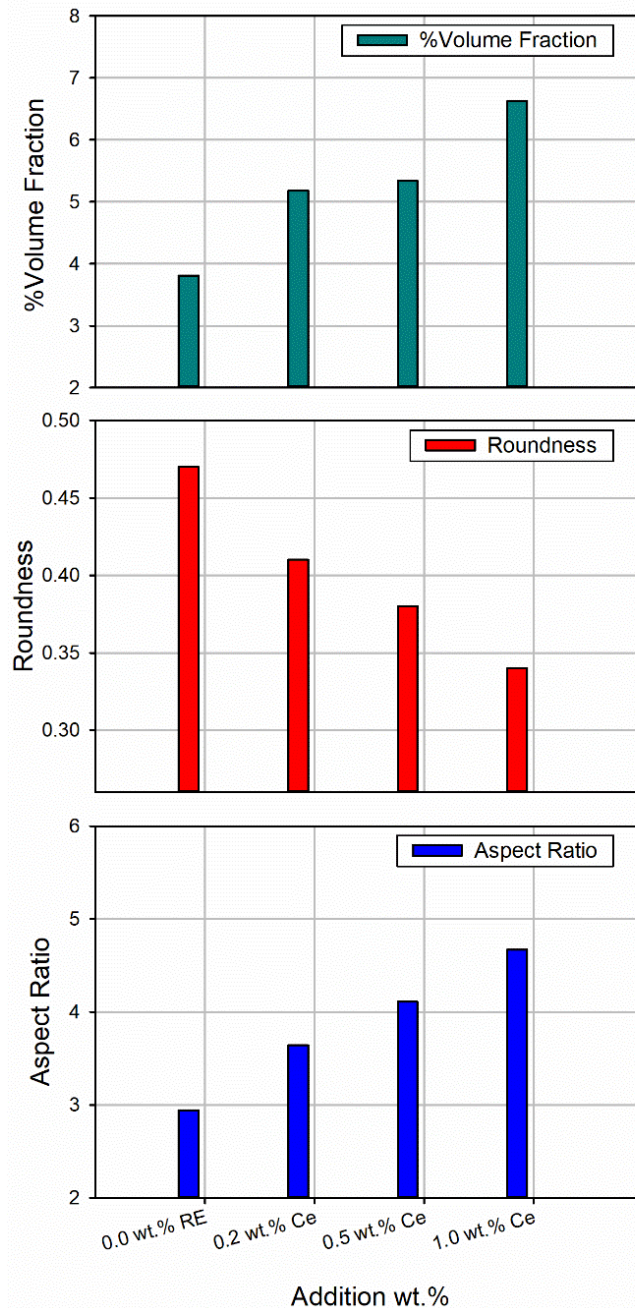
Figure 6.3: Key parameters of %volume fraction, roundness and aspect ratio describing the characteristics of intermetallic compounds in as-cast B0 alloy with various additions of Ce.
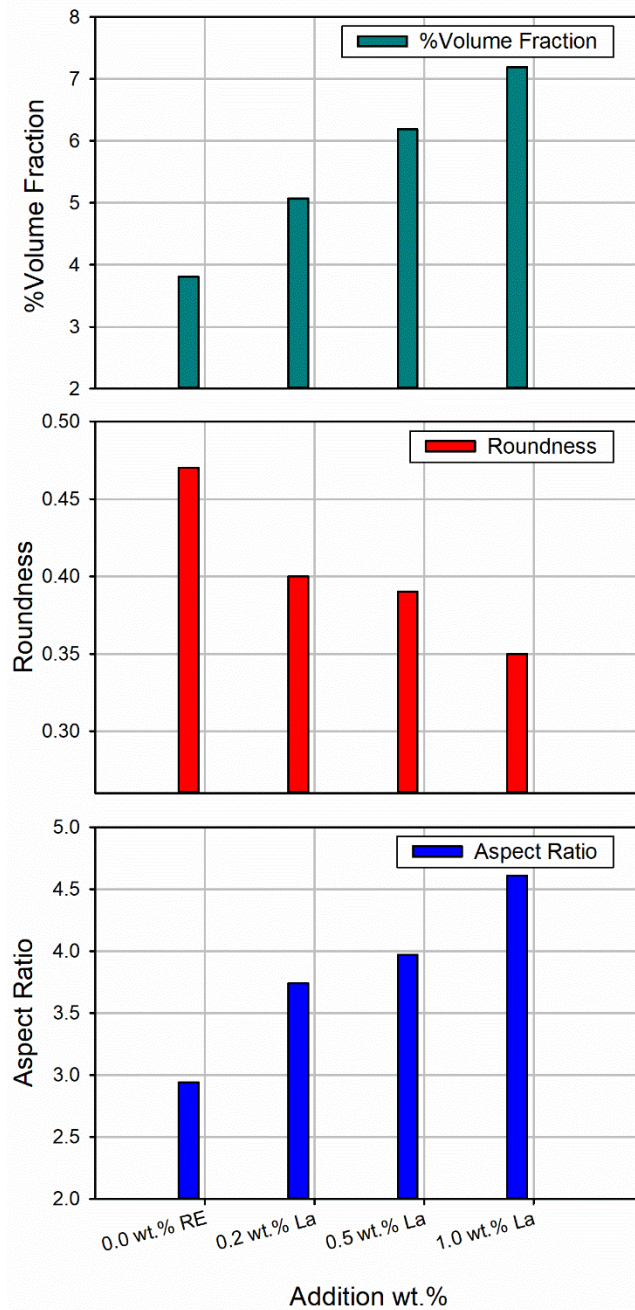
Figure 6.4: Key parameters of %volume fraction, roundness and aspect ratio describing the characteristics of intermetallic compounds in as-cast B0 alloy with various additions of La.

6.1.1.2 Al-Si-Cu (D0) Alloy

Backscattered electron (BSE) images depicting the morphology, size and distribution of intermetallic compounds observed in the D0 alloys with addition of Ce and La, and obtained in the as-cast condition are presented in Figure 6.5 and Figure 6.6. Figure 6.1(b-d) and Figure 6.6(b-d) reveals that as the RE(Ce/La) addition increases from 0.2 to 1.0 wt.%, relative amount of intermetallics increases and this could be attributed to the formation of new RE-containing intermetallic compounds. Figure 6.5 and Figure 6.6 also show that these RE intermetallic compounds appear in the interdendritic regions, along the dendrite boundaries.
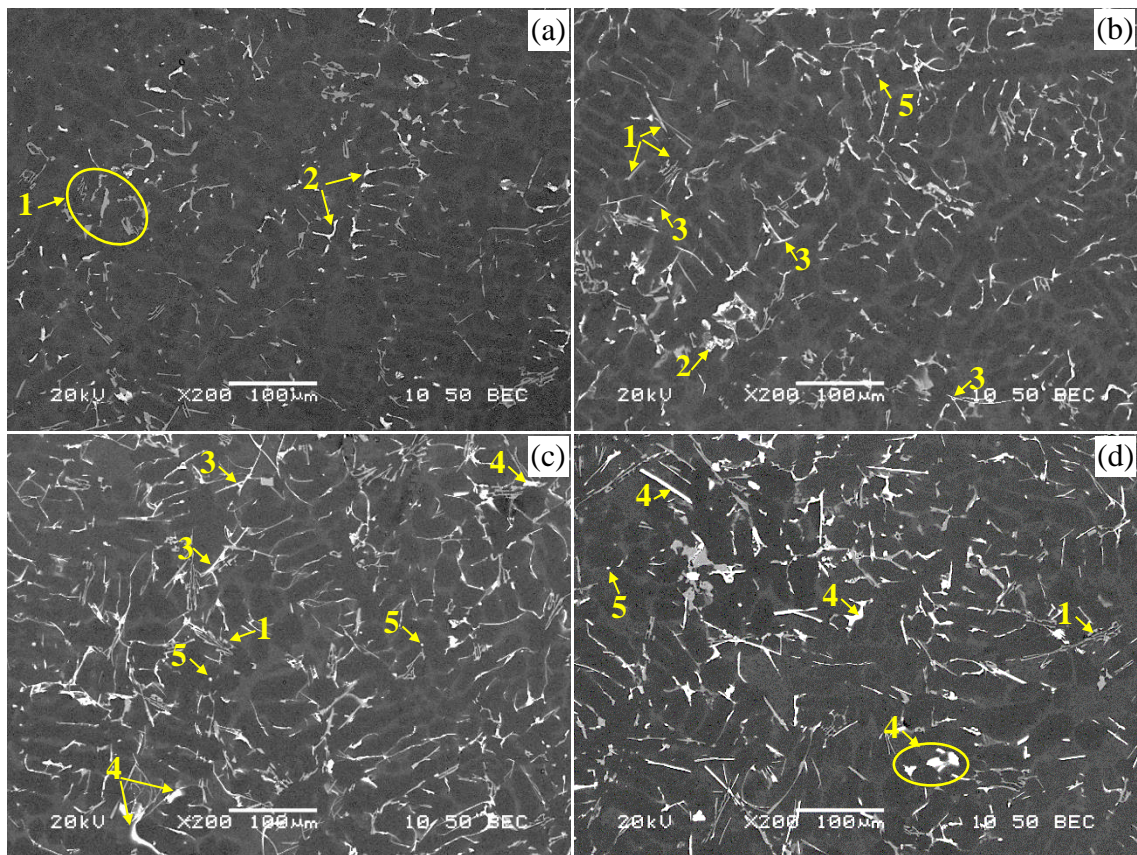
Figure 6.5: Backscattered electron (BSE) images showing the microstructures of the D0 alloys: (a) 0.0 wt.% RE, (b) 0.2 wt.% Ce, (c) 0.5 wt.% Ce, (d) 1.0 wt.% Ce. The arrows indicate (1) α-Fe, (2) Al_2Cu, (3) Ce containing intermetallic phase, (4) Ce rich containing intermetallic phase, and (5) Ce containing intermetallic phase (Cu free).
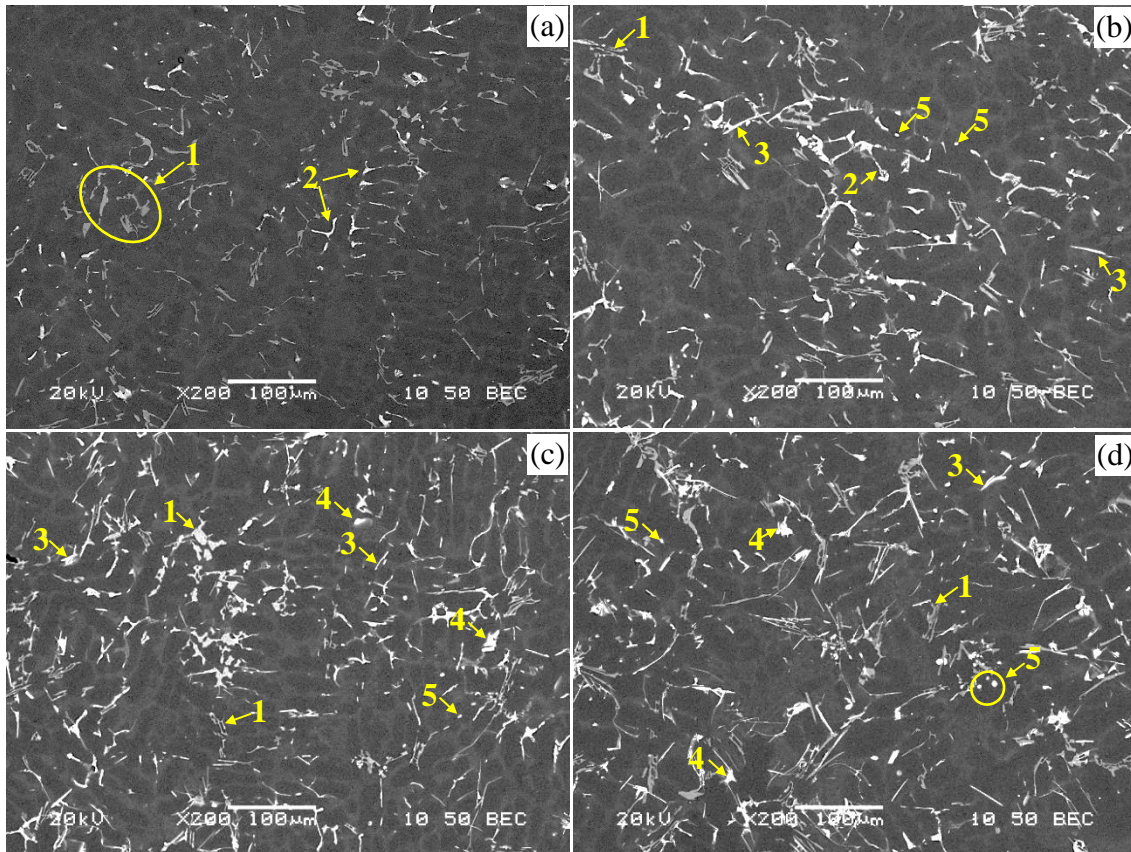
Figure 6.6: Backscattered electron (BSE) images showing the microstructures of the D0 alloys. (a) 0.0 wt.% RE, (b) 0.2 wt.% La, (c) 0.5 wt.% La, (d) 1.0 wt.% La. The arrows indicate (1) α-Fe, (2) Al_2Cu, (3) La containing intermetallic phase, (4) La rich containing intermetallic phase, and (5) La containing intermetallic phase (Cu free).

In addition, the morphology of the RE intermetallic is based on the RE level of addition since, as shown in Figure 6.5(b) and Figure 6.6(b), 0.2 wt.% RE, results in the formation of RE intermetallics which appear as small spot-like particles. Whereas, when the RE addition increases to 1.0 wt.%, the RE-containing intermetallic compounds have coarse block-like and coarse lath-like morphologies, as may be observed in the images shown in Figure 6.5(d) and Figure 6.6(d).

Figure 6.7 and Figure 6.8 display the average aspect ratio, roundness, and volume fraction values of the intermetallic compounds in the D0 alloy with Ce and La additions, respectively. The volume fraction increases from 4.93% to 7.8% as the addition of Ce

increases to 1.0 wt.%, and from 4.93% to 7.0% in the case of the La additions. As may be seen from Figure 6.7, the increasing the Ce addition increases the aspect ratio from 3.63 to 4.73 and decreases the average roundness value from 0.41 to 0.34. The increase in the addition level of La provides very similar results: the average value of roundness decreasing from 0.41 to 0.36 and the average aspect ratio increasing from 3.63 to 4.45, respectively as seen in Figure 6.8.

A comparison between the B0 and D0 alloys reveals that the B0 alloy exhibits both lower volume fractions and better morphological characteristics (lower aspect ratio and high roundness value) than the D0 alloy. This could be ascribed to the increased Si content of D0 alloy (8.0 wt.%) which results in coarsening of the α-Fe phase, as seen in Figure 6.6. In addition, it is apparent that the coarsening of the α-Fe phase is also observed in the RE-containing D0 alloys, as shown in Figure 6.5(b-c) and Figure 6.6(b-c). The same phenomenon was noted earlier in Chapter 5 in relation to the microstructural characterization of D0 alloy samples obtained at low cooling rate (see section 5.2.2).

An important point to consider in the current case is that the grey phase observed in the alloy samples obtained at low cooling rate, as described in CHAPTER 5 5, was not observed in the microstructure of both alloys- examined using tensile test samples that were obtained at high cooling rate. Thus, it is reasonable to conclude that cooling rate plays a decisive role in the formation of the grey phase. However, this point needs further investigation. Finally, the findings reported in the previous section (6.1.1) are in accordance with the results presented in reference [129]. It is worth noting mentioning here that this work is considered as the first investigation of its kind to study the influence of the morphology, size and distribution of RE-containing intermetallics on the tensile properties of aluminum alloys.
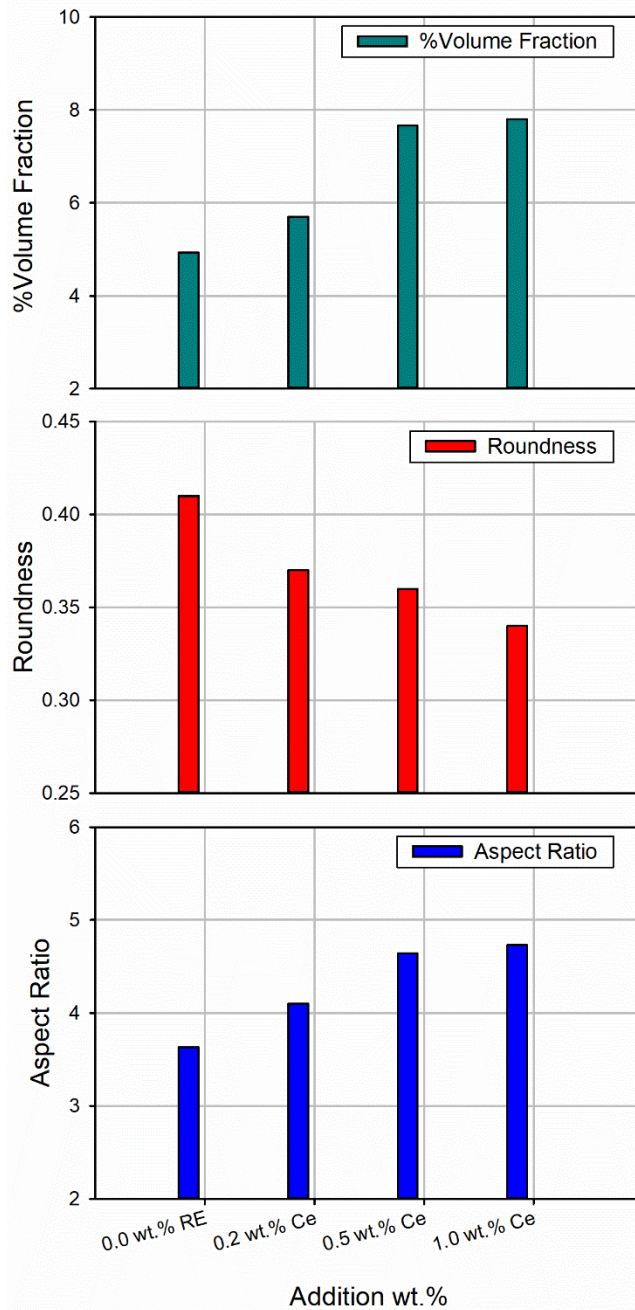
Figure 6.7: Key parameters of %volume fraction, roundness and aspect ratio describing the characteristics of intermetallic compounds in as-cast D0 alloy with various additions of Ce.
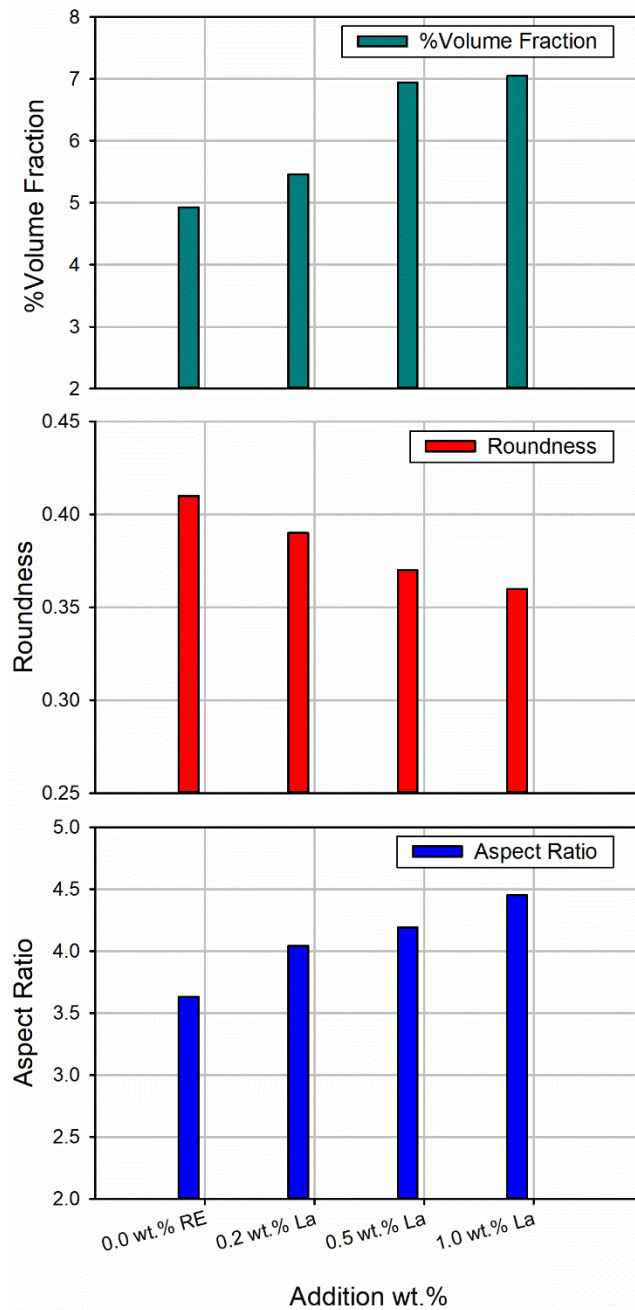
Figure 6.8: Key parameters of %volume fraction, roundness and aspect ratio describing the characteristics of intermetallic compounds in as-cast D0 alloy with various additions of La.

6.1.2 Silicon Particle Characterization

Parameters describing the eutectic silicon particle characteristics, including mean diameter, roundness, circularity, and aspect ratio, were measured and quantified using a Leica LM optical microscope in conjunction with Clemex image analyzer. For each sample, ten fields were examined at a magnification of 500x.

Optical micrographs of samples of D0 alloy without and with Ce addition obtained in as-cast condition and after solution heat treatment are displayed in Figure 6.9. Generally, the high temperature exposure during the solution heat treatment caused partial spheroidization and fragmentation the eutectic Si in D0 alloy, as shown in Figure 6.9 (b, d, f). As expected, Figure 6.9(c) displays the fibrous morphology of the eutectic silicon observed in the as-cast Sr modified D0 alloy. The addition of 0.2 wt.% Ce obviously modified the eutectic silicon structure, as shown in Figure 6.9(e). Such a modification effect of Ce was previously reported in A356 alloy [140]. The eutectic Si particle measurements, including mean diameter, roundness, circularity, and aspect ratio Si eutectic particles, presented in Figure 6.10, confirmed this effect. However, Figure 6.10 shows that the modification efficiency depends on the addition level of Ce. Interestingly, in Figure 6.9(e, f) the presence of Ce-Intermetallic phases is observed in both the as-cast and T6 heat-treated D0 alloy, which indicates that these intermetallic compounds are not soluble in the Al matrix, even when the alloy is heat treated at the high temperatures comprising the T6 treatment.
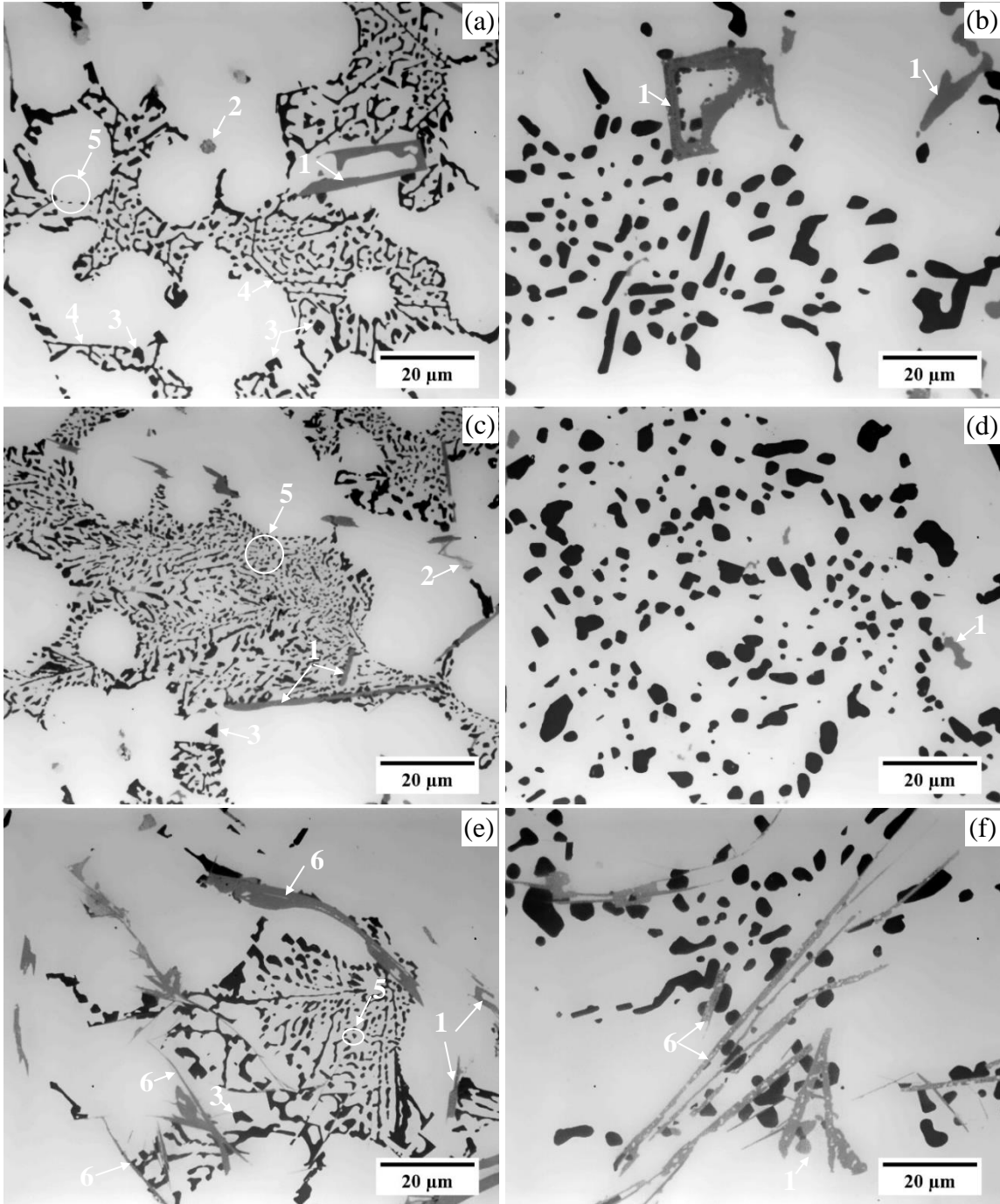
Figure 6.9 : Typical optical microstructures showing the morphology of eutectic silicon in D0 alloys in the as-cast (a, c, e) and T6 (b, d, f) conditions: (a, b) 0.0 wt.% RE; (c, d) 150 ppm Sr; (e, f) 0.2 wt.% Ce. The arrows indicate (1) α-Fe, (2) Al_2Cu, (3) blocky eutectic Si, (4) acicular eutectic Si, (5) fibrous eutectic Si, and (6) Ce-containing intermetallic phase.
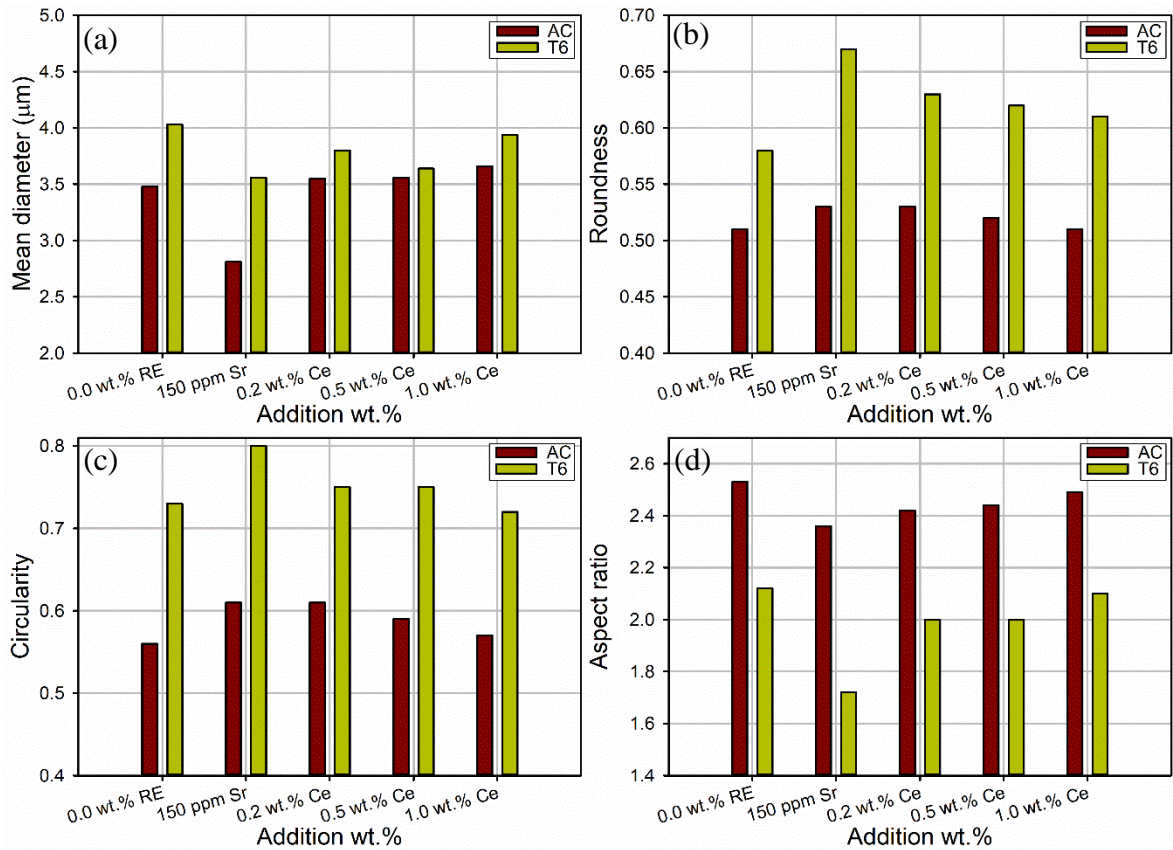
Figure 6.10: Parameters describing eutectic silicon particles in the D0 alloys as a function of Ce additions. (a) mean diameter, (b) roundness, (c) circularity and (d) aspect ratio.

With regard to the La-containing alloys, Figure 6.11(a-f) compares the optical micrographs of D0 alloy containing 0.2 wt.% La with the D0 base alloy and Sr modified D0 alloy obtained in the as-cast and T6 heat-treated conditions. It can be observed that the acicular eutectic silicon particles in D0 base alloy in Figure 6.11(a) transform into finer and more spherical particles with the 0.2 wt.% La addition. However, Figure 6.12 indicates that elemental La may also act as a modifier when it is added to D0 alloy in concentrations up to 0.5 wt.% La. Similar results were reported by Yi and Zhang [150], they noted that simultaneous modification of both primary and eutectic Si particles is obtained with the addition of pure La to hypereutectic Al-17%Si alloys, and that the optimal modification effect is achieved at 3.3 wt.% La. As in the case of Ce addition, the La-Intermetallic phases are also

141

observed in both the as-cast and T6 heat-treated D0 alloy samples, as seen in Figure 6.11(e-f), indicating the insoluble nature of the La-intermetallic phase.
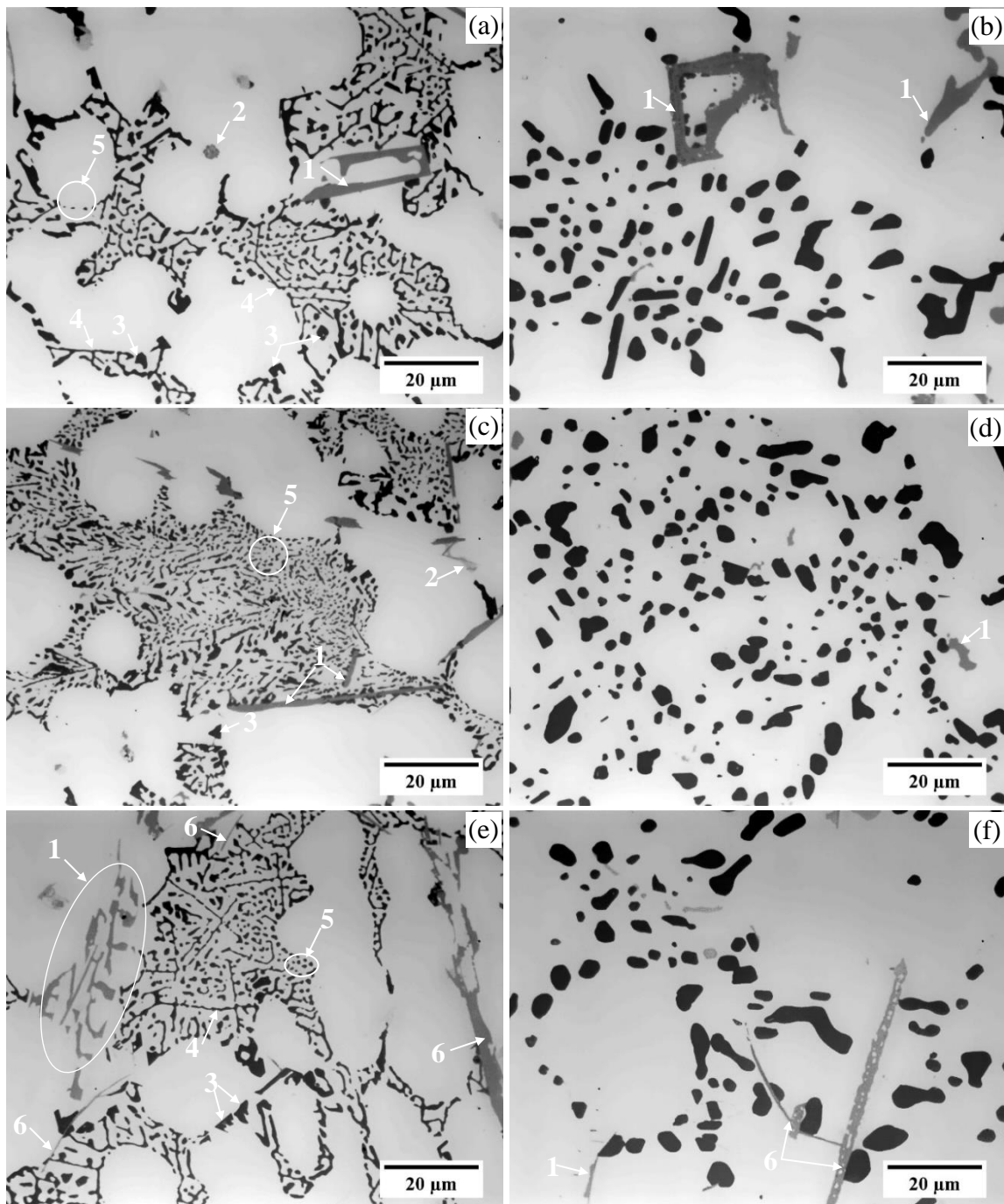
Figure 6.11 : Typical optical microstructures showing the morphology of eutectic silicon of the D0 alloys under As cast (a, c, e) and T6 (b, d, f) conditions. (a, b) 0.0 wt.% RE; (c, d) 150 ppm Sr; (e, f) 0.2 wt.% La. The arrows indicate (1) α-Fe, (2) Al$_2$Cu, (3) blocky eutectic Si, (4) acicular eutectic Si, (5) fibrous eutectic Si, and (6) La containing intermetallic phase.
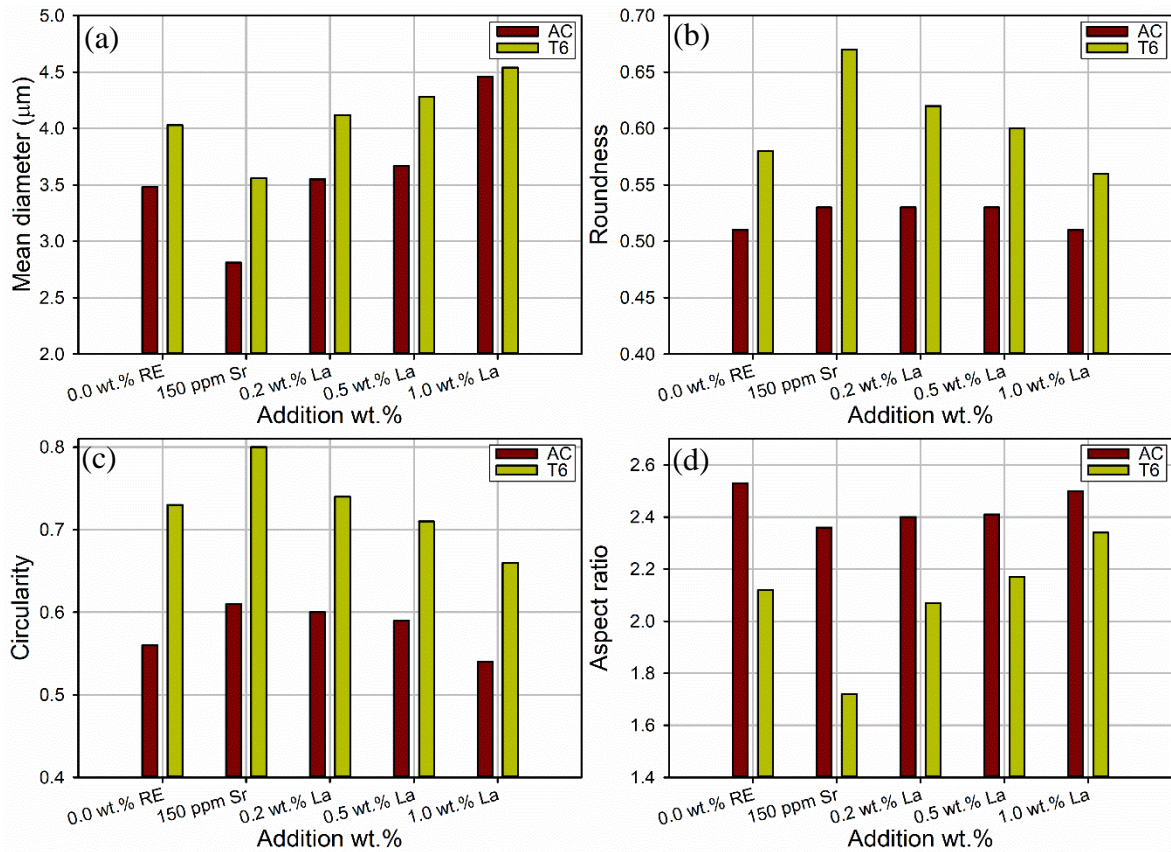
Figure 6.12: Parameters describing eutectic silicon particles in the D0 alloys as a function of La additions. (a) mean diameter, (b) roundness, (c) circularity and (d) aspect ratio.

6.2 ROOM TEMPERATURE TENSILE TEST RESULTS

Tensile tests were carried out to determine the effect of different individual additions of rare earth (RE) elements Ce and La on the ultimate tensile strength (UTS), yield strength (YS), and percent elongation (%El) of Al-Cu (B0) and Al-Si-Cu (D0) alloys in the as-cast (AC) and solution heat-treated (SHT) conditions, as well as after T5, T6 and T7 heat treatments with reference to the properties exhibited by the base alloys and their Sr-modified counterparts.

6.2.1 Mechanical properties (UTS, YS and %El)

In general, the results show that for all alloys, whether the base alloy, or the Sr-modified alloy, or those containing RE additions, the T6-heat treated alloys exhibit high (UTS) values compared to the SHT, T5, and T7 heat-treatment conditions, whereas the solution heat treated alloys display ductility values higher than those obtained for the other conditions . With respect to the effect of RE additions, the results indicate that the level of RE addition plays an effective role in the influence of La and Ce on the tensile properties. Alloys with Low level of additions of Ce and La additions exhibit comparatively better UTS values, which tend to decrease with higher additions.

The decrease in tensile properties with RE additions to the B0 and D0 alloys may be attributed to an increase in the total intermetallic volume fraction in the alloy, and the harmful acicular morphology of the RE-containing intermetallic particles, particularly at a high addition level of Ce and La (see subsection 6.1.1). As mentioned previously in the subsection 6.1.2, the fact that these RE intermetallic phases are observed in the as-cast, as well as in the heat-treated samples, implies that these intermetallic compounds are not soluble in the Al matrix, even when the alloy is heat treated at temperatures as high as 500 $^{\circ}$C. In addition, it is worth noting that these intermetallic compounds are Cu-rich, which would consequently affect the amount of Al_2Cu phase available for precipitation hardening. Therefore, the presence of the undissolved intermetallic compounds and the decrease in the Al_2Cu precipitates formed would lower the alloy strength. The tensile test results obtained in the current study are in keeping with those reported in other studies [88, 101, 133].

6.2.1.1 Al-Cu (B0) Alloy Results

Figure 6.13 and Figure 6.14 display the effects of Sr and RE (Ce and La) additions on the room temperature tensile properties of B0 alloys. In the as-cast condition, as may be seen from Figure 6.13, the base alloy exhibits UTS, YS, and % El values of 254 MPa, 186 MPa and 3%, respectively. The introduction of 150-ppm Sr improves the UTS and YS by about 30 MPa, while the ductility remains almost the same. Strength-wise, addition of 0.2 wt.% Ce produces more or less the same effect as the addition of 150 ppm Sr. The plots showing the variations in strength for the different heat treatments are also similar. With 0.5 and 1.0 wt.% Ce additions, while the UTS and YS decrease by about 50 MPa, the ductility values drop to less than 2%, even in the solution treated case, where the base alloy (without any additions) showed a ductility of 9.3%. From Figure 6.14 it may be noted that La addition has a similar effect as that of Ce, however, with somewhat better ductility values (3-4%) in the solution heat-treated condition at the higher additions

Compared to the as-cast B0 alloy, Figure 6.13 shows that addition of 150 ppm Sr to the base alloy improves the UTS and YS to 387 MPa and 340 MPa, respectively, in the T6 heat-treated condition, with a slight decrease in ductility from 3% to 2.1%. Elgallad [8], reported that the additions of Sr refined the morphology of the α-Fe Chinese script phase and led to a slight improvement in the ductility which is in good accordance with obtained results from the B0 alloy. As Figure 6.13 shows, addition of 0.2 wt.% Ce results in improving the UTS to 360 MPa and the YS to 338 MPa in the T6-treated condition, with a corresponding decrease in ductility from 3.0% to 1.1%. Similarly, addition of 0.2 wt.% La results in improving the UTS and YS to 381 MPa and 341 MPa, respectively, with a corresponding decrease in ductility from 3.0% to 1.7% in the T6-treated condition, Figure 6.14.
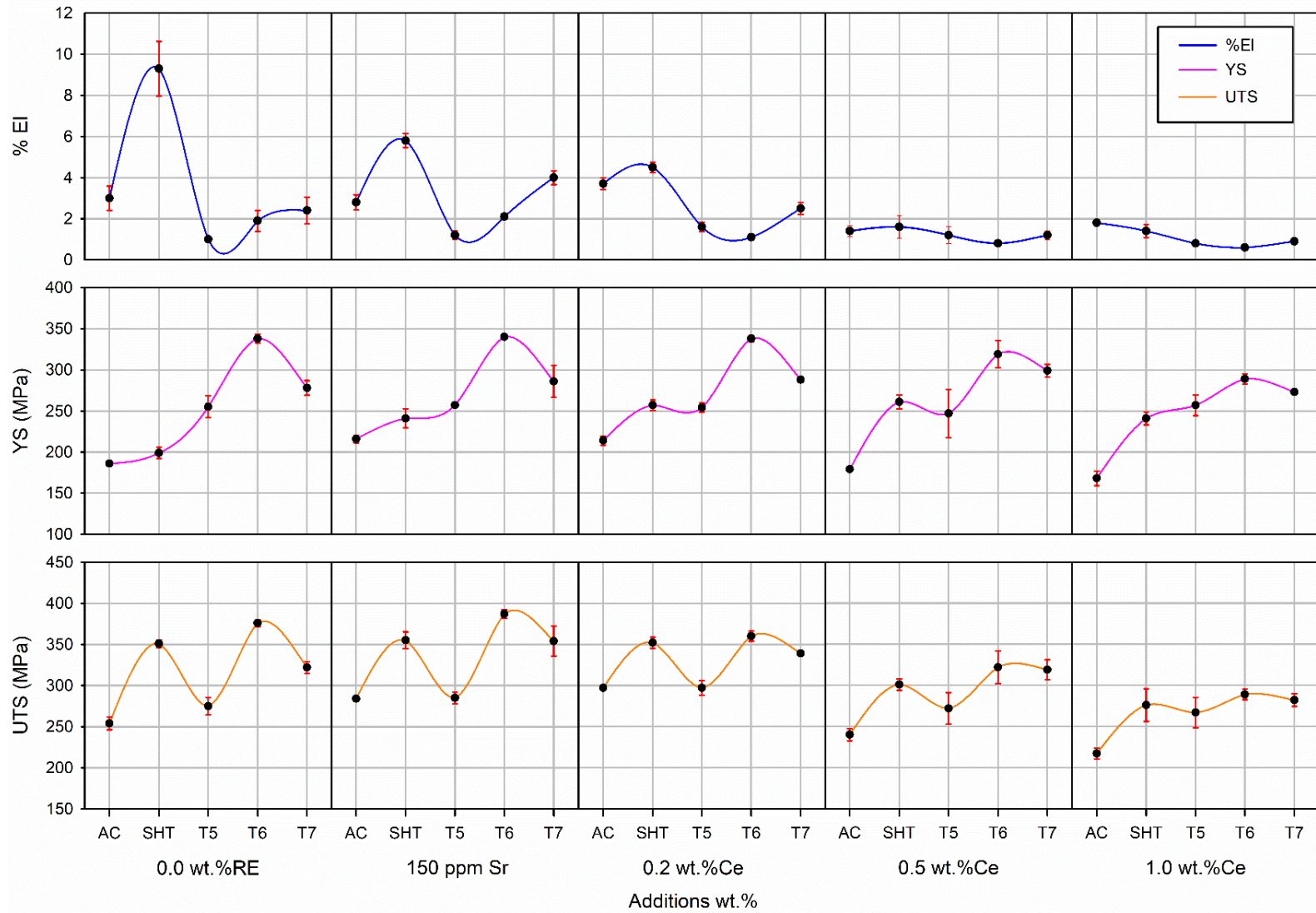
Figure 6.13: Effect of Sr and RE Ce addition on the mechanical properties (UTS, YS, and %El) of B0 alloys.
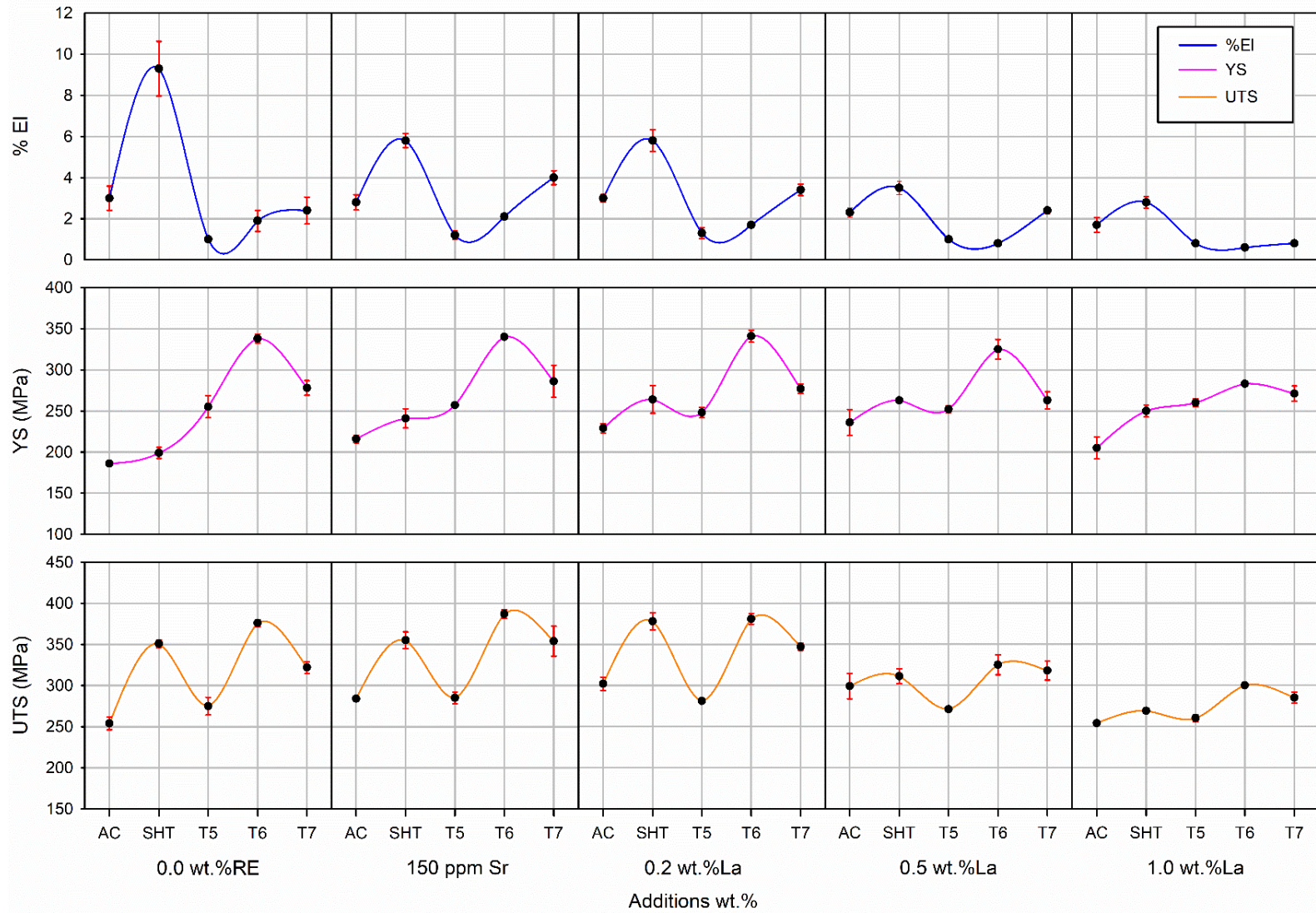
Figure 6.14: Effect of Sr and RE La addition on the mechanical properties (UTS, YS, and %El) of B0 alloys.

6.2.1.2 Al-Si-Cu (D0) Alloy Results

Figure 6.15 and Figure 6.16 show the effects of Sr, Ce and La additions on the room temperature tensile properties (UTS, YS, and %El) of D0 alloys corresponding to various heat treatment conditions. From Figure 6.15, it can be seen that the values of UTS, YS, and % El of the as-cast D0 base alloy are 300 MPa, 224 MPa, and 1.7%, respectively. Figure 6.15 also shows that adding 150 ppm Sr lowers the UTS, and YS values to 278 MPa and 199 MPa, respectively, with a corresponding increase in ductility from 1.7 to 2.0%. Addition of Ce or La lowers the tensile strength further, to about 210 MPa in the as-cast case, for the different levels of RE addition, whereas the YS drops to around 149 MPa. For the 0.2 wt.% La addition, however, the drop in UTS and YS values in somewhat less, by about 43 MPa and 36 MPa, as shown in Figure 6.16.

Figure 6.15 also show that in the T6 heat-treated condition, the addition of 150 ppm Sr improves the UTS from 300 MPa in the as-cast condition to 361 MPa and the YS from 224 MPa to 346 MPa, with a corresponding decrease in the ductility from 1.7% to 1.0%. The presence of 0.2 wt.% of Ce in the T6-treated D0 alloy results in enhancing the UTS and YS values of the as-cast D0 base alloy from 300 to 320 MPa and from 224 to 320 MPa, respectively accompanied by a decrease in the percent elongation from 1.7 to 0.7% as shown in Figure 6.15. In comparison, Figure 6.16 depicts that 0.2 wt.% addition of La results in UTS and YS values of 374 and 368 MPa, respectively in the T6-heat-treated alloy, and a ductility of 0.9%. Thus, in T6-treated condition, addition of 0.2 wt.% La is much more effective in enhancing the alloy strength compared to 150 ppm Sr addition, while maintaining almost the same ductility at the same time.
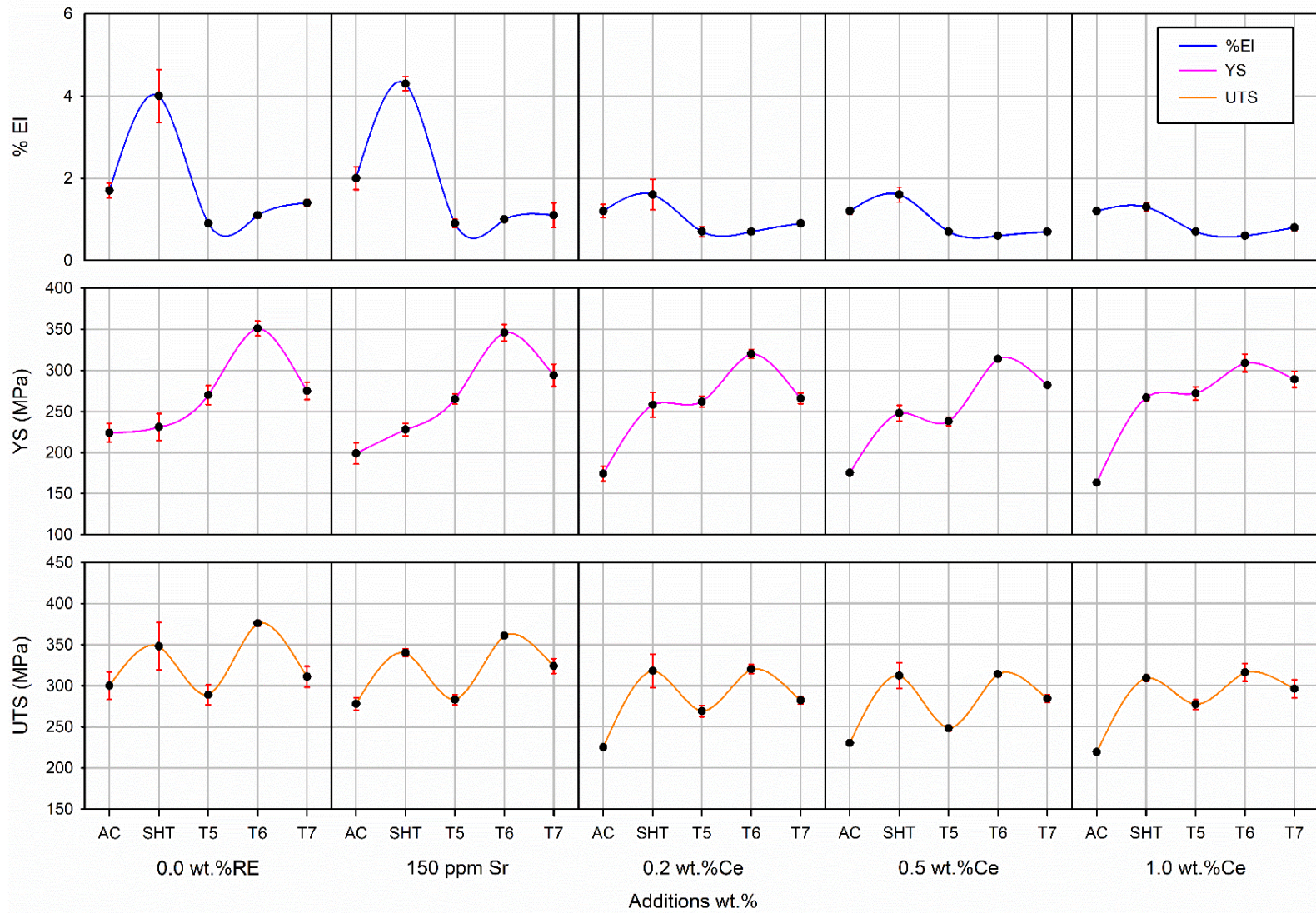
Figure 6.15: Effect of Sr and RE Ce addition on the mechanical properties (UTS, YS, and %El) of D0 alloys.
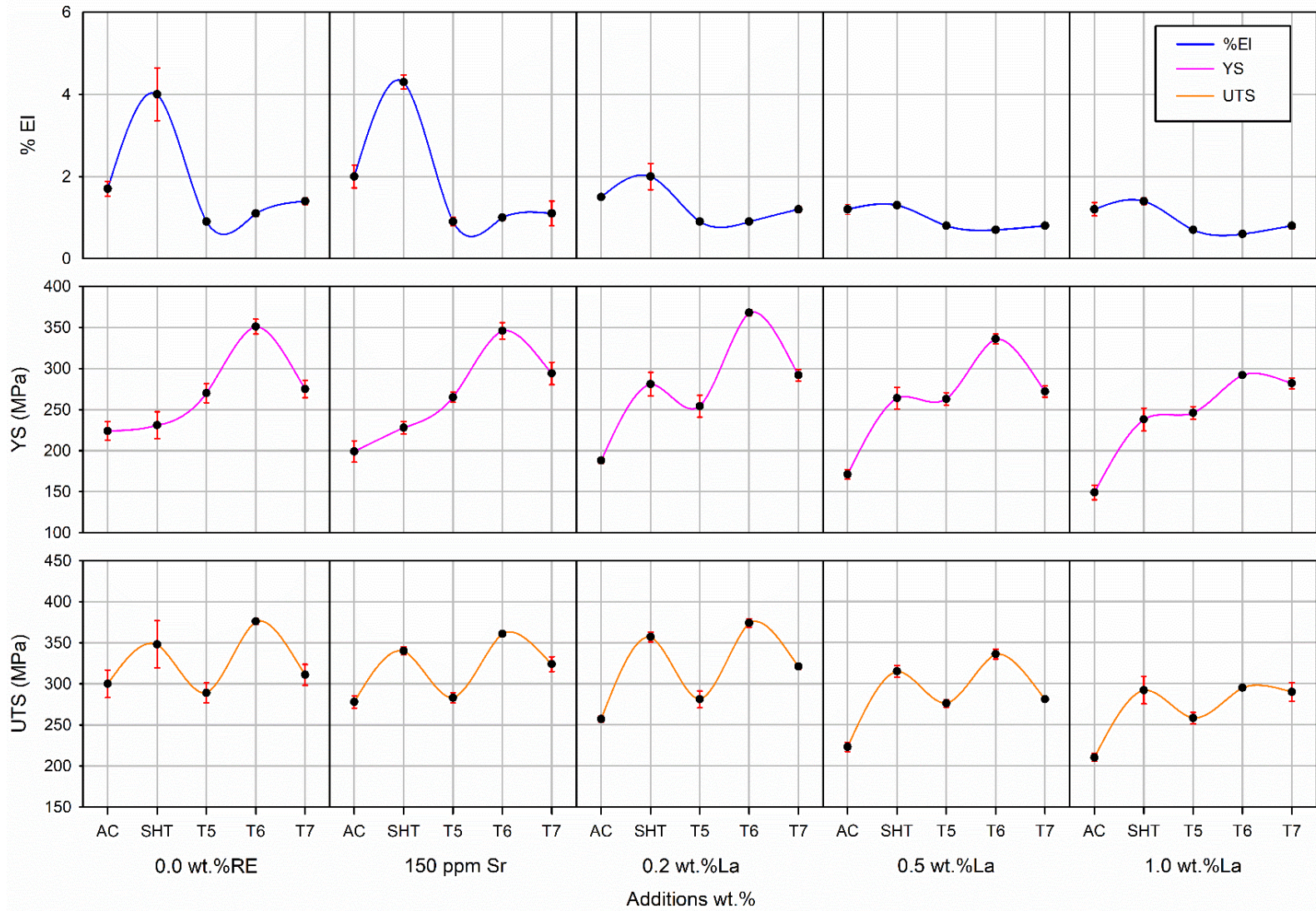
Figure 6.16: Effect of Sr and RE La addition on the mechanical properties (UTS, YS, and %El) of D0 alloys.

6.2.2 Construction Methodology of the Quality Charts

In Chapter 2, section 2.2.1 presented the concept of the quality index proposed by Drouzy et al [46] and Câceres [48, 49]. Previous work done by Elgallad [8] showed that the quality index (Q) proposed by Drouzy et al. is not applicable to the Al-Cu B0 type alloys. On the other hand, the universal applicability of Equation 2.7 and Equation 2.10 which were respectively used to draw the "iso-YS" lines and "iso-q" lines of the quality chart introduced by Câceres makes it possible to use this chart to assess the quality of the B0 alloys. The alloy quality is expressed in terms of the relative ductility parameter, q, based on the correlation between the "iso-q" lines of Câceres' chart and the "iso-Q" lines of Drouzy's chart. Accordingly, the quality charts of the B0 and D0 alloys used in this study were constructed based on Câceres model (see Figure 2.6), and are presented in Figure 6.18 to Figure 6.21. Two charts were plotted for each alloy, corresponding to the Ce and La additions. The methodology used to construct these maps is as follows:

1) Transforming the engineering stress-strain curves of each alloy composition studied into the equivalent true stress-strain curves. Each of these engineering stress-strain curves corresponds to the average of five curves obtained from the tensile testing of five tensile bars representing the alloy composition under consideration and the heat treatment conditions (Figure 6.17).

2) Calculating the strength coefficient of the material, *K,* and the strain-hardening exponent, *n* based on the parameters of the true stress-strain curves obtained in step (1), as shown in Figure 6.17.

3) Determining *K* and *n* for each alloy composition as the mean values calculated over the respective values corresponding to the heat treatment conditions

4) Calculating the *K*-value for each alloying group as the average of the *K*-values of the alloys involved in such group.

5) Substituting the K-value in Equation 2.7 and Equation 2.10 to plot the families of the *"iso-n"* lines and *"iso-q"* lines, respectively, of the quality chart under construction for the given values of the strain-hardening exponent, *n,* engineering strain, *s,* and relative ductility, *q.*

6) Plotting the data points for each alloy composition on the relevant quality chart. Each point represents the UTS and %El values of that alloy composition for a specific heat treatment conditions.

$$UTS, YS, E_f$$

$$TUTS = UTS(1 + \frac{E_f}{100})$$
$$TYS = YS(1 + 0.002)$$
$$TE_f = Ln(1 + \frac{E_f}{100})$$

$$n = \frac{Ln(\frac{TYS}{TUTS})}{ln(\frac{Ln(1.002)}{TE_f})}$$

$$K = \frac{TUTS}{TE_f{}^n}$$
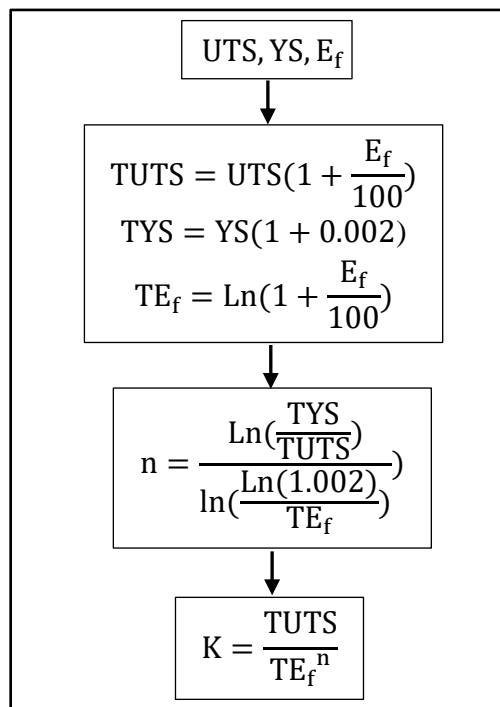
Figure 6.17: Equations required to obtain true stress-strain curves (TUTS, TYS, TE$_f$) parameters, strain hardening exponent (n), and the strength coefficient (K). Detailed explanation of these equations is provided in Appendix F.

The quality index results of B0 and D0 alloys are presented in subsections 6.2.2.1 and 6.2.2.2, respectively. The value of the quality of the investigated alloy will be expressed by the relative ductility parameter, q. The higher the value of q, the higher the combination of both UTS and %El. As previously shown in Chapter 2 (see Figure 2.6), the higher q-value lines are located close to the upper right hand corner of the Câceres quality chart.

6.2.2.1 Al- Cu (B0) Alloy

The quality charts for the RE-containing B0 alloy are shown in Figure 6.18 and Figure 6.19 for the Ce and La additions, respectively for the various heat treatment condition studied, e.g., SHT, T5, T6, and T7. For purposes of comparison, the quality index values of the B0 base alloy and the Sr-modified B0 alloy are also presented in the two charts.

Generally, it can be observed from Figure 6.18 and Figure 6.19 that the alloys in the solution heat-treated condition displays higher q-values compared to the other conditions, particularly so in the case of the B0 base alloy (with no addition). This could be ascribed to the increase in %El value obtained after solution heat treatment, which in turn increases the q-value as it is determined by a combination of UTS and %El. This combined effect is also noted in the quality values of the B0 alloy displays after T6 and T7 treatments. Whereas the T6 treatment produces peak strength, and the T7 treatment results is alloy softening, the increase in ductility in the latter case is more influential in improving the q value when considering the strength-ductility combination.

With respect to additions, the Sr-modified alloy possesses the best q-value compared to the RE (Ce/La) additions. In regard to the RE addition level, B0 alloy with 0.2 wt.% RE displays the best quality among all RE additions. In fact, for the 0.2 wt.% La addition, the q-value surpasses that obtained with Sr addition, as seen in Figure 6.19. Obviously, at the 1.0

wt.% RE addition level, the B0 alloy possess the lowest q-values, due to the increased volume fraction of RE-containing intermetallics formed in the alloy, as shown in Figure 6.18 and Figure 6.19. Consequently, solution heat treatment provides no improvement in the alloy quality, unlike that observed in the case of the Sr-modified and 0.2 wt.% RE-containing alloys.
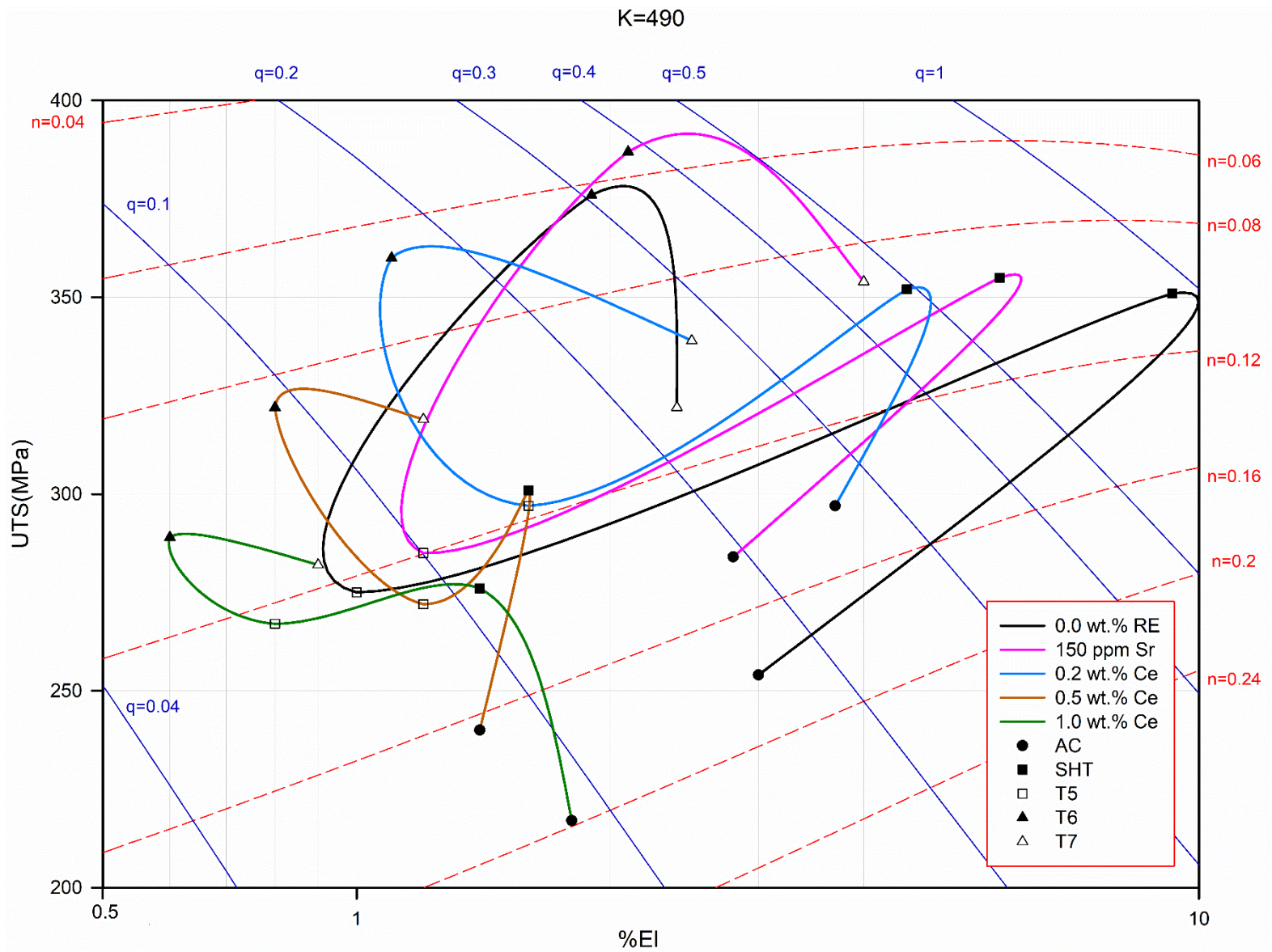
Figure 6.18: Quality map showing the relation between UTS and %El for the B0 alloys with Sr and Ce additions for various heat treatment conditions.
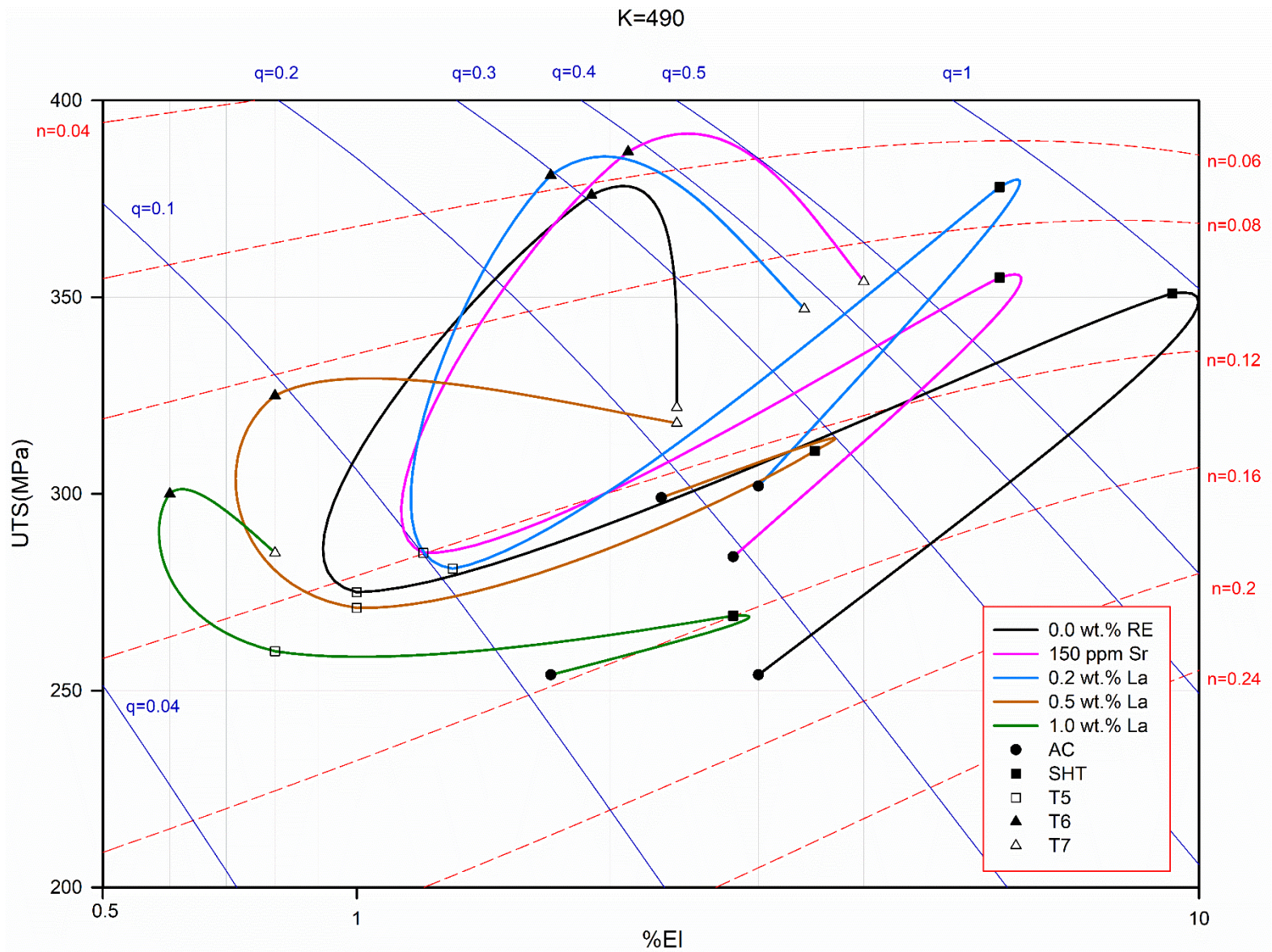
Figure 6.19: Quality map showing the relation between UTS and %El for the B0 alloys with Sr and La additions for various heat treatment conditions.

6.2.2.2 Al- Si-Cu (D0) Alloy

The quality charts for D0 alloy are presented in Figure 6.20 and Figure 6.21 corresponding to the Ce and La additions made to the D0 alloy, respectively, for the various heat treatment conditions studied. For purposes of comparison, the quality index values of the D0 base alloy and the Sr-modified D0 alloy are also presented in the two charts.

It can be inferred from Figure 6.20 and Figure 6.21 that the solution heat-treated alloys exhibit the best quality values among all the heat treatment conditions studied. The significant enhancements in quality after solution heat treatment may be related to the increase in ductility associated with solutionizing treatment (see Figure 6.15 and Figure 6.16). Figure 6.20 and Figure 6.21 also show that the quality of the T6-and T7-treated D0 alloys is improved, compared to as-cast condition.

The quality charts in Figure 6.20 and Figure 6.21 show that in the T6 heat treatment condition, the Sr–modified alloy possesses the best q-value compared to the alloys with RE (Ce/La) additions. With respect to the RE (Ce/La) additions, alloys with a small level (0.2 wt.%) of RE (Ce/La) display best quality compared to those containing higher levels of RE additions, with the 1.0 wt.% RE-containing alloys having the lowest quality, as was also observed in the case of the B0 alloys as shown in Figure 6.18 and Figure 6.19. It is interesting to note that with 0.2 wt.% La addition, the alloy quality is enhanced to higher level than that obtained with 0.2 wt.% Ce, even slightly higher than that observed for the Sr-modified D0 alloy.
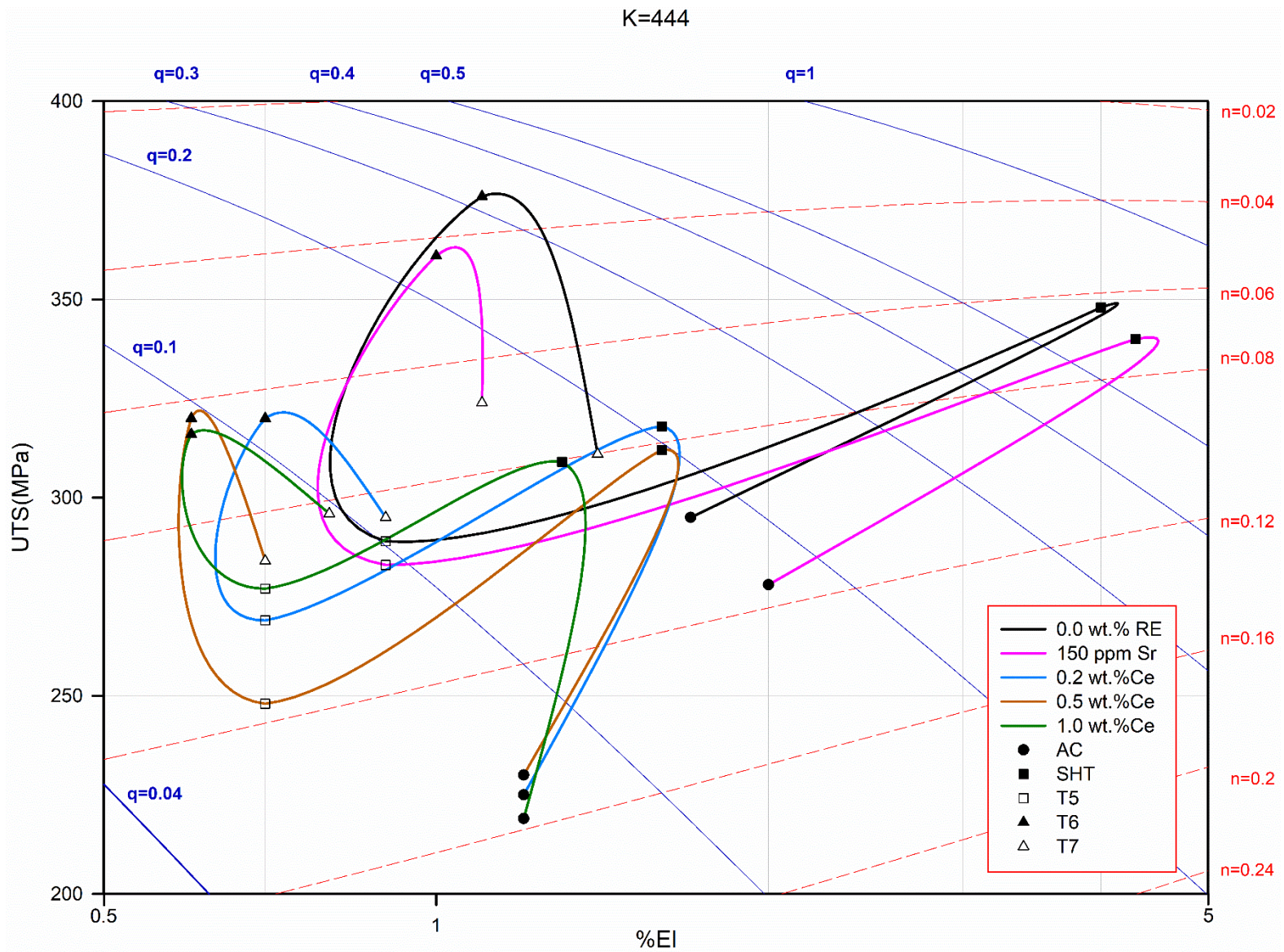
Figure 6.20: Quality map showing the relation between UTS and %El for the D0 alloys with Sr and Ce additions for various heat treatment conditions.
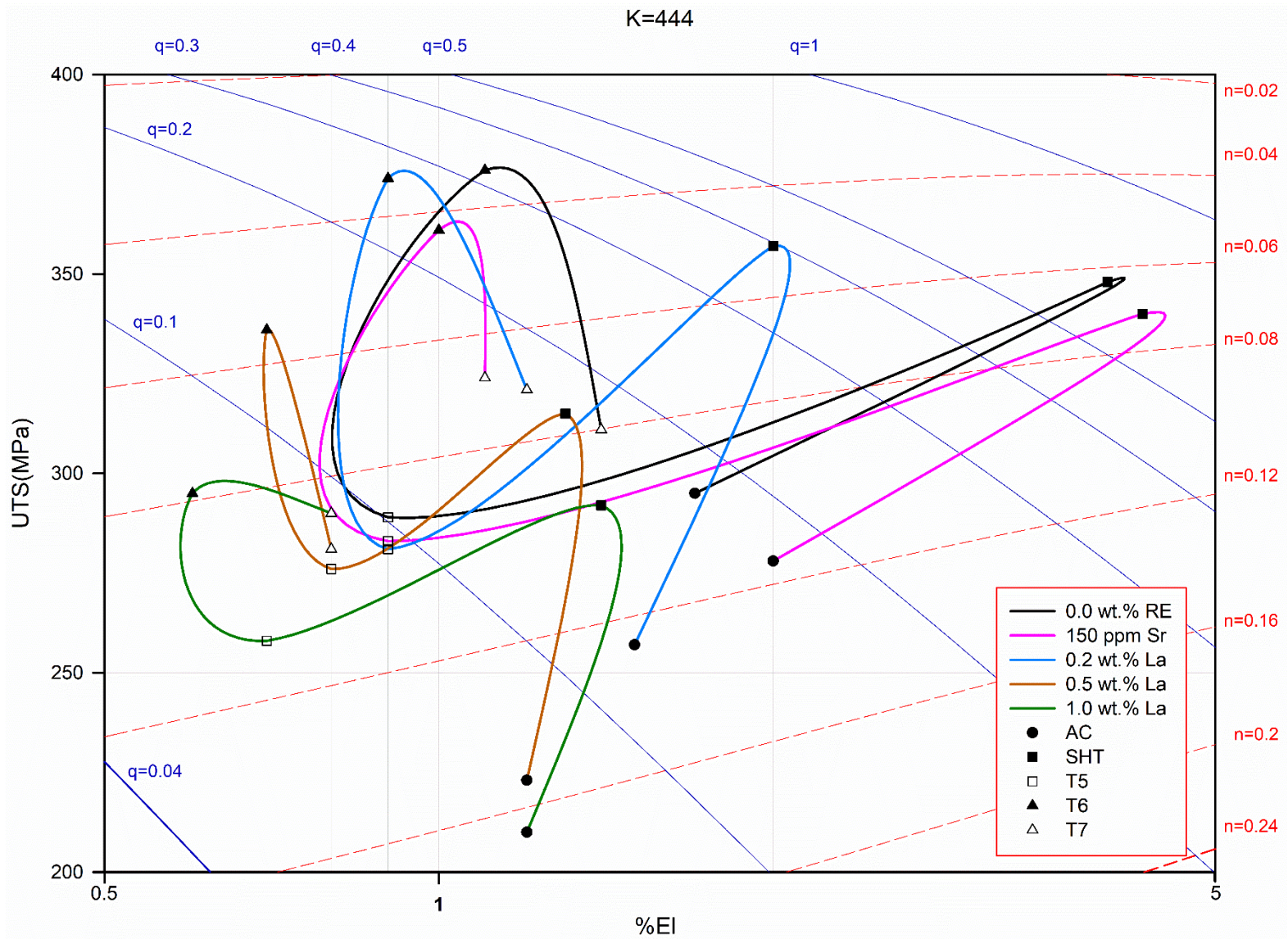
Figure 6.21: Quality map showing the relation between UTS and %El for the D0 alloys with Sr and La additions for various heat treatment conditions.

6.2.3 Statistical analysis

Figure 6.22 and Figure 6.23 present the tensile properties obtained for B0 and D0 alloys, respectively, with Sr and RE (Ce/La) additions under various heat treatment conditions relative to the values obtained for the as-cast (AC) base alloys, namely, subtracting the values obtained for the base alloys B0 and D0 in each case, and plotting them as ΔP values on the Y-axis (P = Property = YS, UTS or %El), with the X-axis representing the base line for alloys B0 and D0. The use of this method provides an effective means of directly seeing how the various additions used and the different heat treatment conditions applied affect the properties of the B0 and D0 alloys.

Generally speaking, as may be seen from Figure 6.22 and Figure 6.23, alloys B0 and D0 with the Sr and 0.2 wt.% RE(Ce/La) additions exhibit the best strength values, depending on the heat treatment applied. The T6 treatment provides the best improvements in UTS and YS, followed by the T7 treatment, while the solution heat-treated alloys display the best enhancements in ductility with reference to the baseline or base alloys.

Figure 6.22 shows that at higher levels (0.5, 1.0 wt.%) of RE (Ce/La) addition, although the UTS and YS of the as-cast B0 alloys are lowered somewhat with the Ce additions, the La additions provide better results in comparison. The heat treatments used tend to maintain the YS values similar to those obtained for the Sr-modified and 0.2 wt.% RE-containing alloys. However, the UTS values are reduced considerably with the 1.0 wt.% addition for both Ce and La additions, with no discernable impact due to heat treatment.

In general, it is observed that the T6 treatment produces the highest strength values for the various additions, and that La provides somewhat better values than Ce. This increase in strength is reflected by a corresponding decrease in ductility, so that the %EL-ΔP values

in most cases lie below the reference baseline expect for the solution heat-treated alloys, the best ductility values corresponding to the Sr- and 0.2 wt.% La additions. For achieving a balance between strength and ductility values, the best choice would be to use the solution-treated 0.2 wt.% La-containing alloys.

With respect to D0 alloys, Figure 6.23 depicts that all the as-cast D0 alloys containing the different additions exhibit lower strength values than the as-cast base alloy. While no improvement in UTS is obtained with heat treatment for the Ce-containing alloys, the 0.2 wt.% La-containing alloy shows relatively improved UTS values, particularly in the T6 condition. The YS shows a better response to heat treatment, with the T6 condition exhibiting the highest YS value for each addition, with the 0.2 wt.% La-containing alloy possessing the maximum YS among all the D0 alloys. The ductility values, on the other hand, are all lower by 2.0% on average compared to the D0 base alloy for all additions and heat treatments used.

For the D0 alloys, therefore, the ΔP plots reveal that the best addition and heat treatment combination for achieving maximum strength would be 0.2 wt.% La and T6 treatment. The best ductility value, on the other hand, is offered by the Sr-modified solution heat-treated D0 alloy. For a reasonable compromise of strength and ductility values, the 0.2 wt.% La-containing alloy in the solution treated condition would offer the best choice.
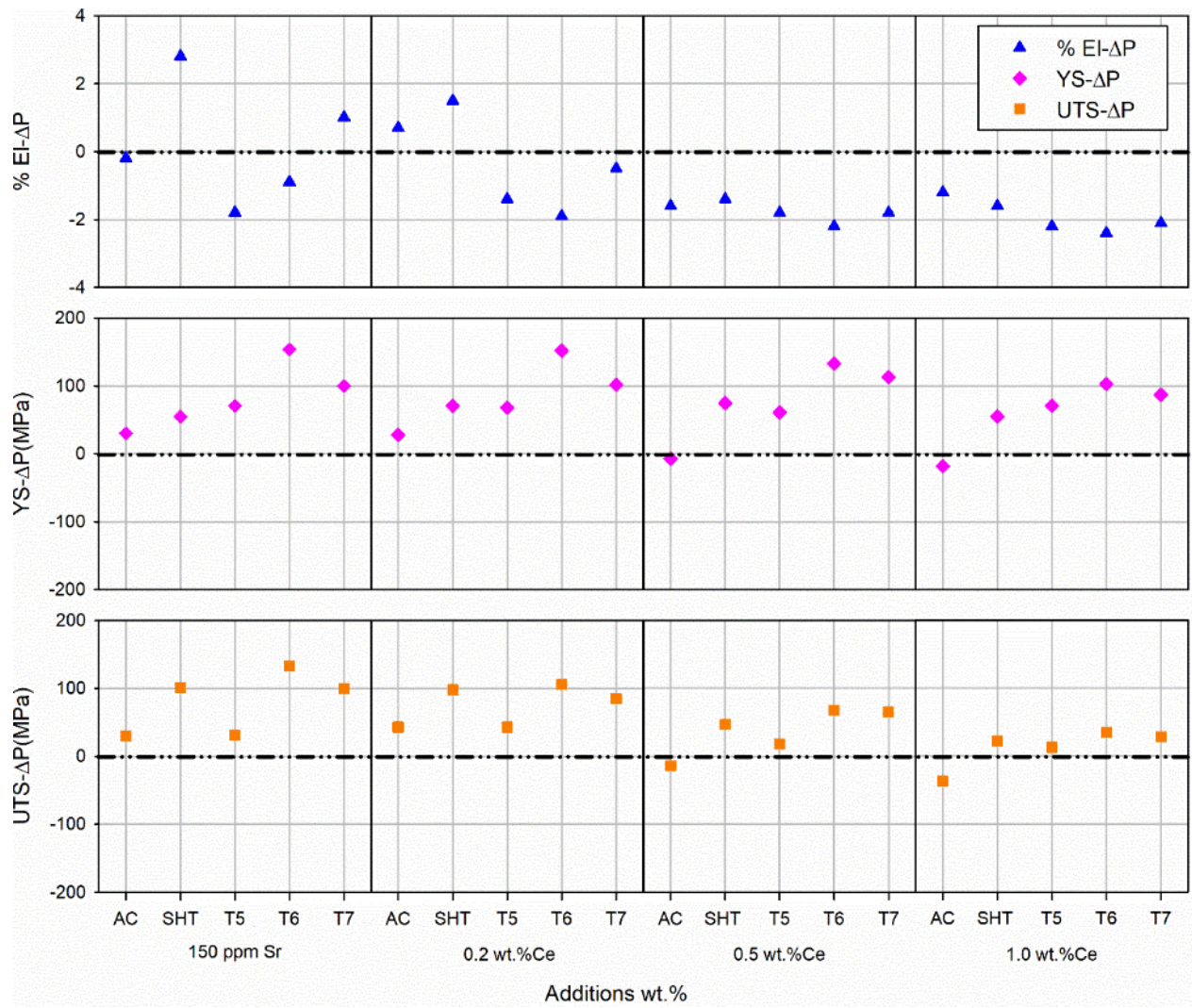
(a)

Figure 6.22 Cont.
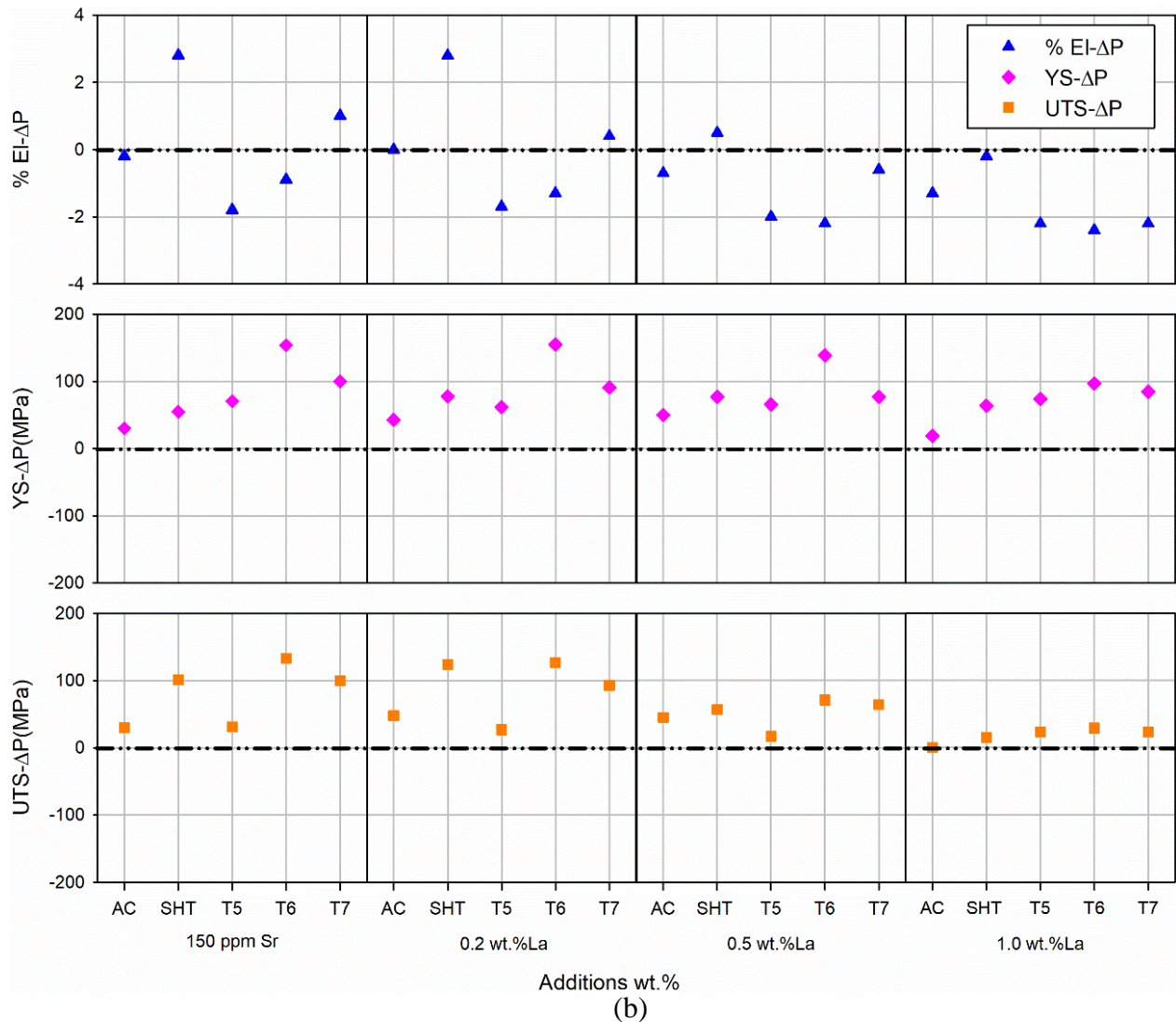
Figure 6.22: Comparison of tensile properties (UTS, YS, %El) of Sr-modified, and (a) Ce-, (b) La-containing B0 alloys relative to those of the as-cast B0 base alloy.

163

(a)
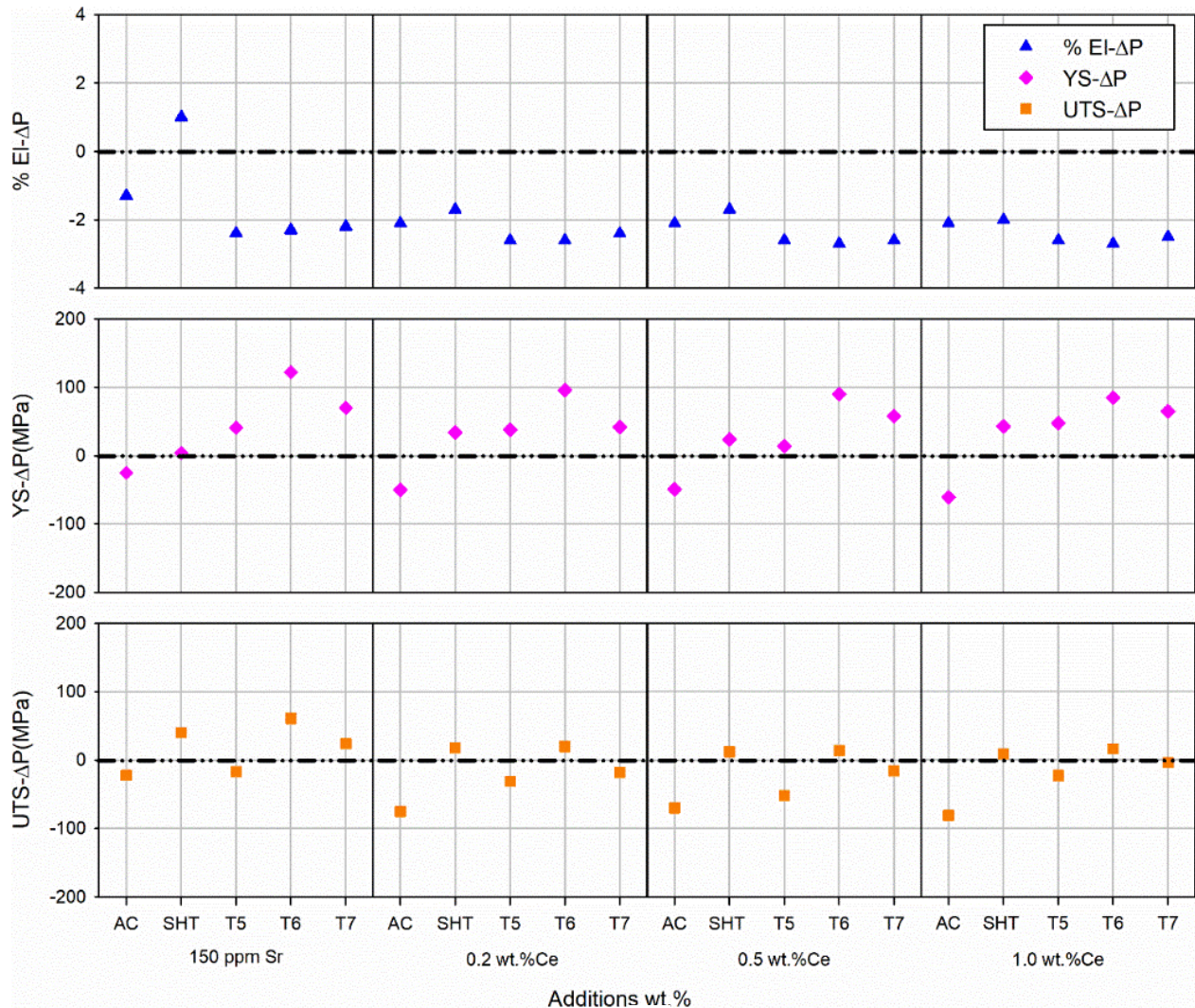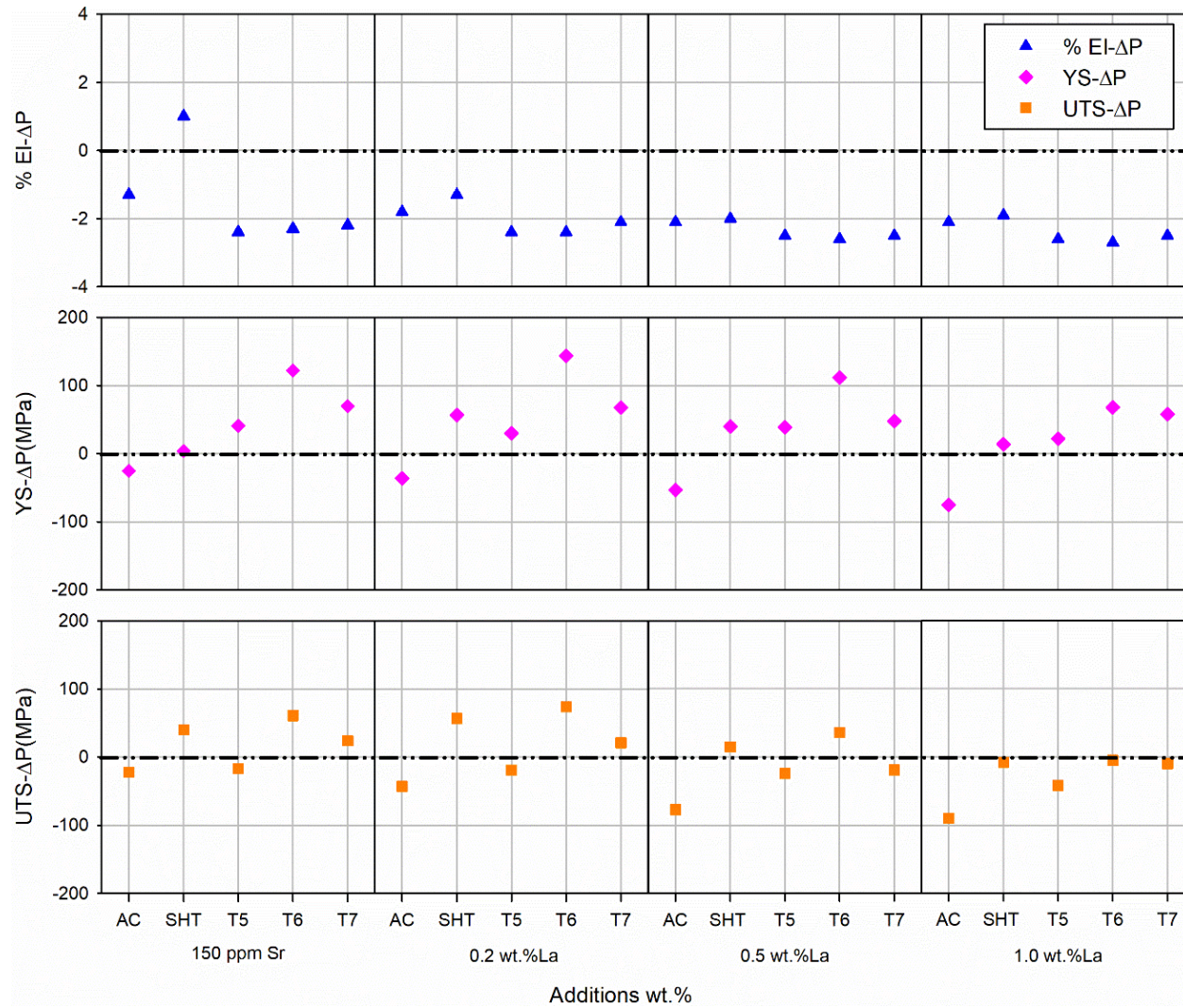
Figure 6.23 Cont.

(b)

Figure 6.23: Comparison of tensile properties (UTS, YS, %El) of Sr-modified and (a)Ce-, (b) La-containing D0 alloys relative to those of the as-cast D0 base alloy.

CHAPTER 7

HIGH TEMPERARURE TENSILE TEST RESULTS

CHAPTER 7

HIGH TEMPERARURE TENSILE TEST RESULTS

7.1 TENSILE PROPERTIES AT HIGH TEMPERATURE

The B0 and D0 alloys are intended for use in automotive applications, specifically in car engine blocks, which operate under high temperature service conditions. Alloys such as 356 and 319 alloys are not able to maintain their optimum properties at temperatures above 150 or 200 $^{\circ}$C. For this reason, it was considered necessary to study the tensile properties of B0 and D0 alloy at elevated temperature, in particular at 250 $^{\circ}$C. In addition, the effect of long stabilization periods (200 hrs) on the performance of these alloys was also investigated, to emulate actual working conditions.

In this section, the high temperature tensile properties of T6 heated B0 and D0 alloys subjected to one and 200 hrs of stabilization at the testing temperature of 250°C will be compared with the tensile properties obtained with the different additions of Ce and La. In general, for Both B0 and D0 alloys, the results show that 200 hrs of stabilization at 250 $^{\circ}$C produces a sharp decrease in the UTS and YS, and a large increase in ductility compared to the values obtained following one hour of stabilization at the same temperature.

Regarding the effect of rare earth additions, similar to the room temperature results, 0.2 wt.% Ce or La improves the UTS and YS of the B0 and D0 alloys by about 10-15 MPa following one hour stabilization, with little or no change in the ductility. Compared to the room temperature tensile test results, alloys with higher RE (Ce/La) still exhibit good strength

properties at high temperature with (with negligible decrease), comparable to those of the base alloys, following one hour of stabilization.

Alyaldin et al. [184] investigated the precipitation behavior in A354 alloy using transmission electron microscopy (TEM), more specifically to determine the change in the precipitates over prolonged periods of heating. The 354 alloy samples were tested at high temperature, following one and 200 hrs stabilization time at the testing temperature, similar to the current work. They concluded that after one hour of stabilization, the precipitates observed were fine, but after 200 hrs of stabilization, the precipitates had coarsened considerably, which resulted in the degradation in the tensile properties.

As mentioned previously, the addition of RE elements to the investigated alloys leads to formation of RE- containing intermetallic compounds with high thermal stability, which do not dissolve during the heat treatment and therefore improve the mechanical properties at high temperature as reported in the literature [87].

7.1.1 Al- Cu (B0) Alloy

Figure 7.1 and Figure 7.2 presents the effects of stabilization and various additions of Ce and La, respectively, on the high temperature tensile properties of T6 heat-treated B0 alloys. The UTS, YS and %El values obtained for B0 alloys following one hour of stabilization at 250°C prior to testing are 228 MPa, 227 MPa and 2%, respectively, as shown in Figure 7.1. With 200 hours of stabilization, however, these values are reduced to 80 MPa (UTS), 75 MPa (YS) that is, by 64% and 67%, respectively, while the ductility values increase to 18 %.

For RE additions, it can be noted from Figure 7.1 that with 0.2 wt.% Ce addition, the strength values increase from 228 to 242 MPa (UTS) and from 227 to 242 MPa (YS), negligible increase in %El from 2.0% to 2.2%. With 0.2 wt.% La addition, the B0 alloy exhibit a moderate increase in UTS and YS from 228 to 249 MPa and 227 to 248 MPa respectively and a small increase in ductility from 2.0% to 2.7 % as shown in Figure 7.2 at higher RE additions, UTS and YS values slightly decrease by 3-16 MPa, whereas the ductility varies between 2.0 to 1.0%.

Following 200 hrs stabilization, the UTS and YS values remain the same, around 80 -93 MPa and 69-73 MPa, respectively. At 2.0% Ce addition, the ductility changes from 18.3% to 17.4%, whereas with 0.2% La addition, it increases from 18.3 %to 21.2%. At higher RE additions (0.5 and 1.0 wt.%), the ductility is reduced to 8.5% and 6.2% in the case of Ce, and to 7.7% and 4.2% in the case of La.
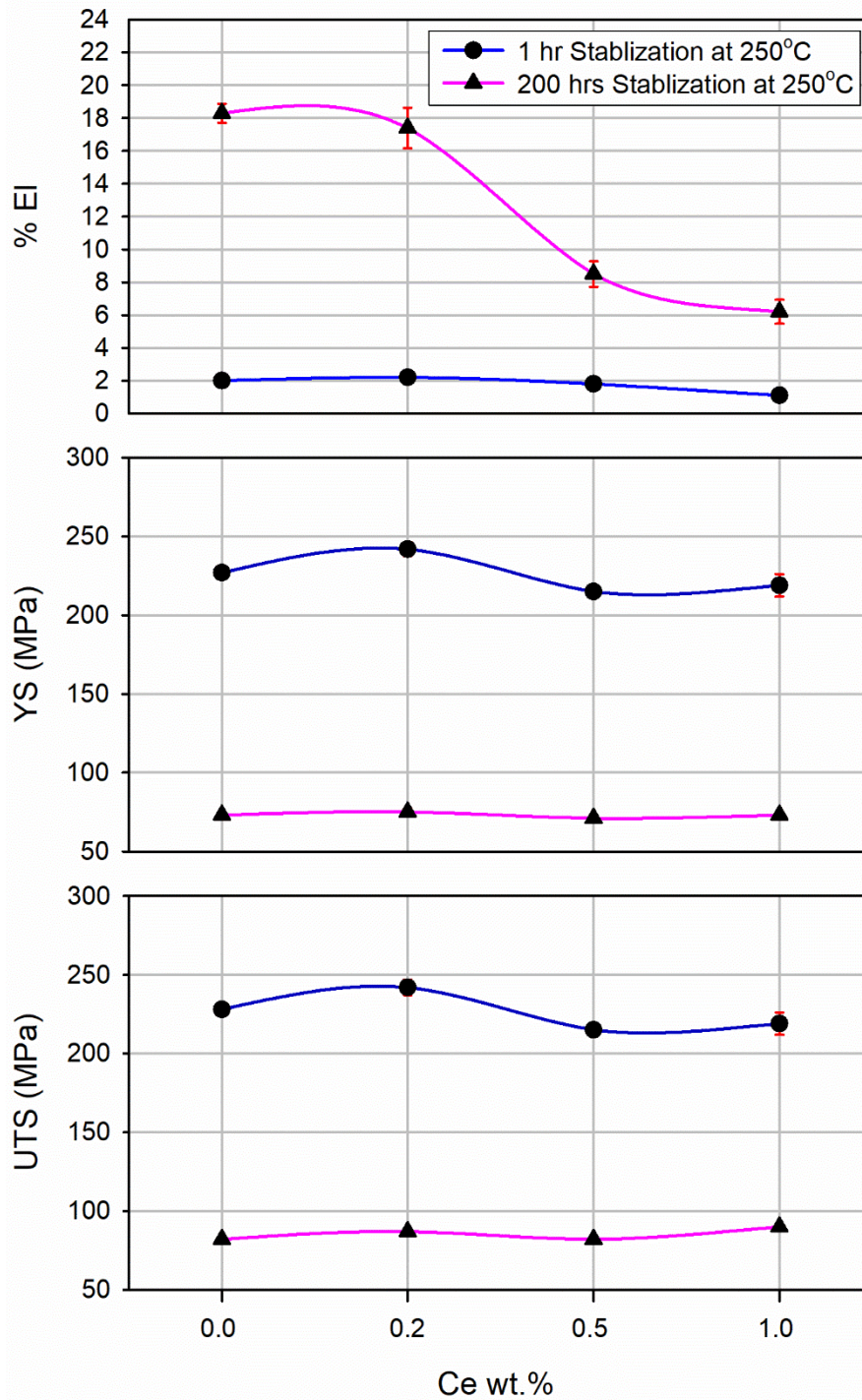
Figure 7.1 : Effect of Ce additions and stabilization time on the tensile properties (UTS, YS, and %El) of B0 alloys at elevated temperature 250 ºC.
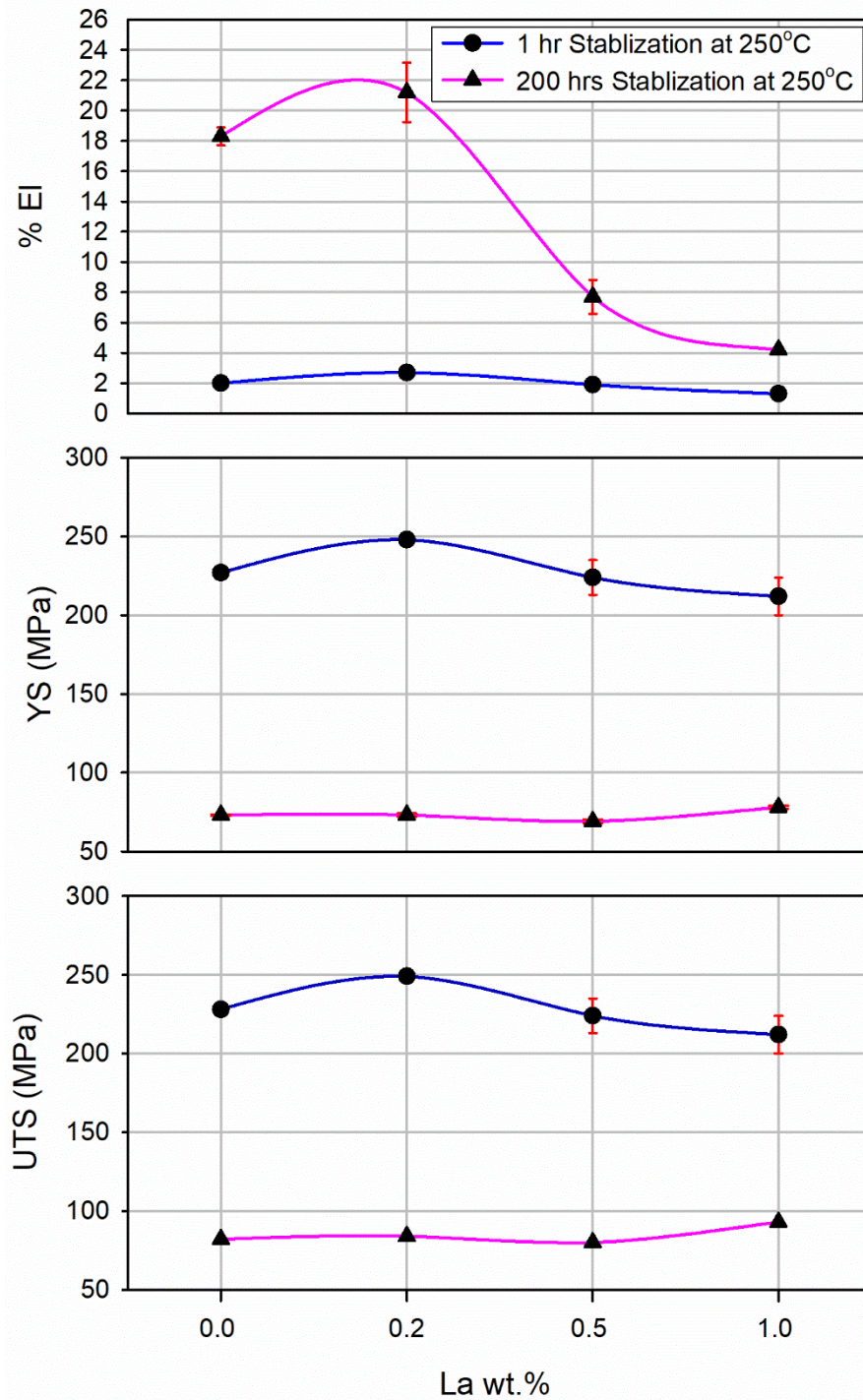
Figure 7.2 : Effect of La additions and stabilization time on the tensile properties (UTS, YS, and %El) of B0 alloys at elevated temperature 250 $^\circ$C.

7.1.2 Al-Si-Cu (D0) Alloy

Figure 7.3 and Figure 7.4 illustrate the impact of stabilization time and the different additions of Ce and La, respectively, on the tensile properties of T6 heat-treated D0 alloys. The UTS, YS and %El values of the D0 base alloy after 1 hour of stabilization at 250 ^{o}C prior to testing are 256 MPa, 256 MPa and 0.9% respectively. With 200 hrs of stabilization, the strength values are reduced to 95 MPa (UTS), and 78 MPa (YS), that is, by 63% and 69 %, respectively.

Regarding the influence of RE addition, the results presented in Figure 7.3 and Figure 7.4 show that the tensile properties of the D0 base alloy remain more or less the same even with the addition of Ce and La. In particular, with 0.2 wt.% Ce addition the D0 alloy exhibits a moderate increase in UTS and YS from 256 to 275 MPa and 256 to 275 MPa, respectively and a negligible drop in ductility from 0.9% to 0.8 %, as shown in Figure 7.3. Whereas with 0.2% La addition, Figure 7.4 indicates that the strength values increase from 256 to 271 MPa (UTS) and from 256 to 271 MPa (YS), with an increase in the %El from 0.9 % to 1.8 %. At the higher levels of RE (Ce/La) additions, the UTS and YS values slightly decrease by 10-22 MPa, while the ductility varies between 1.0 to 0.8 %.

With regard to the effect of 200 hrs stabilization, in general, the investigated alloy exhibit a negligible increase in UTS and YS with RE addition, as shown in Figure 7.3 and Figure 7.4. Upon 0.2 % Ce addition, the ductility changes from 10.4% to 8.6 %, whereas with 0.2% La addition, it drops from 10.4% to 7.3%. In case of higher RE additions (0.5 and 1.0 wt.%), Figure 7.3 reveals that the ductility drops to 8.1% and 6.1% in the case of Ce addition, and to 5.8% and 5.5%, in the case of La addition, as shown in Figure 7.4.
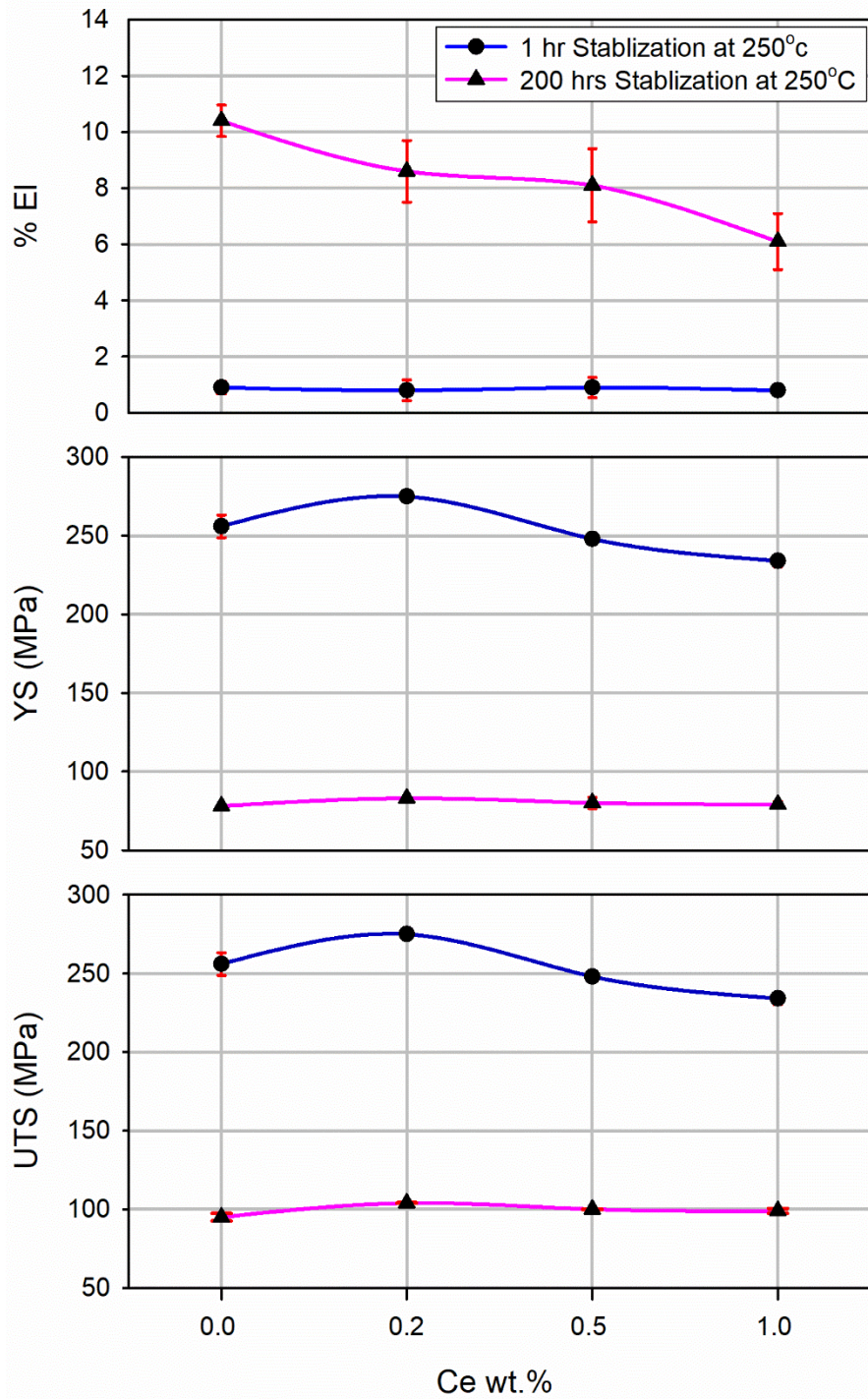
Figure 7.3 : Effect of Ce additions and stabilization time on the tensile properties (UTS, YS, and %El) of D0 alloys at elevated temperature 250 °C.
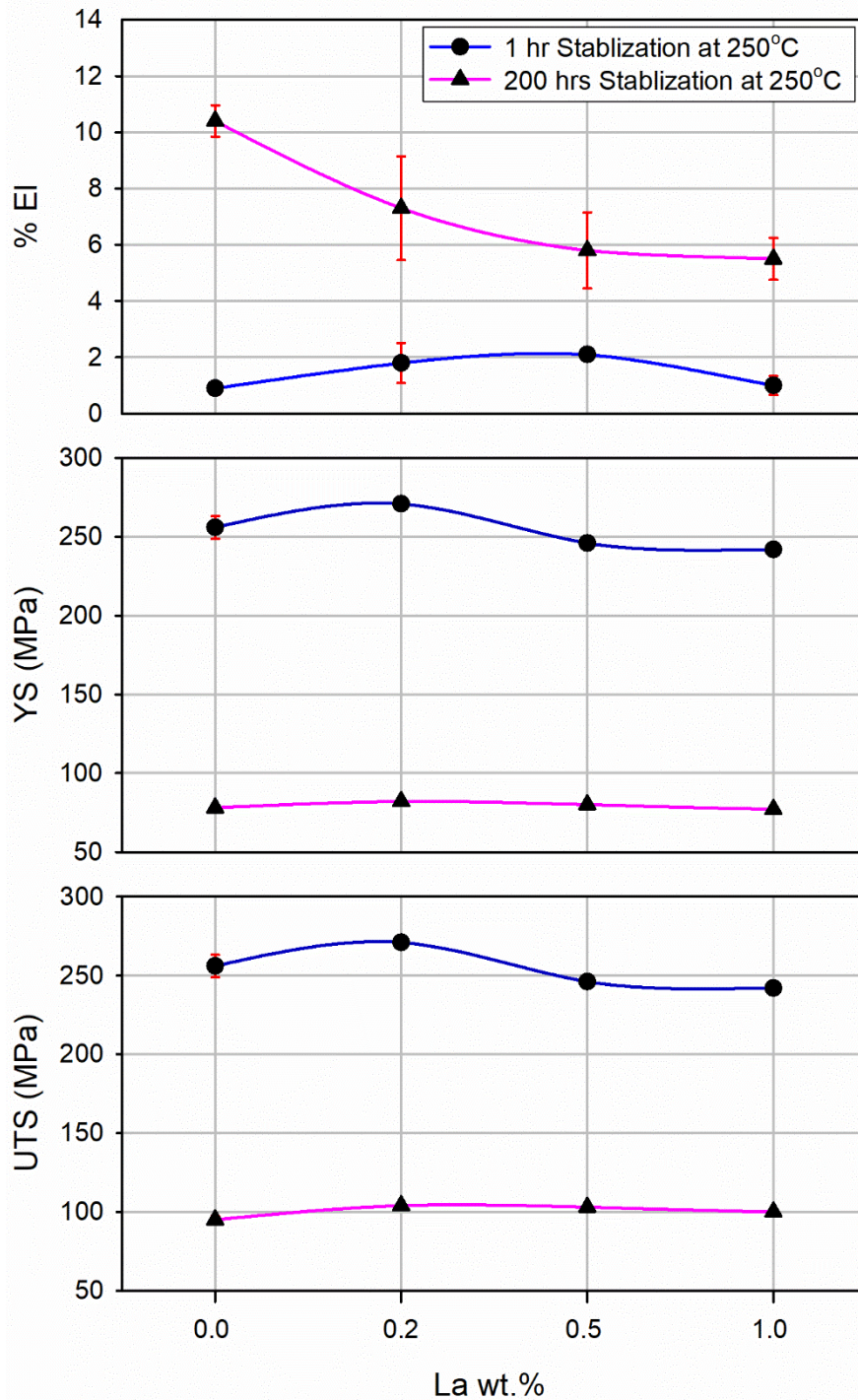
Figure 7.4 : Effect of La additions and stabilization time on the tensile properties (UTS, YS, and %El) of D0 alloys at elevated temperature 250 °C.

7.2 FRACTOGRAPHY RESULTS

Fractography is defined as the study of the fracture surfaces [185], the objective being to analyze the fracture features in order to relate the topography of the fracture surface to the causes and/or basic mechanisms of fracture. A study of the characteristics of fracture surfaces is often carried out using (i) optical microscopy, when a low magnification of the fracture surface is adequate, and (ii) scanning electron microscope (SEM), when very fine details of the fracture surface, e.g., dimples and microvoids, are required to be observed [186].

In order to arrive at a better understanding of the high temperature tensile test results, both optical microscopy and SEM techniques were used, to examine the facture surfaces of selected high temperature tensile-tested samples. In each alloy, samples with the highest levels (1.0 wt.%) of RE (Ce/La) were examined corresponding to 200 hrs stabilization at 250 $^{\circ}$C. The fracture surfaces were analyzed based on the features observed in relation to the silicon particles, and the α-Fe and RE (Ce/La) intermetallic phases present in the alloys.

7.2.1 SEM Fractography

The great advantages of employing a scanning electron microscope is its ability to examine specimens at low magnifications and then enlarge regions of special interest for examination at very high magnifications. Both backscattered electron and secondary electron modes of operation are normally used for fractographic purposes. The secondary electron image (SE) offers a better resolution, whereas the backscattered electron image (BSE) offers an improved image contrast that is necessary in the case of smooth specimens and at low magnifications. The high image contrast in the backscattered mode is accompanied by EDS analysis. The fracture surface of selected samples of B0 and D0 alloys containing 1.0 wt.% (Ce/La) additions are presented in this section. Backscattered and secondary electron images

were taken from the central region of the fracture surface and the crack initiation edge, accompanied by EDS analysis, all of which was carried out with a view to investigating the role of the phases in the fracture process of investigated alloys.

7.2.1.1   Al-Cu (B0) Alloy

SEM images of the fracture surfaces of the T6-treated B0 base alloy sample tested after 200 hrs stabilization at 250 ^{o}C are presented in Figure 7.5. The features exhibited in the secondary electron image shown in Figure 7.5(a) revealed the presence of microvoids and a fine and uniformly distributed dimples, indicating that the sample underwent a large amount of plastic deformation prior to fracture. The inset in the upper left corner of Figure 7.5(a) shows a view of how the fracture appears in the actual sample (45° shear angle). These observations are in keeping with the high temperature tensile test results, as the B0 base alloy exhibited high ductility, 18%. The backscattered electron image in Figure 7.5(b), which is an enlarged images of the circled area in (a), illustrates the presence of α-Fe intemettlllic particles on the fracture surface, as was confirmed by the corresponding EDX spectrum shown in Figure 7.5(c). Solution heat treatment of this alloy resulted in the dissolution of Al$_2$Cu phase, as deduced from the absence of any Cu peaks in Figure 7.5(c). Also, Figure 7.5(b) shows a presence of crack within α-Fe intemettlllic which confirms how crack formation is facilitated when the α-Fe phase is present in the microstucutre.
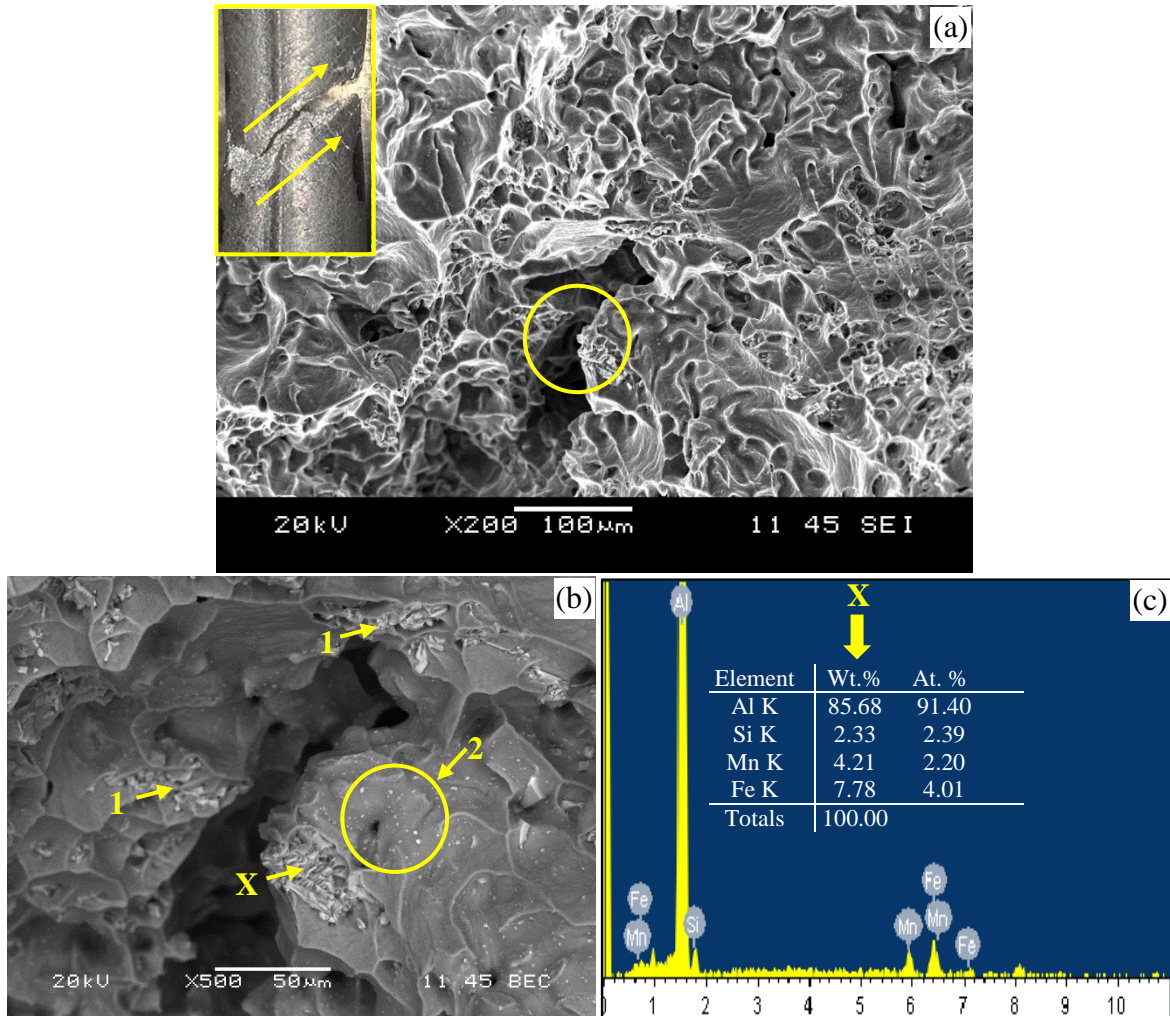
Figure 7.5: (a) Secondary electron image showing the fracture surface of T6-treated B0 base alloy; (b) enlarged BSE image of circled area in (a); (C) EDS spectrum corresponding to the α-Fe phase (b).The arrows indicate (1) α-Fe phase, and (2) Al₂Cu precipitation.

In the case of T6-treated B0 alloy containing 1.0 wt.% Ce and obtained after 200 hrs stabilization at 250°C, the SEM images shown in Figure 7.6 revealed considerably different characteristics. The fracture surface in Figure 7.6(a) shows large sized dimples, rather than the uniformly distributed dimples that were observed in Figure 7.5(a) for the B0 base alloy. The cleavage observed on the fracture surface in Figure 7.6(a) is characteristic of a brittle fracture. Figure 7.6(b) shows that addition of 1.0 wt.% Ce leads to the formation of a Ce containing intermetallic phase (Al-Si-Cu-Ce), observed in the form of bright irregularly

shaped particles on the fracture surface, as confirmed by the corresponding EDX spectrum shown in Figure 7.6(c). In addition, Figure 7.6(c) also reveals the existence of α-Fe intermetallic and Al_2Cu precipitates. The presence of cracks within the Ce-based intermetallic and α-Fe phase noted in Figure 7.6(b) indicated how crack formation is facilitated when these intermetallic phases are present in the microstructure.
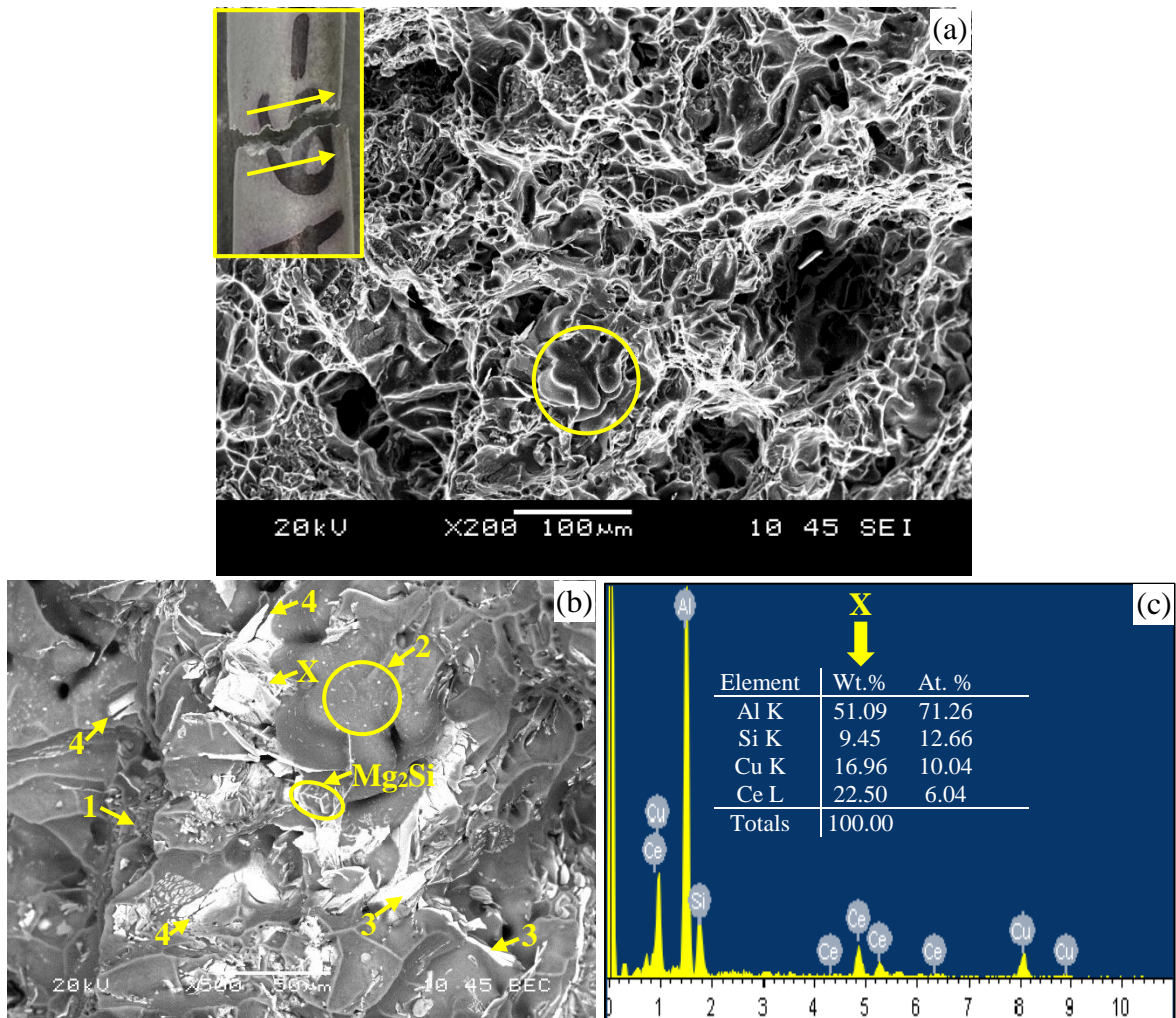
Figure 7.6: (a) Secondary electron image showing the fracture surface of T6-treated B0 alloy with 1.0 wt.% Ce; (b) enlarged BSE image of circled area in (a); (C) EDS spectrum corresponding to the Ce containing intermetallic (AlSiCuCe) phase. The arrows indicate (1) α-Fe phase, (2) Al_2Cu precipatation, (3) AlSiCuCe phase, and (4) cracked particles.

Regarding the 1.0 wt.% La-containing T6-heat treated alloy samples, tested after 200 hrs stabilization at 250 $^{\circ}$C, the fracture surface shown in Figure 7.7(a) consists of ductile dimples and small brittle fractures compared to the B0 base alloy. A high magnification BSE image of the circled area in (a) is presented in Figure 7.7(b), where the fracture surface reveals the presence of La-containing intermetallic (Al-Si-Cu-La) particles, as confirmed by the corresponding EDX spectrum show in Figure 7.7(c). As noted from Figure 7.7(b), the α-Fe intermetallic phase and Al_2Cu precipatates were also observed. In addition, Figure 7.7(b) shows the existence of cracks within La-based intermetallic and α-Fe phase particles, indicating once more that crack formation is facilitated when both the α-Fe phase and La based intermetallic are present in the microstrucutre.
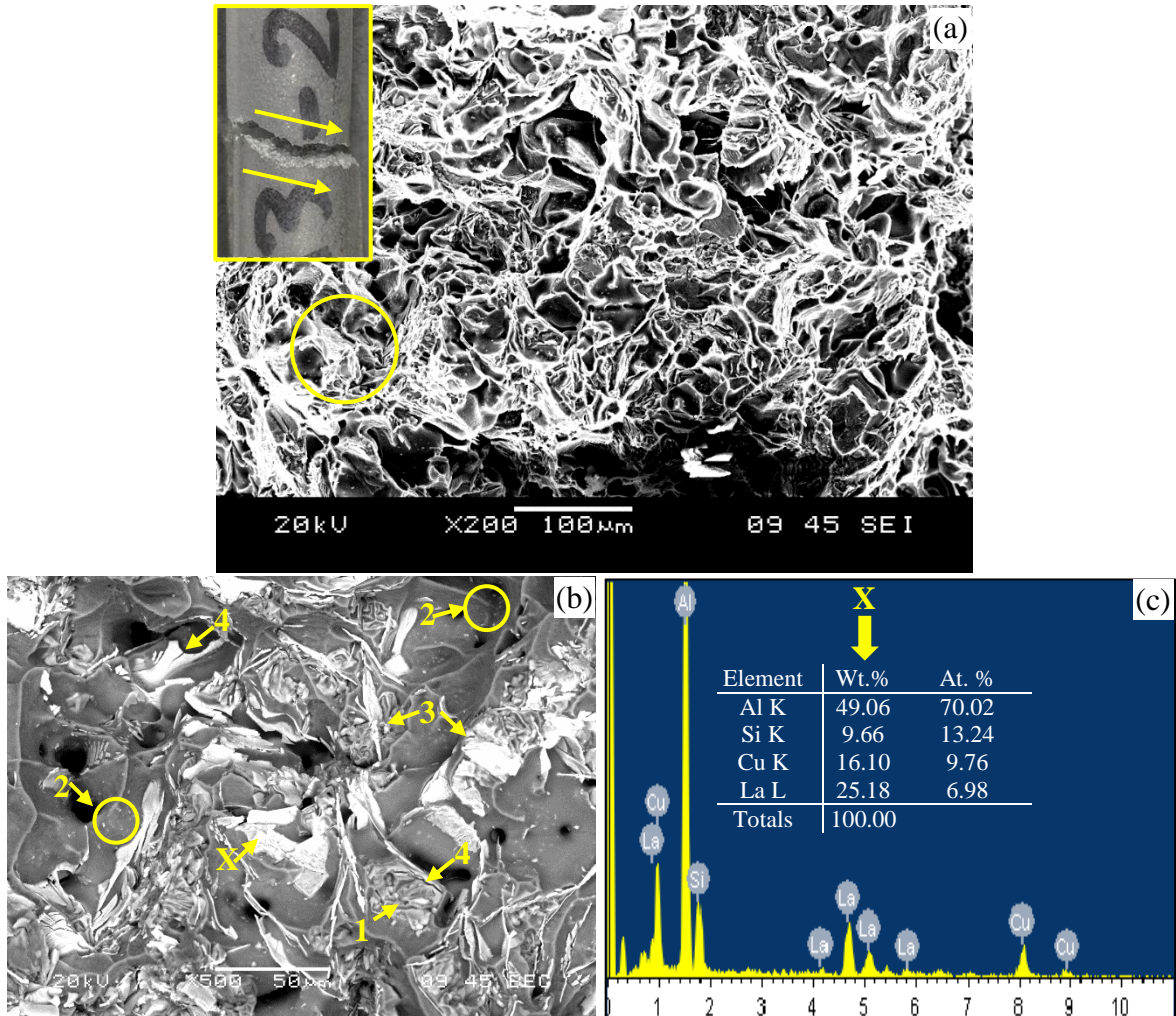
Figure 7.7: (a) Secondary electron image showing the fracture surface of T6-treated B0 alloy with 1.0 wt.% La; (b) enlarged BSE image of the circled area in (a); (C) EDS spectrum corresponding to La containing intermetallic (AlSiCuLa) phase. The arrows indicate (1) α-Fe phase, (2) Al_2Cu precipatation, (3) AlSiCuLa phase, and (4) cracked particles.

7.2.1.2 Al-Si-Cu (D0) Alloy

The SEM images taken from T6-heat treated D0 base alloy tested at high temperature after stabilization for 200 hrs at 250°C are presented in Figure 7.8. Compared to the B0 base alloy, the fracture surface in Figure 7.8(a) exhibits several instances of cleavage patterns. This cleavage results from the debonding of Si particles from Al matrix, which is the main mode of crack initiation reported in the Al-Si alloys [187].

The inset at the upper left corner of Figure 7.8(a) shows how the fracture propagated in the actual tensile-tested samples (33 ^{o} shear angle). The BSE image in Figure 7.8(b) reveals the existence of the α-Fe intemettlllic phase on the fracture surface, as was confirmed by the corresponding EDX spectrum in Figure 7.8(c). The presence of Si particles is also observed in Figure 7.8(b). Also, the crack observed in the α-Fe intermetallic particle indicates how crack formation is facilitated when these α-Fe phase particles are present in the microstucutre.
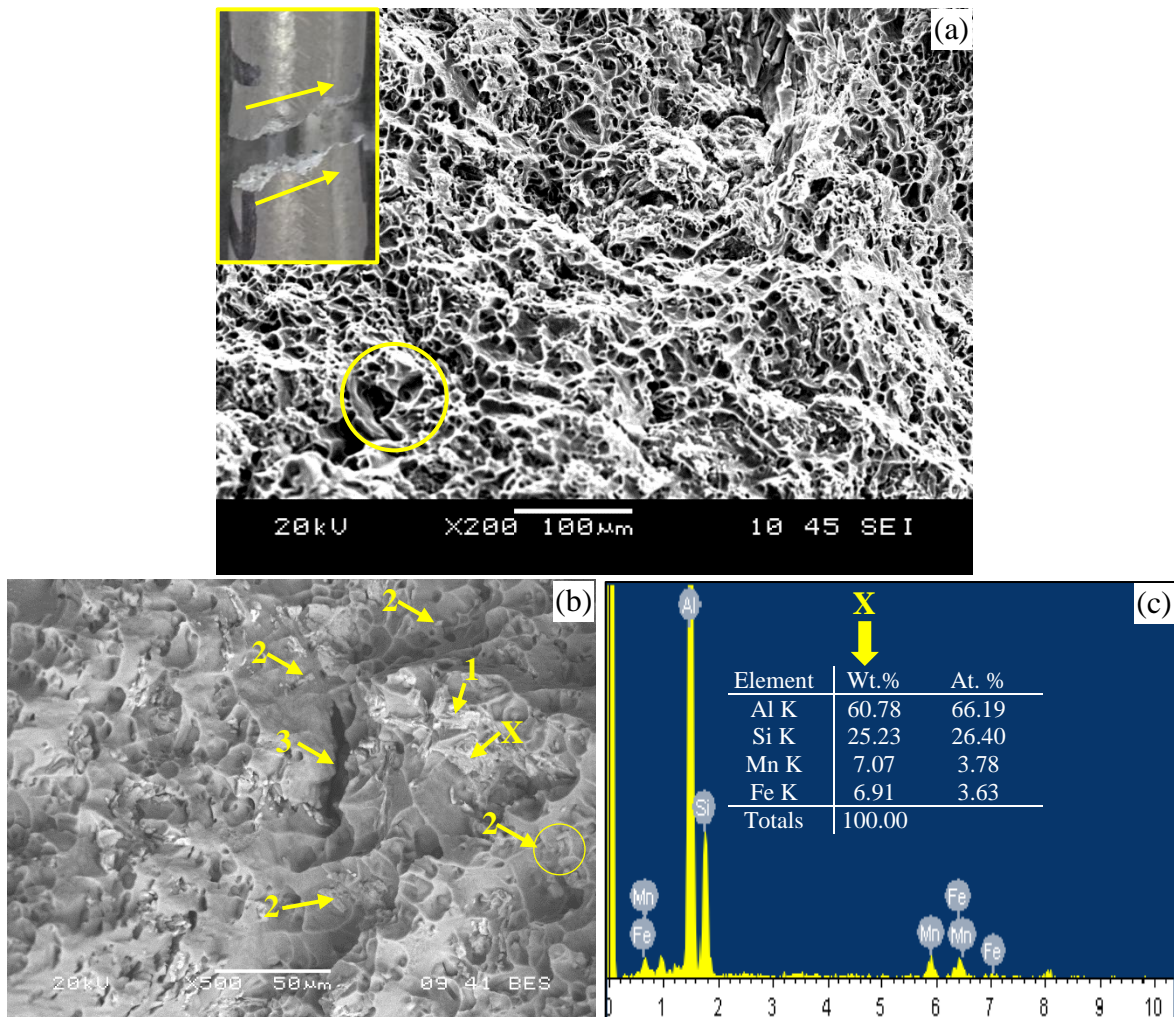
Figure 7.8: (a) Secondary electron image showing the fracture surface of T6-treated D0 base alloy; (b) enlarged BSE image of circled area in (a); (c) EDS spectrum corresponding to the α-Fe phase in (b). The arrows indicate (1) α-Fe phase, (2) Si, and (3) crack.

Figure 7.9 shows the SEM images of the T6-treated D0 alloy sample containing 1.0 wt.% Ce, tested after stabilization for 200 hrs at 250 $^{\circ}$C. It is noted that the addition of Ce has increased the size of dimples, and that the fracture surface is covered by cleavage planes, as seen from Figure 7.9(a). The BSE image in Figure 7.9(b) reveals the presence of several large bright particles of Ce-containing intermetallic phase (AlSiCuCe) on the fracture surface, as confirmed by the EDS spectrum shown in Figure 7.9(c). Cracks observed within some of these particles in Figure 7.9(b), indicates the role they play in the fracture process.

Element	Wt.%	At. %
Al K	30.72	53.97
Si K	7.94	13.40
Cu K	29.12	21.72
Ce L	32.23	10.90
Totals	100.00	
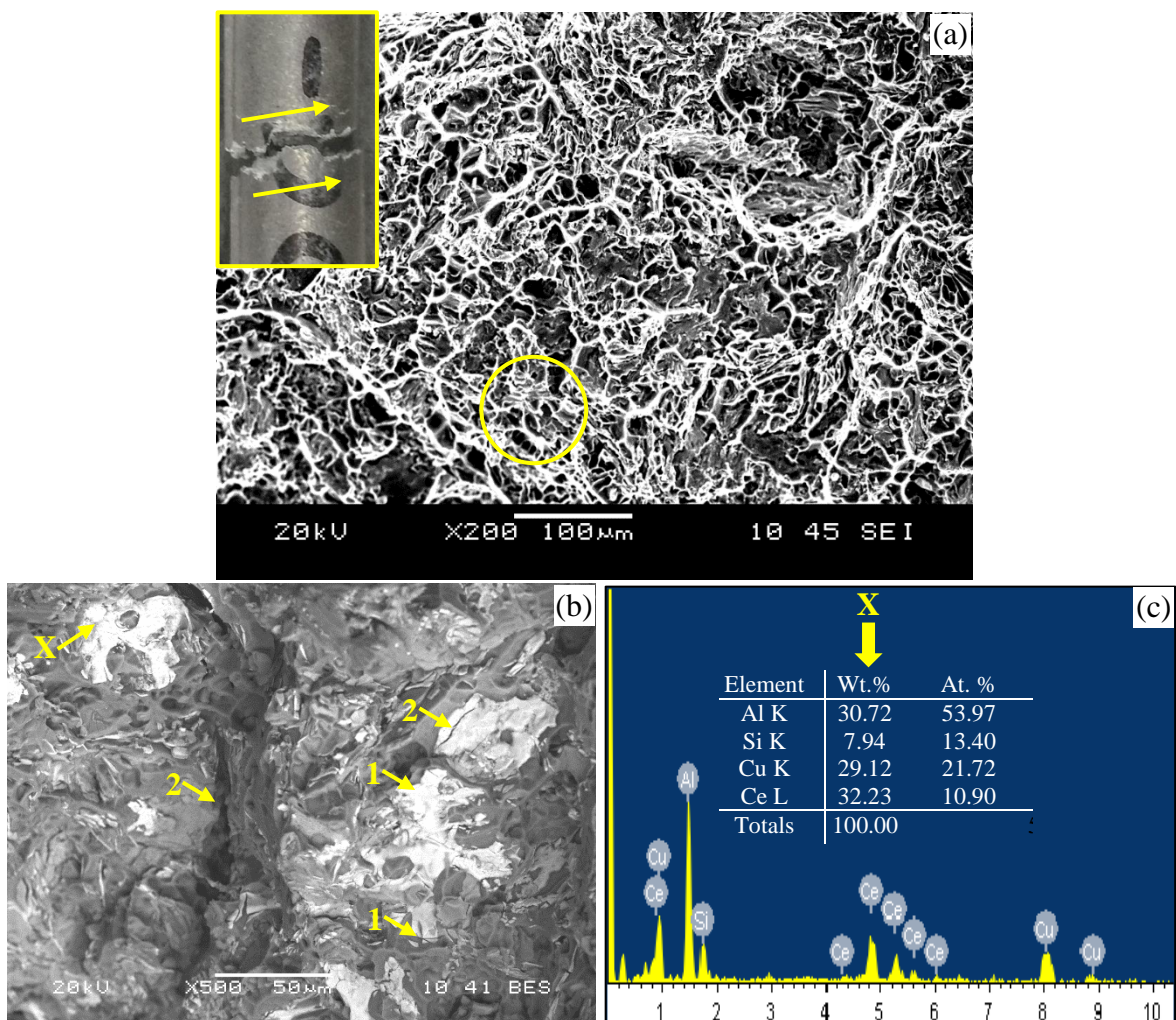
Figure 7.9: (a) Seconday electron images showing the fracture surface of T6-treated D0 alloy with 1.0 wt.% Ce; (b) enlarged BSE image of circled area in (a); (c) EDS spectrum corresponding to Ce-containing intermetallic (AlSiCuCe). The arrows indicate (1) AlSiCuCe phase, and (2) cracks.

Figure 7.10 exhibits the SEM images of the T6-treated D0 alloy with 1.0 wt.% La tested after stabilization for 200 hrs at 250°C. As can be seen from Figure 7.10(a), the fracture surface in this case is brittle in nature, and the quasi-cleavage fracture can be observed on the outer surface of the tensile-tested specimen shown in the inset, leading to lower elongation value compared to the base alloy. The EDS spectrum in Figure 7.10(c), confirms the presence of the La-containing intermetallic compounds seen in Figure 7.10(b). The existence of cracks within the La-based intermetallic phase which means that the crack formation is facilitated when such intermetallic particles are present in the microstucutre. Figure 7.10(b) also shows cracks within La based intermetallic phase which means that this phase is responsible for material fracture during the tensile test .
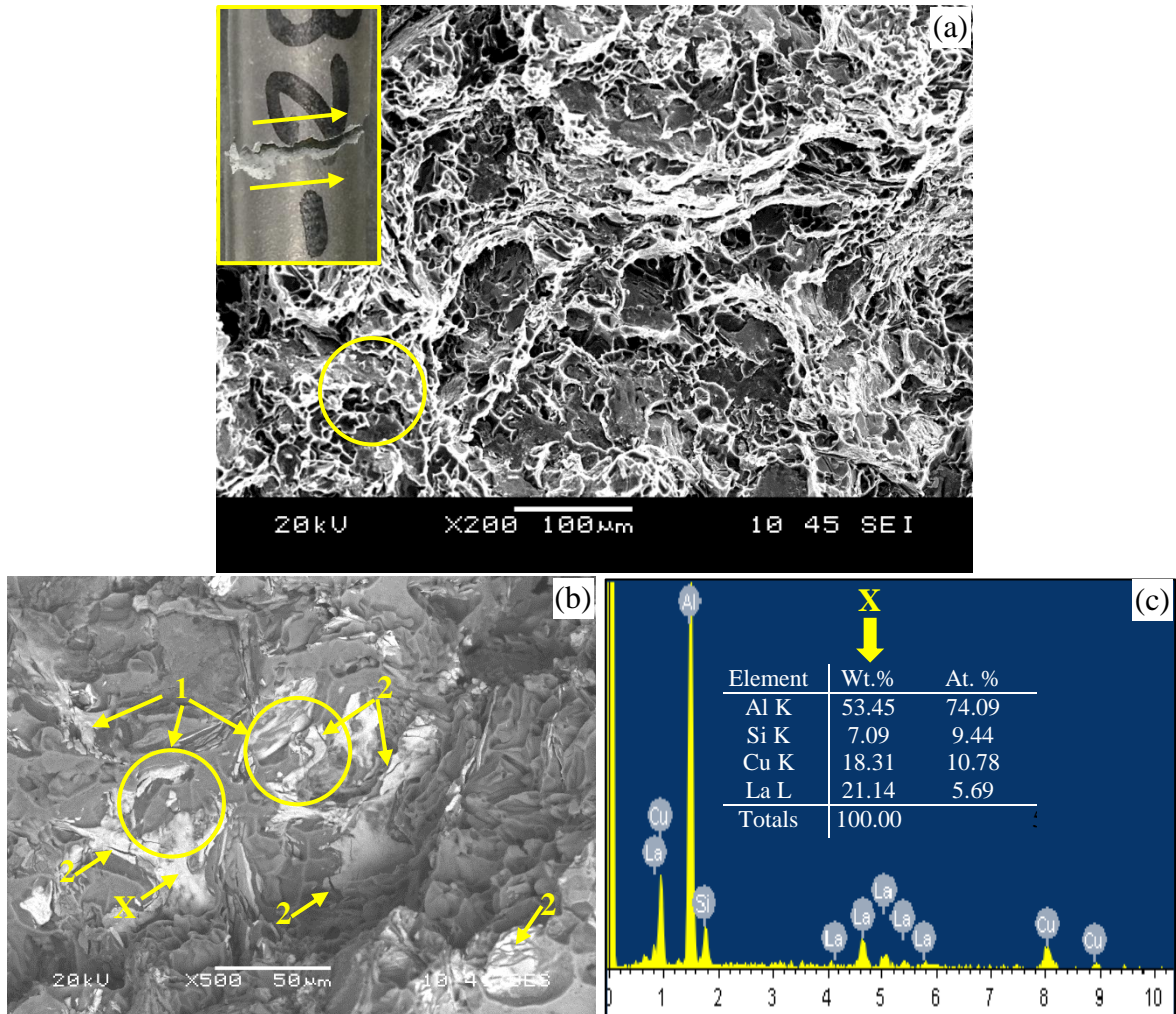
Figure 7.10: (a) Secondary electron image showing the fracture surface of T6-treated D0 alloy with 1.0 wt.% La; (b) enlarged BSE image of circled area in (a); (C) EDS spectrum corresponding to La-containing intermetallic (AlSiCuLa). The arrows indicate (1) AlSiCuLa phase, and (2) cracks.

7.2.2 Examination of Longitudinal Sections beneath the Fracture Surface

In addition to SEM examination of the fracture surface, it is also quite useful to examine the fracture profile on sections perpendicular to the fracture surface. This can be carried out easily using an optical microscope. In this way, the origin of the fracture can be examined to determine if important microstructural abnormalities are present that either caused or contributed to fracture initiation. It is also possible to determine if the fracture path at the initiation site is transgranular or intergranular and to determine if the fracture path is

184

specific to any phase or constituent present [188]. Some examples of the longitudinal sections of the B0 and D0 alloy samples containing 1.0 wt.% Ce/La samples are presented in this section with a view to further clarify the fracture process in these samples as their SEM fractographs did not display as good a phase contrast.

7.2.2.1   Al-Cu (B0) Alloy

Figure 7.11 shows the longitudinal section beneath the fracture surface of the T6-treated B0 base alloy after 200 hrs stabilization at 250 ℃. Figure 7.11(a) shows that the sample edge is curved and rounded which indicates a ductile mode of ruptures. Figure 7.11(a) also shows interdendritic shrinkage and extended cracks from the aluminum matrix can be found on the fracture surface. By magnifying the crack, as shown in Figure 7.11(b, c), the breakage of α-Fe phase can be observed adjacent to the cracks. It can be inferred that when alloy B0 receives an external force, α-Fe phase breaks easily and forms a crack initiation point. When alloy B0 continues to receive external force, the combination of crack growth and shrinkage accelerates the material fracture, resulting in a fracture surface with cracks and interdendritic shrinkage.
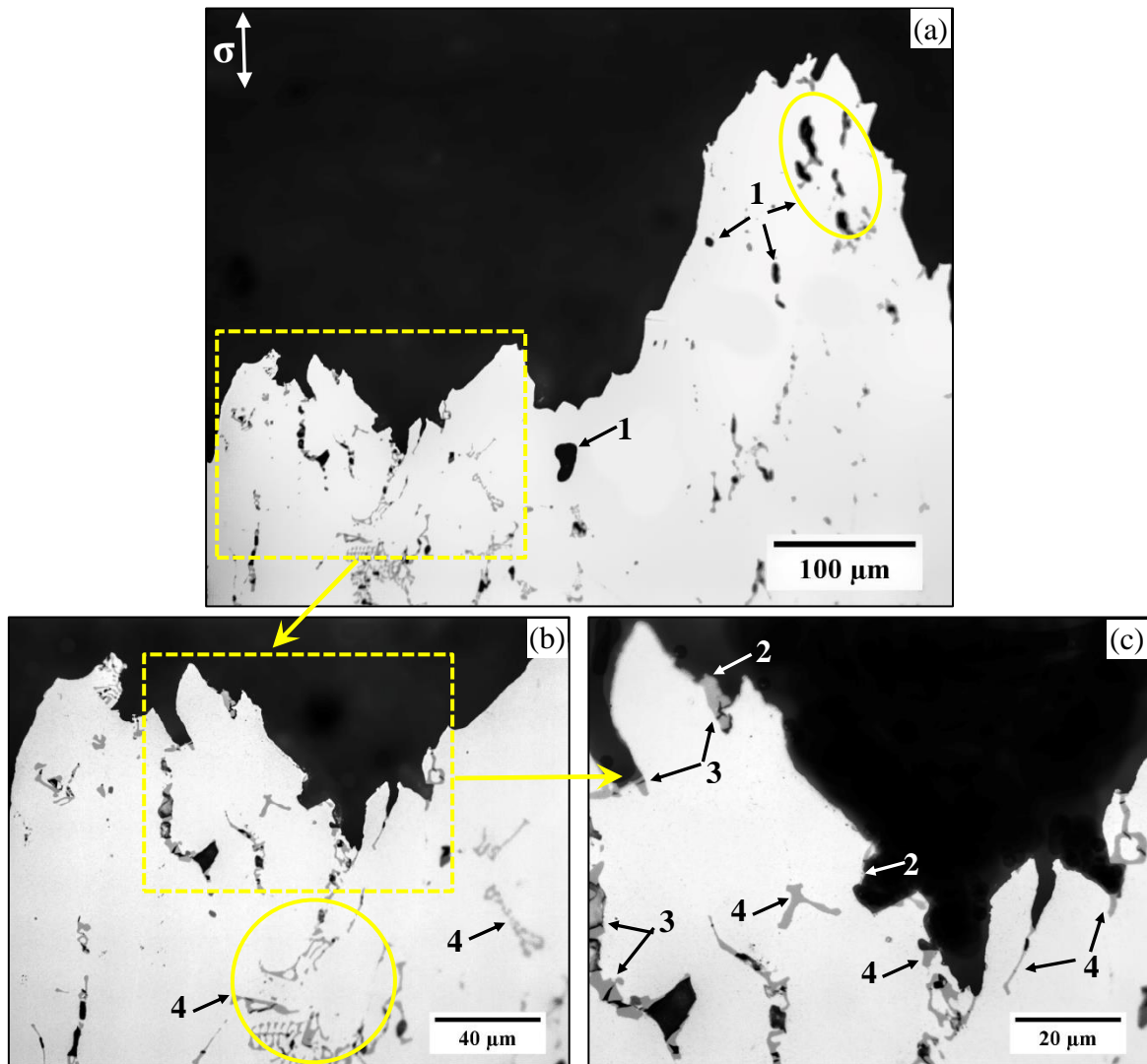
Figure 7.11: Optical micrographs showing longitudinal sections below the fracture surface of B0 alloy, taken at: (a) low, (b) high, and (c) very high magnification. The arrows indicate (1) inderdendritic shrinkage, (2) debonding crack, (3) intercrystalline crack, and (4) α-Fe phase.

The optical micrographs presented in Figure 7.12 show the polished longitudinal section beneath the fracture surface of the T6-heat treated B0 alloy sample containing 1.0 wt.% Ce and tested after 200 hrs stabilization at 250 °C. Figure 7.12(a) shows that the fracture edges are sharp which indicates a relatively a brittle mode of fracture compared to alloy without RE additions. Figure 7.12(a) also illustrates that the fracture path of the tensile samples passed through the α-Al, α-Fe phase and Ce-containing intermetallic compounds.

High magnification micrographs of the crack area, Figure 7.12(b, c) show that near and beneath the fracture surfaces, many micro-cracks in α-Fe and the Ce-containing intermetallic particles area clearly observed. These observations indicate that these intermetallics are the main sources of stress concentration in the alloy.
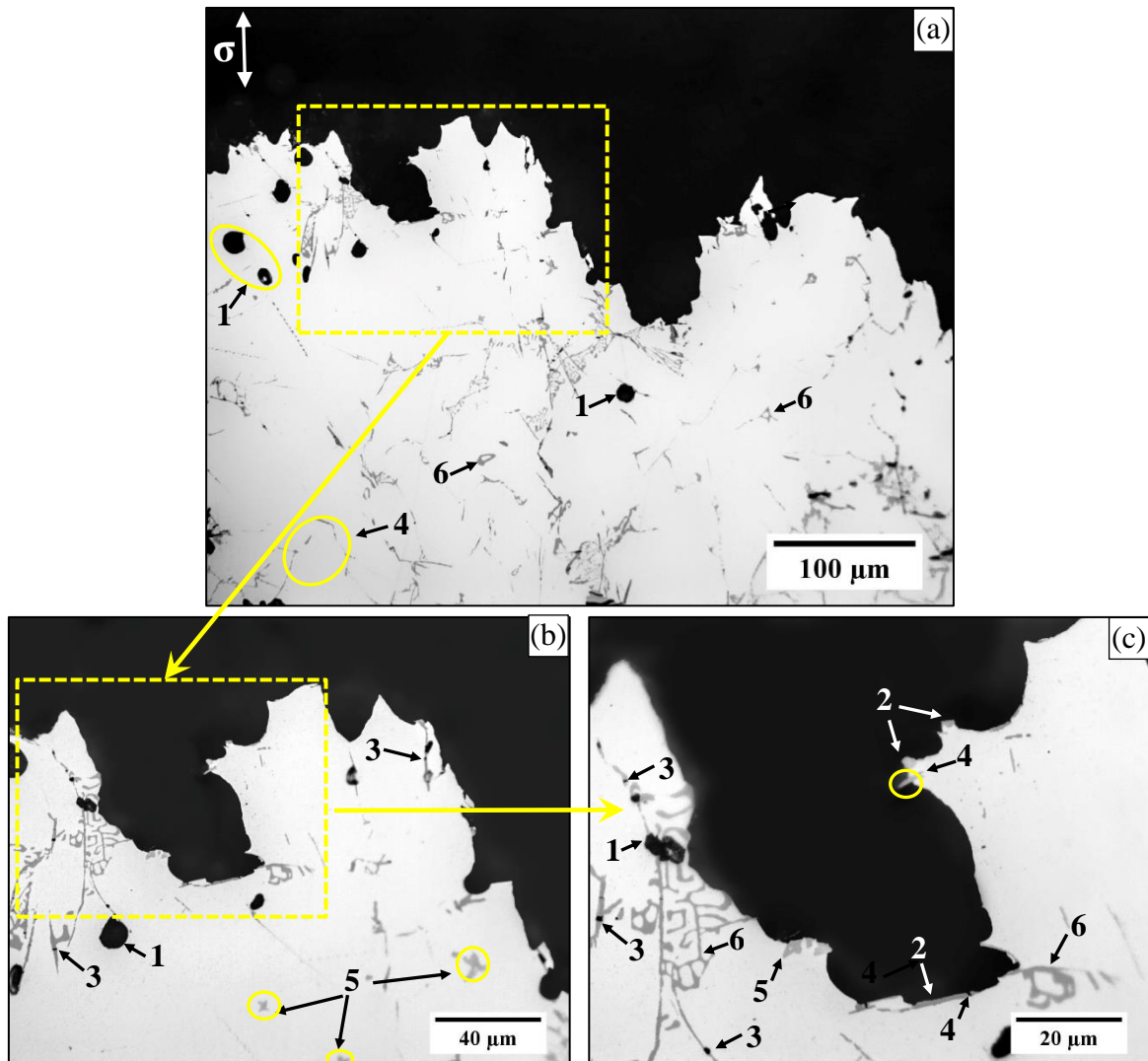
Figure 7.12: Optical micrographs showing longitudinal sections below the fracture of B0 alloy with 1.0 wt.% Ce, taken at: (a) low, (b) high, and (c) very high magnification. The arrows indicate (1) inderdendritic shrinkage, (2) debonding crack, (3) intercrystalline crack, (4) white Ce-intermetallic phase, (5) grey Ce-intermetallic phase, and (6) α-Fe phase.

Figure 7.13 depicts the optical micrographs of the longitudinal section beneath the fracture surface of T6-heat treated B0 alloy containing 1.0 wt.% La and tested at 250 ℃ after 200 hrs stabilization at 250 ℃. Figure 7.13(a) shows that the final fracture path tends to propagate through the α-Al matrix, α-Fe phase and La-containing intermetallic particles. Fracture particles of these intermetallic phases are seen in Figure 7.13(b, c). As the circled areas delineated by A in Figure 7.13(c) reveal, Ce-containing intermetallic particles with a small aspect ratio have a lower probability to cracking. These indicates that the fracture behaviour of Ce-containing intermetallic particles is based on their geometry, which mean that compounds with acicular geometry are easier to crack and separate from Al matrix under applied loads. In conclusion the combination effects of fracture of α-Fe and La-containing intermetallic compounds are key factors in the failure process of the 1.0 wt.% La-containing B0 alloy.
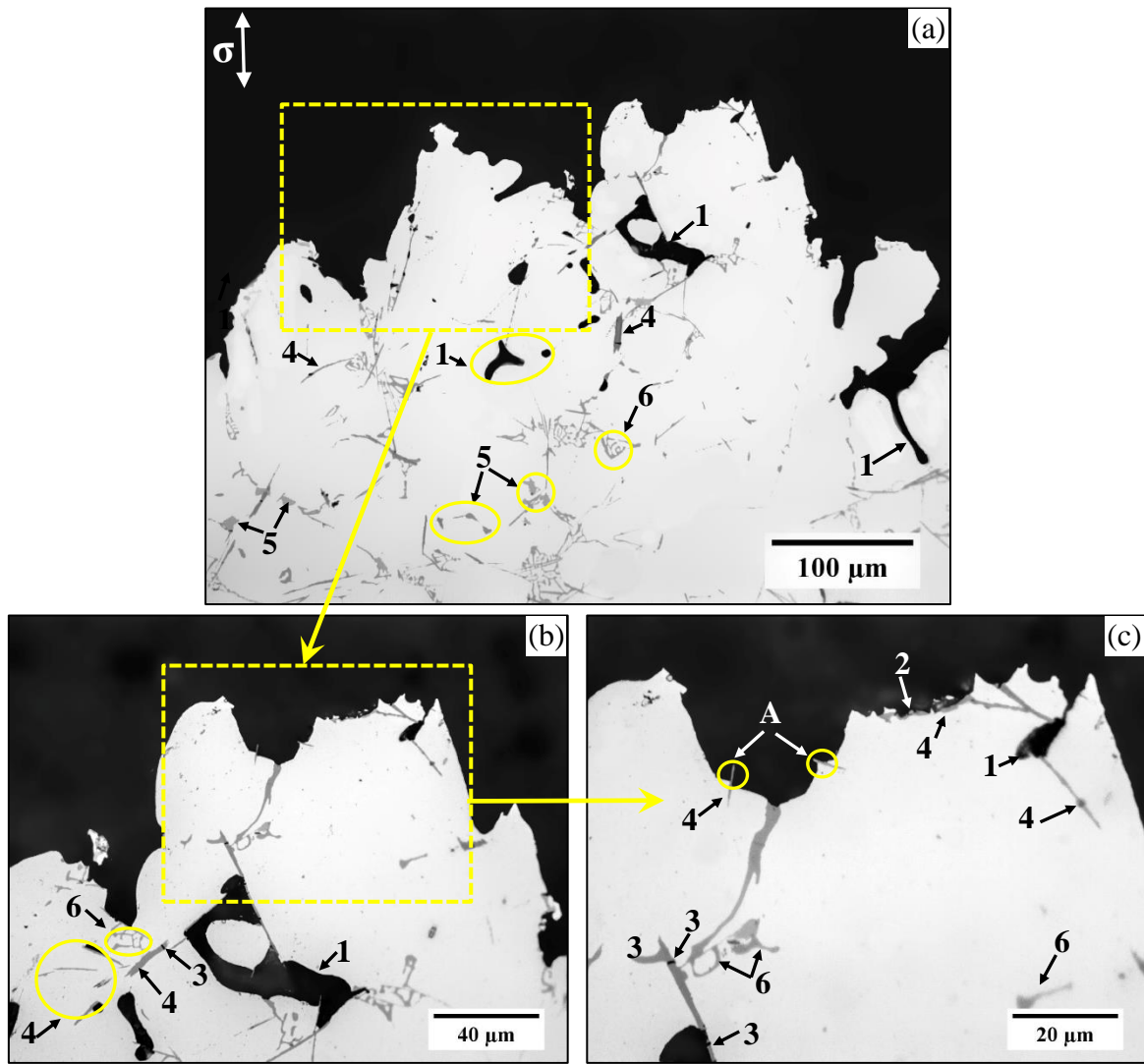
Figure 7.13: Optical micrographs showing longitudinal sections below the fracture surface of B0 alloy with 1.0 wt.% La, taken at: (a) low, (b) high, and (c) very high magnification. The arrows indicate (1) inderdendritic shrinkage, (2) debonding crack, (3) intercrystalline crack, (4) white La-intermetallic phase, (5) grey La-intermetallic phase, and (6) α-Fe phase.

7.2.2.2 Al-Si-Cu (D0) Alloy

Figure 7.14 shows the optical micrographs of the longitudinal section beneath the fracture surface of the T6-treated D0 base alloy sample, tested after 200 hrs stabilization at 250 ^{o}C. It can be seen from Figure 7.14(a) that the fracture surface profile is sharp, which indicates a brittle mode of ruptures compared to the case of the B0 Alloys. Figure 7.14(b) shows that the specimen fractured mainly across α-Al, eutectic silicon and α-Fe phases. At still higher magnification, Figure 7.14(c) reveals the debonding and inter-crystaline crack of eutectic silicon particles and α-Fe phase at, and beneath the fracture surface. Near the fracture surface, the eutectic silicon particles show inter-crystalline cracking, with the crack direction normal to the tensile direction. It worth noting that most of small, rounded eutectic silicon particles are not cracked, whereas the longish rod-like eutectic silicon particles are prone to crack easily. The cracks may occur anywhere in the particle. The cracking behavior of eutectic silicon particles are quite similar to that reported by Zhu et al.[130].
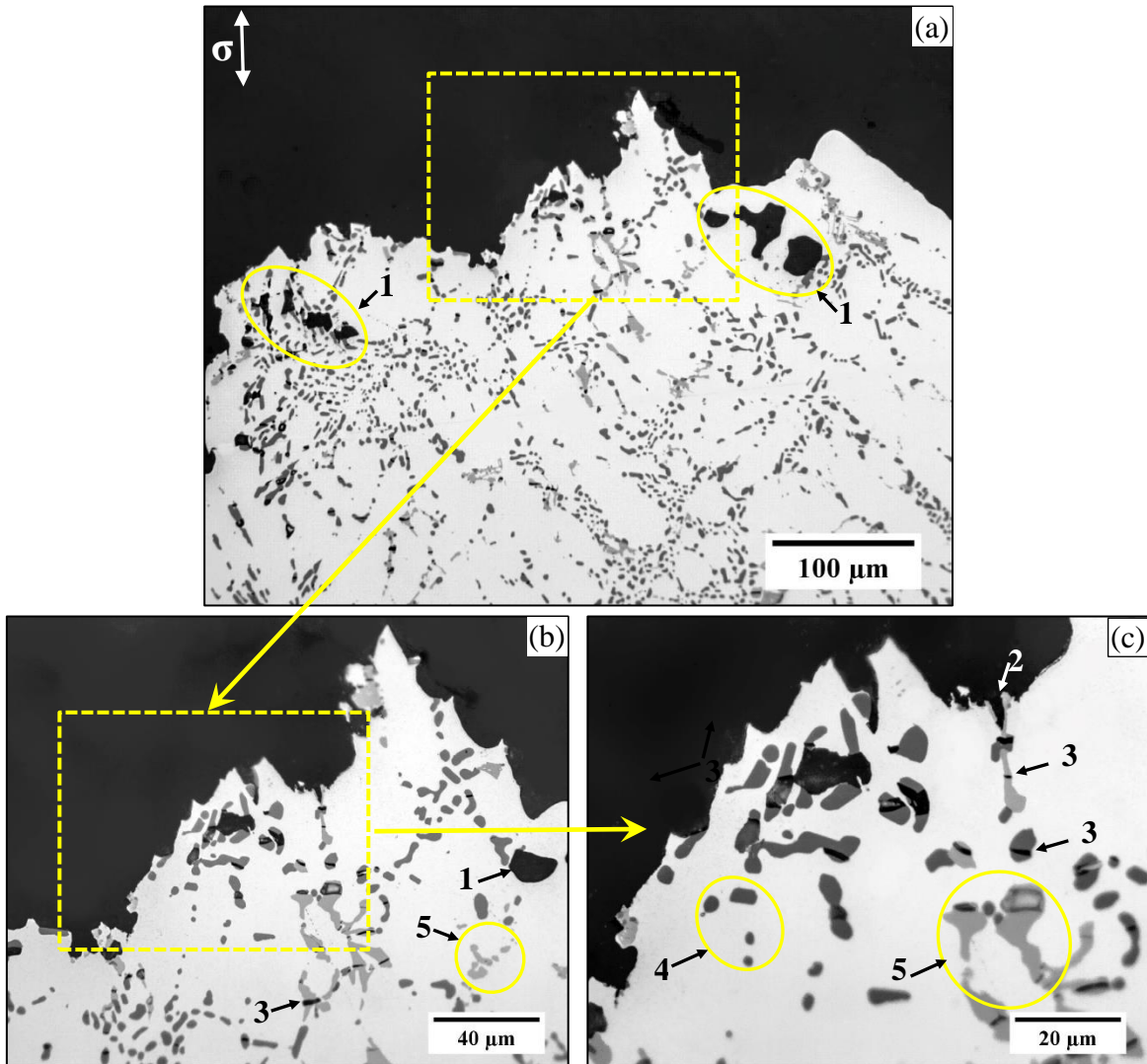
Figure 7.14: Optical micrographs showing longitudinal sections below the fracture surface of T6-treated D0 base alloy, taken at: (a) low, (b) high, and (c) very high magnification. The arrows indicate (1) inderdendritic shrinkage, (2) debonding crack, (3) intercrystalline crack, (4) round eutecti Si particles, and (5) α-Fe phase.

Figure 7.15 shows optical micrographs of the longitudinal section beneath the fracture surface of the T6-treated D0 base alloy with 1.0% Ce and tested after 200 hrs stabilization at 250 °C. Figure 7.15(a) reveals that the fracture path traverses mainly through the α-Al matrix, and the eutectic silicon, α-Fe phase and Ce-containing intermetallic particles in the interdendritic regions. Figure 7.15(a) also shows that the fracture surface edge is sharp, which indicates a brittle mode of ruptures, compared to the D0 base alloy without RE

191

additions. The fracture or debonding of Ce-containing intermetallic particles can be seen in the fracture area, which means that these intermetallic compounds influence the tensile failure process (Figure 7.15(b)). As may be seen in Figure 7.15(c), the fracture of the Ce-containing intermetallic particles depends on their average aspect ratio and roundness values, so that the particles with a large aspect ratio value would tend to crack easily.
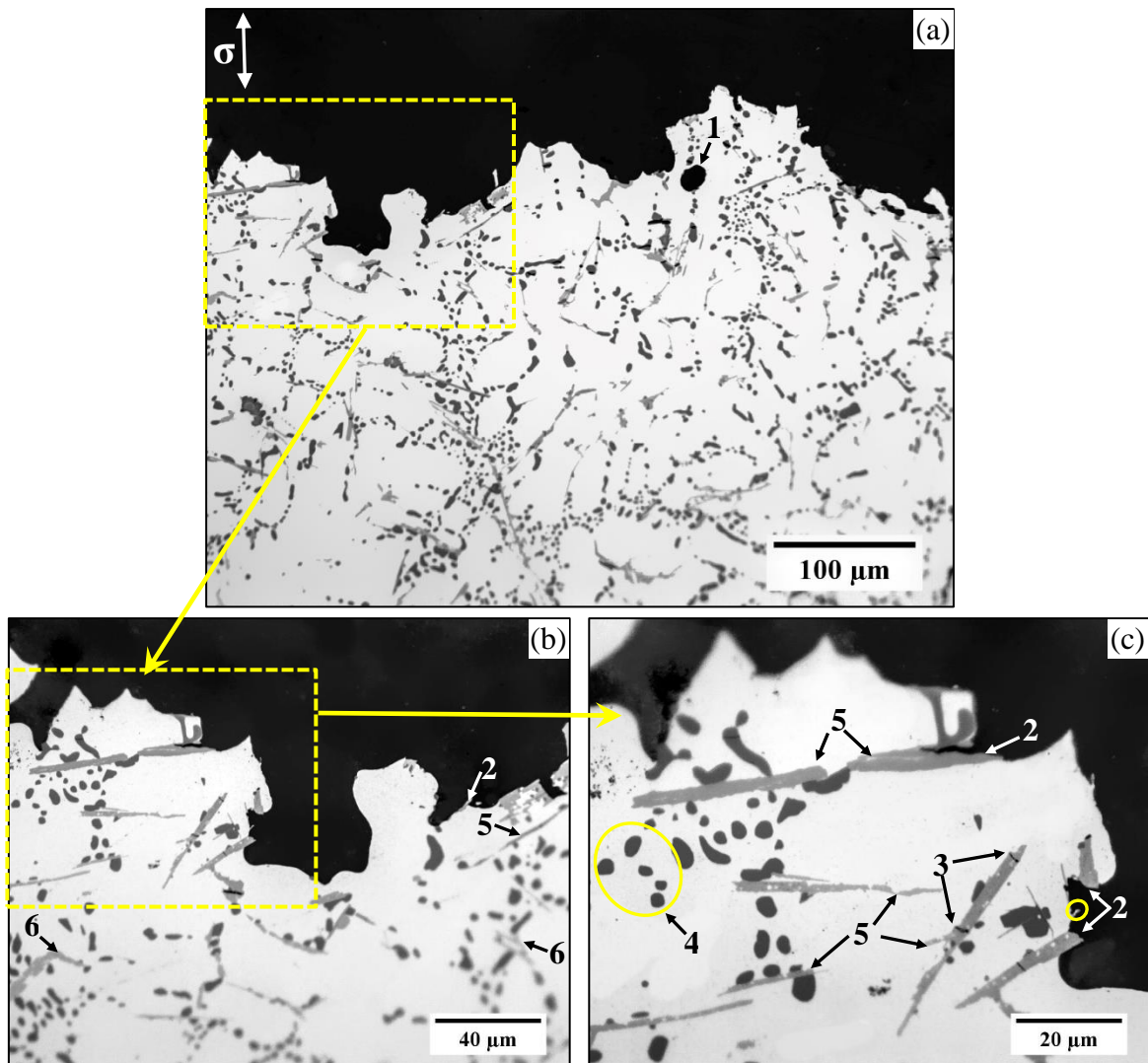
Figure 7.15: Optical micrographs showing longitudinal sections below the fracture surface of T6-treated D0 base alloy with 1.0 wt.% Ce, take at: (a) low, (b) high, and (c) very high magnification. The arrows indicate (1) inderdendritic shrinkage, (2) debonding crack, (3) intercrystalline crack, (4) eutectic Si, (5) white Ce intermetallic phase, and (6) α-Fe phase.

Figure 7.16 displays optical micrographs of the longitudinal section beneath the fracture surface of the T6-treated D0 alloy with 1.0 wt.% La, and tested after 200 hrs stabilization at 250 °C. Figure 7.16(a) shows that the crack path tends to propagate through the α-Al matrix, and eutectic silicon, α-Fe phase and La-containing intermetallic particles. A higher magnification micrograph of the crack area, Figure 7.16(b), reveals the presence of several micro-cracks in the eutectic Si, α-Fe and the La-containing intermetallic particles near, and beneath the fracture surfaces. Figure 7.16(b) also show that the crack behavior of the RE-containing intermetallic compounds is quite in accordance with that of eutectic silicon. It can be seen from Figure 7.16(c) that regardless of the orientation of the particles, the cracks are all perpendicular to the applied tensile strength, suggesting that cracking occurs due to the development of tensile stress.

In summary, the results presented in this section highlight the following points. The fracture process of the B0 and D0 base alloys consists of three events: (i) particle cracking (α-Fe, Si), (ii) micro-crack formation and growth, and (iii) local linkage of micro-cracks [129, 189]. With the addition of Ce and La RE elements, the RE-containing intermetallic compounds formed also influence the fracture behavior. During plastic deformation, stresses are imposed by the matrix (α-Al) on the particles in the microstructures. Internal stresses are induced in the α-Fe (B0 and D0), eutectic silicon (D0), and RE-containing intermetallic particles (B0 and D0) due to inhomogeneous deformation in the alloys with RE addition. When the internal stress in the particles approaches the particle fracture stresses, the particles crack. As the deformation continues, more particles crack, and the existing cracks become extended. Subsequent the linkage of these cracks results in final fracture of the sample [129].
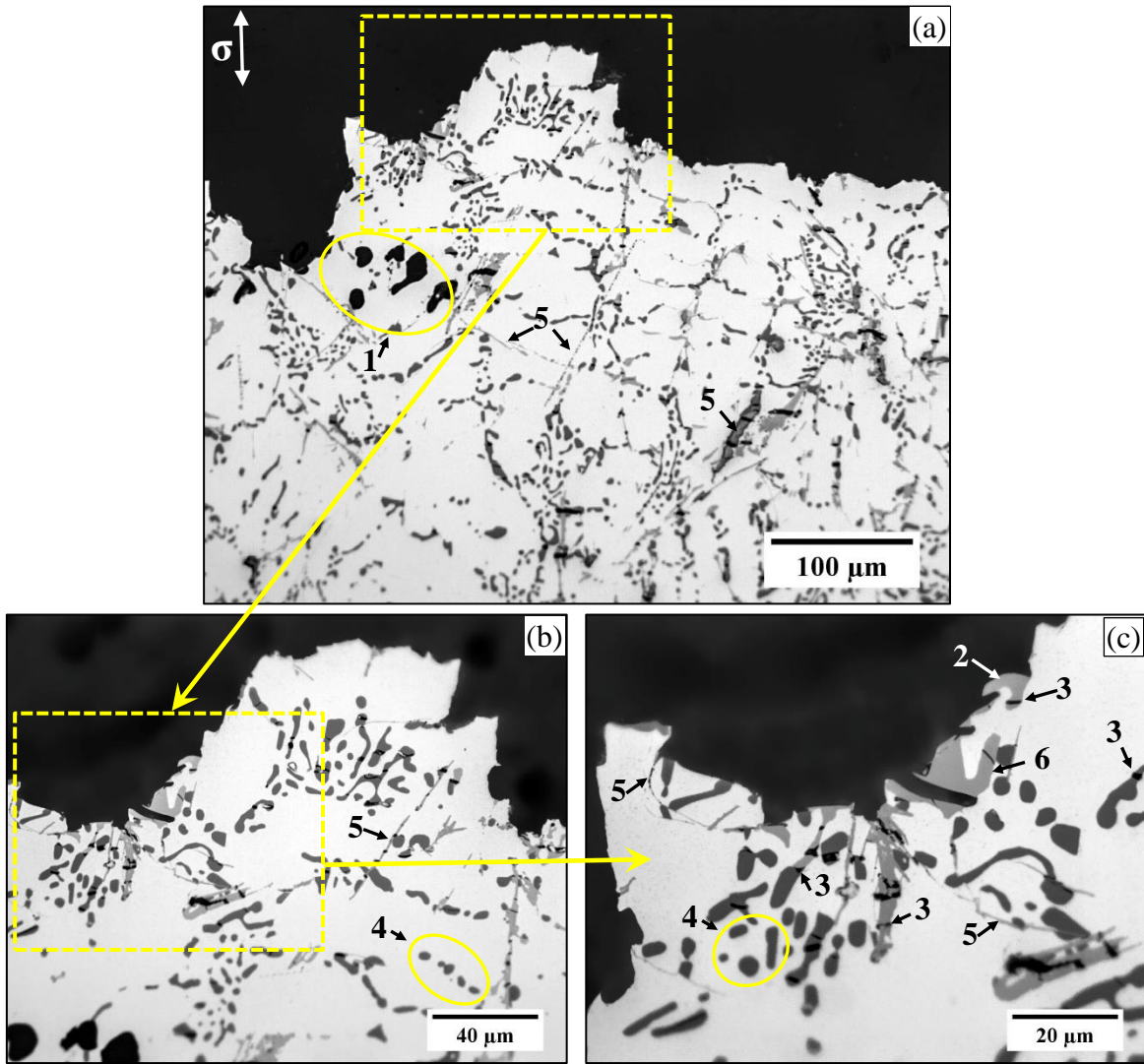
Figure 7.16: Optical micrographs showing longitudinal sections below the fracture surface of the T6-treated D0 alloy with 1.0 wt.% La, taken at: (a) low, (b) high, and (c) very high magnification. The arrows indicate (1) inderdendritic shrinkage, (2) debonding crack, (3) intercrystalline crack , (4) eutectic Si, (5) white La intermetallic phase, and (6) α-Fe phase.

CHAPTER 8

CONCLUSIONS

CHAPTER 8

CONCLUSIONS

The current study investigated the effects of different additions of La and Ce on the, solidification behaviour, microstructural characteristics, tensile properties at room and high temperature and fracture behavior of Al-1.2Si-2.4Cu-0.35Mg-0.4Fe-0.6Mn-0.15Ti (wt.%) and (D0) Al-8.0Si-2.4Cu-0.35Mg-0.4Fe-0.6Mn-0.15Ti (wt.%) (coded B0 and D0 alloys) in the as-cast (AC) and solution heat-treated (SHT) conditions, as well as after T5, T6 and T7 heat treatments. Based on the experimental results obtained, the following points may be summarized.

CHAPTER 4
Thermal Analysis (TA)

- Alloy B0 (Al-Cu)

  i.   The main phases observed in the B0 alloys are α-Al, α-Al$_{15}$(FeMn)$_3$Si$_2$, Al$_2$Cu, and Q-Al$_5$Mg$_8$Si$_6$Cu$_2$.

  ii. As the alloys investigated were refined with 0.15 wt.% Ti, the (recalescence(ΔT$_R$) i.e., the difference between T$_M$ and T$_G$ temperature was not noticeable.

  iii. Upon adding 1.0 wt.% Ce to B0 alloy, the $T_G^{\alpha-Al}$ decreased from 648.6 °C to 643 °C, whereas with 5.0 wt.% Ce addition, the $T_G^{\alpha-Al}$ was further lowered to 628 °C.

  iv. In the case of La additions to B0 alloy, the $T_G^{\alpha-Al}$ also decreased, going from 648.6 °C for the base B0 alloy to 644 °C and 631.5 °C with 1.0 and 5.0 wt.% La additions, respectively.

- Alloy D0 (Al-Si-Cu)

  i. The main phases observed in the D0 alloys are α-Al, α-Al$_{15}$(FeMn)$_3$Si$_2$, Al-Si, Al$_2$Cu, and Q-Al$_5$Mg$_8$Si$_6$Cu$_2$.

  ii. The difference between T_M and T_G is not noticeable in the base alloy, but is clearly noted in the cooling curves for α-Al and Al-Si phases for the alloys containing Ce and La additions, especially at the 5.0 wt.% addition level.

  iii. The minimum temperature $T_M^{\alpha-Al}$ decreased by 4.2 and 6 degrees, with the addition of 1.0 and 5.0 wt.% Ce. Thus, addition of Ce results in lowering the $T_M^{\alpha-Al}$ temperature in the D0 base alloy.

  iv. The minimum eutectic temperature T_M^{Al-Si} decreases slightly, to 568.6 °C upon increasing the Ce addition to 1.0 wt.% but drops sharply, by about 10 degrees, to 558.7 °C with 5.0 wt.% Ce.

  v. The $T_M^{\alpha-Al}$ for D0 alloy was measured at 603.7 °C, and dropped to 599.5 °C and 593.2 °C with 1.0 and 5.0 wt.% La addition, respectively. Furthermore, the growth temperature $T_G^{\alpha-Al}$ decreased by 3.2 and 7.9 degrees for the two additions.

  vi. The minimum eutectic temperature T_M^{Al-Si} dropped slightly, from 568.8 to 568.1 °C with 1.0 wt.% La, whereas with 5.0 wt.% La addition, the T_M^{Al-Si} dropped sharply to 551.2 °C. The T_G^{Al-Si} temperature decreased to 568.3 °C, and further to 552.5 °C, for the two La additions

Differential scanning Calorimetry (DSC)

- The B0 and D0 base alloy exhibited exothermic peaks attributed to the main phases observed by thermal analysis.

- Addition of RE metals (La or Ce) leads to the appearance of exothermic peaks in the solidification and heating curves between the precipitation of the primary α-Al phase and the (Al-Al_2Cu) eutectic reaction.

- The magnitude of the exothermic peak corresponding to the Al_2Cu and Q-phases is noticeably larger in the base alloy B0 and D0 alloys compared to the alloy with 1.0 wt.% RE (La/Ce) addition, and is totally absent in the D0 alloy containing 5.0 wt.%. The disappearance of this peak is attributed to the reaction of Ce/La with the Cu present in the alloy to form Ce-containing intermetallics, thus depleting the formation of the copper phases.

CHAPTER 5

SEM Observations

- The BSE images of B0 and D0 alloy displays the three main phases: θ-Al_2Cu, Q-$Al_5Mg_8Si_6Cu_2$, and the Chinese script-like α-$Al_{15}(Fe,Mn)_3Si_2$ phases. In addition to these three phases, eutectic Al-Si phase is also observed in the D0 alloys.

- With RE(Ce/La) addition to the B0 base alloy, the RE (Ce/La) reacts with other pre-existing elements to form particles of a white RE-containing intermetallic phase, while addition of Ti + RE causes the precipitation of a grey phase in the form of "sludge".

- Compared to 1.0 wt.% Ce addition, increasing the Ce level to 5.0 wt.% resulted in totally consuming the amount of Cu present in the base alloy, so that no θ-Al_2Cu phase is formed, as was confirmed by the DSC analysis results.

- Observations of the intermetallics formed in D0 alloys are similar to those noted for the B0 alloys; that is, the amount of Si seems to have no bearing on the precipitation of the RE-containing intermetallic phases. However, two important points distinguish the D0 alloy:

  i. With 1.0 wt.% RE(Ce/La) addition, the white phase AlSiRE appears in the form of spots, and contains no Cu. This type of phase was not observed in the case of the B0 alloy when the same level of RE addition was used.

  ii. Addition of an appropriate amount of RE (Ce/La) markedly enhances the volume fraction of the Chinese script α-$Al_{15}(Fe,Mn)_3Si_2$ phase.

- La and Ce found to have more or less the same effect on the microstructures, with the La- and Ce-containing intermetallics also displaying similar morphologies.

EPMA Observations

- BSE images obtained show that Ti is the main element in the grey phase, with trace of RE and Si. Precipitation of the grey phase on existing Ti-rich particles may also be observed.

- Based on WDS analysis, the grey phase has a fixed composition and may be written as $Al_{21}Ti_2RE$ (RE = La or Ce).

- The white phase particles are very thin (less than 1.5 µm), and have different compositions caused the reactivity of the RE elements with the other elements in the matrix, particularly Si, Cu, and Fe. The suggested chemical formulas for the white phase particles formed in the B0 and D0 alloys are listed below:

  i. B0 alloy

  a) $Al_{11}Ce_3(Cu,Fe)_4Si_2$ in 1.0 wt.% La-containing alloy;

b) $Al_{11}La_3(Cu,Fe)_4Si_2$, $Al_5La_3Si_2$, and $Al_6La_2(Cu,Fe)_2Si$ in 5.0 wt.% La-containing alloy;

c) $Al_{11}La_3(Cu,Fe)_4Si_2$ in 1.0 wt.% Ce-containing alloy; and

d) $Al_4Ce_3Si_2$ and $Al_{11}Ce_3(Cu,Fe)_4Si_2$ in 5.0 wt.% Ce-containing alloy.

ii. D0 alloy

a) $Al_9Ce_4Cu_2Si_4$ in 1.0 wt.% Ce-containing alloy;

b) Al_2CeSi in 5.0 wt.% Ce-containing alloy;

c) $Al_9La_4Cu_2Si_4$ in 1.0 wt.% La-containing alloy; and

d) $AlLaSi$, Al_2LaSi, and $Al_9La_4Cu_2Si$ in 5.0 wt.% La-containing alloy.

CHAPTER 6

Quantitative Metallographic Analysis

- Quantitative Analysis of Seconday Phases

  i.   As the RE (Ce/La) addition increases from 0.2 to 1.0 wt.%, the relative amount of intermetallic phases observed increases compared to the B0 and D0 base alloys, due to formation of RE-containing intermetallic compounds. These RE intermetallic compounds appear in the interdendritic regions, along the dendrite boundaries.

  ii. The morphology of the RE intermetallic phases is based on the RE level of addition, as they appear in the form of spot-type particles in the microstructure with a small amount of RE addition (0.2 wt.%), but with coarse block-like and lath-like morphologies when the RE addition increases to 1.0 wt.%.

  iii. As the addition level of Ce increases, the volume fraction of intermetallics in B0 alloy increases from 3.8% to 6.63%. Likewise, the volume fraction increases from 3.8% to 7.19% as the addition of La is increased.

iv.   The volume fraction of intermetallics in D0 alloy increases from 4.93% to 7.8% as the addition of Ce increases to 1.0 wt.%, and from 4.93% to 7.0% in the case of the La additions.

v.   B0 alloy exhibits both lower volume fractions and better morphological characteristics (lower aspect ratio and high roundness value) than the D0 alloy.

vi.   The grey phase observed in the alloy samples obtained at low cooling rate was not observed in the microstructure of the tensile test samples that were obtained at high cooling rate.

- Silicon Particle Characterization

  i.   The fibrous morphology of the eutectic silicon is observed in the as-cast Sr modified D0 alloy.

  ii.   The presence of Ce-Intermetallic phases is observed in both the as-cast and T6 heat-treated D0 alloy, which indicates that these intermetallic compounds are not soluble in the Al matrix, even when the alloy is heat treated at the high temperatures comprising the T6 treatment.

  iii.   The addition of 0.2 wt.% (Ce/La) modifies the eutectic silicon structure of D0 alloys.

Room Temperature Tensile Testing

- With respect to the effect of La and Ce as modifiers, the level of La and Ce added is the main parameter that controls the modification effect. Addition of 0.2 wt.% of La or Ce results in modification, however with high level of addition (0.5 and 1.0 wt.%), the effect of modification begins to deteriorate.

- Both unmodified and modified T6-heat treated alloys exhibit high (UTS) values compared to other heat treatment conditions (SHT, T5 and T7).

- Alloy B0 (Al-Cu)

  i.   Addition of 150 ppm Sr to the Al-Cu base alloy results in improving the UTS from
       254 MPa in the as-cast condition to 387 MPa in the T6 heat-treated condition, i.e.
       by 52%, with a corresponding decrease in ductility from 3% to 2.1%.

  ii. Addition of 0.2 wt.% La to the Al-Cu base alloy results in improving the UTS from
       254 MPa in the as-cast condition to 381 MPa in the T6-treated condition, i.e. by
       50%, with a corresponding decrease in ductility from 3% to 1.7%.

  iii. Similarly, addition of 0.2 wt.% Ce results in improving the UTS to 360 MPa in the
       T6-treated condition, i.e. by about 42%, with a corresponding decrease in ductility
       from 3% to 1.1%.

- Alloy D0 (Al-Si-Cu)

  i.   Addition of 150 ppm Sr to the Al-Si-Cu base alloy results in improving the UTS
       from 300 MPa in the as-cast condition to 361 MPa in the T6 heat-treated condition,
       i.e. by 20%, with a corresponding decrease in ductility from 1.7% to 1.0%.

  ii. Addition of 0.2 wt.% La results in improving the UTS of the as-cast base alloy by
       25% after T6 heat treatment, i.e., the UTS increases from 300 MPa to 374 MPa,
       with a corresponding decrease in ductility from 1.7% to 0.9%.

  iii. Addition of 0.2 wt.% Ce, however, only improves the UTS by about 7% (from 300
       MPa in the as-cast base alloy to 320 MPa in the T6-treated alloy), with a
       corresponding decrease in ductility from 1.7% to 0.7%.

CHAPTER 7

High Temperature Tensile Testing

- Alloy B0 (Al-Cu)

    i.   Under high temperature testing conditions, and after stabilization for 1 hr at 250°C prior to testing, the RE-modified T6-treated Al-Cu alloys exhibit a moderate increase in UTS with 0.2 wt.% La or Ce addition (249 and 242 MPa), compared to the unmodified T6-treated alloy. For RE additions of over 0.2 wt.%, however, the UTS values exhibit a slight decrease (about 2-8 MPa).

    ii. The ductility values also show a slight increase, increasing from 2% in the unmodified T6-treated alloy to 2.7% and 2.2% with 0.2 wt.% La and 0.2 wt.% Ce additions, respectively.

    iii. The RE-modified T6-treated Al-Cu alloys exhibit much better UTS values (219-249 MPa) after 1 hr stabilization at 250oC than those obtained after 200 hrs stabilization (80-93 MPa).

    iv. The ductility values of the T6-treated alloys improve considerably after 200 hrs stabilization, exhibiting 18.3% for the unmodified alloy, and 21.2% and 17.4% with 0.2 wt. % La and 0.2 wt. % Ce additions. Even at higher RE additions (0.5 and 1.0 wt.%), the ductility values range from 4.2 to 8.5% (*cf.* 1.1 to 1.9% after 1 hr stabilization).

- Alloy D0 (Al-Si-Cu)

    v.   Under high temperature testing conditions, and after stabilization for 1 hr at 250 °C prior to testing, the RE-modified T6-treated Al-Si-Cu alloys exhibit UTS values of 271 and 253 MPa with 0.2 wt.% La and 0.2 wt.% Ce addition, respectively,

compared to 256 MPa obtained for the unmodified T6-treated alloy. For RE additions of over 0.2 wt.%, however, the UTS values range from 234 to 248 MPa.

vi.   The ductility values also show a slight increase, going from 0.9% in the unmodified T6-treated alloy to 2.7% and 2.2%, respectively, with 0.2 wt.% La and 0.2 wt.% Ce additions. For RE additions of over 0.2 wt.%, the ductility values vary between 1.9 and 1.1%.

vii.   The RE-modified T6-treated Al-Si-Cu alloys exhibit much better UTS values (~234-250 MPa) after 1 hr stabilization at 250oC than those obtained after 200 hrs stabilization (~97-104 MPa).

viii.   The ductility values of the T6-treated alloys are relatively improved after 200 hrs stabilization, going from 0.9% to 10.4% for the unmodified alloy, and 7.3% with 0.2 wt.% La, and 8.1% with 0.2 wt.% Ce additions, respectively. Even at higher RE additions (0.5 and 1.0 wt.%), the ductility values range from 5.5 to 8.6% (*cf.* 1.1 to 1.9% after 1 hr stabilization).

<u>Fractography</u>

- SEM Observations

i.   The fracture surface of the T6-treated B0 base alloy sample tested after 200 hrs stabilization at 250 $^{\circ}$C exhibits microvoids and fine and uniformly distributed dimples, indicating that the sample underwent a large amount of plastic deformation prior to fracture.

ii.   Compared to the B0 base alloy, the fracture surface of D0 alloys exhibits several instances of cleavage patterns. This cleavage results from the debonding of Si

particles from the Al matrix, which is the main mode of crack initiation reported in Al-Si alloys.

iii. The fracture surface of T6-treated B0 and D0 alloy containing 1.0 wt.% Ce/La and obtained after 200 hrs stabilization at 250°C, reveals considerably different characteristics, namely, an increase in the size of dimples observed, and a fracture surface covered by cleavage planes.

- Examination of Longitudinal Sections beneath the Fracture Surface

    i. The longitudinal section beneath the fracture surface of the T6-treated B0 base alloy after 200 hrs stabilization at 250 °C shows shows a curved and rounded sample edge, indicating a ductile mode of ruptures. Interdendritic shrinkage and extended cracks from the aluminum matrix are also found on the fracture surface. By magnifying the crack region, the fracture of α-Fe phase particles can be observed adjacent to the cracks.

    ii. The longitudinal section beneath the fracture surface of the T6-treated D0 base alloy sample, tested after 200 hrs stabilization at 250 °C, shows a sharp fracture profile, indicating a brittle mode of ruptures compared to the case of the B0 Alloys. The fracture occurs mainly across α-Al matrix, eutectic silicon and α-Fe phases.

    iii. With the addition RE (Ce/La) elements, the RE-containing intermetallic compounds formed also influence the fracture behavior. During plastic deformation, stresses are imposed by the matrix (α-Al) on these phases in the microstructures. Internal stresses are induced in the α-Fe (B0 and D0), eutectic silicon (D0), and RE-containing intermetallic particles (B0 and D0) due to inhomogeneous deformation in the alloys with the RE addition.

RECOMMENDATIONS FOR FUTURE WORK

The research carried out in the present study could be explored further along the following directions:

1. By using the Thermo-Calc TCW 5 software program combined with the data base COST507, the experimental results obtained for the investigated alloys B0 and D0 with 0.0, 0.2,0.5, 1.0 wt.% RE(Ce/La) additions could be examined to

    a) Simulate the equilibrium solidification and equilibrium phase diagrams;

    b) Predict the phases formed during solidification; and

    c) Calculate the phase fraction of these phases.

2. Study the influence of the cooling rates on the formation of the grey intermetallic phase Al-Ti-RE(Ce/La).

3. The Al-RE (Ce/La) master alloys, which were used in the current study, were added to the molten B0 and D0 alloys in the as-received condition. Another possible route would be to prepare the Al-RE (Ce/La) master alloys using mechanical alloying, and to study their effectiveness in (i) fragmenting the La/Ce phase particles in the Al-RE (Ce/La) master alloys, and (ii) achieving homogeneous dispersion of the fine particles containing La/Ce in the B0 and D0 alloys. Such investigations have been reported previously [165, 190].

4. Investigated the effect of RE (Ce/La) addition on the machining performance of B0 and D0 alloys.

5. Carry out transmission electron microscopic (TEM) examination to understand the effect of RE (Ce/La) on the precipitation hardening behavior of B0 and D0 alloys.

REFERANCES

REFERENCES

1-A. E. Atabani, I. A. Badruddin, S. Mekhilef, and A. S. Silitonga, "A review on global fuel economy standards, labels and technologies in the transportation sector," Renewable & Sustainable Energy Reviews, vol. 15, 2011, pp. 4586-4610.

2-B. C. O'Neill, and M. Oppenheimer, "Climate change. Dangerous climate impacts and the Kyoto Protocol," Science, vol. 296, 2002, pp. 1971-1972.

3-H. H. Braess, and U. W. Seiffert. Handbook of automotive engineering: SAE Technical Paper; 2005.

4-C. Engler-Pinto, H. Sehitoglu, H. Maier, and T. Foglesong, "Thermo-mechanical fatigue behavior of cast 319 aluminum alloys," European Structural Integrity Society, vol. 29, 2002, pp. 3-13.

5-L. Miller. Investigation of Thermo-Mechanical Fatigue Characteristics for Cast Aluminum (AL319-T7) 2014.

6-G. A. Zaki, A. M. Samuel, F. H. Samuel, and H. W. Doty, "Effect of Metallurgical Parameters on the Performance of Al-2%Cu-Based Alloys," International Journal of Metalcasting, vol. 11, 2017, pp. 581-597.

7-A. Nabawy. Influence of zirconium and scandium on the microstructure, tensile properties, and hot-tearing susceptibility of Al-2wt% Cu-based alloys: Université du Québec à Chicoutimi; 2010.

8-E. E. Elgallad. Effect of additives on the mechanical properties and machinability of a new aluminum-copper base alloy [PhD Thesis]: Université du Québec à Chicoutimi; 2010.

9-H. W. Doty, F. H. Samuel, and A. M. Nabawy, inventors; Google Patents, assignee. Metal treatment to eliminate hot tear defects in low silicon aluminum alloys2015.

10-A. M. Nabawy, A. M. Samuel, F. H. Samuel, and H. W. Doty, "Effects of grain refiner additions (Zr, Ti-B) and of mould variables on hot tearing susceptibility of recently developed Al-2 wt-%Cu alloy," International Journal of Cast Metals Research, vol. 26, 2013, pp. 308-317.

11-A. M. Nabawy, A. M. Samuel, F. H. Samuel, and H. W. Doty, "Influence of additions of Zr, Ti-B, Sr, and Si as well as of mold temperature on the hot-tearing susceptibility of an experimental Al-2% Cu-1% Si alloy," Journal of materials science, vol. 47, 2012, pp. 4146-4158.

12-E. M. Elgallad, A. M. Samuel, F. H. Samuel, and H. W. Doty, "Effects of Additives on the Microstructures and Tensile Properties of a New Al-Cu Based Alloy Intended for Automotive Castings," Transactions of the American Foundry Society, vol. 118, 2010, pp. 39-56.

13-E. Elgallad, F. Samuel, A. Samuel, and H. Doty, "Development of New Al-Cu Based Alloys Aimed at Improving the Machinability of Automotive Castings," International Journal of Metalcasting, vol. 3, 2009, pp. 29-41.

14-G. A. S. Zaki. On the performance of low pressure die-cast Al-Cu based automotive alloys: role of additives [Master Thesis]: Université du Québec à Chicoutimi; 2014.

15-R. Aparicio, G. Barrera, G. Trapaga, M. Ramirez-Argaez, and C. Gonzalez-Rivera, "Solidification kinetics of a near eutectic Al-Si alloy, unmodified and modified with Sr," Metals and Materials International, vol. 19, 2013, pp. 707.

16-S. D. McDonald, K. Nogita, and A. K. Dahle, "Eutectic nucleation in Al–Si alloys," Acta Materialia, vol. 52, 2004, pp. 4273-4280.

17-S. Farahany, A. Ourdjini, M. Idrsi, and S. Shabestari, "Evaluation of the effect of Bi, Sb, Sr and cooling condition on eutectic phases in an Al–Si–Cu alloy (ADC12) by in situ thermal analysis," Thermochimica Acta, vol. 559, 2013, pp. 59-68.

18-S. Khan, and R. Elliott, "Quench modification of aluminium-silicon eutectic alloys," Journal of materials science, vol. 31, 1996, pp. 3731-3737.

19-K. Nogita, S. D. McDonald, and A. K. Dahle, "Eutectic modification of Al-Si alloys with rare earth metals," Materials Transactions, vol. 45, 2004, pp. 323-326.

20-K. Nogita, J. Drennan, and A. K. Dahle, "Evaluation of silicon twinning in hypo-eutectic Al-Si alloys," Materials transactions, vol. 44, 2003, pp. 625-628.

21-K. Nogita, H. Yasuda, M. Yoshiya, S. D. McDonald, K. Uesugid, A. Takeuchi, and Y. Suzuki, "The role of trace element segregation in the eutectic modification of hypoeutectic Al-Si alloys," Journal of Alloys and Compounds, vol. 489, 2010, pp. 415-420.

22-H. R. Zhang, Z. B. Liu, Z. Z. Li, G. W. Li, and H. Zhang, "Cooling Rate Sensitivity of RE-Containing Grain Refiner and Its Impact on the Microstructure and Mechanical Properties of A356 Alloy," Acta Metallurgica Sinica-English Letters, vol. 29, 2016, pp. 414-421.

23-W. M. Jiang, Z. T. Fan, Y. C. Dai, and C. Li, "Effects of rare earth elements addition on microstructures, tensile properties and fractography of A357 alloy," Materials Science and Engineering a-Structural Materials Properties Microstructure and Processing, vol. 597, 2014, pp. 237-244.

24-R. Ahmad, M. B. A. Asmael, N. R. Shahizan, and S. Gandouz, "Reduction in secondary dendrite arm spacing in cast eutectic Al–Si piston alloys by cerium addition," International Journal of Minerals, Metallurgy, and Materials, vol. 24, 2017, pp. 91-101.

25-M. Hosseinifar, and D. V. Malakhov, "Effect of Ce and La on microstructure and properties of a 6xxx series type aluminum alloy," Journal of materials science, vol. 43, 2008, pp. 7157-7164.

26-L. Backerud, G. Chai, and J. Tamminen, "Solidification characteristics of aluminum alloys. Vol. 2. Foundry alloys," American Foundrymen's Society, Inc, 1990, 1990, pp. 266.

27-"Reviews on the Influences of Alloying elements on the Microstructure and Mechanical Properties of Aluminum Alloys and Aluminum Alloy Composites," International Journal of Scientific and Research Publications.

28-Z. Ma, A. Samuel, F. Samuel, H. Doty, and S. Valtierra, "A study of tensile properties in Al–Si–Cu and Al–Si–Mg alloys: Effect of β-iron intermetallics and porosity," Materials Science and Engineering: A, vol. 490, 2008, pp. 36-51.

29-P. Crepeau, "Effect of Iron in Al-Si Casting Alloys: A Critical Review (95-110)," Transactions of the American Foundrymen's Society, vol. 103, 1995, pp. 361-366.

30-L. Lu, and A. Dahle, "Iron-rich intermetallic phases and their role in casting defect formation in hypoeutectic Al-Si alloys," Metallurgical and Materials Transactions A, vol. 36, 2005, pp. 819-835.

31-J. Hatch, "Aluminum Properties and Physical Metallurgy,‖ American Society for Metals, Metals Park, OH, May 1984," APPENDICES.

32-F. Samuel, "Incipient melting of Al5Mg8Si6Cu2 and Al2Cu intermetallics in unmodified and strontium-modified Al–Si–Cu–Mg (319) alloys during solution heat treatment," Journal of materials science, vol. 33, 1998, pp. 2283-2297.

33-O. Reiso, N. Ryum, and J. Strid, "Melting of secondary-phase particles in Al-Mg-Si alloys," Metallurgical and Materials Transactions A, vol. 24, 1993, pp. 2629-2641.

34-D. Apelian, S. Shivkumar, and G. Sigworth, "Fundamental aspects of heat treatment of cast Al-Si-Mg alloys," AFS transactions, vol. 97, 1989, pp. 727-742.

35-E. Tillová, and M. Panušková, "Effect of solution treatment on intermetallic phases morphology in AlSi 9 Cu 3 cast alloy," Metalurgija, vol. 47, 2008, pp. 207-210.

36-H. Li, S. Shivkumar, X. Luo, and D. Apelian, "Influence of Modification on the Solution Heat-treatment Response of Cast Al-Si-Mg Alloys," Cast Metals, vol. 1, 1988, pp. 227-234.

37-J. G. Kaufman, and E. L. Rooy. Aluminum alloy castings: properties, processes, and applications: Asm International; 2004.

38-J. Jorstad, W. Rasmussen, and D. Zalensas, "Aluminum Casting Technology, American Foundrymen's Society," Inc, Des Plaines, IL, USA, 1993.

39-D. Steele, D. Evans, P. Nolan, and D. Lloyd, "Quantification of grain boundary precipitation and the influence of quench rate in 6XXX aluminum alloys," Materials Characterization, vol. 58, 2007, pp. 40-45.

40-D. S. Mackenzie, "Design of quench systems for aluminum heat treating Part I- quenchant selection," Industrial Heating, vol. 73, 2006, pp. 53-58.

41-G. E. Byczynski, W. T. Kierkus, D. O. Northwood, D. Penrod, and J. Sokolowski, editors. The effect of quench rate on mechanical properties of 319 aluminum alloy castings. Materials Science Forum; 1996: Trans Tech Publ.

42-T. Gladman, "Precipitation hardening in metals," Materials Science and Technology, vol. 15, 1999, pp. 30-36.

43-J. W. Martin. Precipitation hardening: theory and applications: Butterworth-Heinemann; 2012.

44-A. Kelly, "Precipitation hardening," Progress in materials science, vol. 10, 1963, pp. 324-334.

45-R. E. Smallman, and A. Ngan. Physical metallurgy and advanced materials: Butterworth-Heinemann; 2011.

46-M. Drouzy, S. Jacob, and M. Richard, "Interpretation of Tensile Results by Means of Quality Index And Probable Yield Strength-Application to Al-Si7 Mg Foundry Alloys-France," International Cast Metals Journal, vol. 5, 1980, pp. 43-50.

47-T. Din, A. Rashid, and J. Campbell, "High strength aerospace casting alloys: quality factor assessment," Materials Science and Technology, vol. 12, 1996, pp. 269-273.

48-C. Cáceres, "A rationale for the quality index of Al-Si-Mg casting alloys," International Journal of Cast Metals Research, vol. 10, 1998, pp. 293-299.

49-C. Cáceres, "A phenomenological approach to the Quality Index of Al-Si-Mg casting alloys," International Journal of Cast Metals Research, vol. 12, 2000, pp. 367-375.

50-N. Alexopoulos, and S. G. Pantelakis, "Evaluation of the effects of variations in chemical composition on the quality of Al-Si-Mg, Al-Cu, and Al-Zn-Mg cast aluminum alloys," Journal of Materials Engineering and Performance, vol. 12, 2003, pp. 196-205.

51-N. Alexopoulos, and S. G. Pantelakis, "A new quality index for characterizing aluminum cast alloys with regard to aircraft structure design requirements," Metallurgical and Materials Transactions A, vol. 35, 2004, pp. 301-308.

52-N. Alexopoulos, and S. G. Pantelakis, "Quality assessment of artificially aged A357 aluminum alloy cast ingots by introducing approximate expressions of the quality index Q D," Metallurgical and Materials Transactions A, vol. 35, 2004, pp. 3079-3089.

53-N. Alexopoulos, and S. G. Pantelakis, "Quality evaluation of A357 cast aluminum alloy specimens subjected to different artificial aging treatment," Materials & Design, vol. 25, 2004, pp. 419-430.

54-M. Tiryakioğlu, J. T. Staley, and J. Campbell, "Evaluating structural integrity of cast Al–7% Si–Mg alloys via work hardening characteristics: II. A new quality index," Materials Science and Engineering: A, vol. 368, 2004, pp. 231-238.

55-H. Ammar. Infulence of Metallurgical Parameters on The Mechanical Propeties and Quality Indices of Al-Si-Cu-Mg and Al-Si-Mg Casting Alloys: University of Quebec at Chicoutimi; 2010.

56-J. R. Davis. Tensile testing: ASM international; 2004.

57-G. E. Dieter, and D. J. Bacon. Mechanical metallurgy: McGraw-hill New York; 1986.

58-Necking (engineering) - Wikipedia 2018 [Available from: https://en.wikipedia.org/wiki/Necking_(engineering)#cite_note-considere-3.

59-M. Considère, "Memoir on the use of iron and steel in structures," Ann Ponts Chaussees, vol. 9, 1885, pp. 574.

60-A. Knuutinen, K. Nogita, S. McDonald, and A. Dahle, "Modification of Al–Si alloys with Ba, Ca, Y and Yb," Journal of Light Metals, vol. 1, 2001, pp. 229-240.

61-K. Nogita, A. Knuutinen, S. McDonald, and A. Dahle, "Mechanisms of eutectic solidification in Al–Si alloys modified with Ba, Ca, Y and Yb," Journal of Light Metals, vol. 1, 2001, pp. 219-228.

62-B. Li, F. Kong, and Y. Chen, "Effect of yttrium addition on microstructures and room temperature tensile properties of Ti-47 Al alloy," Journal of Rare Earths, vol. 24, 2006, pp. 352-356.

63-H. Z. Li, X. P. Liang, F. F. Li, F. F. Guo, Z. Li, and X. M. Zhang, "Effect of Y content on microstructure and mechanical properties of 2519 aluminum alloy," Transactions of Nonferrous Metals Society of China, vol. 17, 2007, pp. 1194-1198.

64-L. Zheng, and H. Yongmei, "Effect of yttrium on the microstructure of a semi-solid A356 Al alloy," Rare Metals, vol. 27, 2008, pp. 536-540.

65-M. Li, H. Wang, Z. Wei, and Z. Zhu, "The effect of Y on the hot-tearing resistance of Al–5wt.% Cu based alloy," Materials & Design, vol. 31, 2010, pp. 2483-2487.

66-B. Li, H. Wang, J. Jie, and Z. Wei, "Effects of yttrium and heat treatment on the microstructure and tensile properties of Al–7.5 Si–0.5 Mg alloy," Materials & Design, vol. 32, 2011, pp. 1617-1622.

67-J. H. Li, and P. Schumacher, "Effect of Y addition and cooling rate on refinement of eutectic Si in Al-5 wt-%Si alloys," International Journal of Cast Metals Research, vol. 25, 2012, pp. 347-357.

68-B. Wan, W. Chen, L. Liu, X. Cao, L. Zhou, and Z. Fu, "Effect of trace yttrium addition on the microstructure and tensile properties of recycled Al–7Si–0.3 Mg–1.0 Fe casting alloys," Materials Science and Engineering: A, vol. 666, 2016, pp. 165-175.

69-M. O. Shabani, and A. Mazahery, "Automotive copper and magnesium containing cast aluminium alloys: report on the correlation between Yttrium modified microstructure and mechanical properties," Russian Journal of Non-Ferrous Metals, vol. 55, 2014, pp. 436-442.

70-M. Sheng, Z. Tao, P. Jia, J. Leng, and H. Geng, "Effects of Y and Y combined with Al-5Ti-1B on the microstructure and mechanical properties of hypoeutectic Al-Si alloy," Jom, vol. 67, 2015, pp. 330-335.

71-Z. R. Nie, T. Jin, J. Fu, G. Xu, J. Yang, J. X. Zhou, and T. Y. Zuo, editors. Research on rare earth in aluminum. Materials Science Forum; 2002: Trans Tech Publ.

72-Z. Nie, J. Fu, J. Zou, T. Jin, J. Yang, G. Xu, H. Ruan, and T. Zuo, editors. Advanced aluminum alloys containing rare-earth erbium. Materials Forum; 2004.

73-G. F. Xu, S. Z. Mou, J. J. Yang, T. N. Jin, Z. R. Nie, and Z. M. Yin, "Effect of trace rare earth element Er on Al-Zn-Mg alloy," Transactions of Nonferrous Metals Society of China, vol. 16, 2006, pp. 598-603.

74-Y. T. Li, Z. Y. Liu, Y. B. Liu, P. Dang, Q. K. Xia, and R. C. Yu, editors. Alloying behavior of rare-earth Er in Al-Cu-Mg-Ag alloy. Materials science forum; 2007: Trans Tech Publ.

75-S. P. Wen, Z. B. Xing, H. Huang, B. L. Li, W. Wang, and Z. R. Nie, "The effect of erbium on the microstructure and mechanical properties of Al-Mg-Mn-Zr alloy," Materials Science and Engineering a-Structural Materials Properties Microstructure and Processing, vol. 516, 2009, pp. 42-49.

76-X. Pengfei, G. Bo, Y. Zhuang, L. Kaihua, and T. Ganfeng, "Effect of erbium on properties and microstructure of Al-Si eutectic alloy," Journal of Rare Earths, vol. 28, 2010, pp. 927-930.

77-C. Booth-Morrison, D. N. Seidman, and D. C. Dunand, "Effect of Er additions on ambient and high-temperature strength of precipitation-strengthened Al-Zr-Sc-Si alloys," Acta Materialia, vol. 60, 2012, pp. 3643-3654.

78-X. W. Hu, F. G. Jiang, F. R. Ai, and H. Yan, "Effects of rare earth Er additions on microstructure development and mechanical properties of die-cast ADC12 aluminum alloy," Journal of Alloys and Compounds, vol. 538, 2012, pp. 21-27.

79-X. D. Wang, S. P. Lin, J. J. Yang, Z. L. Tang, and Z. R. Nie, "Microstructure and mechanical properties of Al-Mg-Mn alloy with erbium," Rare Metals, vol. 31, 2012, pp. 237-243.

80-Z. M. Shi, Q. Wang, G. Zhao, and R. Y. Zhang, "Effects of erbium modification on the microstructure and mechanical properties of A356 aluminum alloys," Materials Science and

Engineering a-Structural Materials Properties Microstructure and Processing, vol. 626, 2015, pp. 102-107.

81-M. Colombo, E. Gariboldi, and A. Morri, "Er addition to Al-Si-Mg-based casting alloy: Effects on microstructure, room and high temperature mechanical properties," Journal of Alloys and Compounds, vol. 708, 2017, pp. 1234-1244.

82-M. Colombo, E. Gariboldi, and A. Morri, "Influences of different Zr additions on the microstructure, room and high temperature mechanical properties of an Al-7Si-0.4 Mg alloy modified with 0.25% Er," Materials Science and Engineering: A, 2017.

83-Q. L. Li, B. Q. Li, J. B. Li, C. F. Zhang, and Y. F. Lan, editors. Effect of Rare Earth Er on Microstructure and Mechanical Properties of Cast Al-Si-Mg Alloy. Materials Science Forum; 2017: Trans Tech Publ.

84-C. Xu, H. Wang, Y. Yang, and Q. Jiang, "Effect of Al–P–Ti–TiC–Nd 2 O 3 modifier on the microstructure and mechanical properties of hypereutectic Al–20wt.% Si alloy," Materials Science and Engineering: A, vol. 452, 2007, pp. 341-346.

85-W. X. Shi, B. Gao, G. F. Tu, and S. W. Li, "Effect of Nd on microstructure and wear resistance of hypereutectic Al-20%Si alloy," Journal of Alloys and Compounds, vol. 508, 2010, pp. 480-485.

86-S. Weixi, G. Bo, T. Ganfeng, L. Shiwei, H. Yi, and Y. Fuxiao, "Effect of neodymium on primary silicon and mechanical properties of hypereutectic Al-15% Si alloy," Journal of Rare Earths, vol. 28, 2010, pp. 367-370.

87-X. Ren, L. Peng, G. Huang, R. Zong, H. Xie, and J. Li, "Effect of Nd on microstructure and properties of 2A70 alloy," Journal of Alloys and Compounds, 2017.

88-Q. Tang, J. Zhao, T. Wang, J. Chen, and K. He, "The effects of neodymium addition on the intermetallic microstructure and mechanical properties of Al-7Si-0.3 Mg-0.3 Fe alloys," Journal of Alloys and Compounds, 2018.

89-R. Ahmad, M. Asmael, and M. Amzar, "Effect of ytterbium addition on microstructure and hardness of Al-6.5Si-1Zn secondary cast alloy," 2006.

90-D. Xiao, M. Song, K. Chen, and B. Huang, "Effect of rare earth Yb addition on mechanical properties of Al–5· 3Cu–0· 8Mg–0· 6Ag alloy," Materials Science and Technology, vol. 23, 2007, pp. 1156-1160.

91-X. M. Zhang, W. T. Wang, M. A. Chen, Y. Z. Jia, L. Y. Ye, D. W. Zheng, L. Liu, and X. Y. Kuang, "Effects of Yb addition on microstructures and mechanical properties of 2519A aluminum alloy plate," Transactions of Nonferrous Metals Society of China, vol. 20, 2010, pp. 727-731.

92-B. Li, H. W. Wang, J. C. Jie, and Z. J. Wei, "Microstructure evolution and modification mechanism of the ytterbium modified Al-7.5%Si-0.45%Mg alloys," Journal of Alloys and Compounds, vol. 509, 2011, pp. 3387-3392.

93-J. H. Li, S. Suetsugu, Y. Tsunekawa, and P. Schumacher, "Refinement of Eutectic Si Phase in Al-5Si Alloys with Yb Additions," Metallurgical and Materials Transactions a-Physical Metallurgy and Materials Science, vol. 44a, 2013, pp. 669-681.

94-Z. Hu, Z. Dong, Z. Yin, H. Yan, J. Tian, and H. Xie, "Solidification behavior, microstructure and silicon twinning of Al-10Si alloys with Yb addition," Journal of Rare Earths, 2018.

95-Q. Li, J. Li, B. Li, Y. Zhu, D. Liu, Y. Lan, and S. Wang, "Mechanical Properties and Microstructural Evolution of Yb-Modified Al-20% Si Alloy," Journal of Materials Engineering and Performance, 2018, pp. 1-10.

96-Z. W. Chen, P. Chen, and C. Y. Ma, "Microstructures and mechanical properties of Al-Cu-Mn alloy with La and Sm addition," Rare Metals, vol. 31, 2012, pp. 332-335.

97-H. Qiu, H. Yan, and Z. Hu, "Effect of samarium (Sm) addition on the microstructures and mechanical properties of Al–7Si–0.7 Mg alloys," Journal of Alloys and Compounds, vol. 567, 2013, pp. 77-81.

98-R. Yuansheng, Y. Hong, and H. Zhi, "Modification of eutectic silicon and β-Al 5 FeSi phases in as-cast ADC12 alloys by using samarium addition," Journal of Rare Earths, vol. 31, 2013, pp. 916-922.

99-H. Zhi, Y. Hong, and Y.-s. RAO, "Effects of samarium addition on microstructure and mechanical properties of as-cast Al-Si-Cu alloy," Transactions of Nonferrous Metals Society of China, vol. 23, 2013, pp. 3228-3234.

100-H. X. Qiu, H. Yan, and Z. Hu, "Modification of near-eutectic Al-Si alloys with rare earth element samarium," Journal of Materials Research, vol. 29, 2014, pp. 1270-1277.

101-Q. Li, J. Li, B. Li, Y. Lan, and T. Xia, "Effect of Samarium (Sm) Addition on the Microstructure and Tensile Properties of Al–20% Si Casting Alloy," International Journal of Metalcasting, 2017, pp. 1-11.

102-V. V. Zakharov, and T. D. Rostova, "Effect of scandium, transition metals, and admixtures on strengthening of aluminum alloys due to decomposition of the solid solution," Metal Science and Heat Treatment, vol. 49, 2007, pp. 435-442.

103-M. S. Kaiser, S. Datta, A. Roychowdhury, and M. K. Banerjee, "Effect of scandium on the microstructure and ageing behaviour of cast Al-6Mg alloy," Materials Characterization, vol. 59, 2008, pp. 1661-1666.

104-W. Prukkanon, N. Srisukhumbowornchai, and C. Limmaneevichitr, "Influence of Sc modification on the fluidity of an A356 aluminum alloy," Journal of Alloys and Compounds, vol. 487, 2009, pp. 453-457.

105-D. Emadi, A. K. P. Rao, and M. Mahfoud, "Influence of scandium on the microstructure and mechanical properties of A319 alloy," Materials Science and Engineering a-Structural Materials Properties Microstructure and Processing, vol. 527, 2010, pp. 6123-6132.

106-W. Zhang, Y. Liu, J. Yang, J. Dang, H. Xu, and Z. Du, "Effects of Sc content on the microstructure of As-Cast Al-7wt.% Si alloys," Materials Characterization, vol. 66, 2012, pp. 104-110.

107-U. Patakham, J. Kajornchaiyakul, and C. Limmaneevichitr, "Modification mechanism of eutectic silicon in Al–6Si–0.3 Mg alloy with scandium," Journal of Alloys and Compounds, vol. 575, 2013, pp. 273-284.

108-M. Yi, Z.-h. Zhao, and J.-z. Cui, "Effect of minor Zr and Sc on microstructures and mechanical properties of Al–Mg–Si–Cu–Cr–V alloys," Transactions of Nonferrous Metals Society of China, vol. 23, 2013, pp. 1882-1889.

109-J. Ma, D. S. Yan, L. J. Rong, and Y. Y. Li, "Effect of Sc addition on microstructure and mechanical properties of 1460 alloy," Progress in Natural Science-Materials International, vol. 24, 2014, pp. 13-18.

110-Y.-C. Tzeng, C.-T. Wu, H.-Y. Bor, J.-L. Horng, M.-L. Tsai, and S.-L. Lee, "Effects of scandium addition on iron-bearing phases and tensile properties of Al–7Si–0.6 Mg alloys," Materials Science and Engineering: A, vol. 593, 2014, pp. 103-110.

111-C. Xu, W. L. Xiao, R. X. Zheng, S. Hanada, H. Yamagata, and C. L. Ma, "The synergic effects of Sc and Zr on the microstructure and mechanical properties of Al-Si-Mg alloy," Materials & Design, vol. 88, 2015, pp. 485-492.

112-J. H. Li, X. D. Wang, T. H. Ludwig, Y. Tsunekawa, L. Arnberg, J. Z. Jiang, and P. Schumacher, "Modification of eutectic Si in Al-Si alloys with Eu addition," Acta Materialia, vol. 84, 2015, pp. 153-163.

113-F. Mao, G. Y. Yan, J. Q. Li, T. M. Wang, and Z. Q. Cao, "The interaction between Eu and P in high purity Al-7Si alloys," Materials Characterization, vol. 120, 2016, pp. 129-142.

114-F. Mao, G. Yan, Z. Xuan, Z. Cao, and T. Wang, "Effect of Eu addition on the microstructures and mechanical properties of A356 aluminum alloys," Journal of Alloys and Compounds, vol. 650, 2015, pp. 896-906.

115-W. Y. Liu, W. L. Xiao, C. Xu, M. W. Liu, and C. L. Ma, "Synergistic effects of Gd and Zr on grain refinement and eutectic Si modification of Al-Si cast alloy," Materials Science and Engineering a-Structural Materials Properties Microstructure and Processing, vol. 693, 2017, pp. 93-100.

116-C. Y. Young, L. Qingchaun, and J. Zhuling, "Influence of cerium and mischmetal on the hardness and brightness of Al-Mg-Si alloys," Journal of the Less Common Metals, vol. 110, 1985, pp. 175-178.

117-M. Ravi, U. T. S. Pillai, B. C. Pai, A. D. Damodaran, and E. S. Dwarakadasa, "A study of the influence of mischmetal additions to ai-7si-0.3 mg (lm 25/356) alloy," Metallurgical and Materials Transactions A, vol. 27, 1996, pp. 1283-1292.

118-J. Y. Chang, G. H. Kim, I. G. Moon, and C. S. Choi, "Rare earth concentration in the primary Si crystal in rare earth added Al-21wt.%Si alloy," Scripta Materialia, vol. 39, 1998, pp. 307-314.

119-J. Y. Chang, I. G. Moon, and C. S. Choi, "Refinement of cast microstructure of hypereutectic Al-Si alloys through the addition of rare earth metals," Journal of materials science, vol. 33, 1998, pp. 5015-5023.

120-J. Zhang, Z. Fan, Y. Q. Wang, and B. L. Zhou, "Microstructural development of Al–15wt.% Mg 2 Si in situ composite with mischmetal addition," Materials Science and Engineering: A, vol. 281, 2000, pp. 104-112.

121-M. Ravi, U. T. S. Pillai, B. C. Pai, A. D. Damodaran, and E. S. Dwarakadasa, "The effect of mischmetal addition on the structure and mechanical properties of a cast Al-7Si-0.3 Mg alloy containing excess iron (up to 0.6 Pct)," Metallurgical and Materials Transactions A, vol. 33, 2002, pp. 391-400.

122-W. A. N. Weiwei, H. A. N. Jianmin, L. Weijing, and W. Jinhua, "Study of rare earth element effect on microstructures and mechanical properties of an Al-Cu-Mg-Si cast alloy," Rare Metals, vol. 25, 2006, pp. 129-132.

123-C. Chong, Z. X. Liu, B. Ren, M. X. Wang, Y. G. Weng, and Z. G. Liu, "Influences of complex modification of P and RE on microstructure and mechanical properties of hypereutectic Al-20Si alloy," Transactions of Nonferrous Metals Society of China, vol. 17, 2007, pp. 301-306.

124-O. El Sebaie. The Effect of Mischmetal, Cooling Rate and Heat Treatment on the Microstructure and Hardness of 319, 356, and 413 Aluminum-silicon Alloys: UQAC; 2006.

125-O. El Sebaie, A. M. Samuel, F. H. Samuel, and H. W. Doty, "The effects of mischmetal, cooling rate and heat treatment on the hardness of A319. 1, A356. 2 and A413. 1 Al–Si casting alloys," Materials Science and Engineering: A, vol. 486, 2008, pp. 241-252.

126-O. El Sebaie , A. M. Samuel, F. H. Samuel, and H. W. Doty, "The effects of mischmetal, cooling rate and heat treatment on the eutectic Si particle characteristics of A319.1, A356.2 and A413.1 Al–Si casting alloys," Materials Science and Engineering: A, vol. 480, 2008, pp. 342-355.

127-O. Elsebaie, F. H. Samuel, and S. Al Kahtani, "Intermetallic phases observed in non-modified and Sr modified Al-Si cast alloys containing mischmetal," International Journal of Cast Metals Research, vol. 26, 2013, pp. 1-15.

128-Y. G. Li, Y. Y. Wu, Z. Qian, and X. F. Liu, "Effect of co-addition of RE, Fe and Mn on the microstructure and performance of A390 alloy," Materials Science and Engineering a-Structural Materials Properties Microstructure and Processing, vol. 527, 2009, pp. 146-149.

129-M. Zhu, Z. Y. Jian, L. J. Yao, C. X. Liu, G. C. Yang, and Y. H. Zhou, "Effect of mischmetal modification treatment on the microstructure, tensile properties, and fracture behavior of Al-7.0%Si-0.3%Mg foundry aluminum alloys," Journal of materials science, vol. 46, 2011, pp. 2685-2694.

130-M. Zhu, Z. Y. Jian, G. C. Yang, and Y. H. Zhou, "Effects of T6 heat treatment on the microstructure, tensile properties, and fracture behavior of the modified A356 alloys," Materials & Design, vol. 36, 2012, pp. 243-249.

131-G. S. Mousavi, M. Emamy, and J. Rassizadehghani, "The effect of mischmetal and heat treatment on the microstructure and tensile properties of A357 Al-Si casting alloy," Materials Science and Engineering a-Structural Materials Properties Microstructure and Processing, vol. 556, 2012, pp. 573-581.

132-B. Dang, Z. Y. Jian, and J. F. Xu, "Effects of rare-earth element addition and heat treatment on the microstructures and mechanical properties of Al-25% Si alloy," International Journal of Materials Research, vol. 108, 2017, pp. 269-274.

133-X. Zhang, Z. H. Wang, Z. H. Zhou, and J. M. Xu, "Influence of Rare Earth (Ce and La) Addition on the Performance of Al-3.0 wt%Mg Alloy," Journal of Wuhan University of Technology-Materials Science Edition, vol. 32, 2017, pp. 611-618.

134-D. H. Xiao, J. N. Wang, D. Y. Ding, and H. L. Yang, "Effect of rare earth Ce addition on the microstructure and mechanical properties of an Al–Cu–Mg–Ag alloy," Journal of Alloys and Compounds, vol. 352, 2003, pp. 84-88.

135-D. H. Xiao, J. N. Wang, and D. Y. Ding, "Effect of minor cerium additions on microstructure and mechanical properties of cast Al – Cu – Mg – Ag alloy," Materials Science and Technology, vol. 20, 2004, pp. 1237-1240.

136-H. H. Zhang, H. L. Duan, G. J. Shao, L. P. Xu, J. L. Yin, and B. Yan, "Modification mechanism of cerium on the Al-18Si alloy," Rare Metals, vol. 25, 2006, pp. 11-15.

137-M. Song, K. H. Chen, and L. P. Huang, "Effects of Ce and Ti on the microstructures and mechanical properties of an Al-Cu-Mg-Ag alloy," Rare Metals, vol. 26, 2007, pp. 28-32.

138-M. Song, D. H. Xiao, and F. Q. Zhang, "Effect of Ce on the thermal stability of the Omega phase in an Al-Cu-Mg-Ag alloy," Rare Metals, vol. 28, 2009, pp. 156-159.

139-S. Kores, M. Von~ina, P. Kosec, P. Mrvar, and J. Medved, "Effect of Cerium additions on the AlSi17 casting alloy," Materiali in tehnologije, vol. 44, 2010, pp. 137-140.

140-Y. C. Tsai, S. L. Lee, and C. K. Lin, "Effect of trace Ce addition on the microstructures and mechanical properties of A356 (AL-7SI-0.35 Mg) aluminum alloys," Journal of the Chinese Institute of Engineers, vol. 34, 2011, pp. 609-616.

141-M. Voncina, S. Kores, P. Mrvar, and J. Medved, "Effect of Ce on solidification and mechanical properties of A360 alloy," Journal of Alloys and Compounds, vol. 509, 2011, pp. 7349-7355.

142-M. Voncina, P. Mrvar, M. Petric, and J. Medved, "Microstructure and grain refining performance of Ce on A380 alloy," Journal of Mining and Metallurgy, Section B: Metallurgy, vol. 48, 2012, pp. 265-272.

143-Z. W. Chen, X. L. Hao, J. Zhao, and C. Y. Ma, "Kinetic nucleation of primary alpha(Al) dendrites in Al-7%Si-Mg cast alloys with Ce and Sr additions," Transactions of Nonferrous Metals Society of China, vol. 23, 2013, pp. 3561-3567.

144-Q. L. Li, T. D. Xia, Y. F. Lan, W. J. Zhao, L. Fan, and P. F. Li, "Effect of rare earth cerium addition on the microstructure and tensile properties of hypereutectic Al-20%Si alloy," Journal of Alloys and Compounds, vol. 562, 2013, pp. 25-32.

145-L. Y. Ye, G. Gu, J. Liu, H. C. Jiang, and X. M. Zhang, "Influence of Ce addition on impact properties and microstructures of 2519A aluminum alloy," Materials Science and Engineering: A, vol. 582, 2013, pp. 84-90.

146-S. L. J. Yii, N. M. Anas, M. N. Ramdziah, and A. S. Anasyida, "Microstructural and mechanical properties of Al-20%Si containing cerium," Procedia Chemistry, vol. 19, 2016, pp. 304-310.

147-R. Ahmad, and M. B. A. Asmael, editors. Effect of Cerium Addition and Cooling Rate on Microstructure of ADC12 Eutectic Cast Alloy. Advanced Materials Research; 2015: Trans Tech Publ.

148-R. Ahmad, and M. B. A. Asmael, "Influence of Cerium on Microstructure and Solidification of Eutectic Al–Si Piston Alloy," Materials and Manufacturing Processes, vol. 31, 2015, pp. 1948-1957.

149-H. K. Yi, and D. Zhang, "Morphologies of Si phase and La-rich phase in as-cast hypereutectic Al-Si-xLa alloys," Materials Letters, vol. 57, 2003, pp. 2523-2529.

150-H. K. Yi, and D. Zhang, "Modification effect of pure rare earth metal La on as—cast hypereutectic Al—17% Si alloys," China Nonferrous Metals Society Journal: english, vol. 13, 2003, pp. 358-364.

151-H. K. Yi, D. Zhang, T. Sakata, and H. Mori, "Microstructures and La-rich compounds in a Cu-containing hypereutectic Al-Si alloy," Journal of Alloys and Compounds, vol. 354, 2003, pp. 159-164.

152-Z. Y. Ouyang, X. M. Mao, and M. Hong, "Multiplex modification with rare earth elements and P for hypereutectic Al-Si alloys," Journal of Shanghai University (English Edition), vol. 11, 2007, pp. 400-402.

153-Y. C. Tsai, C. Y. Chou, S. L. Lee, C. K. Lin, J. C. Lin, and S. W. Lim, "Effect of trace La addition on the microstructures and mechanical properties of A356 (Al–7Si–0.35 Mg) aluminum alloys," Journal of Alloys and Compounds, vol. 487, 2009, pp. 157-162.

154-M. Hosseinifar, and D. V. Malakhov, "The Sequence of Intermetallics Formation during the Solidification of an Al-Mg-Si Alloy Containing La," Metallurgical and Materials Transactions A, vol. 42, 2010, pp. 825-833.

155-W. H. Yuan, Z. Y. Liang, C. Y. Zhang, and L. J. Wei, "Effects of La addition on the mechanical properties and thermal-resistant properties of Al-Mg-Si-Zr alloys based on AA 6201," Materials & Design, vol. 34, 2012, pp. 788-792.

156-X. Huang, and H. Yan, "Effect of trace La addition on the microstructure and mechanical property of as-cast ADC12 Al-Alloy," Journal of Wuhan University of Technology-Materials Science Edition, vol. 28, 2013, pp. 202-205.

157-X. C. Song, H. Yan, and F. H. Chen, "Impact of Rare Earth Element La on Microstructure and Hot Crack Resistance of ADC12 Alloy," Journal of Wuhan University of Technology-Materials Science Edition, vol. 33, 2018, pp. 193-197.

158-Y. Chen, Y. Pan, T. Lu, S. W. Tao, and J. L. Wu, "Effects of combinative addition of lanthanum and boron on grain refinement of Al-Si casting alloys," Materials & Design, vol. 64, 2014, pp. 423-426.

159-T. Lu, Y. Pan, J. L. Wu, S. W. Tao, and Y. Chen, "Effects of La addition on the microstructure and tensile properties of Al-Si-Cu-Mg casting alloys," International Journal of Minerals Metallurgy and Materials, vol. 22, 2015, pp. 405-410.

160-R. Ahmad, and M. B. A. Asmael, "Influence of Lanthanum on Solidification, Microstructure, and Mechanical Properties of Eutectic Al-Si Piston Alloy," Journal of Materials Engineering and Performance, vol. 25, 2016, pp. 2799-2813.

161-C. Qiu, S. Miao, X. Li, X. Xia, J. Ding, Y. Wang, and W. Zhao, "Synergistic effect of Sr and La on the microstructure and mechanical properties of A356. 2 alloy," Materials & Design, 2016.

162-P. Tang, W. Li, Y. zhao, k. Wang, W. Li, and F. Zhan, "Influence of strontium and lanthanum simultaneous addition on microstructure and mechanical properties of the secondary Al-Si-Cu-Fe alloy," Journal of Rare Earths, vol. 35, 2017, pp. 485-493.

163-J. Ding, S. Miao, B. Ma, X. Xia, C. Qiu, and X. Chen, "Effect of Solution Treatment on Microstructure and Mechanical Properties of A356. 2 Aluminum Alloy Treated With Al–Sr–La Master Alloy," Advanced Engineering Materials, 2018.

164-C. Li, Y. Pan, T. Lu, L. Jing, and J. Pi, "Effects of Ti and La Additions on the Microstructures and Mechanical Properties of B-Refined and Sr-Modified Al–11Si Alloys," Metals and Materials International, 2018, pp. 1-10.

165-E. Aguirre-De la Torre, R. Pérez-Bustamante, J. Camarillo-Cisneros, C. Gómez-Esparza, H. Medrano-Prieto, and R. Martínez-Sánchez, "Mechanical properties of the A356 aluminum alloy modified with La/Ce," Journal of Rare Earths, vol. 31, 2013, pp. 811-816.

166-S. C. Wang, N. Zhou, D. F. Song, and D. Nong, editors. Effects of La and Ce Mixed Rare Earth on Microstructure and Properties of Al-Mg-Si Aluminum Alloy. Materials Science Forum; 2017: Trans Tech Publ.

167-J. D. Du, D. Y. Ding, Z. Xu, J. C. Zhang, W. L. Zhang, Y. J. Gao, G. Z. Chen, W. G. Chen, X. H. You, R. Z. Chen, Y. W. Huang, and J. S. Tang, "Effect of CeLa addition on the microstructures and mechanical properties of Al-Cu-Mn-Mg-Fe alloy," Materials Characterization, vol. 123, 2017, pp. 42-50.

168-S. A. Alkahtani, E. M. Elgallad, M. M. Tash, A. M. Samuel, and F. H. Samuel, "Effect of Rare Earth Metals on the Microstructure of Al-Si Based Alloys," Materials (Basel), vol. 9, 2016, pp. 45.

169-E. Elgallad, M. Ibrahim, H. Doty, and F. Samuel, "Microstructural characterisation of Al–Si cast alloys containing rare earth additions," Philosophical Magazine, 2018, pp. 1-23.

170-E. M. Elgallad, H. W. Doty, S. A. Alkahtani, and F. H. Samuel, "Effects of La and Ce Addition on the Modification of Al-Si Based Alloys," Advances in Materials Science and Engineering, vol. 2016, 2016.

171-M. G. Mahmoud, A. M. Samuel, H. W. Doty, S. Valtierra, and F. H. Samuel, "Effect of Solidification Rate and Rare Earth Metal Addition on the Microstructural Characteristics and Porosity Formation in A356 Alloy," Advances in Materials Science and Engineering, 2017, pp. 1-15.

172-M. G. Mahmoud, A. M. Samuel, H. W. Doty, S. Valtierra, and F. H. Samuel, "Effect of Rare Earth Metals, Sr, and Ti Addition on the Microstructural Characterization of A413.1 Alloy," Advances in Materials Science and Engineering, vol. 2017, 2017.

173-A. M. Nabawy, A. M. Samuel, S. A. Alkahtani, K. A. Abuhasel, and F. H. Samuel, "Role of cerium, lanthanum, and strontium additions in an Al-Si-Mg (A356) alloy," International Journal of Materials Research, vol. 107, 2016, pp. 446-458.

174-A. M. Samuel, H. W. Doty, S. Valtierra, and F. H. Samuel, "Intermetallic precipitation in rare earth-treated A413.1 alloy: A metallographic study," International Journal of Materials Research, vol. 109, 2018, pp. 157-171.

175-UK Researchers First to Produce High Grade Rare Earths From Coal: @universityofky; 2017 [updated 2017-11-20. Available from: https://uknow.uky.edu/research/uk-researchers-first-produce-high-grade-rare-earths-coal.

176-Global Supplier of Fabricated Products & Machining Parts | Stanford Advanced Materials 2018 [Available from: http://www.samaterials.com/.

177-Differential scanning calorimetry - Wikipedia 2018 [Available from: https://en.wikipedia.org/wiki/Differential_scanning_calorimetry.

178-M. Ghoncheh, S. Shabestari, and M. Abbasi, "Effect of cooling rate on the microstructure and solidification characteristics of Al2024 alloy using computer-aided thermal analysis technique," Journal of Thermal Analysis and Calorimetry, vol. 117, 2014, pp. 1253-1261.

179-M. Djurdjevic, H. Jiang, and J. Sokolowski, "On-line prediction of aluminum–silicon eutectic modification level using thermal analysis," Materials Characterization, vol. 46, 2001, pp. 31-38.

180-A. M. Cardinale, D. Maccio, G. Luciano, E. Canepa, and P. Traverso, "Thermal and corrosion behavior of as cast Al-Si alloys with rare earth elements," Journal of Alloys and Compounds, vol. 695, 2017, pp. 2180-2189.

181-S. C. Zhang, J. F. Leng, Z. B. Wang, Q. Wang, Y. W. Shao, and X. Y. Teng, "Investigation on the modification behavior of A356.2 alloy with Yb-La composite modifier," Materials Research Express, vol. 5, 2018, pp. 016520.

182-X.-h. Ao, S.-m. Xing, B.-s. Yu, and Q.-y. Han, "Effect of Ce addition on microstructures and mechanical properties of A380 aluminum alloy prepared by squeeze-casting," International Journal of Minerals, Metallurgy, and Materials, vol. 25, 2018, pp. 553-564.

183-ImageJ - Wikipedia 2018 [Available from: https://en.wikipedia.org/wiki/ImageJ.

184-L. Alyaldin. Effects of alloying elements on room and high temperature tensile properties of Al-Si-Cu-Mg base alloys [Master Thesis]: Université du Québec à Chicoutimi; 2017.

185-B. L. Gabriel, "SEM: A user's manual for materials science," 1985.

186-Z. Ma, A. M. Samuel, H. W. Doty, and F. H. Samuel. On the Fractography of Impact-Tested Samples of Al-Si Alloys for Automotive Alloys. Fracture Mechanics-Properties, Patterns and Behaviours: InTech; 2016.

187-G. Zhang, J. Zhang, B. Li, and W. Cai, "Double-stage hardening behavior and fracture characteristics of a heavily alloyed Al–Si piston alloy during low-cycle fatigue loading," Materials Science and Engineering: A, vol. 561, 2013, pp. 26-33.

188-G. F. Van der Voort, "Visual examination and light microscopy," ASM Handbook, vol. 12, 1987, pp. 91-165.

189-Q. Wang, "Microstructural effects on the tensile and fracture behavior of aluminum casting alloys A356/357," Metallurgical and Materials Transactions A, vol. 34, 2003, pp. 2887-2899.

190-R. Pérez-Bustamante, A. Reyna-Cruz, D. Acosta-Peña, C. Santillán-Rodríguez, J. Matutes-Aquino, F. Pérez-Bustamante, M. Maldonado-Orozco, J. Aguilar-Santillán, and R. Martínez-Sánchez, "Effect of cerium/lanthanum addition on microstructure and mechanical properties of Al7075 alloy via mechanical alloying and sintering," Journal of Rare Earths, vol. 34, 2016, pp. 420-427.

APPENDICES

Appendix A. SEM IMAGES AND EDS SPECTRA OF Al-15% Ce and Al-15% La MASTER ALLOYS
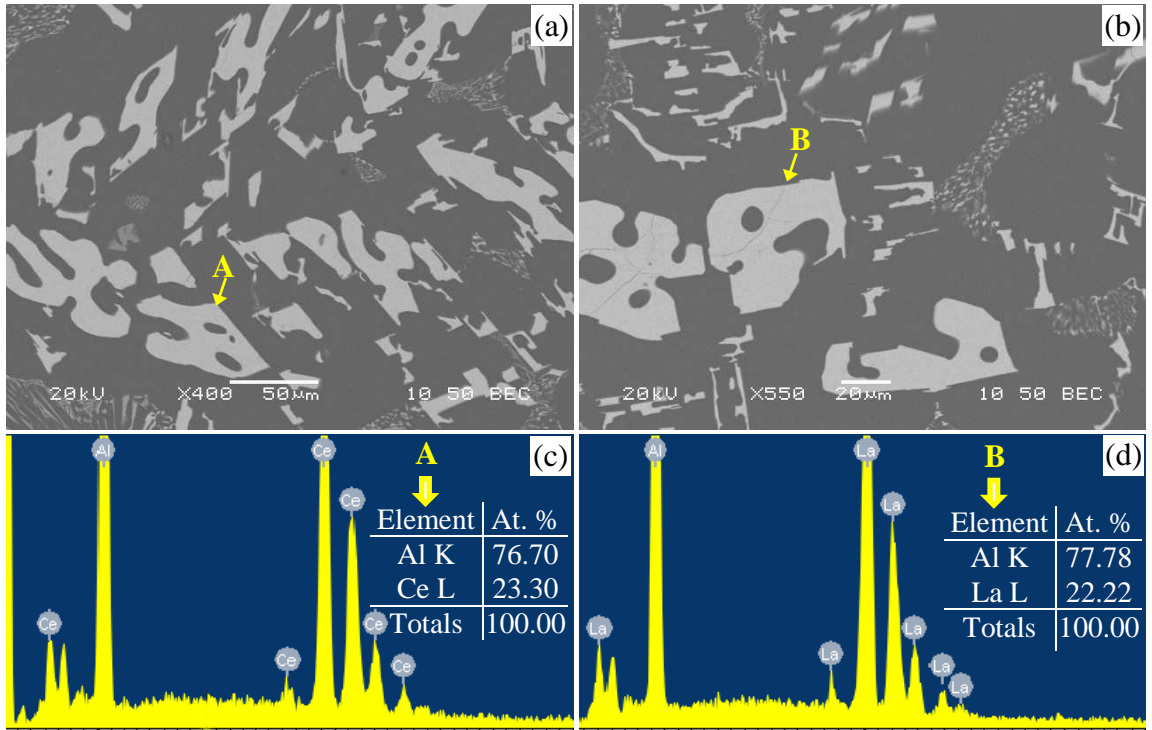
Figure A-1: (a, b) SEM images of (a) Al-15%Ce and (b) Al-15%La master alloys; (c, d) EDS analysis of locations marked A in (a) and B in (b).

Appendix B. ACTUAL CHEMICAL COMPOSITION OF ALLOYS TESTED

Table B.1: Actual chemical composition of the alloys prepared for this study.

Alloy	Cu	Si	Mg	Fe	Mn	Ti	La	Ce	Sr
B0	2.4	1.4	0.39	0.47	0.62	0.11	0.02	<0.01	<0.01
B0 + 0.2 wt.% Ce	2.5	1.3	0.40	0.47	0.62	0.12	0.05	0.26	<0.01
B0 + 0.5 wt.% Ce	2.4	1.2	0.42	0.48	0.60	0.11	0.05	0.59	<0.01
B0 +1.0 wt.% Ce	2.4	1.3	0.45	0.48	0.59	0.10	0.05	1.21	<0.01
B0 + 0.2 wt.% La	2.4	1.4	0.41	0.45	0.61	0.13	0.31	0.05	<0.01
B0 + 0.5 wt.% La	2.4	1.4	0.43	0.46	0.60	0.11	0.64	0.07	<0.01
B0 + 1.0 wt.% La	2.3	1.4	0.53	0.46	0.59	0.15	1.31	0.12	<0.01
Alloy	**Cu**	**Si**	**Mg**	**Fe**	**Mn**	**Ti**	**La**	**Ce**	**Sr**
D0	2.3	7.5	0.41	0.48	0.63	0.11	0.02	<0.01	<0.01
D0 + 0.2 wt.% Ce	2.3	7.4	0.44	0.50	0.61	0.10	0.02	0.26	<0.01
D0 + 0.5 wt.% Ce	2.3	7.3	0.45	0.50	0.61	0.10	0.05	0.57	<0.01
D0 +1.0 wt.% Ce	2.2	7.4	0.44	0.55	0.59	0.10	0.07	1.07	<0.01
D0 + 0.2 wt.% La	2.4	7.3	0.40	0.49	0.60	0.10	0.23	0.02	<0.01
D0 + 0.5 wt.% La	2.4	7.4	0.43	0.51	0.60	0.12	0.54	0.04	<0.01
D0 + 1.0 wt.% La	2.3	7.4	0.42	0.53	0.59	0.10	1.12	0.09	<0.01

Appendix C. OPTIMIZATION OF THE SHT OF B0 AND D0 ALLOYS

The main objective of this step was to examine the effect of different solution heat treatments on the dissolution of the low melting point Cu-rich phases. As it may be noted from Figure C-1, after solutionizing at 495 ºC, Peak A disappeared, indicating the dissolution of the eutectic Al_2Cu and Q-$Al_5Mg_8Si_6Cu_2$ phases. The height of Peak B was also decreased compared to the as-cast condition, indicating that the blocky Al_2Cu phase was partially dissolved. Increasing the temperature or the time of the solution treatment further decreased the height of Peak B or, in other words, increased the dissolution of the blocky Al_2Cu, as demonstrated by the DSC curve of the sample solutionized at 510ºC for 8h, as shown in Figure C-1. Based on these observations, solution heat treatment at 510ºC for 8h was adopted for both B0 and D0 alloys.

Tensile test was carried out on samples of the alloys tested to study the effect of solution heat treatment parameters (temperature and time) one the tensile properties (UTS, YS, and %El) of B0 and D0 in order to support the DSC results. It may be seen from Figure C-2 that the results obtained from the tensile tests are in accordance with the DSC results, where the alloys solution treated at 510 ºC for 8h exhibited better properties than those solution treated at 495 ºC for 5h. When the solution treatment changes from 510ºC for 8h to 495 ºC for 5h this leads to an increase in the UTS and YS of B0 alloys from 324 MPa to 349 MPa and 278 MPa to 348 MPa, respectively, with negligible drop in ductility from 2.28% to 2.17%, as shown in Figure C-2. Whereas with D0 alloy, Figure C-2 indicates that the strength values increase from 357 to 382 MPa (UTS) and from 346 to 361 MPa (YS), with a small increase in the %El from 0.85% to 0.97%. Based on these results, the solution heat treatment of 510 ºC for 8h has was applied to all the samples tested in the current study.
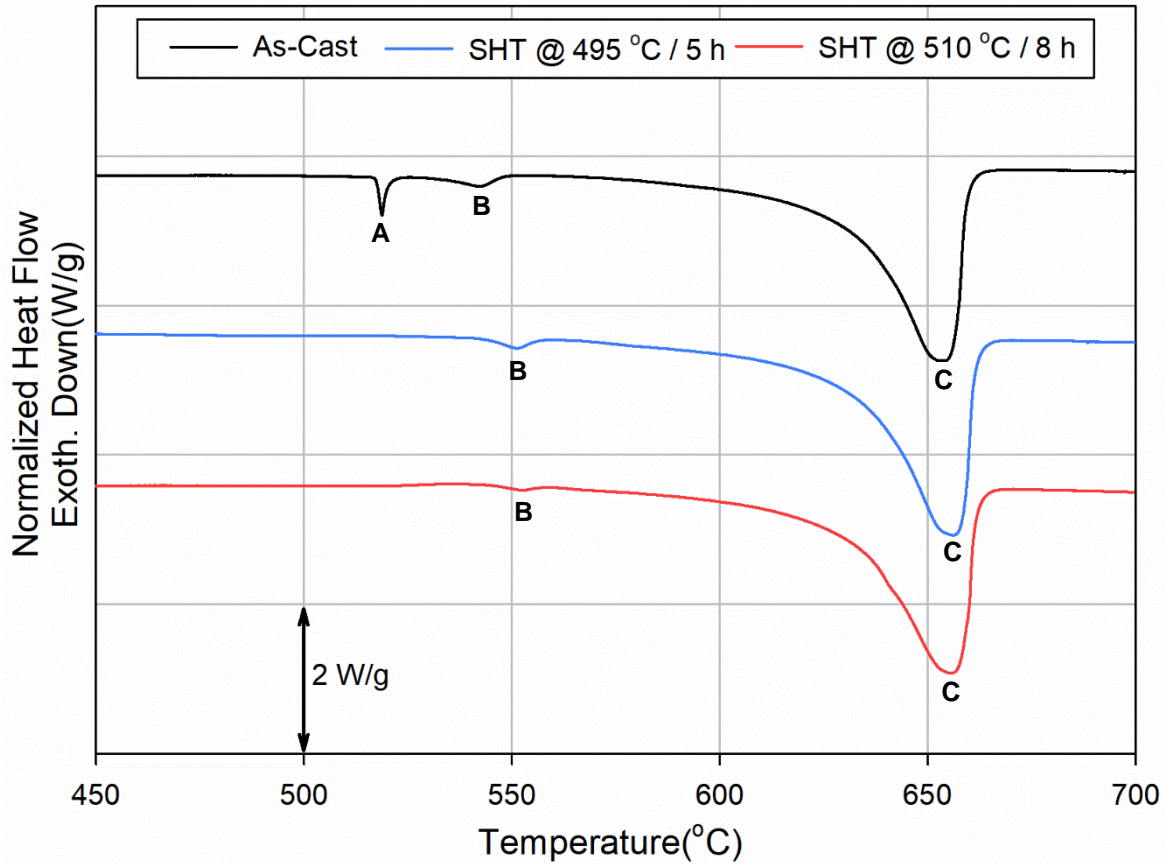
Figure C-1: DSC melting curves of B0 alloy in the as-cast and different solution heat-treated (SHT) conditions.
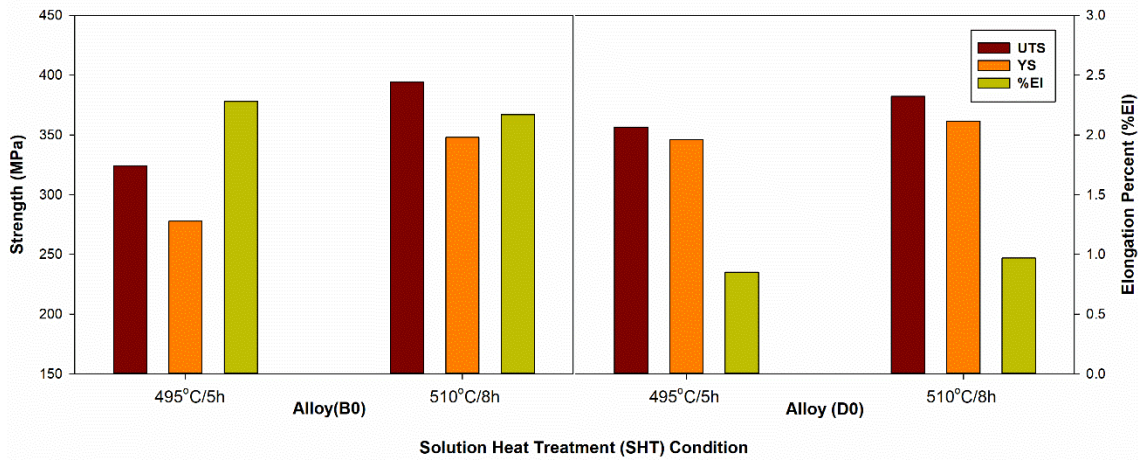
Figure C-2: Effect of solution heat teatment condition on the tensile properties of B0 and D0 alloys.

Appendix D. THERMAL ANALYSIS DATA SMOOTHING PROGRAM CODE
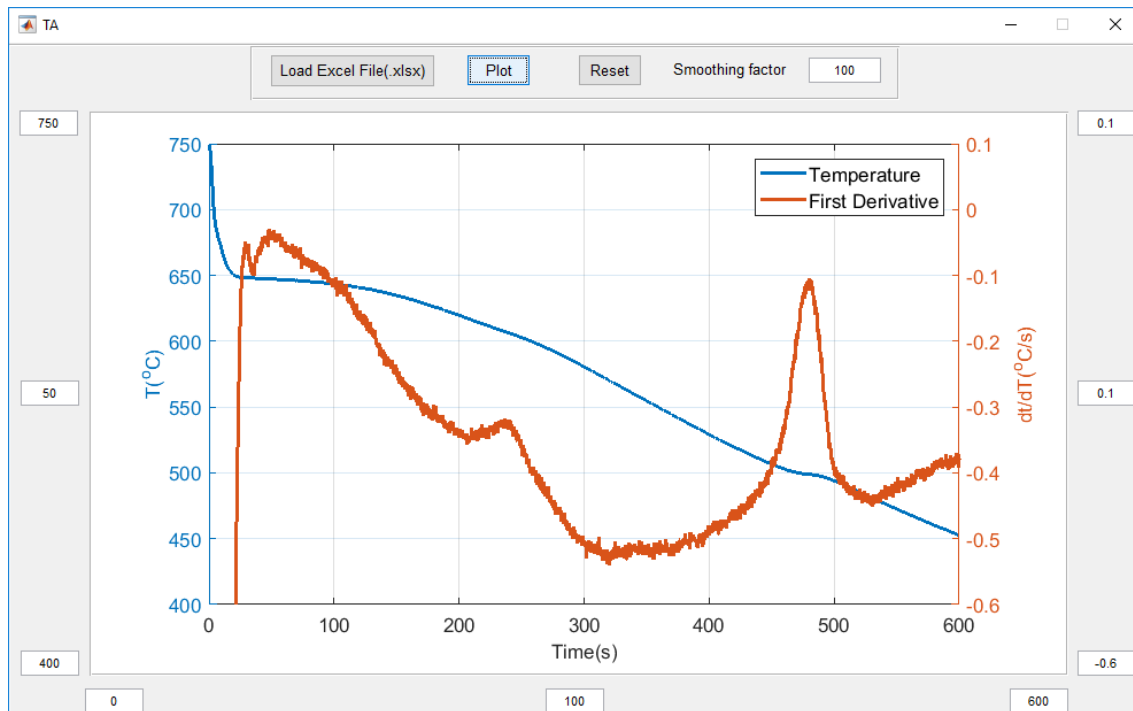
Figure D-1: Graphical user interface of the thermal analysis data smoothing program.

```
function varargout = TA(varargin)
gui_Singleton = 1;
gui_State = struct('gui_Name',        mfilename, ...
                   'gui_Singleton',  gui_Singleton, ...
                   'gui_OpeningFcn', @TA_OpeningFcn, ...
                   'gui_OutputFcn',  @TA_OutputFcn, ...
                   'gui_LayoutFcn',  [] , ...
                   'gui_Callback',    []);
if nargin && ischar(varargin)
    gui_State.gui_Callback = str2func(varargin);
end

if nargout
    [varargout{1:nargout}] = gui_mainfcn(gui_State, varargin{:});
else
    gui_mainfcn(gui_State, varargin{:});
end
function TA_OpeningFcn(hObject, ~, handles, varargin)
handles.output = hObject;
set(handles.Tmax,'string','750');
set(handles.Tmin,'string','400');
set(handles.t1,'string','0');
set(handles.t2,'string','900');
```

```matlab
set(handles.smooth,'string','100');
set(handles.d1,'string','0.1');
set(handles.d2,'string','-0.5');
set(handles.x1,'string','50');
set(handles.x2,'string','100');
set(handles.x3,'string','0.1');
guidata(hObject, handles);
function varargout = TA_OutputFcn(~, ~, handles)
varargout = handles.output;
function pushbuttonLoadXLS_Callback(hObject, ~, handles)
 [FileName,PathName]=uigetfile('*.xlsx');
handles.filename=fullfile(PathName,FileName);
handles.Name=fullfile(FileName);
guidata(hObject,handles);
%%%%%%%%%%%%%%%%%%%%%%%%%%%%%%%%%%%%%%%%%%%%%%%%%%%%%%%%%%%%%%%%%%%%
%function pushbuttonPLOT_Callback(hObject, eventdata, handles)
%%%%%%%%%%%%%%%%%%%%%%%%%%%%
function edit3_Callback(hObject, eventdata, handles)
function edit3_CreateFcn(hObject, eventdata, handles)
if ispc && isequal(get(hObject,'BackgroundColor'),
get(0,'defaultUicontrolBackgroundColor'))
    set(hObject,'BackgroundColor','white');
end
function axes2_CreateFcn(hObject, eventdata, handles)
function pushbutton3_Callback(hObject, eventdata, handles)
function popupmenu1_Callback(hObject, eventdata, handles)
function popupmenu1_CreateFcn(hObject, eventdata, handles)
if ispc && isequal(get(hObject,'BackgroundColor'),
get(0,'defaultUicontrolBackgroundColor'))
    set(hObject,'BackgroundColor','white');
end
 function PLOT_Callback(hObject, eventdata, handles)
t1=str2num(get(handles.Tmax,'string'));
t2=str2num(get(handles.Tmin,'string'));
t3=str2num(get(handles.t1,'string'));
t4=str2num(get(handles.t2,'string'));
t5=str2num(get(handles.smooth,'string'));
t6=str2num(get(handles.d1,'string'));
t7=str2num(get(handles.d2,'string'));
t8=str2num(get(handles.x1,'string'));
t9=str2num(get(handles.x2,'string'));
t10=str2num(get(handles.x3,'string'));
filename=handles.filename;
Name=handles.Name;
[Mat,txt,raw]=xlsread(filename);
t_Mat=Mat(:,1);
T_Mat =Mat(:,2);
d_Mat =diff([eps; T_Mat(:)])./diff([eps; t_Mat(:)]);
Sd_Mat =diff([eps;d_Mat(:)])./diff([eps; t_Mat(:)]);

%%%%%%%%%%%%%%%%%%%%%%%%%%%%%
d_Mat_S=smooth(t_Mat,d_Mat,t5,'moving');
Sd_Mat_S=smooth(t_Mat,Sd_Mat,t5,'moving');
T_Mat_S=smooth(t_Mat,T_Mat,t5,'moving');
[t_Mat_S,ind_Mat]=sort(t_Mat);
```

```matlab
%%%%%%%%%%%%%%%%%%%%%%%%%%%%
[ax, h1,
h2]=plotyy(handles.axes4,t_Mat,T_Mat,t_Mat_S,d_Mat_S(ind_Mat))
grid on
set(h1,'linewidth',2)
set(h2,'linewidth',2)
set(ax(2),'YLim',[t7 t6],'fontSize',13)
set(ax(2),'YTick',[t7:t10:t6],'fontSize',13)
set(ax(1),'YLim',[t2 t1],'fontSize',13)
set(ax(1),'YTick',[t2:t8:t1],'fontSize',13)
set(ax(1),'Xlim',[t3 t4],'fontSize',13)
set(ax(1),'XTick',[t3:t9:t4],'fontSize',13)
set(ax(2),'Xlim',[t3 t4],'fontSize',13)
set(ax(2),'XTick',[t3:t9:t4],'fontSize',13)
set(legend('location','NorthEast','Temperature','First
Derivative'),'fontsize',13)
xlabel('Time(s)','fontsize',13)
ylabel(ax(1),'T(^oC)' ,'fontsize',13)
ylabel(ax(2),'dt/dT(^oC/s)' ,'fontsize',13)
col_header={'Time','Temperature','Smotthed time','Smotthed
Temperature','Smotthed First Derivative'};
xlswrite(Name,[t_Mat(:),T_Mat(:),t_Mat_S(:),T_Mat_S(:),d_Mat_S(:)]
,'Sheet1','A2')
xlswrite(Name,col_header,'Sheet1','A1')
function edit4_Callback(hObject, eventdata, handles)
function edit4_CreateFcn(hObject, eventdata, handles)
if ispc && isequal(get(hObject,'BackgroundColor'),
get(0,'defaultUicontrolBackgroundColor'))
    set(hObject,'BackgroundColor','white');
end
function text5_CreateFcn(hObject, eventdata, handles)
function pushbutton5_Callback(hObject, eventdata, handles)
clear all
cla reset;
function edit6_Callback(hObject, eventdata, handles)
function edit6_CreateFcn(hObject, eventdata, handles)
if ispc && isequal(get(hObject,'BackgroundColor'),
get(0,'defaultUicontrolBackgroundColor'))
    set(hObject,'BackgroundColor','white');
end
function edit7_Callback(hObject, eventdata, handles)
function edit7_CreateFcn(hObject, eventdata, handles)
if ispc && isequal(get(hObject,'BackgroundColor'),
get(0,'defaultUicontrolBackgroundColor'))
    set(hObject,'BackgroundColor','white');
end
function Tmax_Callback(hObject, eventdata, handles)
function Tmax_CreateFcn(hObject, eventdata, handles)
if ispc && isequal(get(hObject,'BackgroundColor'),
get(0,'defaultUicontrolBackgroundColor'))
    set(hObject,'BackgroundColor','white');
end
function Tmin_Callback(hObject, eventdata, handles)
function Tmin_CreateFcn(hObject, eventdata, handles)
if ispc && isequal(get(hObject,'BackgroundColor'),
get(0,'defaultUicontrolBackgroundColor'))
    set(hObject,'BackgroundColor','white');
```

```matlab
end
function t1_Callback(hObject, eventdata, handles)
function t1_CreateFcn(hObject, eventdata, handles)
if ispc && isequal(get(hObject,'BackgroundColor'),
get(0,'defaultUicontrolBackgroundColor'))
    set(hObject,'BackgroundColor','white');
end
function t2_Callback(hObject, eventdata, handles)
function t2_CreateFcn(hObject, eventdata, handles)
if ispc && isequal(get(hObject,'BackgroundColor'),
get(0,'defaultUicontrolBackgroundColor'))
    set(hObject,'BackgroundColor','white');
end
function smooth_Callback(hObject, eventdata, handles)
function smooth_CreateFcn(hObject, eventdata, handles)
if ispc && isequal(get(hObject,'BackgroundColor'),
get(0,'defaultUicontrolBackgroundColor'))
    set(hObject,'BackgroundColor','white');
end
function d1_Callback(hObject, eventdata, handles)
function d1_CreateFcn(hObject, eventdata, handles)
if ispc && isequal(get(hObject,'BackgroundColor'),
get(0,'defaultUicontrolBackgroundColor'))
    set(hObject,'BackgroundColor','white');
end
function d2_Callback(hObject, eventdata, handles)
function d2_CreateFcn(hObject, eventdata, handles)
if ispc && isequal(get(hObject,'BackgroundColor'),
get(0,'defaultUicontrolBackgroundColor'))
    set(hObject,'BackgroundColor','white');
end
function x1_Callback(hObject, eventdata, handles)
function x1_CreateFcn(hObject, eventdata, handles)
if ispc && isequal(get(hObject,'BackgroundColor'),
get(0,'defaultUicontrolBackgroundColor'))
    set(hObject,'BackgroundColor','white');
end
function x3_Callback(hObject, eventdata, handles)
function x3_CreateFcn(hObject, eventdata, handles)
if ispc && isequal(get(hObject,'BackgroundColor'),
get(0,'defaultUicontrolBackgroundColor'))
    set(hObject,'BackgroundColor','white');
end
function x2_Callback(hObject, eventdata, handles)
function x2_CreateFcn(hObject, eventdata, handles)
if ispc && isequal(get(hObject,'BackgroundColor'),
get(0,'defaultUicontrolBackgroundColor'))
    set(hObject,'BackgroundColor','white');
end
```

Appendix E. METALLOGRAPHIC CHARACTERIZATION IMAGES
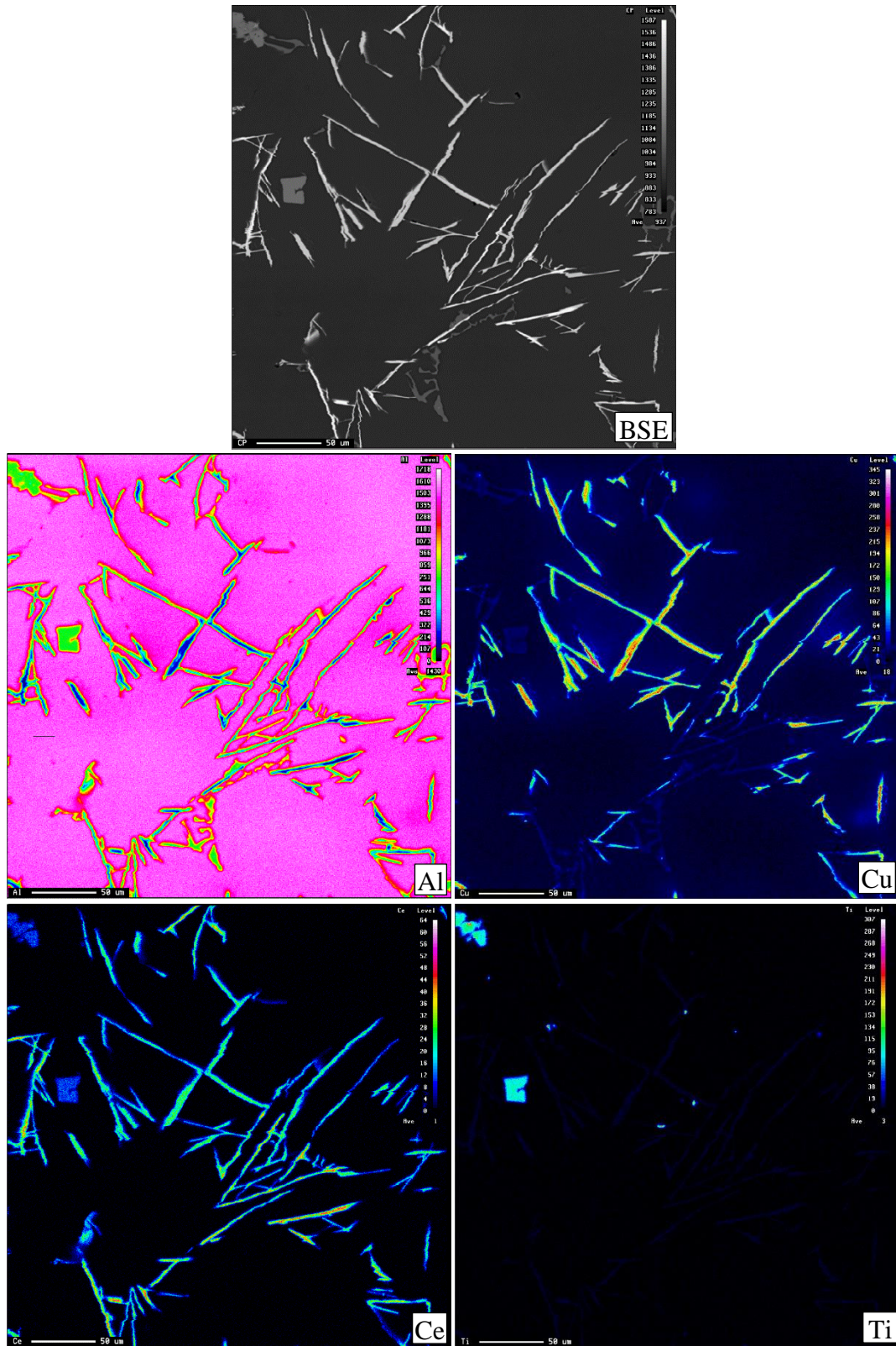
Figure E-1: Backscattered electron image of as-cast B0 alloy with 5.0 wt.% Ce addition, and corresponding X-ray images of Al, Cu, Ce, and Ti.
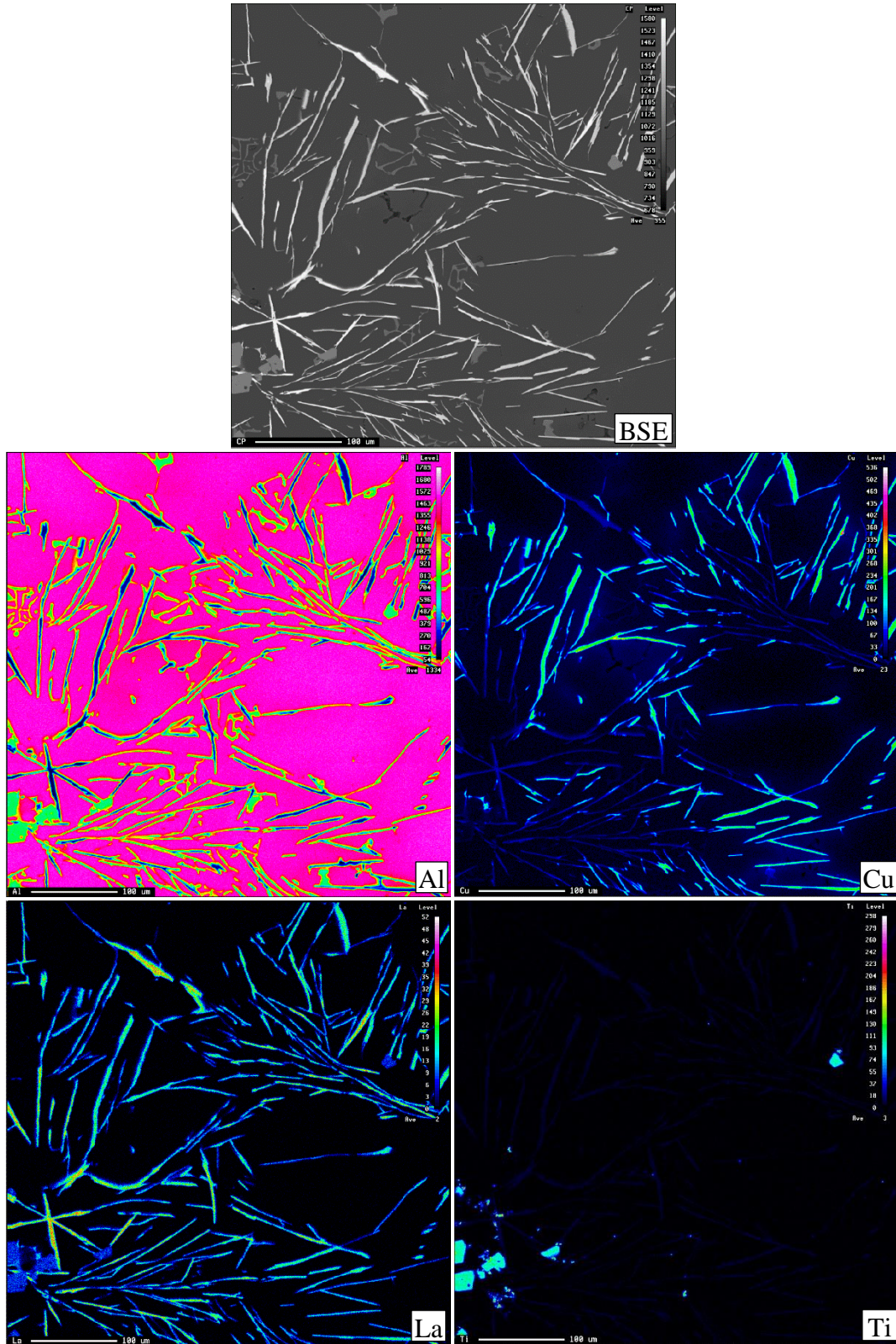
Figure E-2: Backscattered electron image of as-cast B0 alloy with 5.0 wt.% La addition, and corresponding X-ray images of Al, Cu, La and Ti.

Appendix F. EQUATIONS USED FOR CACERCES QUALITY INDEX MODEL ANALYSIS

$$F = \sigma.A_f = P.A_0$$

$$\sigma = P.\frac{A_0}{A_f}$$

$$\frac{A_0}{A_f} = \frac{L_f}{L_0}$$

$$e = \frac{\Delta L}{L_0} = \frac{L_f - L_0}{L_0} = \frac{L_f}{L_0} - 1$$

$$\frac{L_f}{L_0} = e + 1$$

$$\frac{A_0}{A_f} = e + 1$$

$$\sigma = P(1 + e) \rightarrow \boxed{TUTS = UTS(1 + \frac{E_f}{100})}$$

$$TYS = YS + 0.2\%YS \rightarrow \boxed{TYS = YS(1 + 0.002)}$$
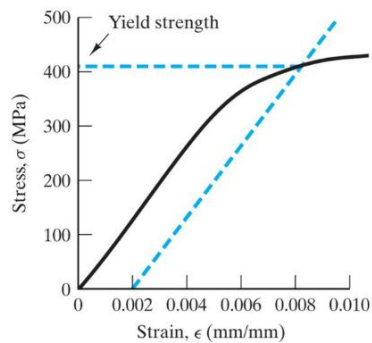
$$\varepsilon = Ln\left(\frac{L_f}{L_0}\right) \rightarrow e = \frac{\Delta L}{L_0} = \frac{L_f - L_0}{L_0} = \frac{L_f}{L_0} - 1 \rightarrow \frac{L_f}{L_0} = 1 + e$$

$$\varepsilon = Ln(1 + e) \rightarrow \boxed{TE_f = LA(1 + \frac{E_f}{100})}$$

$$\sigma_{0.2} = K\,(0.002)^n \rightarrow K = \frac{\sigma_{0.2}}{(0.002)^n}$$

$$\sigma_f = K\,\varepsilon_f{}^n \rightarrow K = \frac{\sigma_f}{\varepsilon_f{}^n}$$

$$\frac{\sigma_{0.2}}{(0.002)^n} = \frac{\sigma_f}{\varepsilon_f{}^n} \rightarrow \frac{\sigma_{0.2}}{\sigma_f} = \frac{(0.002)^n}{\varepsilon_f{}^n} = \left(\frac{0.002}{\varepsilon_f}\right)^n \rightarrow \mathrm{Ln}\left(\frac{\sigma_{0.2}}{\sigma_f}\right) = n\,.\ln\left(\frac{0.002}{\varepsilon_f}\right)$$

$$n = \frac{\ln\left(\dfrac{\sigma_{0.2}}{\sigma_f}\right)}{\ln\left(\dfrac{0.002}{\varepsilon_f}\right)} \rightarrow \boxed{n = \frac{\ln\left(\dfrac{TYS}{TUTS}\right)}{\ln\left(\dfrac{0.002}{TE_f}\right)}}$$

$$\sigma_f = K\,\varepsilon_f{}^n \rightarrow K = \frac{\sigma_f}{\varepsilon_f{}^n} \rightarrow \boxed{K = \frac{TUTS}{TE_f}}$$